ANTENNA LABORATORY
Technical Report No. 52

ANALYSIS AND DESIGN OF THE LOG-PERIODIC DIPOLE ANTENNA

by

ROBERT L. CARREL

Contract AF33(616)-6079
Project No. 9-(13-6279) Task 40572

Sponsored by:
AERONAUTICAL SYSTEMS DIVISION
WRIGHT-PATTERSON AIR FORCE BASE, OHIO

ELECTRICAL ENGINEERING RESEARCH LABORATORY
ENGINEERING EXPERIMENT STATION
UNIVERSITY OF ILLINOIS
URBANA, ILLINOIS

ANTENNA LABORATORY

Technical Report No. 52

ANALYSIS AND DESIGN OF THE LOG-PERIODIC DIPOLE ANTENNA

by

Robert L. Carrel

Contract AF33(616)-6079

Project No. 9-(13-6278) Task 40572

Sponsored by:

AERONAUTICAL SYSTEMS DIVISION

Electrical Engineering Research Laboratory
Engineering Experiment Station
University of Illinois
Urbana, Illinois

ABSTRACT

A mathematical analysis of the logarithmically periodic dipole class of frequency independent antennas, which takes into account the mutual coupling between dipole elements, is described. The input impedance, directivity, and bandwidth, as well as the input current and voltage of the several elements, are calculated. A new concept, the bandwidth of the active region, is formulated and is used to relate the size and operating bandwidth of the antenna. The limiting values of the various parameters that describe the antenna are explored. The results from the mathematical model are shown to be in good agreement with measurements. A step by step procedure is presented which enables one to design a log-periodic dipole antenna over a wide range of input impedance, bandwidth, directivity, and antenna size.

ACKNOWLEDGEMENT

The author wishes to thank all the members of the Antenna Laboratory Staff for their help and encouragement. The guidance of his advisor, Professor G. A. Deschamps, and the continued interest of Professor P. E. Mayes are particularly appreciated. This work would not have been possible without the timely invention of the log-periodic dipole antenna by D. E. Isbell, whose counsel during the initial phase of this research was most helpful. The author is also fortunate to have been associated with V. H. Rumsey and R. H. DuHamel during the time of their original contributions to the field of frequency independent antennas.

Thanks are also due to Ronald Grant and David Levinson, student technicians who built the models and performed many of the measurements. This work was sponsored by the United States Air Force, Wright Air Development Division under contract number AF33(616)-6079, for which the author is grateful.

CONTENTS

CONTENTS (Continued)

ILLUSTRATIONS

ILLUSTRATIONS (Continued)

ILLUSTRATIONS (Continued)

ILLUSTRATIONS (Continued)

ILLUSTRATIONS (Continued)

ILLUSTRATIONS (Continued)

1. INTRODUCTION

The object of this work is to provide a mathematical model of the log-periodic dipole antenna which contains the essential features of the practical antenna and which is amenable to solution. The need for such a model occurs for two reasons. First, the principles of log-periodic antenna design have evolved from the interpretation of laboratory measurements, without the benefit of mathematical analysis. A rigorous formulation of these principles is clearly called for. Second, the task of extending the state of the design art of log-periodic antennas is formidable if carried out on a wholly experimental basis. Even an approximate analysis is quite useful if it lends direction to an experimental program. The conclusions resulting from the solution of the mathematical model proposed herein are sufficiently general to lend insight into the operation of log-periodic dipole antennas, and the results are applicable to the design of LP dipole antennas which must meet given electrical specifications.

Throughout this work it becomes necessary to define as precisely as possible certain concepts relating to wideband antennas, such as "broadband", "frequency independent", "active region", and "end effect". Some of the terms have been objects of disagreement over the past years, and while the definitions herein may not settle the issue, they can provide a common ground of understanding for this work. The terms "wideband" and "broadband" have become so much a part of the engineering vernacular that they express only a notion and must be qualified each time they are used. In the following paragraphs the term "frequency independent" is used. Strictly speaking, there are no frequency independent antennas. However, it

is proposed that a more liberal definition be adopted—one which applies to a special class of antennas. By frequency independence as applied to an antenna, it is meant that the observable characteristics of the antenna such as the field pattern and input impedance vary negligibly over a band of frequencies within the design limits of the antenna, and that this band may be made arbitrarily wide merely by properly extending the geometry of the antenna structure. The ultimate band limits of a given design are determined by non-electrical restrictions: size governs the low frequency limit, and precision of construction governs the high frequency limit.

The idea of frequency independent antennas is based upon the familiar operation of scaling and the principle of similitude[1]. It is well known that the performance of a lossless antenna remains unchanged if its dimensions in terms of wavelength are held constant. Thus, if all dimensions of a lossless antenna are decreased by a factor $\tau < 1$, and the frequency is increased by $1/\tau$, the fields about the two antennas are similar, that is, they differ at most by a constant factor Consider a class of structures which are made up of an infinite number of interconnected "cells" such as shown in Figure 1. Each cell is similar to its neighbor by a constant scale factor τ. Structures of this class are called self-similar because they possess the unique property of transforming into themselves under a uniform expansion by τ or an integral power of τ. If each cell represents an electromagnetic apparatus, the performance of the structure remains the same for all frequencies related by

$$f = f_o \tau^p, \qquad p = 0, \pm 1, \pm 2, \cdots \tag{1}$$

If the structure is a source or sink of electromagnetic waves, then each

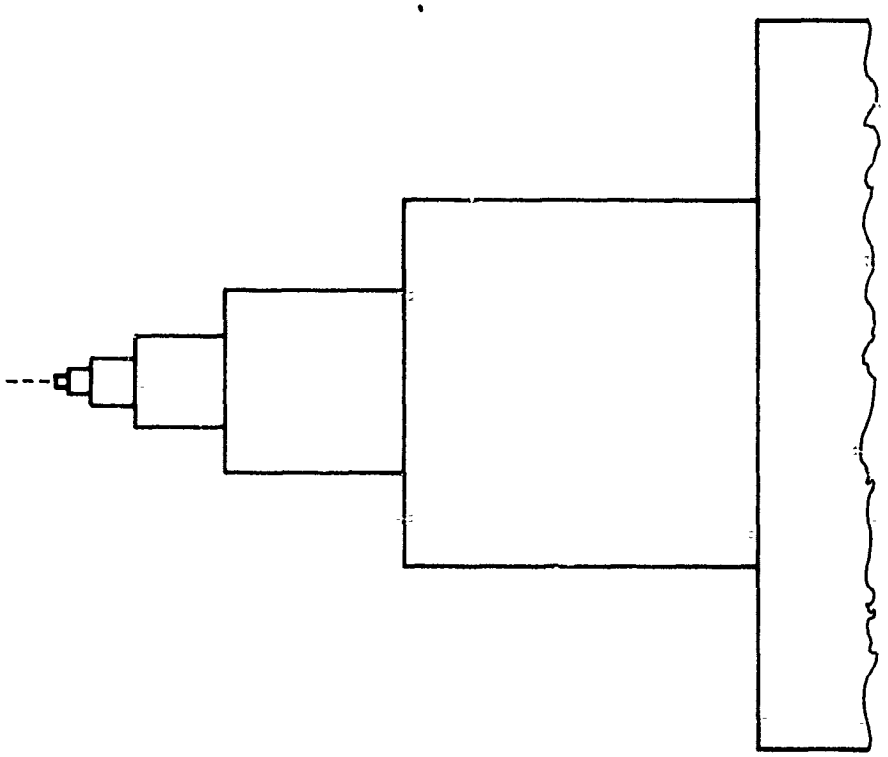

Figure 1. An interconnection of scaled cells resulting in a self-similar structure

cell may contain lumped or distributed generators or loads. To preserve similitude, a generator at frequency f_o in cell n must "scale" into a generator at frequency τf_o in cell n + 1. If it is undesirable to move the generators about, an excitation independent of scaling can be obtained by placing a generator at the small end of the structure. Only the latter method of excitation will be considered.

Such self-similar structures exhibit what is called log-periodic performance. Although the patterns and input impedance may vary with frequency, the variation must be periodic with the logarithm of frequency. In order for the pattern and input impedance to be independent of frequency, the variation in performance over the period, log τ, must be negligible.

To be a practical antenna, the infinite structure must be truncated. That is, the scaling must start with a given small cell and must stop at a given large cell. The requirement that the truncated structure must duplicate the performance of the infinite structure places certain restrictions on the nature of the cells in the aggregate. At a given frequency the electrically small cells must behave as a transmission line. Truncation at the small end is equivalent to the elimination of a section of line; the net effect is a shift in the location of the generator. The electrically large cells must be unexcited, so that their presence or absence makes no difference in the electromagnetic performance at the given frequency. When this is true, the fact that the structure has an end will not be observable, and the "end effect" is said to be eliminated. The foregoing restrictions on the small and large cells require that most of the energy be radiated from a limited number of adjacent, "medium-sized" cells. These

cells constitute the "active region". Thus three regions may be associated with the infinite, self-similar structure—the "transmission region", the "active region", and the "unexcited region". The key problem, therefore, is to determine which finite structures, if any, exhibit performance which approaches that of the infinite structure over a design band.

Let the steps be traced which led to the discovery of several types of frequency independent antennas, leading up to the log-periodic dipole antenna. Prior to 1954 much effort had been expended in attempts at antenna broadbanding. These efforts, for the most part, applied the comparatively advanced knowledge of broadband circuit theory to basically narrow band antennas. Some notable examples resulted[2,3]. However, conventional antennas resisted efforts to extend the usable bandwidth ratio beyond two or three to one.

In the fall of 1954 Rumsey broke the bandwidth barrier in antenna theory and practice with his "angle method"[4]. He stated that if the shape of an antenna were such that it could be specified entirely in terms of angles it would exhibit constant input impedance and patterns independent of frequency because no fixed length is involved in its description. The infinite bi-conical and bi-fin structures shown in Figure 2 are frequency independent,[5,6] but infinite structures are not practical antennas. If one truncates these structures, the frequency independent behavior is lost; the patterns vary with frequency. The variation with frequency is a manifestation of the "end effect", that is, the effect of radiated and/or reflected current at the discontinuity introduced by the truncation. Rumsey suggested that the log-spiral curve defined by $r = \exp(k\varphi)$ could

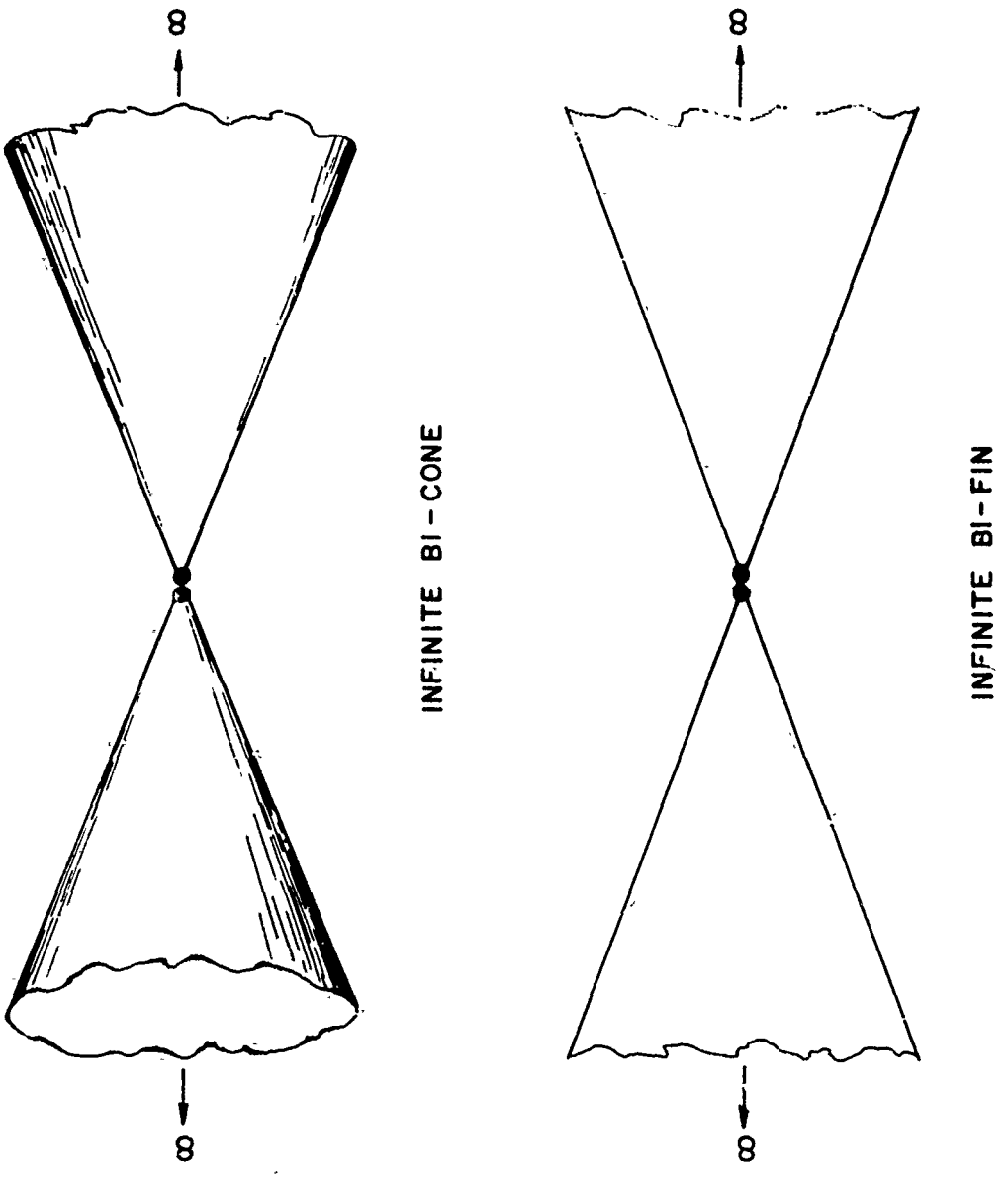

Figure 2. Infinite bi-cone and bi-fin structures

be used to define another infinite structure in terms of angles only. He also showed that the log-spiral family of surfaces are the only surfaces for which an expansion is equivalent to a rotation. For a rotation about the $\theta = 0$ axis this can be expressed symbolically as

$$r = f(\theta,\varphi) = e^{-ac} f(\theta,\varphi + c) \tag{2}$$

The pattern of such a structure rotates with frequency about the $\theta = 0$ axis at a rate which depends on a. A balanced, planar log-spiral antenna is shown in Figure 3.

The log-spiral is an example of a self-similar structure. One cell of the structure is given by the shaded portion of Figure 3. The fact that the expansion from one cell to another can also be accomplished by a rotation sets the log-spiral apart from other self-similar structures in which the expansion must be carried out in a fixed direction. In contrast to the bi-cones and bi-fins, the truncated log-spiral structure is one antenna whose pattern is the same as that of the infinite structure for all wavelengths shorter than twice the length of the truncated spiral arm. The absence of end effect is the result of a rapid diminution of current along the spiral arm. The radiation pattern of the planar log-spiral is bi-directional and centered about the $\theta = 0$ axis. Over a wide range of design parameters the pattern is rotationally symmetric and circularly polarized. The sense of the circular polarization is in the negative φ direction for the log-spiral of Figure 3. The properties of planar and conical log-spiral antennas have been carefully investigated and catalogued by Dyson[7,8].

In 1956 DuHamel[9] considered the possibility of perturbing the smooth geometry of the bi-fin antenna in order to produce a rapid diminution of

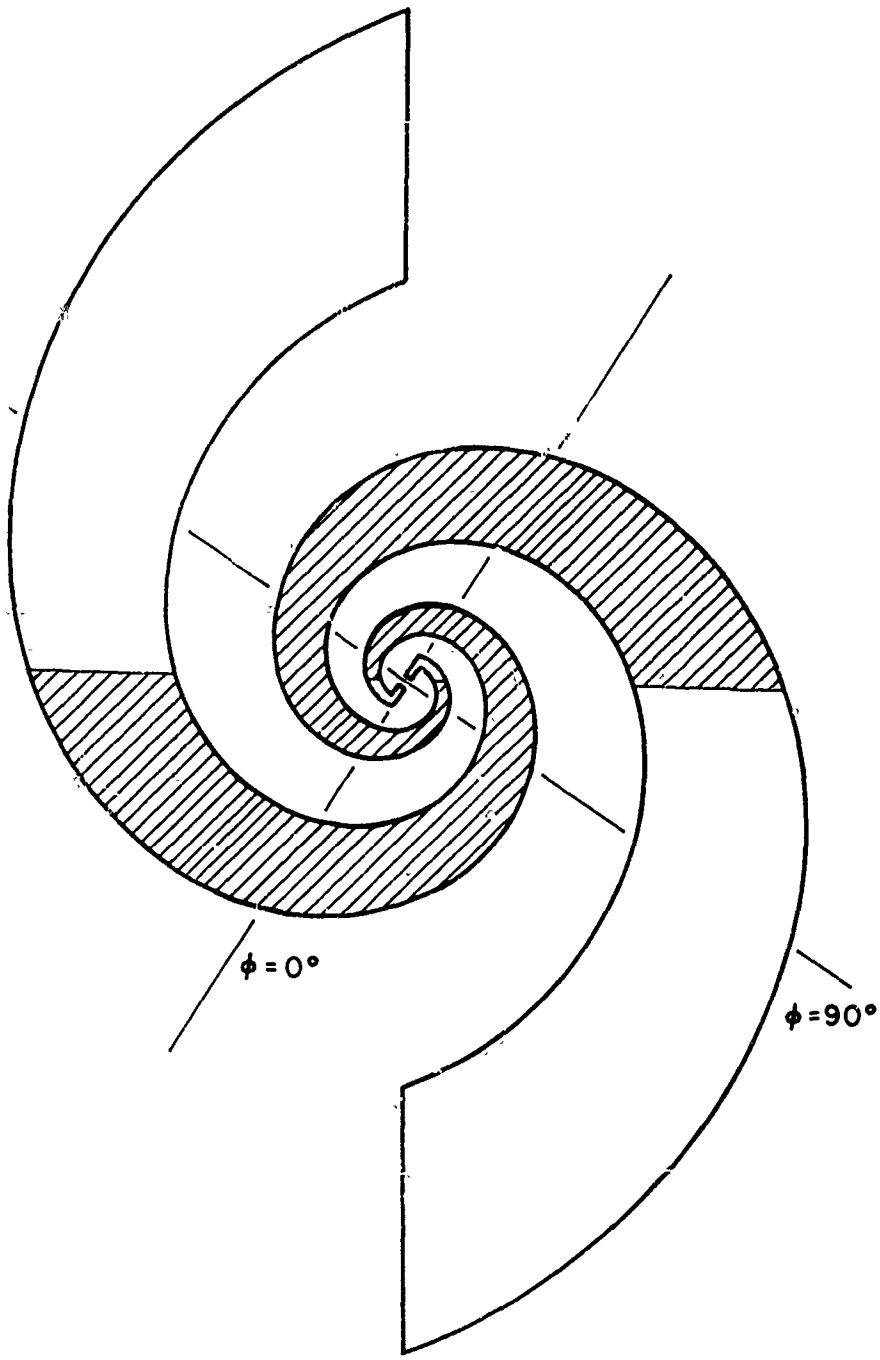

Figure 3. A balanced planar log-spiral antenna
The shaded portion represents one cell

current on the structure. He first considered planar structures which, if extended to infinity, were self-complementary. This was in order to assure a frequency independent input impedance. Figure 4 shows one such structure which consists of a plurality of teeth and slots cut in a bi-fin in such a manner that the widths of successive teeth and slots form a geometric progression. This self-similar structure was called a log-periodic antenna because its geometry repeats periodically with the logarithm of the distance from the apex. The truncated structure exhibited patterns and impedance which varied periodically with the logarithm of frequency; and for a wide range of parameters the variation over a period was negligible, yielding frequency independent operation. The teeth and slots accomplished the necessary reduction of end effect. The radiation pattern of the planar LP is characterized by a bi-directional beam centered on the $\theta = 0$ axis. The antenna is horizontally polarized when oriented as shown in Figure 4. Thus the polarization of the planar LP is orthogonal to the polarization of the smooth bi-fin.

An attempt at providing a uni-directional pattern led to the non-planar LP structures which Isbell[10] investigated. The antenna shown in Figure 5 exhibits a horizontally polarized uni-directional beam off the tip end. Again, a lack of end effect is observed and the patterns are frequency independent over a range of the design parameters. In the LPD antenna of Isbell[11], shown in Figure 6, dipole elements replace the teeth of the non-planar LP and a constant impedance two-wire feeder replaces the central bi-fin section. One observes the frequency independent behavior of the LPD antenna over large ranges of the design parameters.

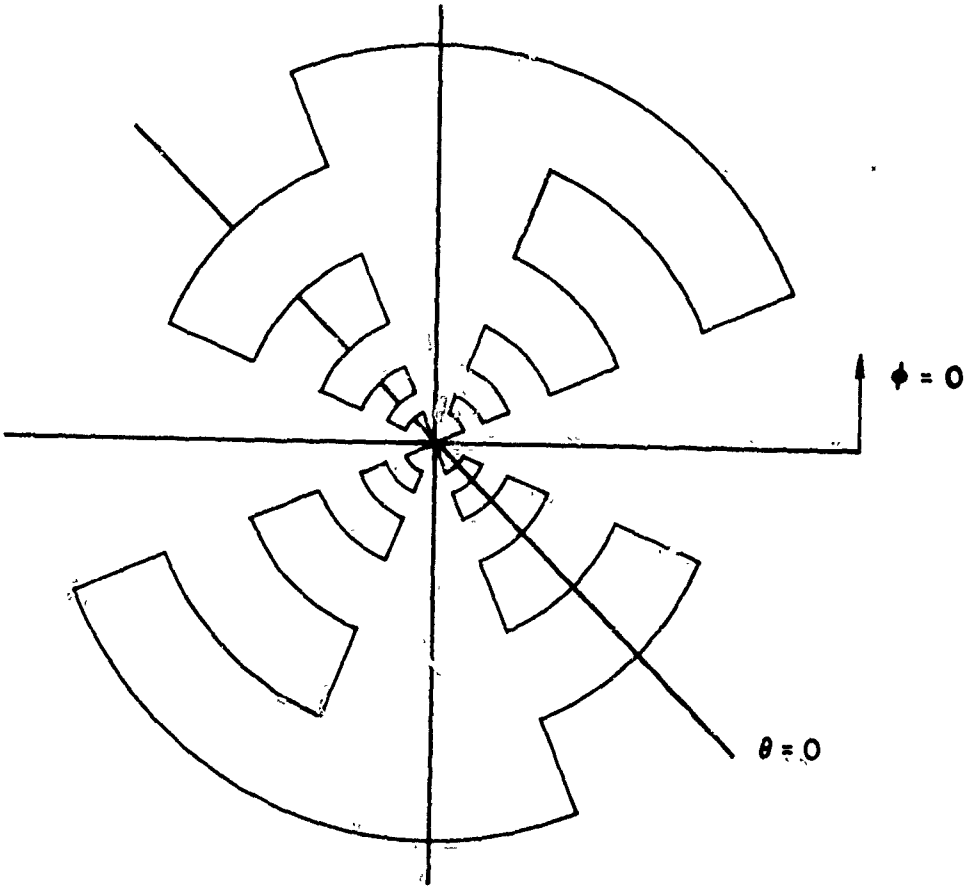

Figure 4. A planar log-periodic antenna

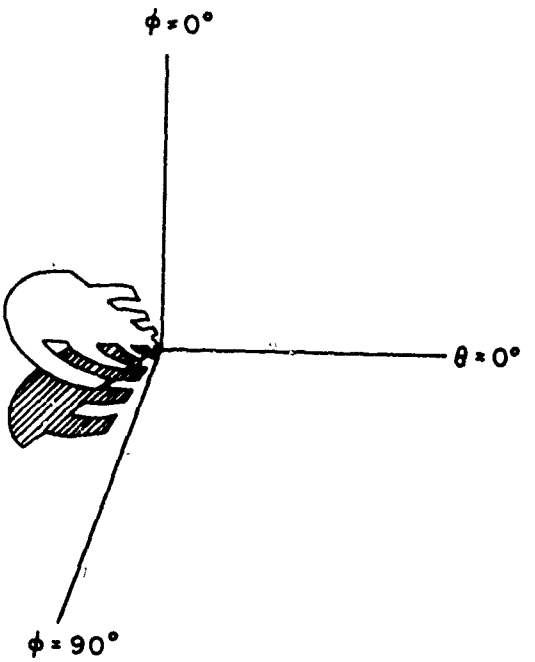

Figure 5. A non-planar log-periodic antenna

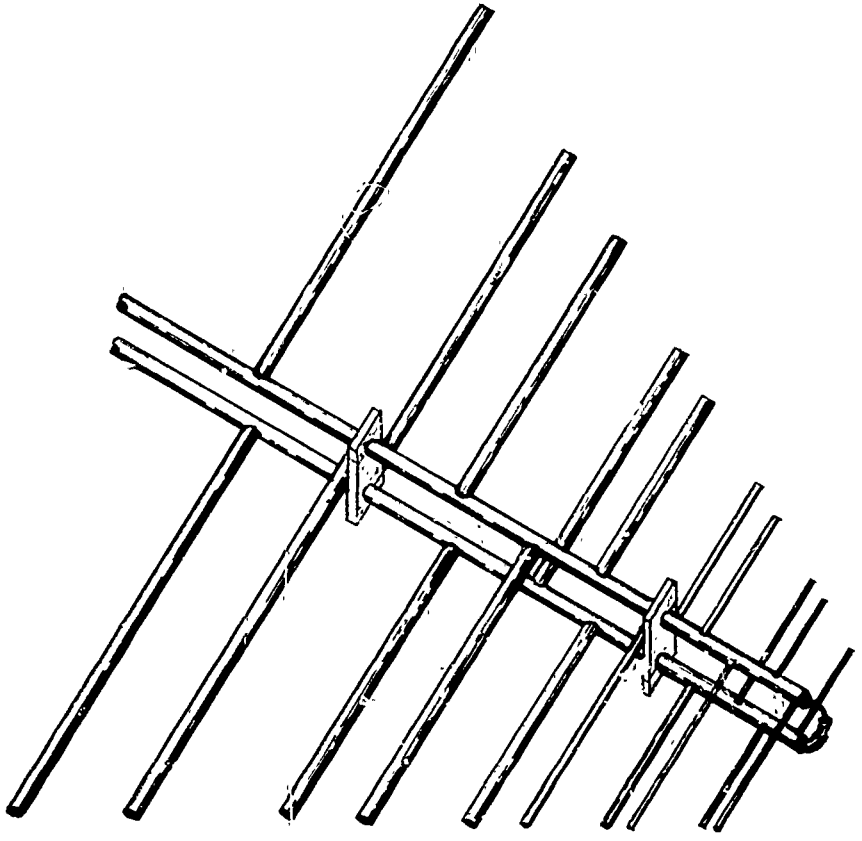

Figure 6. A log-periodic dipole antenna

Table 1 summarizes the preceding discussion by a classification of self-similar structures. There are some finite structures that exhibit only log-periodic electrical characteristics and others that have log-periodic geometry but neither frequency independent nor log-periodic performance. Experience has shown that the latter category contains many members.

The log-periodic dipole antenna was selected for analysis because it is made of conventional linear dipole elements, a fact which allows one to replace the tubular conductors with filamentary currents. In this work electromagnetic field theory is used to calculate the self and mutual impedances of the several dipole elements from an assumption of a sinusoidal form of current on each element. Circuit techniques are used to find the voltage and current at the terminals of each dipole element and the antenna input impedance. Once the element current is known, field techniques are again used to calculate the radiation pattern.

The organization of this work is as follows: The preceding section was an introduction to the idea of frequency independent antennas. In Section 2 the mathematical model of the LPD antenna is formulated using the self and mutual impedances of the several dipole elements. The expressions for input impedance, and voltage and current at the base of each element are determined. The equations for the radiated field and the phase center are also set up. In Section 3 the computed and measured results are displayed and analyzed. Criteria for "optimum" LPD antennas are established. Section 4 presents design information, combining the computed and measured results in simple formulas and nomographs. Section 5 summarizes the work. Appended is a section which considers the computation of the equations of Part 2, and a section devoted to the measurement techniques used in this research.

TABLE 1

Classification of Types of Structures and Their Frequency Response

C, Constant; FI, Frequency Independent; LP, Log-Periodic; V, Variable

Geometry of Structure	Examples	Frequency Response			
		Infinite Structures (no end effects)		Finite Structures (antennas)*	
		Impedance	Fields	Impedance (range of) values	Pattern (type)
Uniform	Bi-Cone Bi-Fin Discone	C	C	V	V
Log-Spiral	Planar Log-Spiral	LP+	LP	FI (50 to 120 ohms)	FI (Bidirectional)
	Conical Log-Spiral	LP	LP	FI (100 to 140 ohms)	FI (Unidirectional)
Log-Periodic	Planar LP	LP+	LP	LP (100 to 200 ohms)	FI (Bidirectional)
	Non-planar	LP	LP	LP (70 to 165 ohms)	FI (Unidirectional)
	LP Dipole	LP	LP	FI (50 to 200 ohms)	FI (Unidirectional)
	LP Zig-Zag	LP	LP	LP	FI (Unidirectional)
	Other	LP	LP	LP or V	LP or V

* The response is for frequencies above a minimum value determined by antenna size.

+ It can be shown that these structures have a constant input impedance if they are self-complementary.

2. FORMULATION OF THE PROBLEM

2.1 Description of the Log-Periodic Dipole Antenna

The log-periodic dipole antenna, shown pictorially in Figure 7 and described by Figure 8, consists of a plurality of parallel, linear dipoles arranged side by side in a plane. The lengths of successive dipole elements form a geometric progression with the common ratio $\tau < 1$. τ is called the scale factor. A line through the ends of the dipole elements on one side of the antenna subtends an angle α with the center line of the antenna at the virtual apex 0. The spacing factor σ is defined as the ratio of the distance between two adjacent elements to twice the length of the larger element, and is a constant for a given antenna. The geometry of the antenna relates σ to τ and α.

$$\sigma = \frac{1}{4}(1 - \tau)\cot \alpha \tag{3}$$

The largest element is called element number 1. The half length of element n is denoted by h_n Therefore,

$$h_n = h_1 \tau^{n-1} \quad . \tag{4}$$

The distance d_n from element n to element n + 1 is given by

$$d_n = d_1 \tau^{n-1} \quad . \tag{5}$$

If a_n is the radius of element number n, the a_n's are given by

$$a_n = a_1 \tau^{n-1} \quad , \tag{6}$$

The ratio of element height to radius is the same for all elements in a given antenna and will be denoted by h/a.

The elements are energized from a balanced, constant impedance feeder,

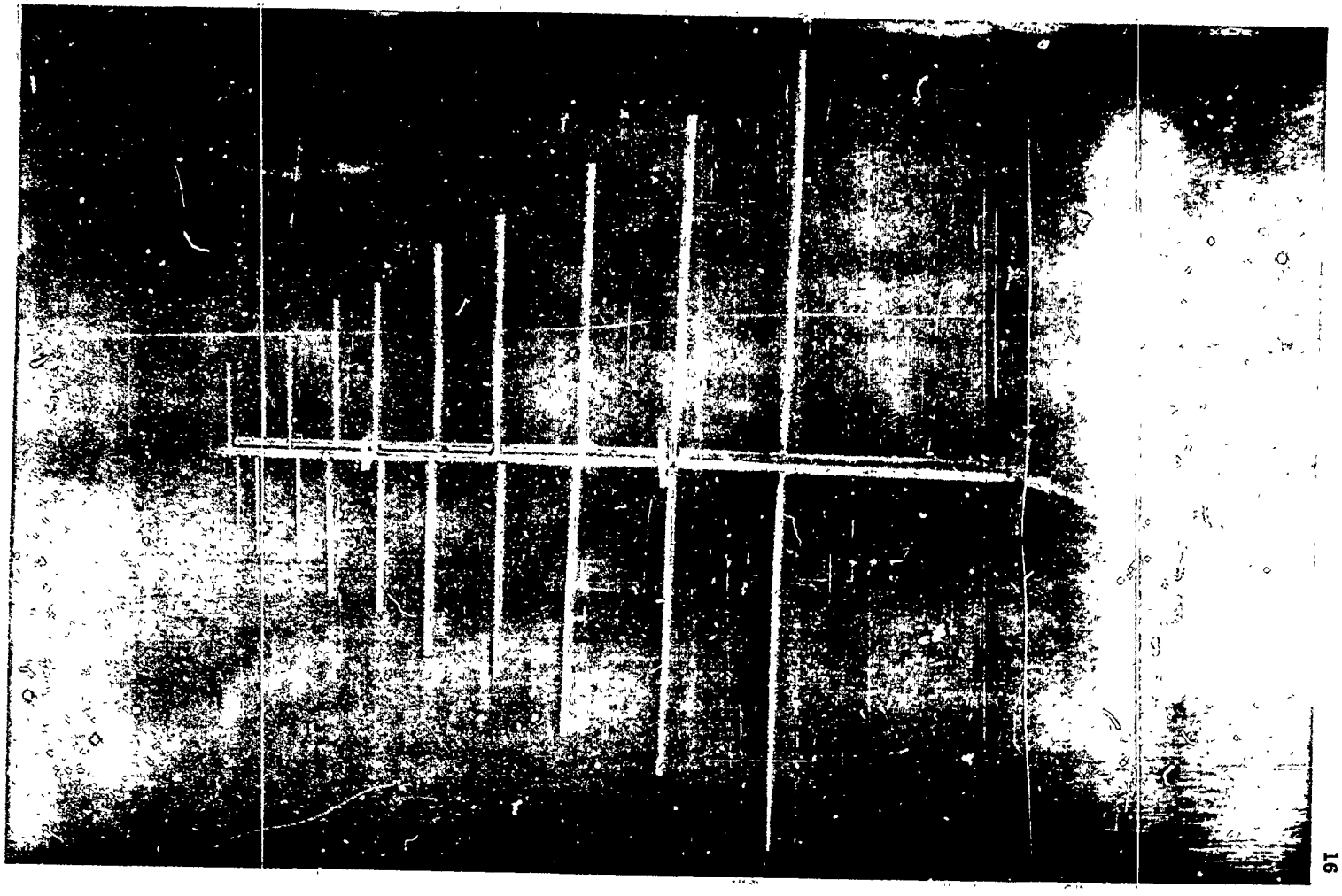

Figure 7. A picture of a log-periodic dipole antenna

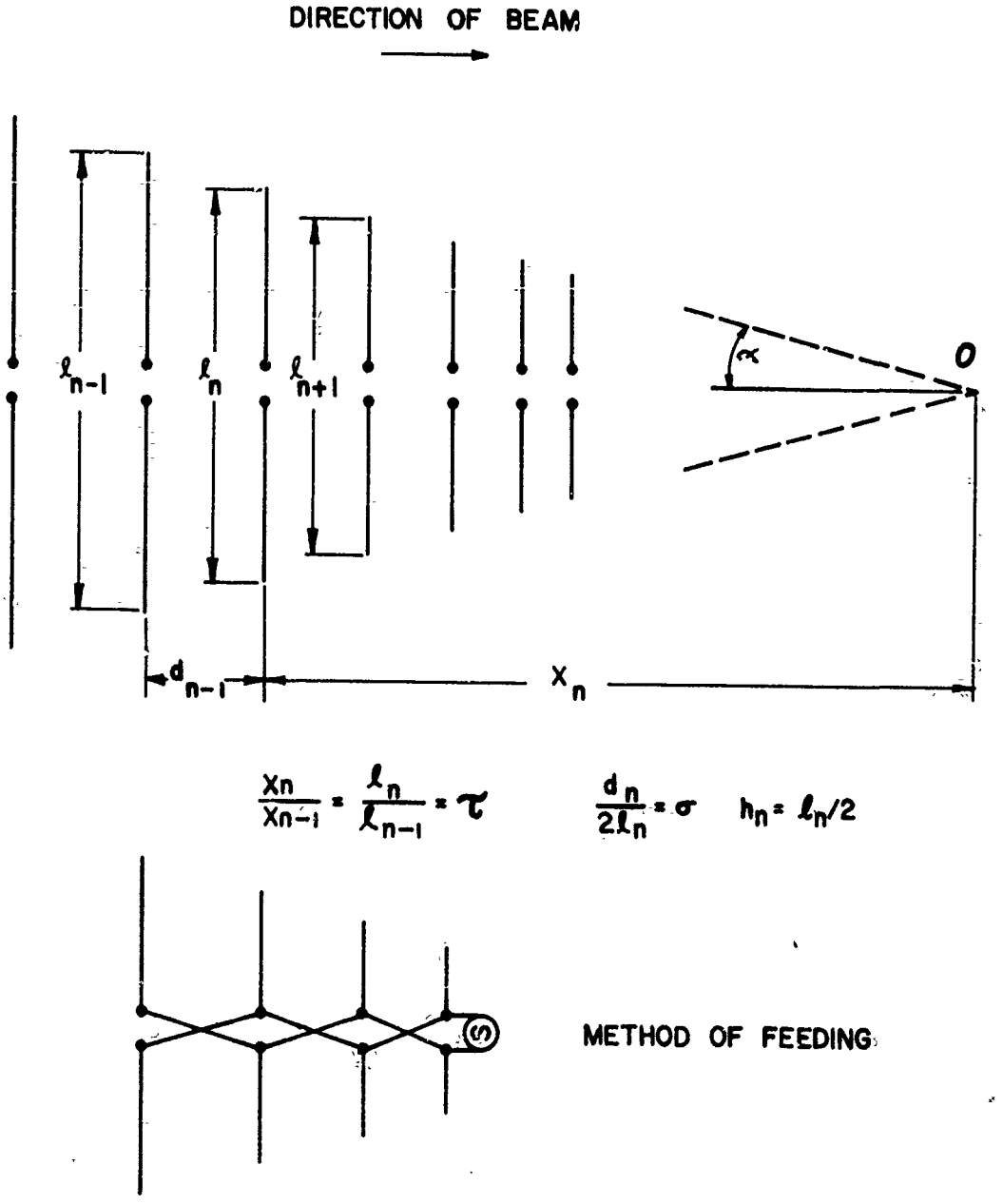

Figure 8. A schematic of the log-periodic dipole antenna, including symbols used in its description

adjacent elements being connected to the feeder in an alternating fashion. Due to the alternating manner in which the elements are connected to the feeder, one cell of the LPD antenna consists of two adjacent dipoles and two sections of feeder. Thus τ as defined above is the square root of the cell scaling factor. Ideally, the feeder should be conical or stepped, to preserve the exact scaling from one cell to the next. However, it has been found in practice that two parallel cylinders can satisfactorily replace the cones as long as the cylinder radius remains small compared to the shortest wavelength of operation. The element feeder configuration is shown in Figure 9. It is seen that the elements do not lie precisely in a plane; the departure therefrom is equal to the feeder spacing, which is always small.

The antenna may be energized from a balanced twin line connected at the junction of the feeder and the smallest element. Alternatively, a coaxial line may be inserted through the back of one of the hollow feeder conductors. The shield of the coax is connected to its half of the feeder at the front of the antenna, the central conductor of the coax is connected to the other side of the feeder as shown in Figure 9 In the latter method the antenna becomes its own balun because the currents on the feeder at the large end of the antenna are negligible, as will be demonstrated later. Due to the diminution of current at the large end, the impedance Z_T which terminates the feeder at that point is immaterial. For definiteness, in most models Z_T will be taken equal to the characteristic impedance Z_o of the feeder. The propagation constant of the feeder alone is β_o and may be different from the free space propagation constant β if dielectric is used.

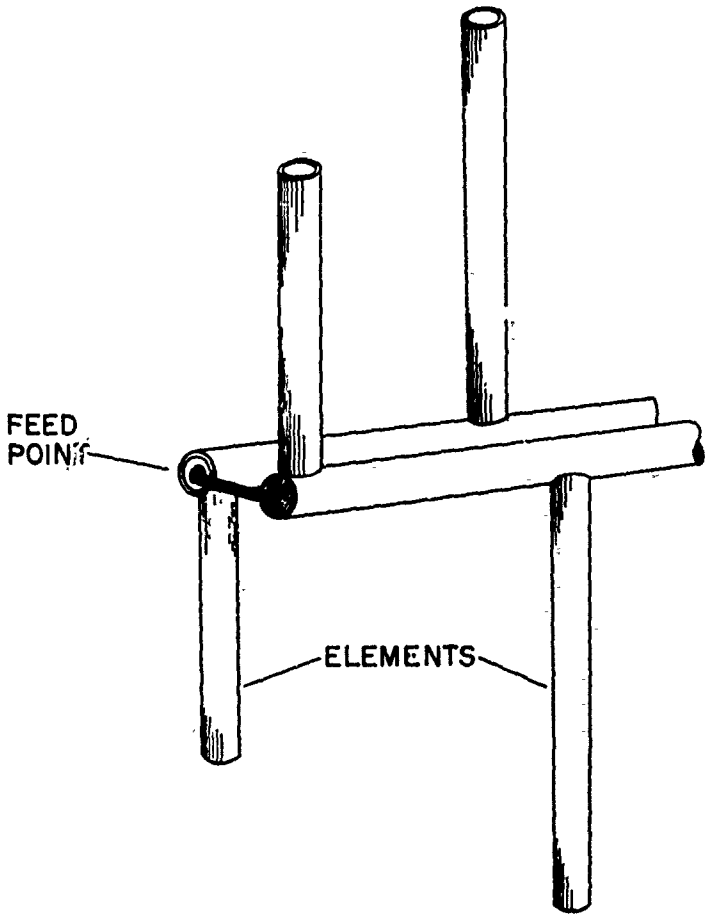

Figure 9. Connection of elements to the balanced feeder and feed point details

When the antenna is operated at a wavelength within the design limits, that is approximately

$$4h_N < \lambda < 4h_1 \tag{7}$$

where N is the total number of elements, a linearly polarized undirectional beam is observed in the direction of the smaller elements. It is found that for any frequency within the design band there are several elements of nearly half-wavelength dimensions. The current in these elements is large compared to the current on the remainder of the elements; these elements contribute most of the radiation, and form the so-called "active region". As the frequency is decreased from f_n to τf_n, the active region shifts from one group of elements to the next. In most cases the variation in performance over a log-period is negligible and frequency independent operation results. Since the LPD antenna is a truncated section of the infinite structure, the performance of the antenna approaches that of the infinite structure only to the extent that a properly constituted active region exists on the antenna. The active region becomes deformed as it begins to include the smallest or largest element on the antenna. When this happens, the upper or lower frequency limit is reached, and it is this phenomenon which determines the useful bandwidth of the antenna.

2.2 Separation of the Problem into Two Parts

The problem may be divided into two parts for the purpose of simplifying the analysis. Finding the voltages and currents along the feeder constitutes the interior part of the problem, and finding the field of the dipole elements constitutes the exterior part of the problem.

Since the feeder has transverse dimensions which are small compared to wavelength, its principal function is to guide and distribute the energy to the radiating elements. There is negligible inductive and capacitive coupling from the feeder to the shunting elements because the fields due to the currents and charges on the feeder are very small at the location of each dipole element.

In the exterior problem, the magnitude and phase of the far field radiation produced by the currents on the elements are of primary interest. The E- and H-plane beamwidths, directivity, front to back ratio, and side lobe level can be determined from the radiation pattern. The phase center can be determined from the phase of the far field.

2.2.1 The Interior Problem

Insofar as the interior problem is concerned, the connection of the dipole elements to the feeder is equivalent to the parallel connection of two N terminal-pair circuits. One circuit consists of the feeder with alternating, properly spaced taps which represent the terminals to which the elements are eventually attached. The feeder circuit is shown schematically in Figure 10b, and includes the arbitrary terminating impedance Z_T. The other circuit, shown schematically in Figure 10a, represents the behavior of the dipole elements as viewed from their input terminals.

Let $\overline{Y}_F$ be the admittance matrix of the feeder circuit. Then

$$\overline{I}_F = \overline{Y}_F \overline{V}_F \tag{8}$$

where $\overline{I}_F$ and $\overline{V}_F$ are column matrices which represent the N driving currents and

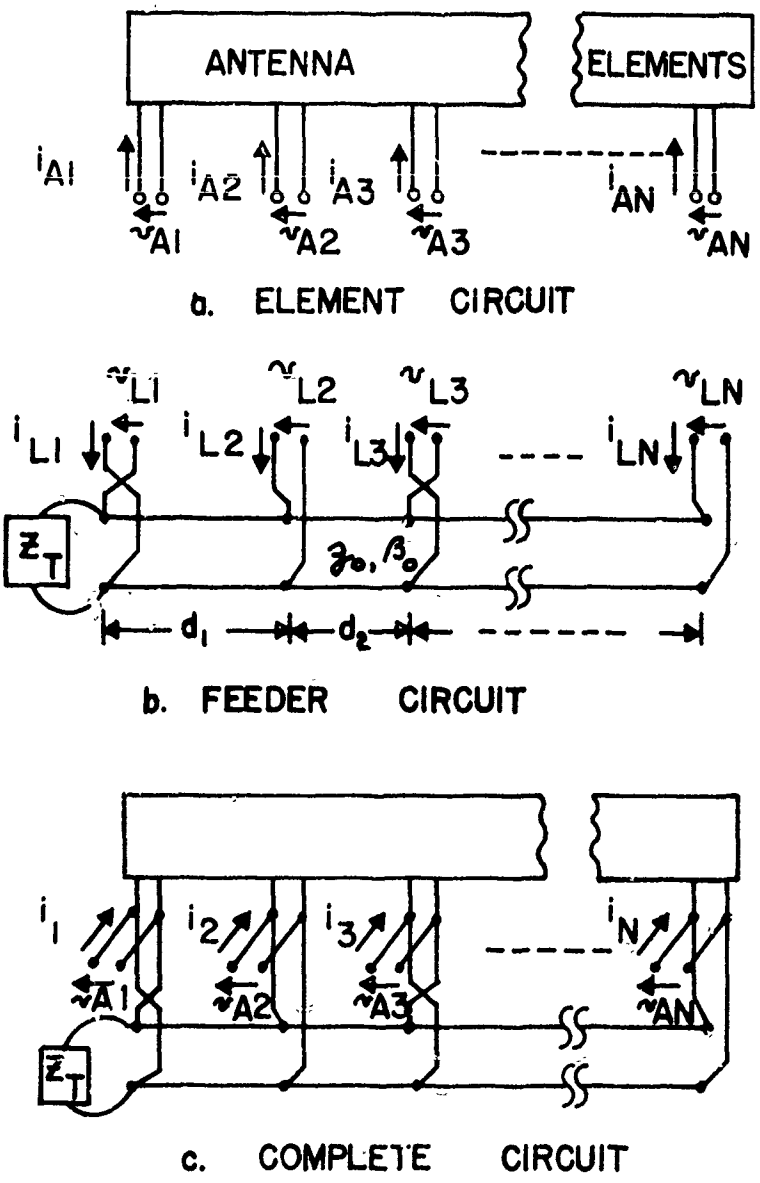

Figure 10. Schematic circuits for the LPD interior problem

response voltages of the feeder circuit. Let $\overline{Y}_A$ be the admittance matrix of the element circuit. Then

$$\overline{I}_A = \overline{Y}_A \overline{V}_A \tag{9}$$

where $\overline{I}_A$ and $\overline{V}_A$ are column matrices which represent the driving currents and response voltages of the element circuit. If the corresponding terminals of the feeder and element circuits are connected in parallel, a new circuit is obtained as shown in Figure 10c. The new response voltage matrix is equal to either $\overline{V}_A$ or $\overline{V}_F$ since they are equivalent. The new driving current matrix is now the sum of $\overline{I}_A$ and $\overline{I}_F$ due to conservation of current at a node. If Equations (8) and (9) are added,

$$\overline{I} = \overline{I}_A + \overline{I}_F = \overline{Y}_A \overline{V}_A + \overline{Y}_F \overline{V}_F \ . \tag{10}$$

$\overline{V}_F$ is set equal to $\overline{V}_A$ and factored,

$$\overline{I} = (\overline{Y}_A + \overline{Y}_F)\overline{V}_A \ . \tag{11}$$

$\overline{I}_A$, the base current at the dipole element terminals, is of primary interest. Therefore

$$\overline{I} = (\overline{Y}_A + \overline{Y}_F)\overline{Z}_A \overline{I}_A \tag{12}$$

where $\overline{Z}_A = \overline{Y}_A^{-1}$. Multiplying $\overline{Z}_A$ inside the parenthesis results in

$$\overline{I} = (\overline{U} + \overline{Y}_F \overline{Z}_A)\overline{I}_A \tag{13}$$

where U is the unit matrix.

The elements of $\bar{I}$ represent the input currents at the terminals of the new circuit of Figure 10c In the actual LP antenna all i_n's are zero except i_N, the current at the feed point, which is the driving current of the antenna. The driving current may be set equal to one ampere. Therefore,

$$\bar{I} = \begin{bmatrix} 0 \\ 0 \\ 0 \\ \cdot \\ \cdot \\ \cdot \\ \cdot \\ \cdot \\ 0 \\ 1 \end{bmatrix} \tag{14}$$

Equation (13) must be solved for $\bar{I}_A$. This can be done by inverting the matrix $\bar{T}$,

$$\bar{T} = \bar{U} + \bar{Y}_F \bar{Z}_A, \tag{15}$$

and multiplying

$$\bar{I}_A = \bar{T}^{-1} \bar{I}, \tag{16}$$

or by solving directly the set of simultaneous Equations (13). The latter method is preferable in terms of computation time and accuracy due to the special form of $\bar{I}$.

Once $\bar{I}_A$ is determined, $\bar{V}_A$ can be found by multiplying

$$\bar{V}_A = \bar{Z}_A \bar{I}_A. \tag{17}$$

Note that $\bar{V}_F$ ($= \bar{V}_A$) is not the voltage between the two feeder members at

each element, but differs therefrom by a phase change of 180° at every other element. The N^{th} element of $\bar{V}_A$ is the voltage across the smallest dipole; it is also the input impedance of the entire antenna since one ampere of driving current was assumed.

The interior problem has been formulated and its solution indicated. It remains to determine explicity the feeder admittance matrix and the element impedance matrix.

2.2.1.1 The Feeder Admittance Matrix

The admittance matrix for one section of transmission line of length d, propagation constant β_o, and characteristic admittance Y_o is

$$\bar{Y} = \begin{bmatrix} -jY_o \cot \beta_o d & +jY_o \csc \beta_o d \\ +jY_o \csc \beta_o d & -jY_o \cot \beta_o d \end{bmatrix} \tag{18}$$

Connecting N-1 of these sections according to the scheme shown in Figure 10 results in the following matrix.

$$\bar{Y}_F = \begin{bmatrix} (Y_T - jY_o \cot \beta_o d_1) & -jY_o \csc \beta_o d_1 & 0 & \cdots 0 \\ -jY_o \csc \beta_o d_1 & -jY_o(\cot \beta_o d_1 + \cot \beta_o d_2) & -jY_o \csc \beta_o d_2 & \cdots 0 \\ 0 & -jY_o \csc \beta_o d_2 & -jY_o(\cot \beta_o d_2 + \cot \beta_o d_3) & \cdots 0 \\ \cdots & \cdots & \cdots & \cdots \\ \cdots & \cdots & \cdots & \cdots \\ 0 & 0 & 0 & \cdots -jY_o \cot \beta_o d_{N-1} \end{bmatrix} \tag{19}$$

Y_T, the terminating admittance, has been added in y_{11}. All the elements off the diagonal by two or more are zero because y_{ij} is the current in terminal i due to a unit voltage at j, all terminal pairs other than j being shorted. The short circuit restricts current flow to sections of line adjacent to the terminals to which the voltage is applied; hence no voltage is induced in the remaining sections.

2.2.1.2 The Element Impedance Matrix

The self and mutual impedances of the dipole elements are calculated using the method of Induced-emf[12]. The following approximations are made in this method:

1. A symmetric sinusoidal current distribution is assumed over the length of each dipole. This assumption is valid as long as the dipole is reasonably less than a full wavelength long, the accuracy being greatest for half-wave and shorter dipoles. Accuracy can be ensured by not using frequencies at which any of the dipole elements are exactly a full wavelength long.

2. In the calculation of mutual impedances the elements are assumed to be infinitesimally thin. This means that the current at a cross-section of the actual dipole has been replaced by an average current concentrated at the center of the cross-section.

3. The mutual term involves only the two dipole elements considered; i.e., the effects of intervening elements are neglected. This assumption is actually implicit in 2 above. In the limiting case of zero element thickness, the current in the first dipole induces a voltage across the terminals of the second, but no current along it since the inductance per unit length of an infinitesimally thin dipole is infinite. Since there is no induced current, there is no reaction on any other dipole, and therefore

no secondary action on the second dipole.

4. The self impedances are calculated from the same formula as the mutuals. The thickness of the dipole is important in the determination of the self reactance. This is taken into account by approximating the self-impedance of a dipole of radius a by the mutual impedance of two identical, infinitesimally thin dipoles spaced a distance $\sqrt{2}a$ apart.

The problem on hand is illustrated in Figure 11, where h_1 and h_2 are the half-lengths of dipoles 1 and 2, d is their separation, z is the coordinate of a typical element dz, and r_o, r_1, and r_2 are distances from fixed points on one dipole to a typical element on the other. The mutual impedance between the two antennas of Figure 11 is defined by

$$Z_{21} = \frac{V_{21}}{I_1(0)} \tag{20}$$

where V_{21} is the open circuit voltage at the terminals of antenna 2 due to a base current $I_1(0)$ at antenna 1. The induced emf at the open terminals of antenna 2 may be found by the application of the reciprocity theorem.

$$\text{emf} = - V_{21} = \frac{1}{I_2(0)} \int_{-h_2}^{h_2} E_{z1}\, I_2(z)\, dz \tag{21}$$

where E_{z1} is the z component of electric field intensity at the location of antenna 2 due to the current on antenna 1, specified by $I_1(0)$, when 2 is removed. The current distribution on antenna 2 is assumed to be sinusoidal and is given by

$$I_2(z) = I_{2\ max} \sin \beta(h_2 - |z|) , \tag{22}$$

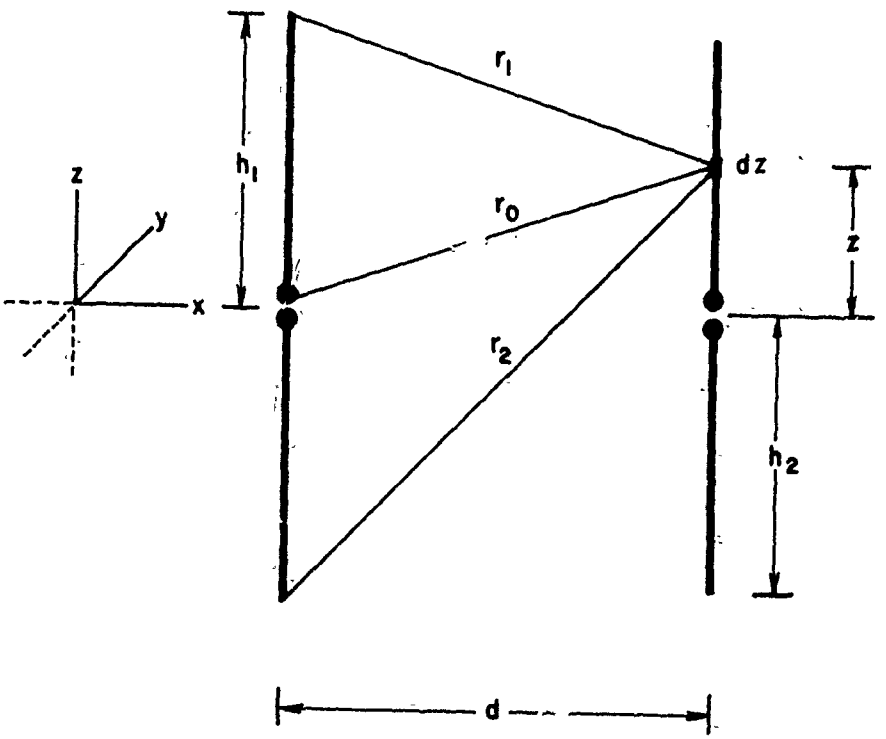

Figure 11. Geometry and notation used in the calculation of mutual impedances

The expression for the parallel component of electric field due to a sinusoidal current distribution in antenna 1 is given by

$$E_{z1} = 30\, I_{1\ max} \left[-j \frac{e^{-j\beta r_1}}{r_1} - j \frac{e^{-j\beta r_2}}{r_2} + \frac{2j \cos \beta h_1 e^{-j\beta r_o}}{r_o} \right]. \quad (23)$$

Inserting (22) and (23) into (21) gives the mutual impedance referred to the base of the antenna.

$$Z_{12} = Z_{21} = -30 \frac{I_{1\ max}\, I_{2\ max}}{I_1(0)\, I_2(0)} \int_{-h_2}^{h_2} \sin \beta(h_2 - |z|) \left[-j \frac{e^{-j\beta r_1}}{r_1} - j \frac{e^{-j\beta r_2}}{r_2} + \frac{2j \cos \beta h_1 e^{-j\beta r_o}}{r_o} \right]. \quad (24)$$

From Figure 11,

$$r_o = \sqrt{d^2 + z^2}$$

$$r_1 = \sqrt{d^2 + (h_1 - z)^2} \quad (25)$$

$$r_2 = \sqrt{d^2 + (h_1 + z)^2}$$

Under the assumption of sinusoidal currents the maximum currents are related to the base currents by

$$I_1(0) = I_{1\ max} \sin \beta h_1$$

$$I_2(0) = I_{2\ max} \sin \beta h_2 \quad (26)$$

Therefore (24) can be rewritten as

$$Z_{12} = -30 \csc \beta h_1 \csc \beta h_2 \int_{-h_2}^{h_2} \sin \beta(h_2 - |z|) \left[\frac{-je^{-j\beta r_1}}{r_1} - \frac{je^{-j\beta r_2}}{r_2} + \frac{2j \cos \beta h_1 e^{-j\beta r_o}}{r_o} \right] dz \tag{27}$$

Integration of (27) yields an expression for the mutual impedance in terms of cosine integral and sine integral functions.

$$Z_{12} = \frac{60}{\cos w_2 - \cos w_1} \left\{ e^{jw_1} [K(u_o)-K(u_1)-K(u_2)] + e^{-jw_1} [K(v_o)-K(v_1)-K(v_2)] + e^{jw_2} [K(u_o')-K(u_1)-K(v_2)] + e^{-jw_2} [K(v_o')-K(v_1)-K(u_2)] + 2K(w_o)[\cos w_1 + \cos w_2] \right\}^* \tag{28}$$

The * denotes the complex conjugate of the expression in the braces.

Here

$$K(x) = Ci(x) + j\, Si(x), \tag{29}$$

where Ci (x) and Si (x) are the cosine integral and sine integral functions of the real argument x; for definitions see Appendix A. Also

$$u_o = \beta \left[\sqrt{d^2 + (h_1 + h_2)^2} - (h_1 + h_2) \right]$$

$$v_o = \beta \left[\sqrt{d^2 + (h_1 + h_2)^2} + (h_1 + h_2) \right]$$

$$u_o' = \beta \left[\sqrt{d^2 + (h_1 - h_2)^2} - (h_1 - h_2) \right]$$

$$v_o' = \beta \left[\sqrt{d^2 + (h_1 - h_2)^2} + (h_1 - h_2) \right]$$

$$u_1 = \beta \left[\sqrt{d^2 + h_1^2} - h_1 \right]$$

$$v_1 = \beta \left[\sqrt{d^2 + h_1^2} + h_1 \right]$$

$$u_2 = \beta \left[\sqrt{d^2 + h_2^2} - h_2 \right] \qquad (30)$$

$$v_2 = \beta \left[\sqrt{d^2 + h_2^2} + h_2 \right]$$

$$w_1 = \beta(h_1 + h_2)$$

$$w_2 = \beta(h_1 - h_2)$$

$$w_o = \beta d$$

where β is the free space propagation constant, d is the separation of the two dipoles, and h_1, and h_2 are the half-lengths of dipoles one and two, respectively.

The self impedance of a dipole antenna can be calculated in a manner similar to that employed in the calculation of mutual impedance. The self reactance of an antenna depends on the induction and electrostatic fields close to the antenna, which in turn depend on the details of the antenna geometry. Figure 12 is pertinent to this discussion. The current which is uniformly distributed around the circumference of the cylinder is assumed to be concentrated at the center. Then the "average" distance S from a point on the cylinder P to a point on a typical ring Q is somewhat greater than the distance S' from P to the center of the ring O[13].

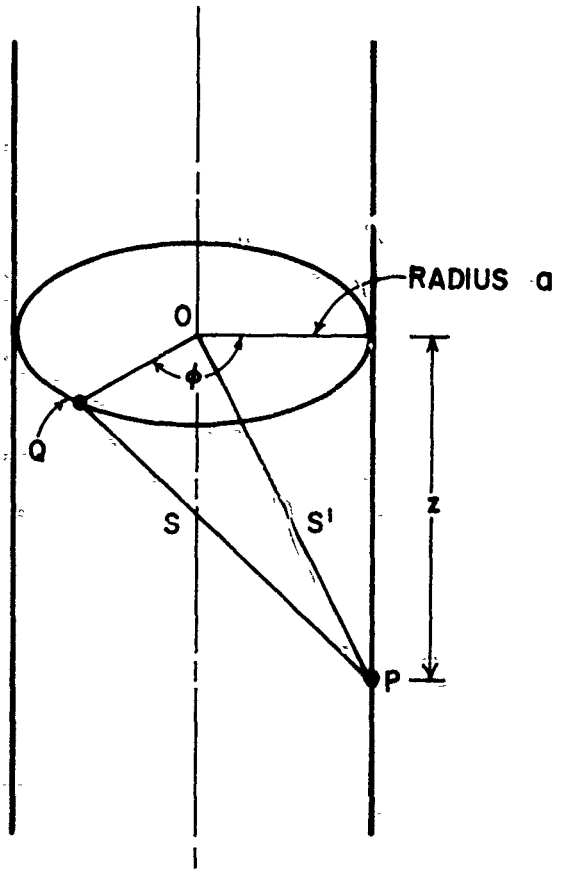

Figure 12. Geometry and notation used in the calculation of self impedances

$$S' = \sqrt{a^2 + z^2}$$

$$S = \sqrt{2a^2(1 - \cos \varphi) + z^2} \tag{31}$$

Factor the expression for S.

$$S = \sqrt{2a^2 + z^2} \cdot \sqrt{1 - \frac{2a^2}{2a^2 + z^2} \cos \varphi} \tag{32}$$

For thin antennas $2a^2/(2a^2 + z^2)$ is small for $z > a$ and may be neglected if $z \gg a$. When $z \approx a$, the current and the field which it produces are in phase. Since the reactance depends on the out of phase components, the contribution to the self reactance is small. Hence the approximate expression for S is given by

$$S \approx \sqrt{2a^2 + z^2} \tag{33}$$

for all z. If r_o, r_1, and r_2 of Equation 25 are replaced by

$$S_o = \sqrt{2a^2 + z^2} \quad ,$$

$$S_1 = \sqrt{2a^2 + (h_1 - z)^2} \quad , \tag{34}$$

and

$$S_2 = \sqrt{2a^2 + (h_1 + z)^2}$$

respectively, it will be found that the final expression for the self impedance of a thin dipole antenna is then given by Equation (28) with h_1 and h_2 set equal to the half length of the dipole and d replaced by $\sqrt{2}a$.

2.2.2 The Exterior Problem

Once the element base currents $\bar{I}_A$ are known from the solution of the interior problem, the far field components can be calculated. The coordinate

system of Figure 13 is used in this section. The antenna is oriented with the dipole elements parallel to the z direction, and the tip of the antenna points in the positive x direction. The z component of vector potential due only to currents on the dipole elements is first determined. The far-field spherical components are then found by a simple transformation.

The vector potential $\bar{A}$ at a distant point P(r, θ, φ) due to a current distribution of density $\bar{J}$ (x, y, z) is given by

$$\bar{A} = \frac{1}{4\pi} \iiint \bar{J}(x', y', z') \frac{e^{-j\beta[r - r'(\hat{r} \cdot \hat{r}')]}}{r} dx'dy'dz'. \qquad (35)$$

Here the integration is performed throughout the volume density of the source $\bar{J}$ (denoted by the primed coordinates). r and r′ are distances from the origin to the observation point P and to the point of integration respectively, while $\hat{r}$ and $\hat{r}'$ are the corresponding unit vectors. For the n^{th} dipole oriented as in Figure 13,

$$\bar{J}_n = \hat{z}\, i_n(z)\, \delta(x - x_n)\, \delta(y), \qquad (36)$$

where $i_n(z)$ is the filamentary current distribution along dipole number n, δ is the Dirac delta function, and $\hat{z}$ is the unit vector in the z direction. Substituting (36) into (35) and using

$$r - r'(\hat{r} \cdot \hat{r}') = r + |x'| \sin\theta \cos\varphi - z' \cos\theta, \qquad (37)$$

one finds

$$A_z = G_o f_z(\theta, \varphi), \qquad (38)$$

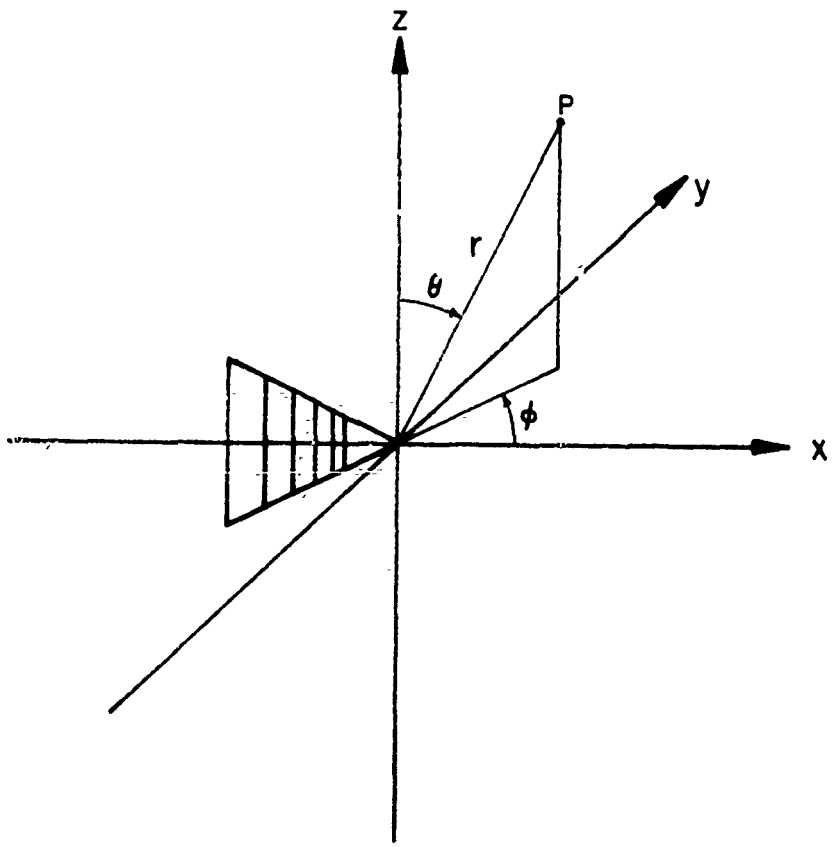

Figure 13. Coordinate system used in the computation of the far field radiation patterns.

where

$$G_o = \frac{e^{-j\beta r}}{4\pi r} \tag{39}$$

and

$$f_{z_n}(\theta,\varphi) = \sum_{n=1}^{N} \int_{-h_n}^{h_n} i_n(z') e^{\pm j\beta(x_n \sin\theta \cos\varphi + z' \cos\theta)} dz' \tag{40}$$

The principal far field components E_θ $(\theta = \frac{\pi}{2}, \varphi)$ and E_θ $(\theta, \varphi = 0, \pi)$ are related to f_z by

$$E_\theta (\theta = \frac{\pi}{2}, \varphi) = P_H(\varphi) = j\beta\eta G_o f_z (\theta = \frac{\pi}{2} ; \varphi) \tag{41}$$

and

$$E_\theta (\theta, \varphi = 0, \pi) = P_E(\theta) = j\beta\eta G_o \sin\theta f_z (\theta, \varphi = 0, \pi) \tag{42}$$

Here P_H and P_E denote the principal H-plane and E-plane patterns, respectively. In the E-plane pattern φ takes on the values 0 or π depending on whether the x coordinate of the point of observation is positive or negative. The magnitude of the far field components are then given by

$$\left| P_H(\varphi) \right| \sim \left| \sum_{n=1}^{N} e^{\pm j\beta x_n \cos\varphi} \int_{-h_n}^{h_n} i_n(z') dz' \right| , \tag{43}$$

and

$$\left| P_E(\theta,\varphi) \right| \sim \left| \sin\theta \sum_{n=1}^{N} e^{\pm j\beta x_n \sin\theta \cos\varphi} \int_{-h_n}^{h_n} i_n(z') e^{j\beta z' \cos\theta} dz' \right| \tag{44}$$

The distribution of current $i_n(z)$ is assumed to be sinusoidal and is related to the element base current i_{An} by

$$i_n(z) = \frac{i_{An} \sin\beta(h_n - |z|)}{\sin\beta h_n} \tag{45}$$

Performing the integration and simplifying yields

$$\left| P_H(\varphi) \right| \sim \left| \sum_{n=1}^{N} \frac{i_{An}(1 - \cos \beta h_n)}{\sin \beta h_n} e^{+j\beta x_n \cos \varphi} \right| , \qquad (46)$$

and

$$\left| P_E(\theta,\varphi) \right| \sim \left| \sin \theta \sum_{n=1}^{N} \frac{i_{An}[\cos (\cos \beta h_n \cos \theta) - \cos \beta h_n]}{\sin \beta h_n} e^{+j\beta x_n \sin \theta \cos \varphi} \right| . \qquad (47)$$

Thus the relative magnitude of the far field can be calculated given the element base currents.

The relative phase in the principal planes of the far field is given by the phase of the complex field components $P_H \exp(-j\beta r)$ and $P_E \exp(-j\beta r)$. The phase which is a function of the polar angles, is used to determine the phase center of a log-periodic dipole antenna, as explained in Section 3.5.2.2.

2.3 Use of the Digital Computer in Solving the Mathematical Model

Because of the large amount of routine computations involved in extracting numerical results from the foregoing analytical expressions, the use of a digital computer became a necessity. By programming the computer to solve the whole problem, starting from the physical dimensions of the antenna, the mathematical model was given at least as much flexibility for experimentation as the corresponding laboratory model. In this way the computer became the electrical analog of the laboratory technician.

To the computer the pertinent design parameters were specified, along with the testing frequencies. The antenna was then modeled and tested by the computer, and the results were displayed. These results are the principal far field radiation patterns, the far field phase, the voltage and current at the terminals of each dipole element, and the input impedance.

To this end the above formulas were programed in complex number arithmetic for use of the ILLIAC, a high speed digital computer operated by the University of Illinois Graduate College. Because of the large amount of intermediate results which must be stored in the fast access electrostatic memory (capacity 1024 forty bit words), the program was split into six different parts, each stored on the slow access magnetic drum (capacity 16,384 forty bit words). They are:

1. Input: The descriptive parameters of the antenna are read into ILLIAC.
2. Computation of $\overline{Z}_A$
3. Computation of $\overline{Y}_F$
4. Matrix multiplications of $\overline{Y}_F\ \overline{Z}_A$ and solution of $\overline{I} = \overline{T}\ \overline{I}_A$.
5. Output $\overline{I}_A$, multiply $\overline{Z}_A\ \overline{I}_A = \overline{V}_A$ and output $\overline{V}_A$.
6. Pattern calculation and scope display of patterns.

A control program calls each section into play as needed.

The input and basic output of the computer is by perforated paper tape which is translated by a teletypewriter. The patterns are calculated point by point and are plotted by the ILLIAC on a scope to which is attached an automatic 35 mm camera which is controlled by the computer. The camera takes a picture of the completed pattern, then advances the film into position for a new exposure. Some of the computational problems are considered in Appendix A, however, the details of the programing are not of general interest and are omitted.

3. RESULTS AND ANALYSIS

In this section the results of the computer solution of 104 different LPD models are presented and analyzed. In any analysis which is made amenable by the use of approximating techniques, justification must be given for each approximation, and appeal is usually made to experimental methods. Therefore this section compares the computed results with measurements of several laboratory models. The presentation of this section is divided into five parts, each part being concerned with one of the aspects of the operation of a log-periodic frequency independent antenna. They are:

1. The transmission region
2. The active region
3. The unexcited region
4. The input impedance
5. The far field radiation

It will be shown how each of these properties relate to the general ideas about frequency independent antennas as outlined in Section 1, and how each is controlled by the several LPD antenna parameters.

3.1 The Transmission Region

The transmission region consists of all dipole elements which are reasonably less than a half-wavelength long at a given frequency, and the portion of feeder to which these elements are attached. It is not necessary to define precisely the extent of the transmission region, since it is not the size of the region but the effects it produces which are of primary interest.

The mechanism of the transfer of energy from the feed point to the radiated wave leads one to consider two fields along the axis of the structure. One field originates at the feed point and propagates along the feeder in the

direction of the larger elements. It is called the transmission field and will be discussed in this section. The other field originates in the vicinity of the half-wavelength dipole and propagates in the direction of smaller elements, manifesting itself in the radiated field. It will be discussed in Section 3.2. Electric field lines of the transmission field and of the radiated field are sketched in Figure 14. The fact that these two fields are perpendicular along the axis of a structure with this particular feeder-element configuration allows one to measure the transmission field along the axis by the use of a properly oriented probe antenna.

As energy is launched from the feed point onto the small element end of this antenna, a TEM type wave is set up, supported by the feeder and the small elements which load the feeder. This transmission line mode is evidenced by the electric field between the feeder conductors. The matrix $\overline{V}_F$ gives the voltage across the base of each dipole element. By convention, this voltage is considered positive at the upper terminal of each element in Figure 9. The transmission line voltage is positive at the feeder conductor to the right in Figure 9. Due to the alternating manner in which the elements are connected to the feeder, the phase of the base voltage must be changed by 180° at every other element to find the correct phase of the transmission line voltage.

3.1.1 Computed and Measured Results

A graph of the computed and measured transmission line voltage is shown in Figure 15. The data was recorded at frequency f_3 as a function of wavelengths from the apex. (f_3 is the frequency for which element three is a half-wavelength long.) The calculated voltage at the location of each element is also plotted. This 13 element antenna has the following parameters:

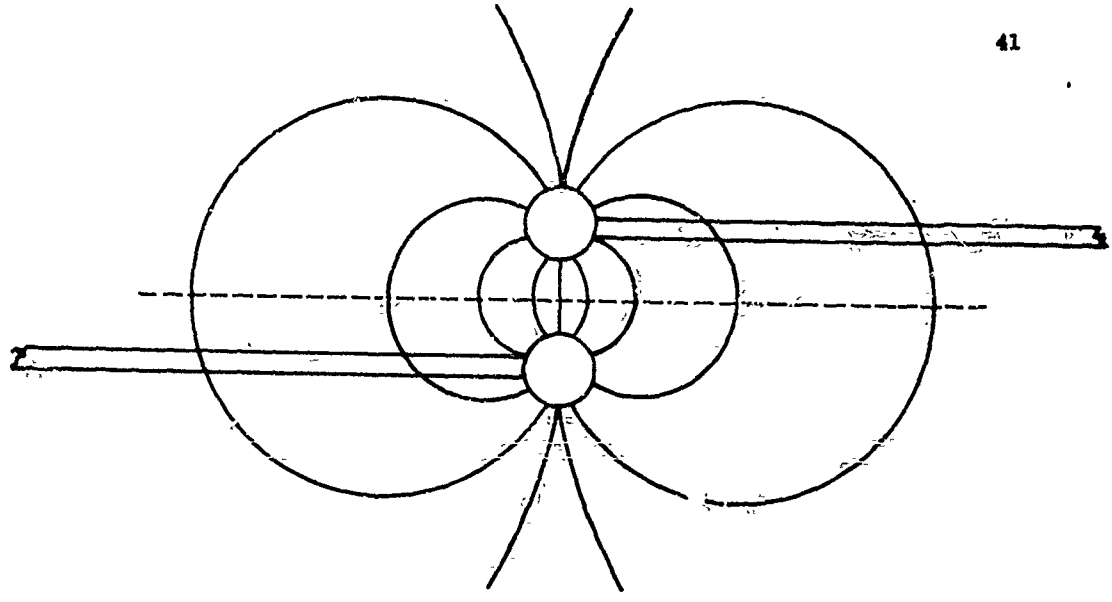

FEEDER FIELD

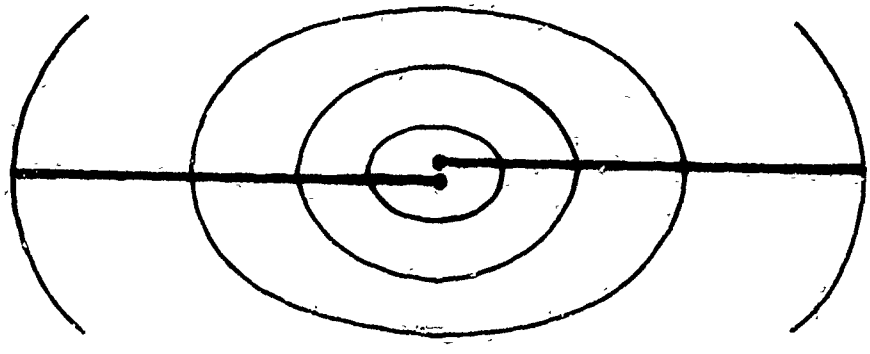

RADIATION FIELD

Figure 14. Sketches of the transmission and radiation field lines

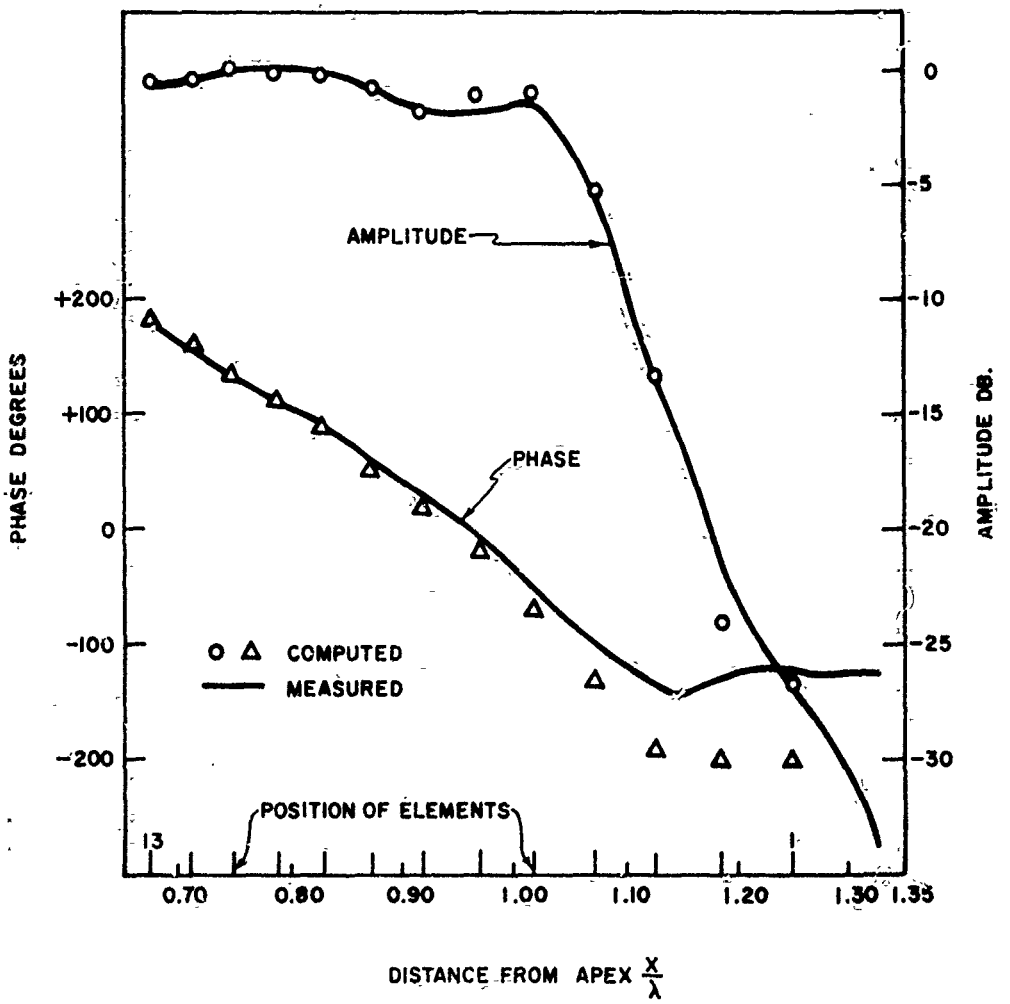

Figure 15. Computed and measured amplitude and phase of the transmission line voltage vs. Relative Distance from the Apex at Frequency f_3; $\tau = 0.95$, $\sigma = 0.0564$, N = 13, $Z_o = 100$, Z_T = short at $h_{1/2}$, $h/a = 177$

$\tau = 0.95$, $\sigma = 0.0364$, $\alpha = 12.5^{\circ}$, h/a = 177, and $Z_o = 100$ ohms. The voltage is essentially constant from the feed point at $x/\lambda = 0.675$ to the beginning of the active region at $x/\lambda = 1.00$. This indicates that the transmission wave propagates with little reflection or attenuation. Since the small elements are closely spaced and fed out of phase, their contribution to the radiated field is negligible, and they act as small shunt capacitors. For $x/\lambda > 1.00$, the feeder voltage decreases rapidly, due to the coupling of energy into the elements of nearly half wavelength dimensions in the active region. Figures 16, 17, 18 and 19 are for frequencies $f_{3\ 1/4}$, $f_{3\ 1/2}$, $f_{3\ 3/4}$ and f_4 respectively, on the same model. The shape of these curves is the same, since the distance from the apex is normalized with respect to wavelength. The feeder on this model was terminated in a short circuit at a constant distance $h_1/2$ from the largest element. That the shape of the curves did not change with frequency, even though a frequency sensitive termination was used, shows the lack of end effect on this antenna. End effects will be discussed in Section 3.3.

The phase of the feeder voltage is plotted in Figures 15, 16, 17, 18 and 19. The phase is essentially linear up to $x/\lambda = 1.00$. This also suggests that the transmission wave propagates away from the feed point with negligible reflection. The computed input standing wave ratio for this antenna was 1.15:1 with respect to 65 ohms and the measured value was 1.17. The low VSWR is also indicative of a small reflected wave. For the case of low VSWR, the slope of the curve of phase versus distance is inversely proportional to the relative velocity of propagation of the transmission wave, $\frac{v_t}{c}$. v_t is the phase velocity of the transmission wave and c is the velocity of light in free space. For this antenna $\frac{v_t}{c} = 0.63$.

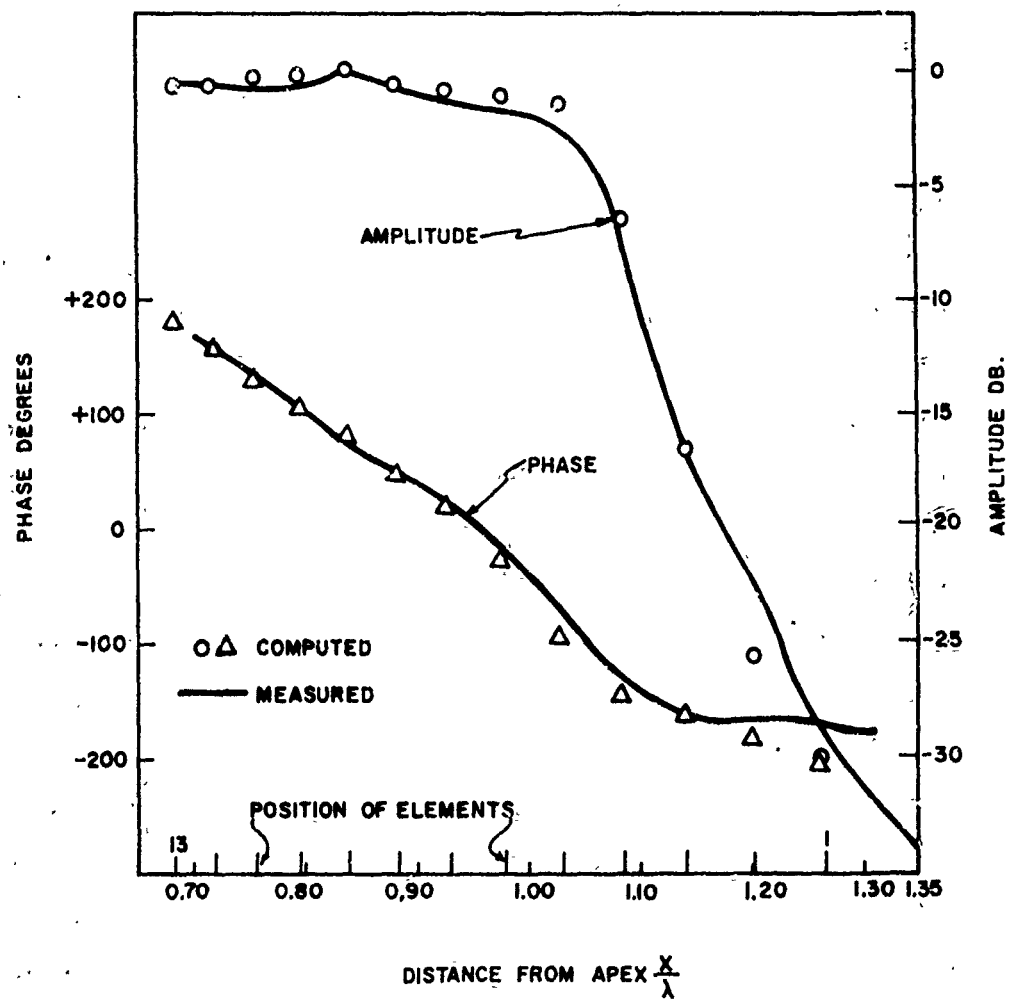

Figure 16. Computed and measured amplitude and phase of the transmission line voltage vs. relative distance from the apex at frequency $f_{3\ 1/4}$; $\tau = 0.95$, $\sigma = 0.05$, $N = 13$, $Z_o = 100$, Z_t = short at $h_{1/2}$, $h/a = 177$

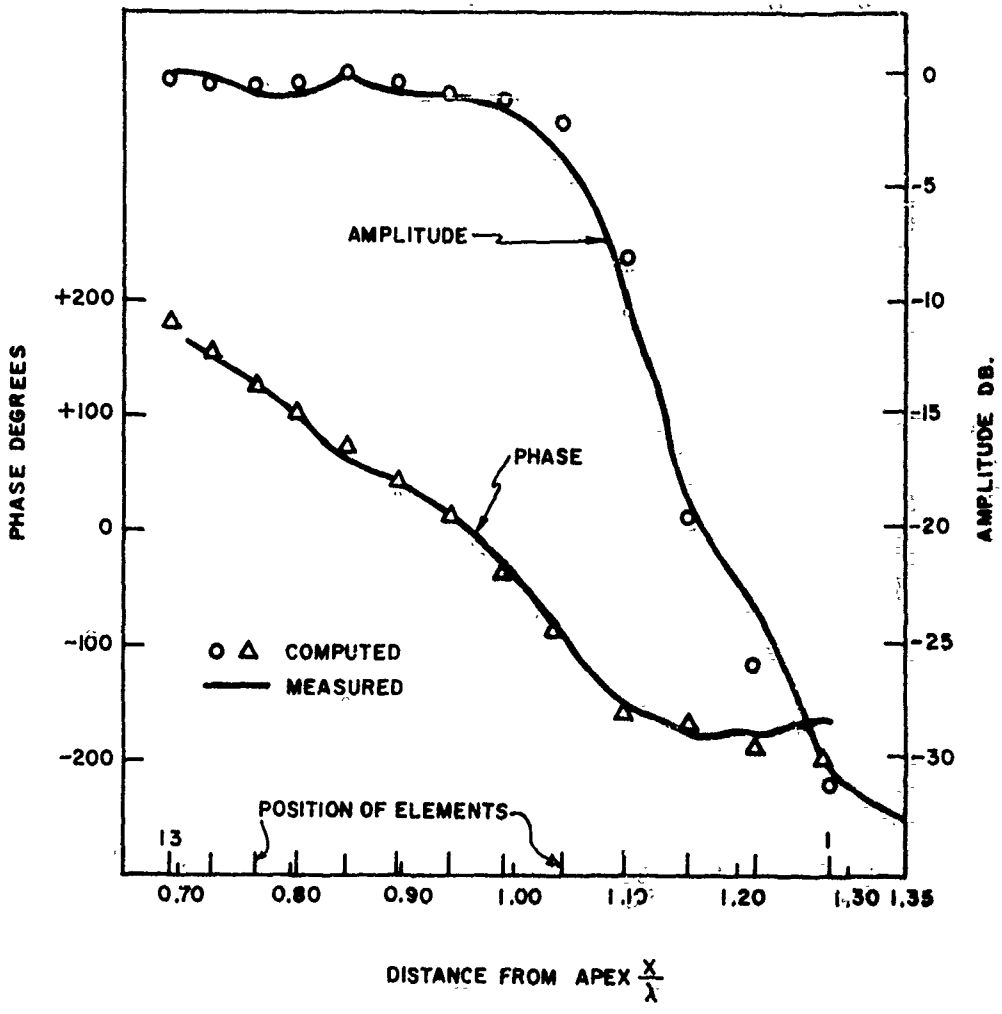

Figure 17. Computed and measured amplitude and phase of the transmission line voltage vs. relative distance from the apex at frequency $f_{3\ 1/2}$; $\tau = 0.95$, $\sigma = 0.0564$, $N = 13$, $Z_o = 100$, Z_t = short at $h_{1/2}$, $h/a = 177$

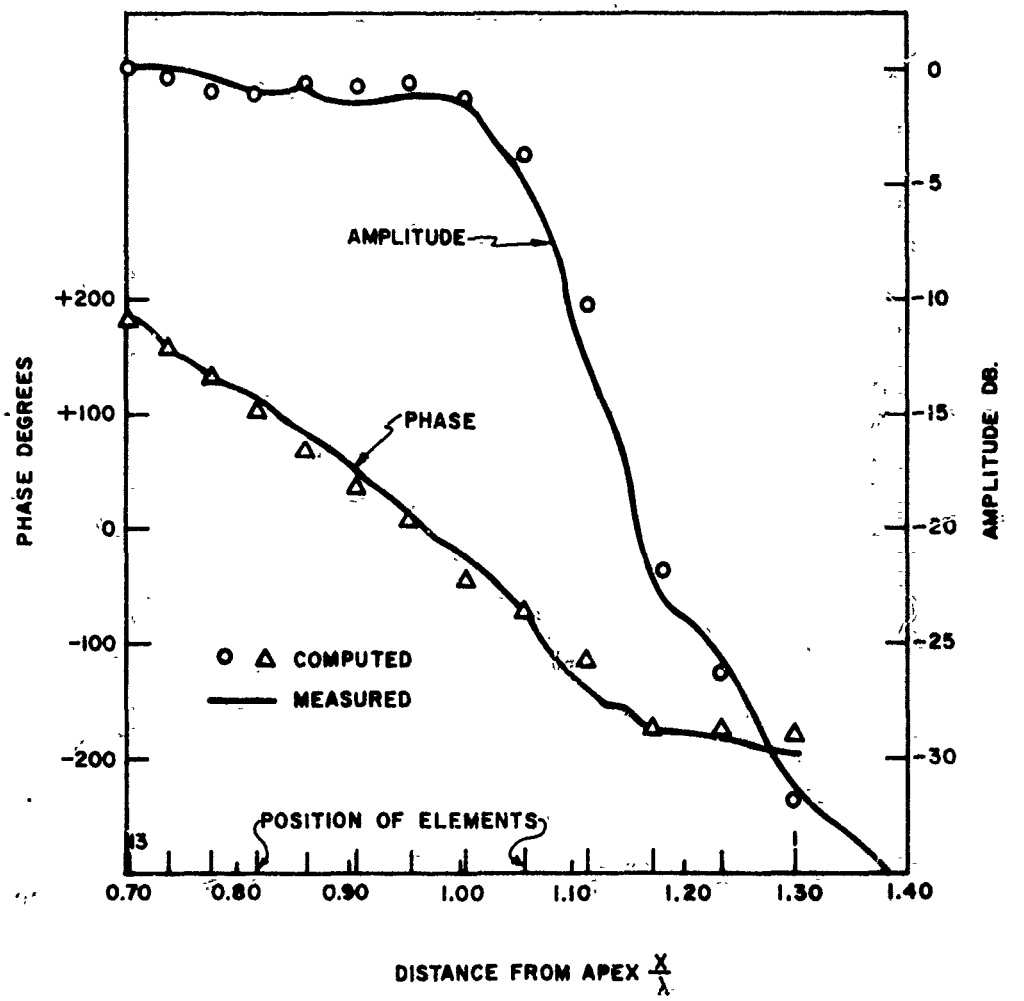

Figure 18. Computed and measured amplitude and phase of the transmission line voltage vs. relative distance from the apex at frequency $f_{3\ 3/4}$; $\tau = 0.95$, $\sigma = 0.0564$, $N = 13$, $Z_o = 100$, $Z_t \approx$ short at $h_{1/2}$, $h/a = 177$

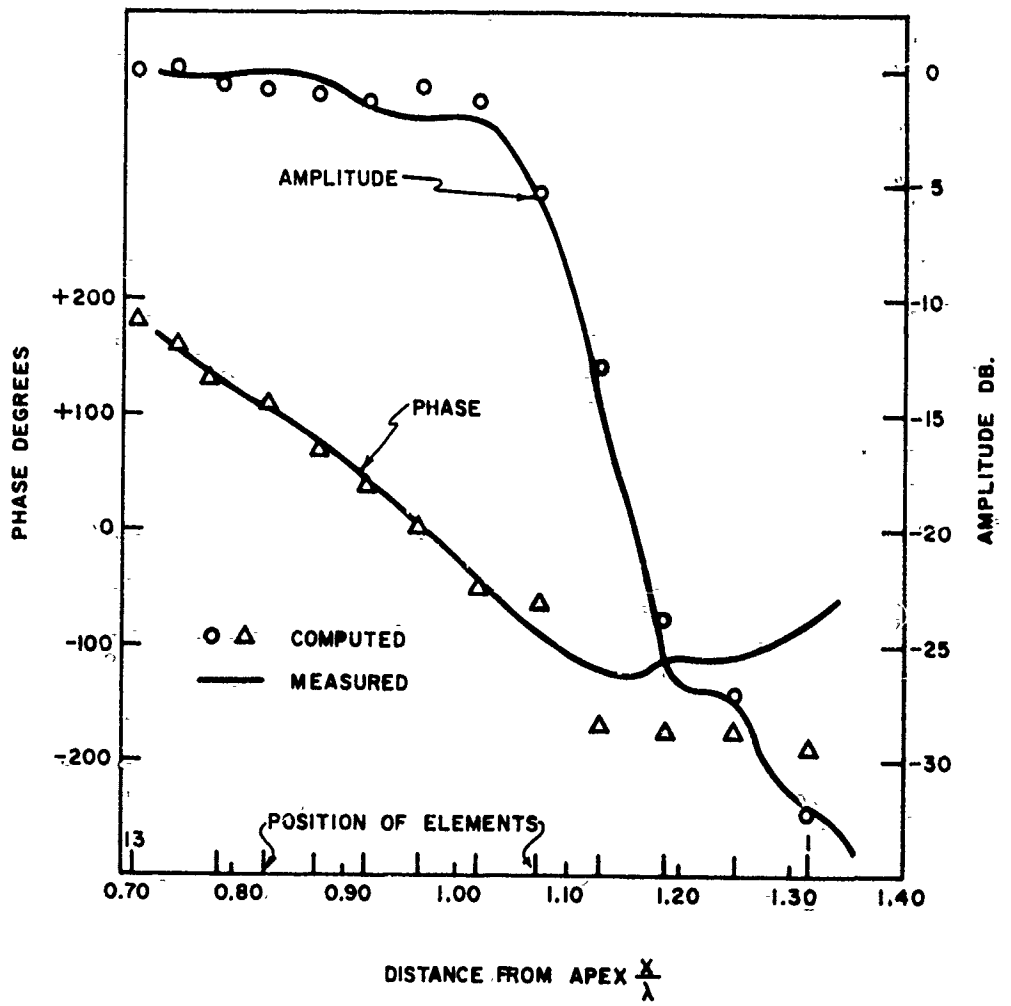

Figure 19. Computed and measured amplitude and phase of the transmission line voltage vs. relative distance from the apex at frequency f_4; $\tau = 0.95$, $\sigma = 0.0564$, $N = 13$, $Z_o = 100$, Z_T = short at $h_{1/2}$, $h/a = 177$

In Section 3.1.2 an approximate formula for the constants of an equivalent line in the transmission region is derived. The graph of Figure 20, based on the approximate formula, shows that the transmission wave phase velocity depends primarily on the relative spacing σ. For small spacing the loading effect of the elements is appreciable; relative phase velocities less than 0.6c have been observed. Since v_t is less than c, the wavelength of the transmission wave λ_t is less than the free space value. λ_t rather than λ must be used if one is to compute the electrical length of any part of the transmission region.

Near field measurements made on a second model are shown in Figure 21. For this 8 element antenna $\tau = 0.888$, $\sigma = 0.089$, $\alpha = 17.5^{\circ}$, $h/a = 125$, and $Z_o = 100$ ohms. The graphs of the magnitude and phase are generally the same as for the previous model. However, the linear portion of the phase curve is smaller, because less elements were used. A phase velocity of 0.75c is given by the slope of the left-most linear portion of the curve. The measured values of phase velocity are plotted on the graph of Figure 20. The slow wave in the transmission field was observed in every computed model. The range of parameters of the computed models was $0.7 \leq \tau \leq 0.98$ and $0.03 \leq \sigma \leq 0.23$.

Measurements on a different type of LP antenna have been made by Bell, Elfving, and Franks[14] at Sylvania Electronic Defense Laboratories. Their results also demonstrate the slow wave nature of the transmission field.

Several computations were made to determine the effect of changing the phase velocity of the unloaded feeder, to simulate the use of a dielectric material in the feeder configuration. Figure 22 shows that the relative velocity of the transmission wave decreases as the relative

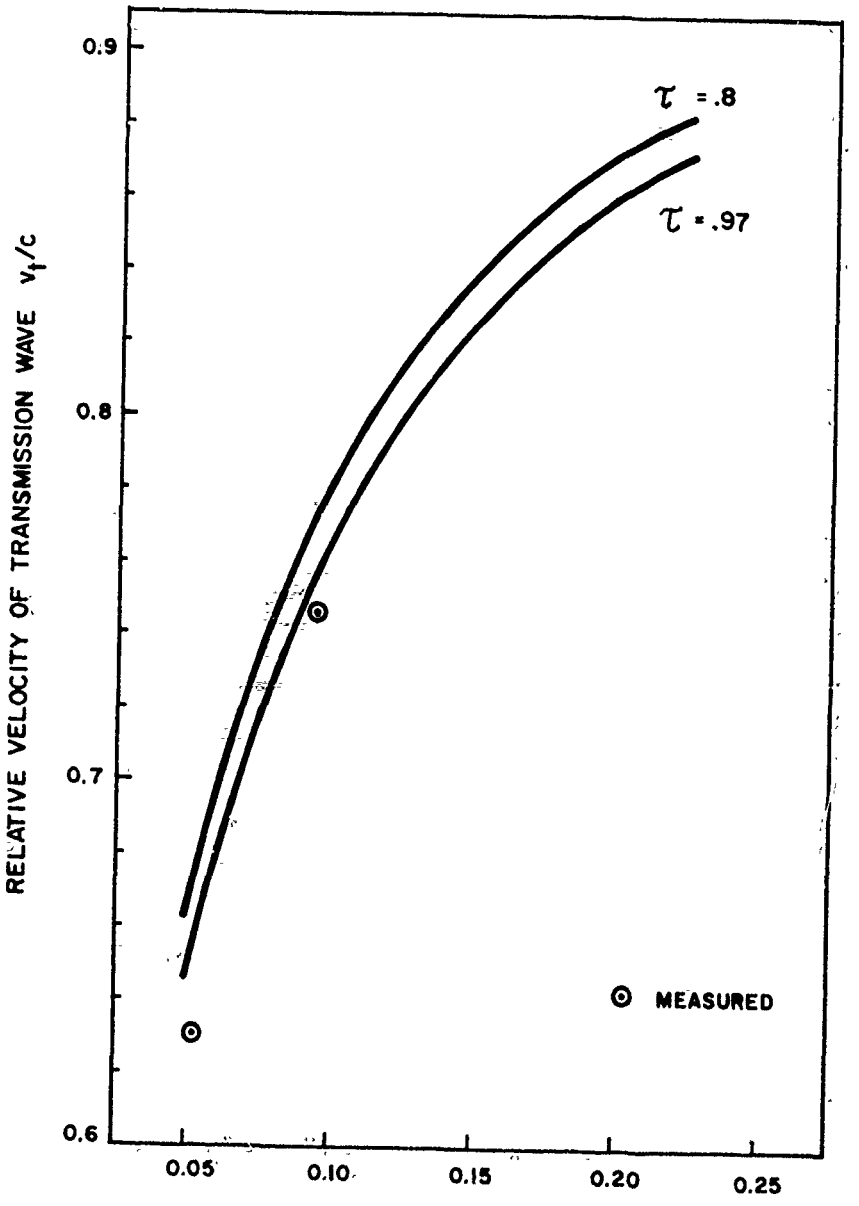

Figure 20. Relative velocity of transmission wave vs. τ and σ with $Z_o/Z_a = 0.33$, computed from the approximate formula (60) page 54.

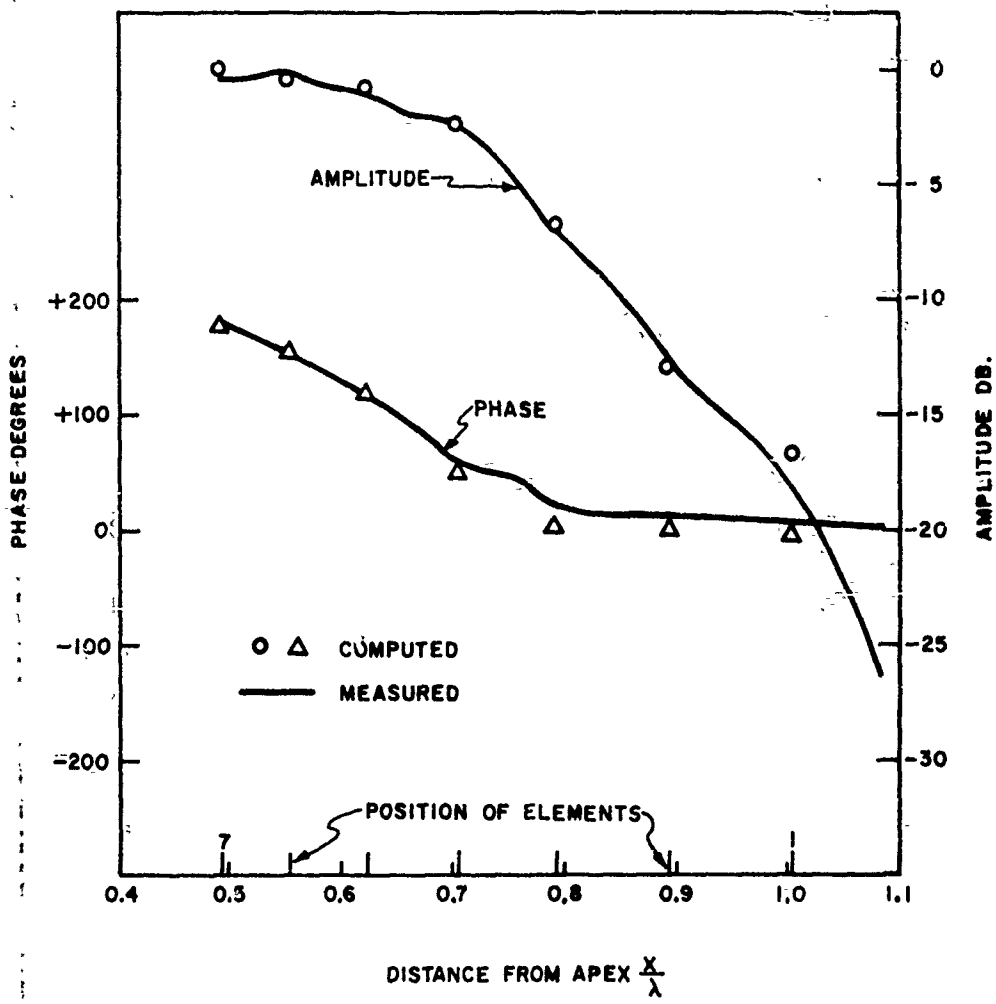

Figure 21. Computed and measured amplitude and phase of the transmission line voltage vs. relative distance from the apex at frequency f_3; $\tau = 0.888$, $\sigma = 0.089$, $N = 8$, $Z_o = 100$, Z_T = short at $b_{1/2}$, $h/a = 125$.

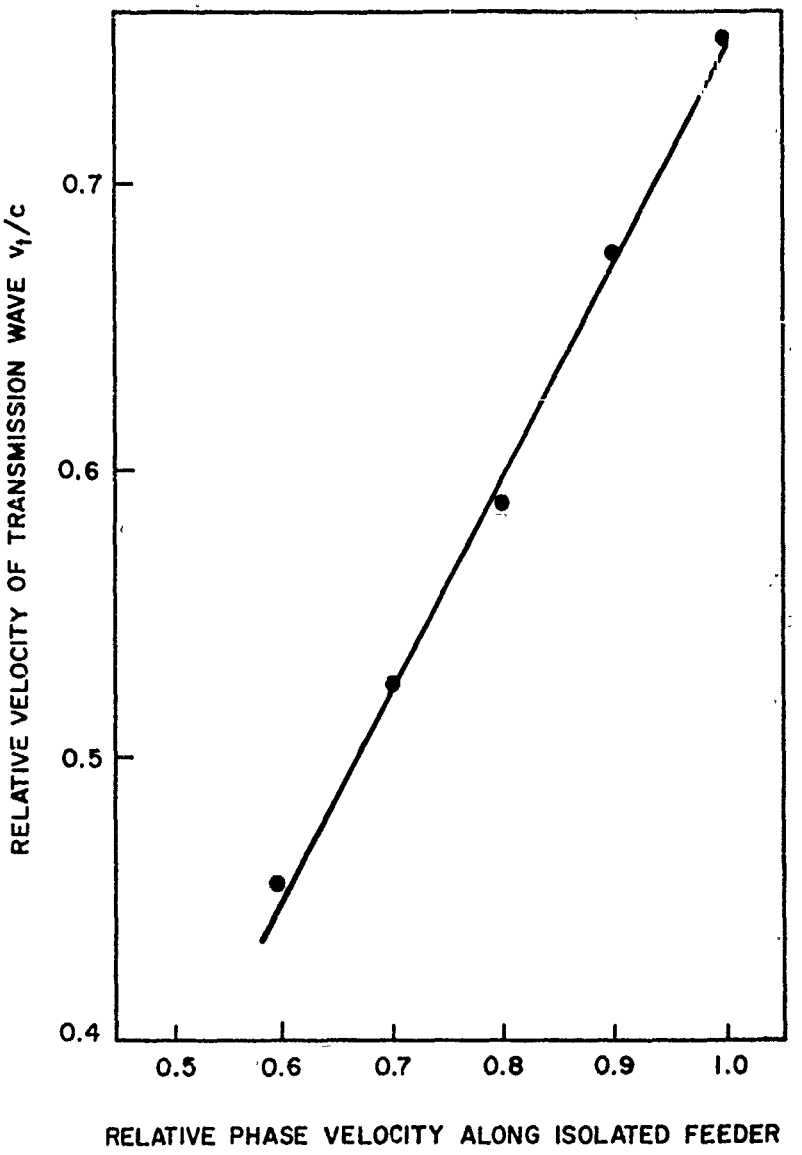

Figure 22. Relative velocity of transmission wave as a function of the relative phase velocity along the feeder with the elements removed.

velocity along the unloaded feeder decreases. The range of feeder velocity shown corresponds to a relative dielectric constant $1 < \epsilon_r < 2.78$. The LPD performs satisfactorily under these conditions; the only noticable change in the computed models was an increase in the input impedance and a shift of the active region towards the shorter elements. These effects are the same as those resulting from an increase in the characteristic impedance of the feeder. (See Sections 3.4.3 and 3.5.1.2). The feasibility of using a dielectric in the antenna structure was shown in a model that was constructed from double copper-clad Rexolite using printed circuit techniques. It exhibited uniform directivity over the design band. This antenna is discussed in Section 5.2.

A discussion of the effects of changing the characteristic impedance of the feeder and the h/a ratio will be taken up in Section 3.4, because these factors can be used to control the input impedance.

3.1.2 An Approximate Formula for the Constants of an Equivalent Line in the Transmission Region.

The transmission region displays some of the characteristics of a uniform transmission line. The small, non-radiating elements load the feeder to produce the slow wave. Furthermore, this loading appears to be uniform because the magnitude of the voltage is constant and the phase is linear throughout the transmission region. This uniform loading is due to the shunting capacitance of each element. To the first approximation, the capacitance of a small dipole is proportional to its length, and on an LPD, the spacing d_j at element j is also proportional to the length of element j, thus, the added capacitance per unit length is constant. Consider the approximate formula for the input impedance of a small dipole

antenna of half-length h,

$$Z = - jZ_a \cot \beta h, \tag{48}$$

where β is the free space propagation constant. Z_a is called the average characteristic impedance of a dipole antenna,

$$Z_a = 120 \ (\ln h/a - 2.25) \tag{49}$$

This is a modification of a formula in Jordan[15] which was derived by Siegel and Labus[16]. The original formula for Z_a contains a term which depends on the height of the dipole relative to wavelength; the factor 2.25 in Equation (49) represents an average height. Replacing the cotangent function in Equation (48) by its small argument approximation, the capacitance of the nth dipole is given by

$$C_n = \frac{h_n}{cZ_a}, \tag{50}$$

where c is the velocity of light in vacuum. Using the mean spacing at dipole n

$$d_{mean} = \sqrt{d_n d_{n-1}} = \frac{d_n}{\sqrt{\tau}}, \tag{51}$$

the capacitance per unit length is given by

$$\Delta C = \frac{C_n}{length} = \frac{h_n \sqrt{\tau}}{c d_n Z_a} \tag{52}$$

But h_n/d_n is related to the spacing factor σ by

$$\sigma = \frac{1}{4} \frac{d_n}{h_n} \tag{53}$$

hence

$$\Delta C = \frac{\sqrt{\tau}}{4c\sigma Z_a} \tag{54}$$

The characteristic impedance of the unloaded feeder is given by

$$Z_o = \sqrt{\frac{L_o}{C_o}} \tag{55}$$

and the characteristic impedance of the equivalent line is given by

$$R_o = \sqrt{\frac{L_o}{C_o + \Delta C}} \tag{56}$$

Using $\sqrt{L_o C_o} = 1/c$ and substituting, one finds

$$R_o = Z_o / \sqrt{m} \tag{57}$$

where

$$m = 1 + \frac{Z_o}{Z_a} \frac{\sqrt{\tau}}{4\sigma} \tag{58}$$

Similarly, the propagation constant for the equivalent line is given by

$$\beta_t = \beta \sqrt{m}. \tag{59}$$

The relative phase velocity of the transmission wave is given by

$$\frac{v_t}{c} = \frac{\beta}{\beta_t} = \frac{1}{\sqrt{m}}. \tag{60}$$

The graph of Figure 20 was plotted according to Equation (60). In Section 3.4, Equation (57) is used to approximate the input impedance of the LPD.

In summary, all the available data suggests that the region which contains electrically small elements acts as a uniform transmission line which is

matched to the active region. This is why the front end of an LPD can be truncated without adverse effects on the frequency independent characteristics.

3.2 The Active Region

The active region in the LPD antenna consists of several dipole elements whose lengths border on a half-wavelength at a given frequency, and the portion of feeder to which these elements are attached. It is this part of the antenna which determines the characteristics of the radiated field. This section presents calculated and measured results which show how the power in the feeder wave is divided among the radiating elements. A useful concept, the bandwidth of the active region, is formulated and its functional dependence on the several LPD parameters is given.

3.2.1 Element Base Current in the Active Region

The dipole elements in the active region transfer the power from the transmission wave to the radiated field. Figure 23 shows the base impedances of the dipole elements in an 8-element LPD operating at f_4. Base impedance here means the ratio of voltage to current at the base of each element, when the antenna is fed in the usual manner. The base impedances of elements 4 and 5 are predominately real, so conditions are favorable for the coupling of energy from the feeder onto the radiating elements in the active region. The small elements 6, 7, and 8 are capacitive and therefore loosely coupled to the feeder. The large elements 1, 2, and 3 are inductive and also loosely coupled. The base impedance of all computed models in the range $0.8 \leq \tau \leq 0.98$ and $0.03 \leq \sigma \leq 0.23$ behaved in a similar manner. For $\tau < 0.8$, the base impedance of only one antenna element was predominately real at any given frequency; for these models the performance was not frequency independent.

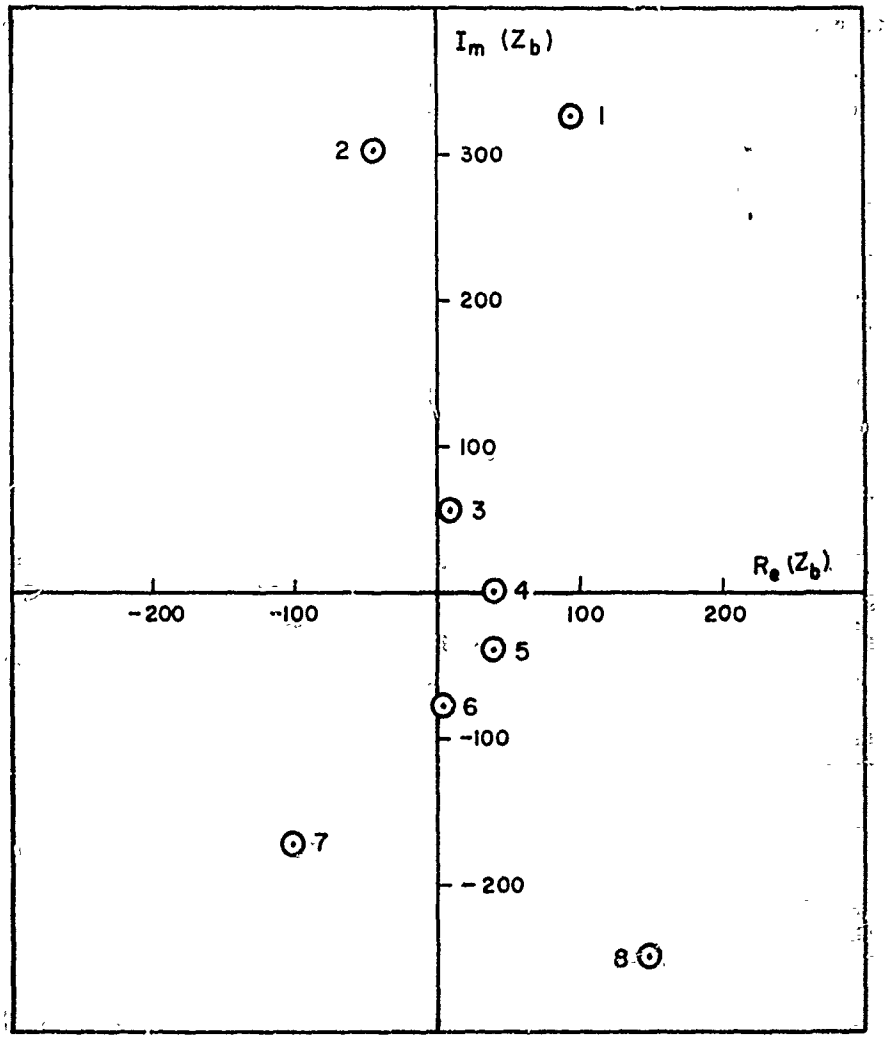

Figure 23. Computed base impedance Z_b vs. element number for an eight element LPD at frequency f_4.

Figure 24 is a graph of the relative amplitude of element base current as a function of x/λ, which is the normalized distance from the apex of the antenna. The location of each element is indicated in the figure. The lines which connect the values of current at the discrete location of each element are for clarity of presentation only. A loop-probe technique was used to measure the base current, as explained in Appendix B. The element base currents in the active region rise to a peak in the element which is somewhat shorter than a half-wavelength. As frequency is changed, the shape of this curve remains unchanged as shown in Figures 25, 26, 27 and 28. That is, the active region moves along the antenna as frequency is changed, but its distance in wavelengths from the apex remains constant. Figure 29 shows the computed magnitude of the base currents in the active region of an eight element antenna at frequencies related by τ. These curves are identical except for f_1 and f_6. At these frequencies the active region becomes deformed as it begins to include the largest or smallest element on the antenna. When this happens, the lower or upper frequency limit is reached.

The phase of the current from element to element in the active region is also plotted in Figures 24 through 28. This is the phase which has to be considered when computing the radiation pattern. Since the phase can be determined only within a multiple of 2π, many phase velocities are compatible with a given phase progression. In Figures 24 through 28, the slope of the phase curve in the active region was chosen to yield the largest phase velocity compatible with the given phase progression. This phase velocity is approximately equivalent to that of the first backward space harmonic of a periodic structure made up of cells identical to the central cell of the active region. Mayes, Deschamps and Patton[17] have explained the operation of unidirectional

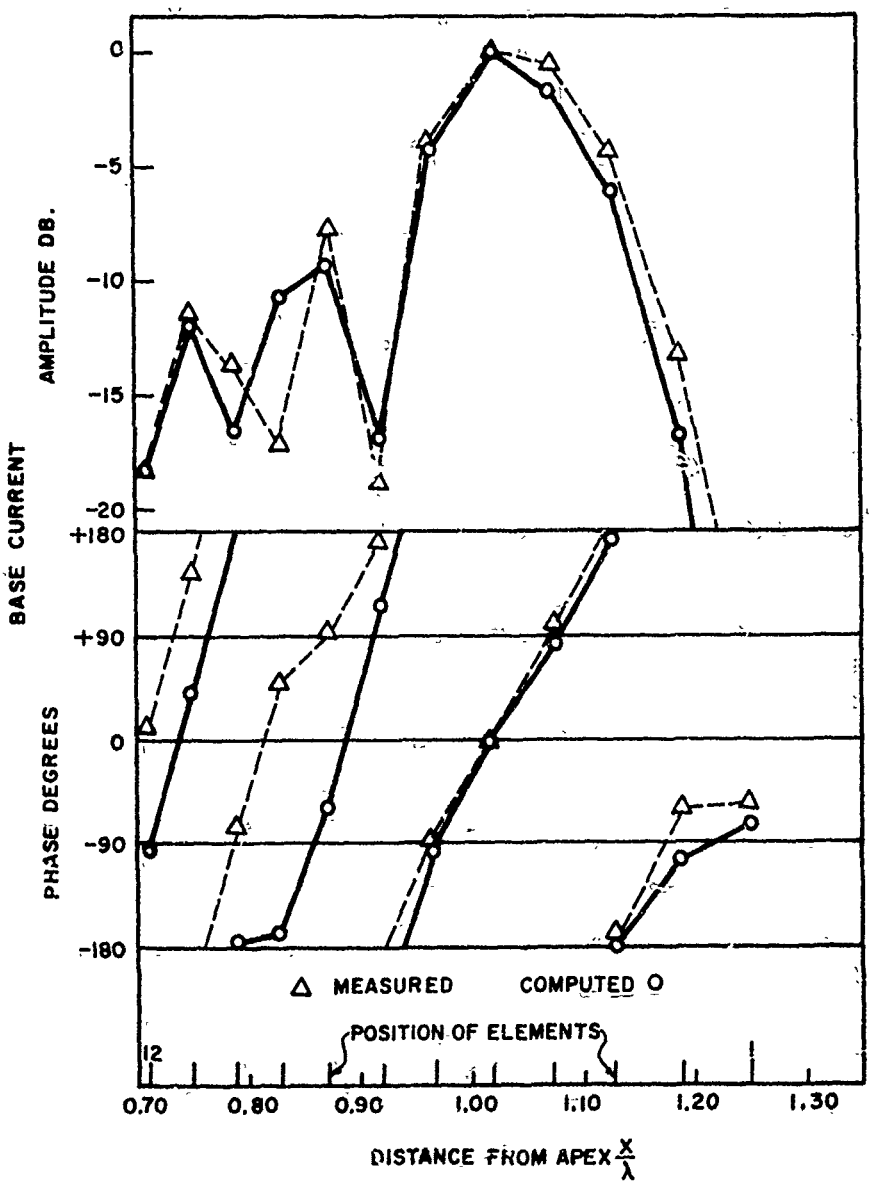

Figure 24. Computed and measured amplitude and phase of the element base current vs. relative distance from the apex, at frequency f_3; $\tau = 0.95$, $\sigma = 0.0564$, $Z_o = 100$, $h/a = 177$, 2_T = short circuit at $h_1/2$.

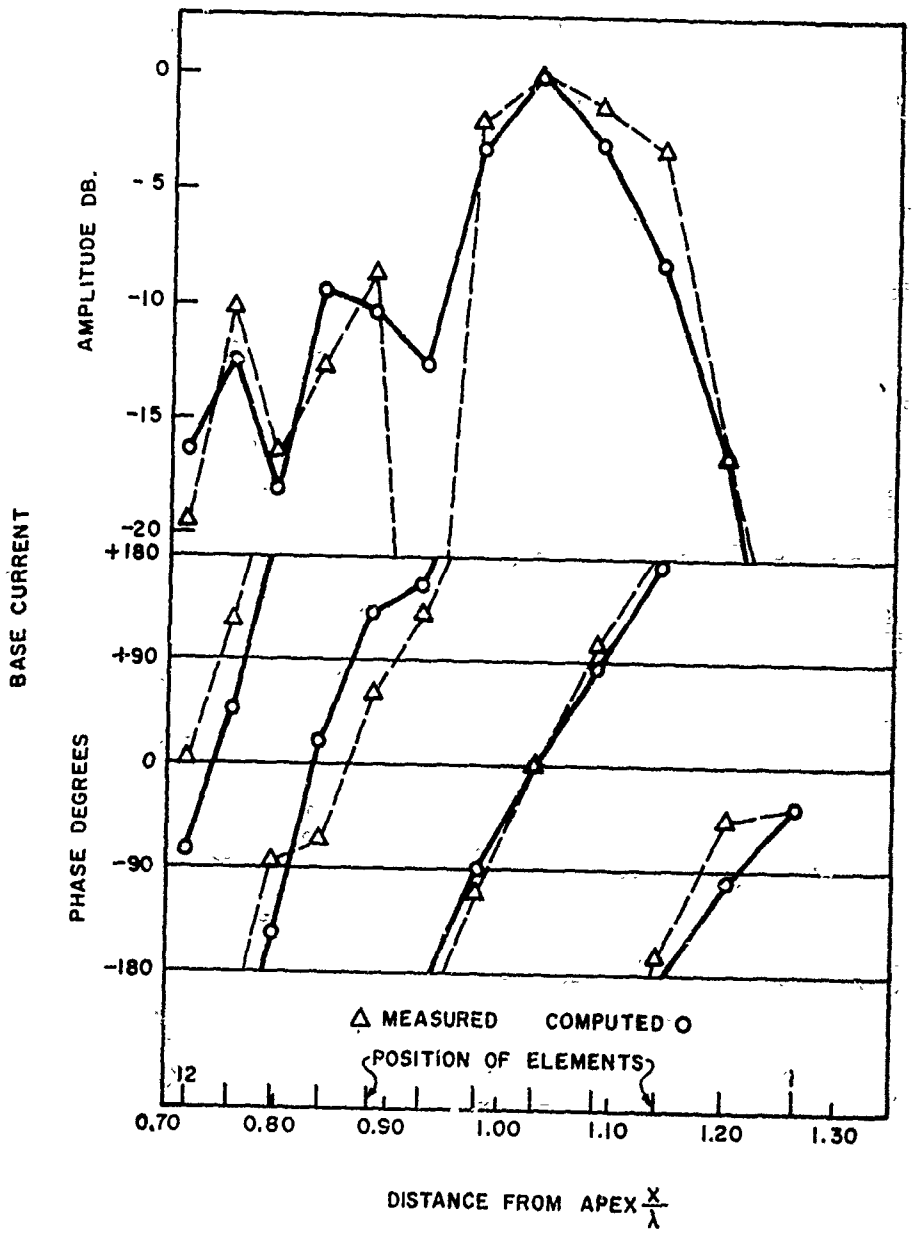

Figure 25. Computed and measured amplitude and phase of the element base current vs. relative distance from the apex, at frequency $f_{3\ 1/4}$; $\tau = 0.95$, $\sigma = 0.0564$, $Z_c = 100$, h/a = 177, Z_T = short circuit at $h_1/2$.

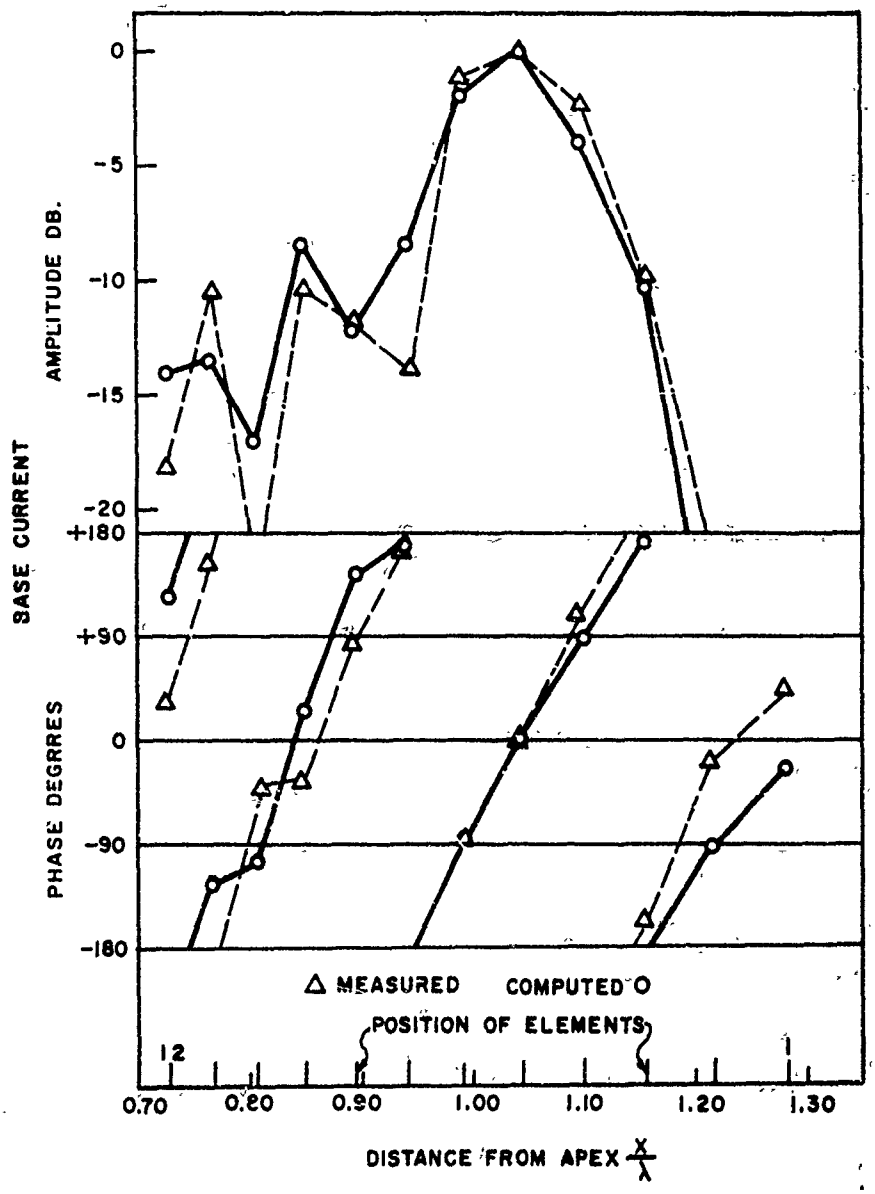

Figure 26. Computed and measured amplitude and phase of the element base current vs. relative distance from the apex, at frequency $f_{3\ 1/2}$; $\tau = 0.95$, $\sigma = 0.0564$, $Z_o = 100$, $h/a = 177$, Z_T = short circuit at $h_1/2$.

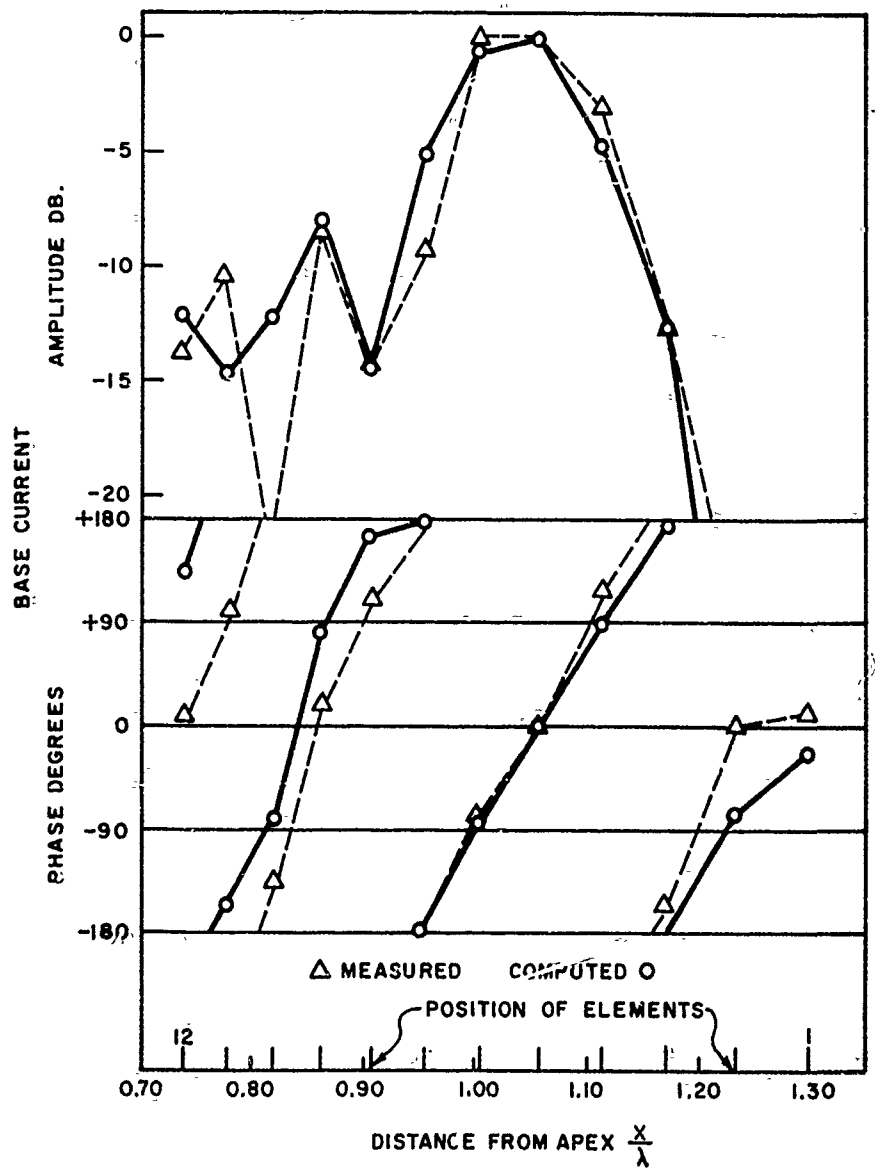

Figure 27. Computed and measured amplitude and phase of the element base current vs. relative distance from the apex, at frequency $f_{3\ 3/4}$; $\tau = 0.95$, $\sigma = 0.0564$, $Z_o = 100$, $h/a = 177$, Z_T = short circuit at $h_1/2$.

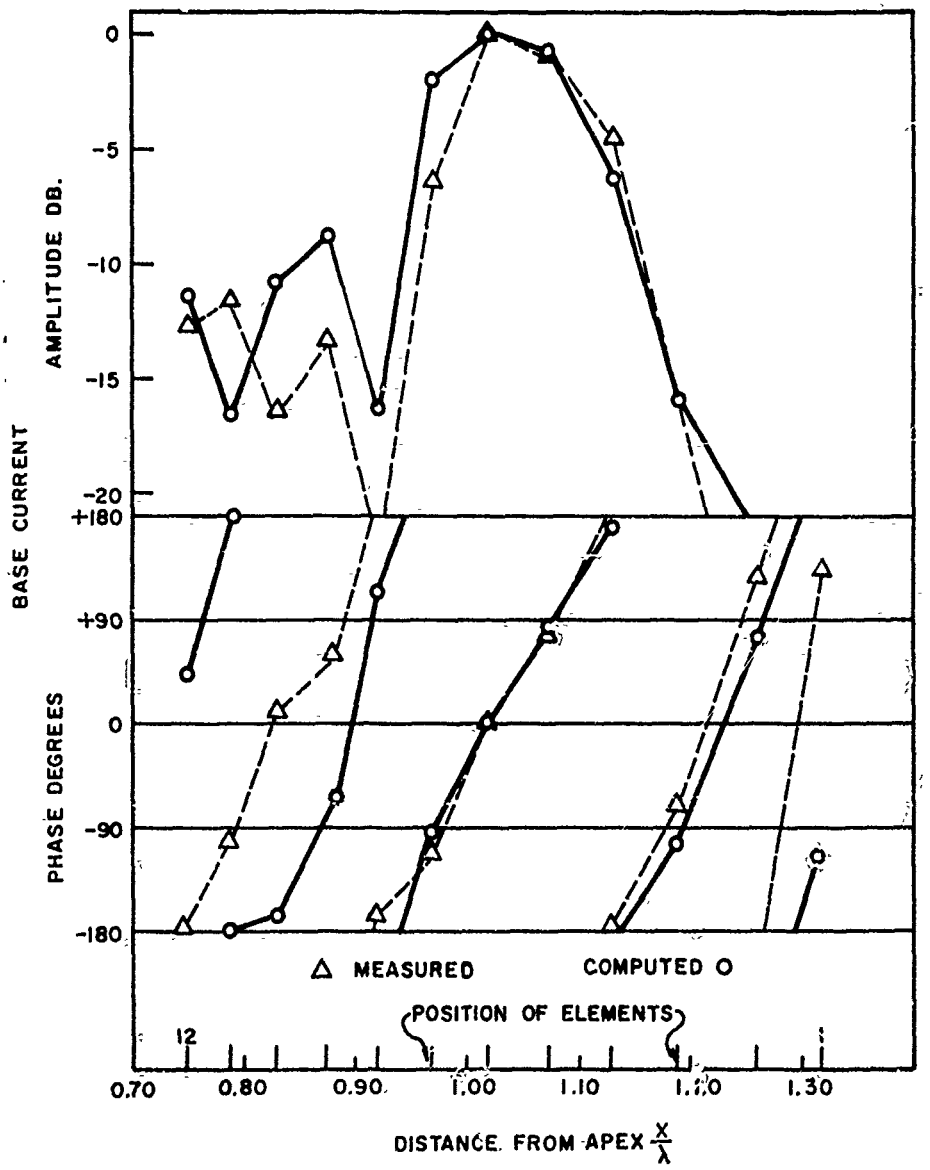

Figure 28. Computed and measured amplitude and phase of the element base current vs. relative distance from the apex, at frequency f_4; $\tau = 0.95$, $\sigma = 0.0564$, $Z_o = 100$, $h/a = 177$, Z_T = short circuit at $h_1/2$.

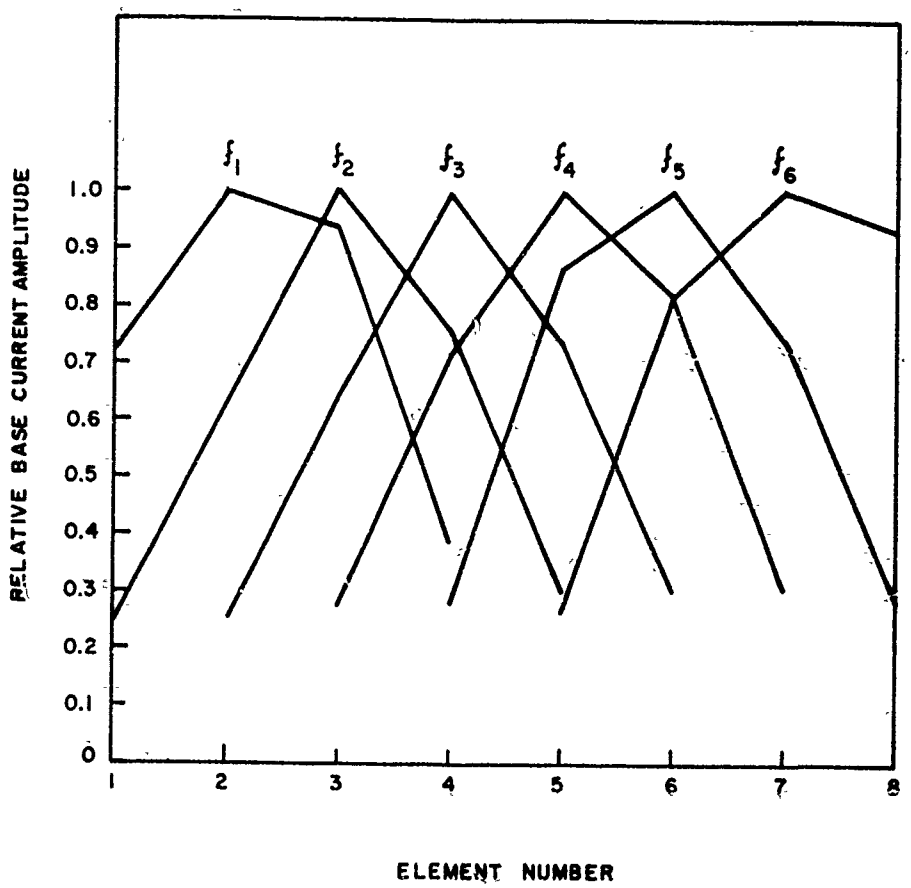

Figure 29. Relative amplitude of base current in the active region vs. element number, frequencies f_1 thru f_6. $\tau = 0.888$, $\sigma = 0.089$, $N = 8$, $Z_o = 100$, $h/a = 125$, Z_T = short at $h_1/2$.

frequency independent antennas in terms of backward wave radiation.

The computed phase velocity of the first backward space harmonic as a function of σ is shown in Figure 30 for several values of τ. These curves represent average values taken over several frequencies. As the spacing increases, the phase velocity increases. For low values of τ the relative phase velocity increases rapidly with increasing σ, indicating the possibility of radiation broadside to the antenna. Several models have exhibited broadside radiation patterns; these ar discussed in Section 3.5.

The mutual impedance of the elements in the active region plays a fundamental role in determining the amplitude and phase of the element currents. To find if any of the mutual terms in the element impedance matrix could be neglected, several tests were made in which the range of the mutual coupling was changed. If z_{ij} is the mutual impedance between element i and element j, the range is given by the number $|i-j|$. Thus range 0 means all mutual terms are zero, range 1 means all mutual terms excepting those for adjacent elements are zero, etc. Limiting the mutual effect to range 2 causes distortion of the computed patterns. The average input impedance level remains about the same, but the input standing wave ratio increases from its actual value for full range coupling. This means that one must take into account interaction at range 3 or greater to determine the relative excitation of each element.

3.2.2 Width and Location of the Active Region

For a given antenna, the usable bandwidth for frequency independent operation depends on the relative distance the active region can move before it becomes distorted by the smallest or largest element. Thus the width of

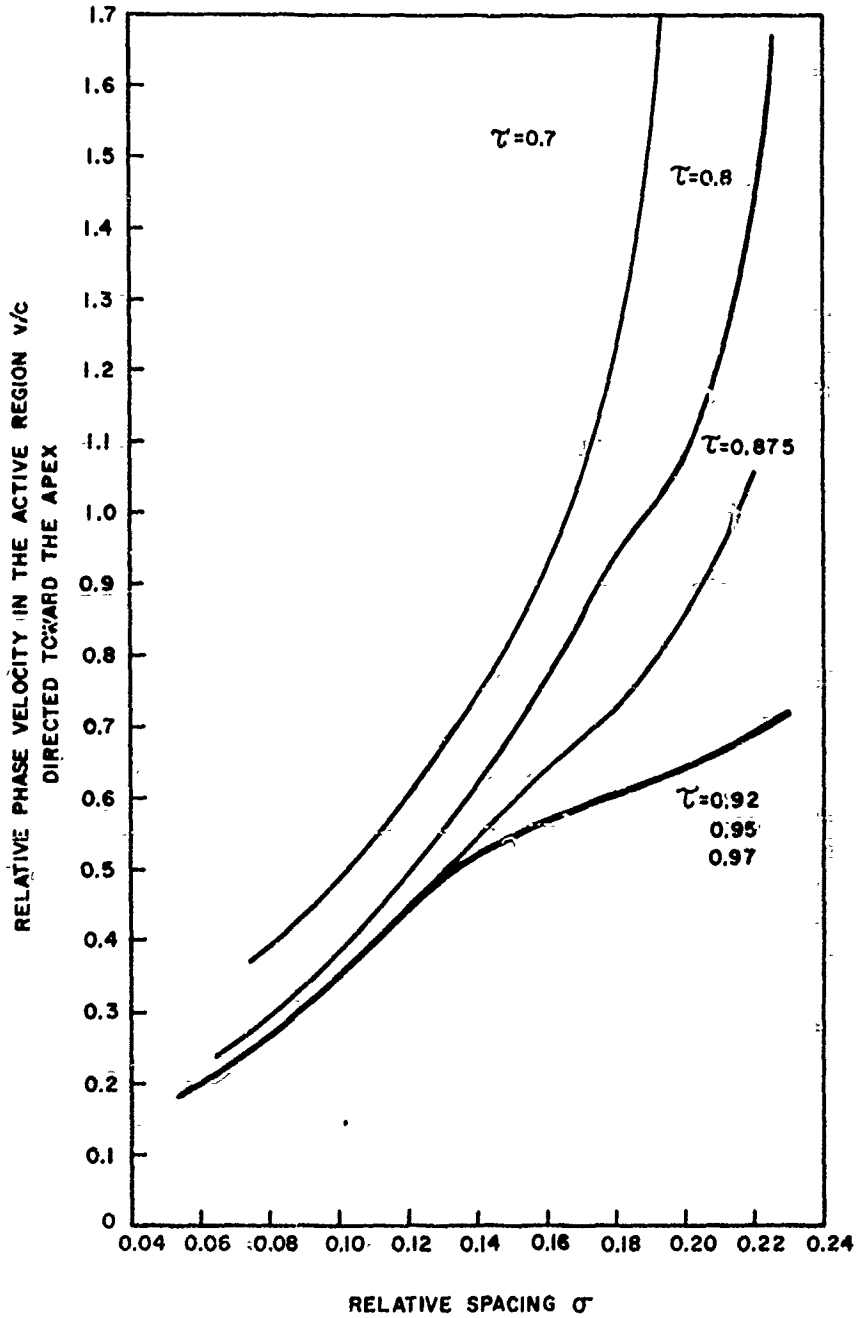

Figure 30. Computed relative phase velocity of the first backward space harmonic in the active region vs. σ for several values of τ $Z_o = 100$ and $h/a = 177$.

the active region, if properly defined, can be used to measure the bandwidth capability of a given antenna. Furthermore, the knowledge of the width of the active region is prerequisite to the design of an antenna to cover a given bandwidth. The lower cut-off frequency of a given antenna is determined by the length of the longest element. Conversely, if the lower cut-off frequency is given, the relative length of the longest required element in the active region must be known to fix the length of the longest element on the antenna.

If the active region was very narrow, the operating bandwidth of the antenna would be given substantially by the ratio of the length of the largest to smallest element. This ratio will be called the structure bandwidth, B_s.

$$B_s = \frac{\ell}{\frac{1}{N}} = \tau^{1-N} \tag{61}$$

Since the active region has some width, it is apparent that the operating bandwidth B is always less than B_s by a factor which can be called the bandwidth of the active region, B_{ar}. Thus

$$B = B_s/B_{ar}. \tag{62}$$

Placing numerical values on B and B_{ar} is complicated by the fact that the width of the active region is not easily quantified. This is because the observable characteristics of an LPD, such as the pattern and input impedance, do not change abruptly from the values which characterize frequency independent operation to values which are unquestionably outside the range of operation. Actually, the characteristics change slowly, and only by applying a tolerance to the pattern, or input impedance, can a figure be chosen which represents the operating bandwidth of an LPD.

It was impractical to hunt for the limits of operation of all the computed models; this would have involved testing each model at many closely spaced frequencies. Instead, empirical values of the bandwidth and location of the active region were determined in the following manner.

Figure 31 is a sketch of a typical curve of base current versus distance from the apex. As the high frequency limit is approached, the active region moves toward the apex and the amplitude of the current in the shortest element increases. When this current increases to within 10 db of the maximum, it is observed that the input VSWR begins to depart from its mid-band value. This occurs somewhat before a significant change in the pattern is observed. Therefore x^-, the location of the -10 db point nearest the apex, can be taken as a definition of the high frequency edge of the active region.

At the low frequency limit, distortion of the active region is accompanied by an increase in the H-plane beamwidth and a change of impedance. The beamwidth was chosen as a criterion because the low frequency patterns are always smooth and single-lobed, facilitating unambiguous measurement. When the current in the longest element increases to $I_{\ell o}$, an amount sufficient to increase the H-plane beamwidth by 10 percent, the low frequency limit is said to be reached. The distance from the apex to the $I_{\ell o}$ point, $x_{\ell o}$, depends on Z_o and h/a but is substantially independent of τ and σ. For the cases with Z_c = 100 ohms and h/a = 177, $x_{\ell o}$ is equal to $x_{\lambda/2}$, the distance to the half-wave element. As the feeder impedance Z_o is increased or the ratio h/a is decreased on a given model, the active region is found to move toward the apex in a manner where x^+ is the distance to the -10 db point farthest from the apex, such that $x_{\ell o}/x^-$ and x^+/x^-, remain constant. As a consequence, the location of the half-wavelength element with respect to the active region

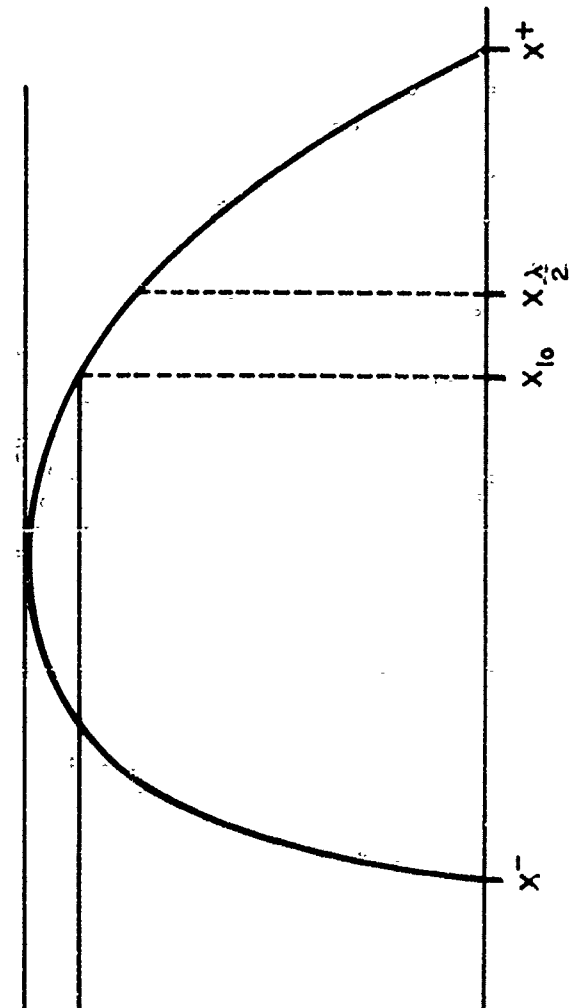

Figure 31. A typical curve of base current vs. distance from the apex, showing the quantities used in the definition of the bandwidth and location of the active region.

changes.

Knowing the high and low frequency edges of the active region, the bandwidth of the active region is given by

$$B_{ar} = \frac{x_{\ell o}}{x^-}, \tag{63}$$

In many practical applications the requirements will be less stringent and the bandwidth of the active region can be decreased accordingly. In a previous paper[18] x^+ was taken as the low frequency edge. The old definition was subsequently found to result in B_{ar}'s greater than necessary for values of τ less than 0.875. A graph of B_{ar} versus σ for several values of τ is shown in Figure 32. The circles are computed values and the straight lines are based on an empirical formula fitted to the computed results,

$$B_{ar} = 1.1 + 30.7\ \sigma(1-\tau) \tag{64}$$

The empirical formula agrees with the computed and measured results for all but the lowest values of τ, so its use should be restricted to $\tau \geq 0.875$. For a fixed τ, the bandwidth of the active region increases as σ increases. This is an important design consideration, because the size of an antenna to cover a given band increases as B_{ar} increases.

The relationship between $x_{\ell o}$ and $x_{\lambda/2}$ takes the form

$$x_{\ell o} = S(Z_o,\ h/a)\ x_{\lambda/2} \tag{65}$$

Due to the geometry of the antenna, an identical relation exists between the half-wavelength transverse dimension and the length of the largest required element in the active region.

$$\ell_{\ell o} = S(Z_o,\ h/a)\frac{\lambda}{2} \tag{66}$$

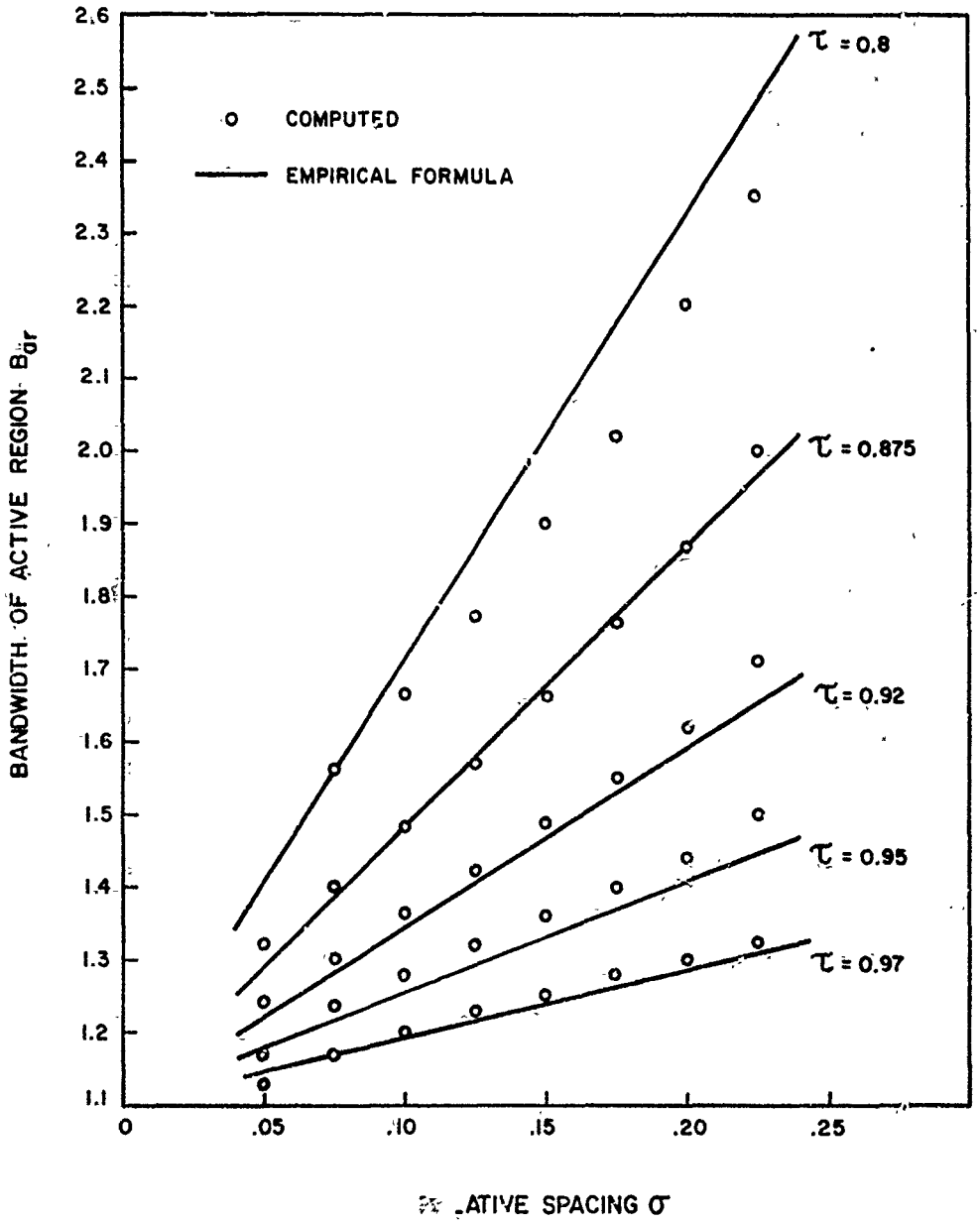

Figure 32. Bandwidth of the active region, B_{ar}, vs. σ and τ.

Thus S represents a shortening factor, and it serves to locate the active region with respect to the half-wavelength transverse dimension. Figure 33 is a graph of the computed shortening factor as a function of Z_o for several values of h/a. S was found to be essentially independent of τ and σ in the range $0.5 \leq \tau \leq 0.95$, and $0.075 \leq \sigma \leq 0.21$. In the computed models, low values of h/a which correspond to thick elements were not extensively investigated; in these cases the approximations of the theory are not well satisfied. The curves have been extrapolated to low values of h/a by the inclusion of measured results. The S factor is significant; for high values of feeder impedance the shortening can be equivalent to scaling the antenna by a factor τ, resulting in the saving of one element at the large end of the antenna. Work done by Isbell[11] on models in which the radii of the elements were held constant, so that h/a varied from 20 to 100, showed that the largest element was roughly 0.47λ at the low frequency cut-off, and this agrees with the trend observed in Figure 33. Another researcher in the field[19] agrees with the location of the active region, but finds that the stated values of B_{ar} are somewhat high if the front-to-back ratio of the pattern is used as a criterion. At any rate, the above results can be used as a guide in the design of LPD antennas for specific applications.

3.3 The Unexcited Region

The unexcited region consists of all dipole elements larger than a half-wavelength at a given frequency, and the portion of feeder to which these elements are attached. This section shows that an unexcited region exists on an LPD because of the efficient manner in which the power in the feeder wave is radiated by the active region. In this case the operation of the LPD antenna is unaffected by the truncation at the large end. The results of

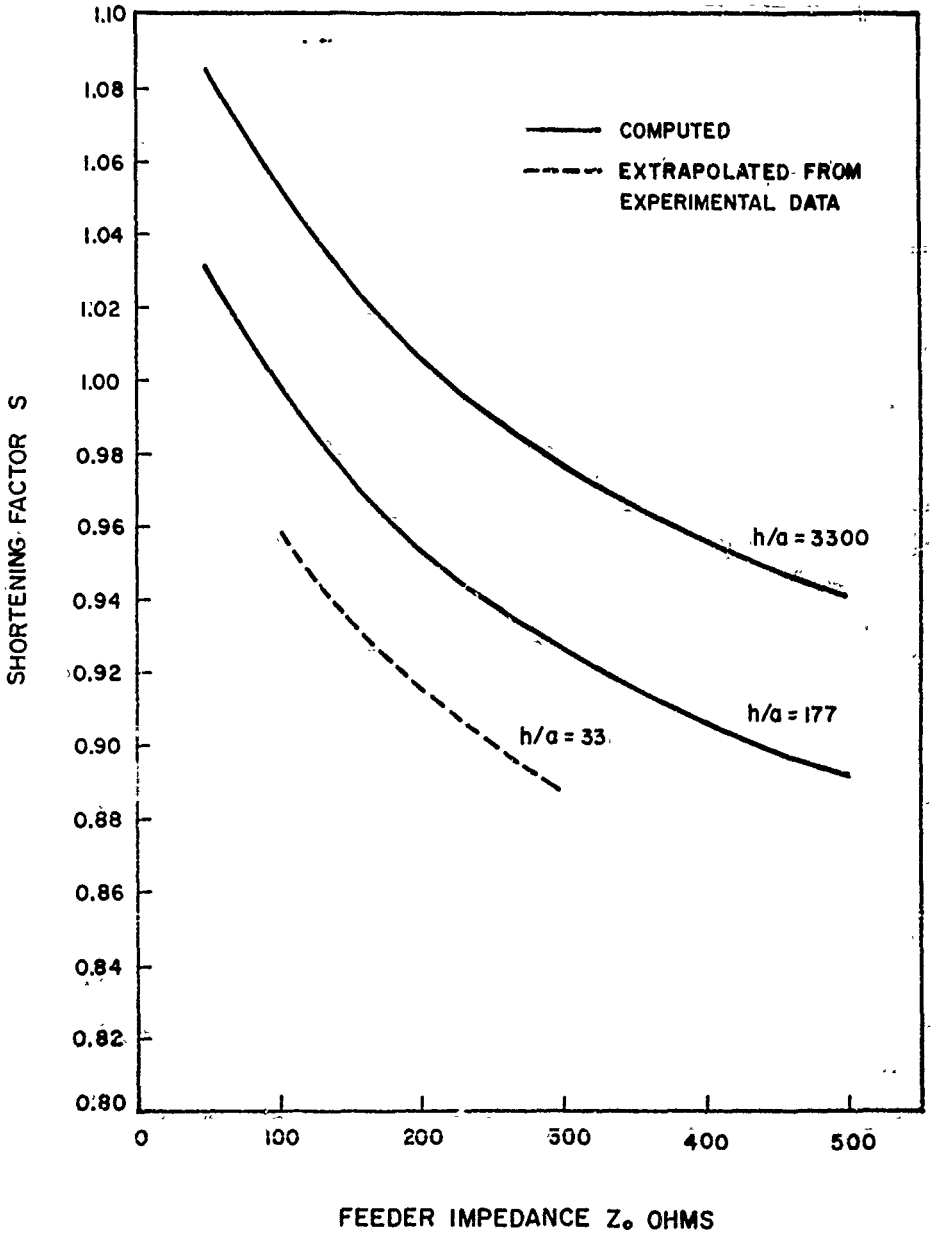

Figure 33. Shortening factor S, vs. Z_0 and h/a.

several measurements of this property are presented.

Perhaps the most easily observed property of a successful log-periodic antenna is the insensitivity of the pattern and input impedance to the abrupt discontinuity at the large end of the antenna between the structure and free space. The absence of end effects can be verified by distorting the structure at the large end of the antenna or by operating the antenna in front of a conducting screen. In either case the characteristics of the antenna performance should not change. This lack of end-effect was observed by the original researchers in the field and was postulated as a necessary condition for log-periodic performance. Furthermore, it was thought that a necessary condition for lack of end effect was that the major portion of the radiated field should be in the direction of shorter elements, so that the longer elements are not illuminated.

As shown in the preceding section, the magnitude of the element current decreases rapidly in the unexcited region. This is because most of the incident power in the transmission wave has been radiated by the elements of the active region. One might reason that the elements which are longer than a half wavelength are not efficiently coupled to the feeder, due to a difference in impedance levels. This is true to an extent, but the fact remains that on a successful LPD there is no practical amount of power on the feeder to excite the longer elements, even if they were efficiently coupled. In fact, there do exist many regions where coupling is favorable; they are in the neighborhood of elements whose lengths are odd multiples of a half-wavelength. These regions will radiate if power is delivered to them by the feeder. This effect has been exploited by Professor Mayes and the author in the design of high gain multi-mode LP antennas[20].

The amount of end effect or excitation of $\frac{3\lambda}{2}$ elements depends on the radiating efficiency of the active region. Assuming the rest of the structure lossless, the radiating efficiency can be defined as

$$\eta \doteq \frac{P_{IN} - P_T}{P_{IN}} \tag{67}$$

P_{IN} is the total input power and P_T is the power dissipated in a matched resistor at the large end of the antenna, i.e. $Z_T = Z_o$. End effect depends on the amount of power delivered to the termination, and one would expect P_T to be negligible when the antenna is performing satisfactorily. Figure 34 is a graph of η versus the length of the longest element in wavelengths. Computed values for feeder impedances of 100 and 300 ohms are plotted for an LPD with $\tau = 0.888$ and $\sigma = 0.089$. The relative length of the longest element was varied by changing the frequency; identical results would obtain by changing the antenna size. When the longest element is a half-wavelength, more than 80% of the incident power has been dissipated by radiation from the active region. The antenna is more efficient for $Z_o = 300$ ohms than for $Z_o = 100$ ohms for fixed ℓ_1/λ. This is partially the result of the movement of the active region toward the smaller elements as Z_o is increased, as was discussed in Section 3.2.2. The X's on the graph correspond to values measured by Isbell[11] on an LPD with $\tau = 0.89$ and $\sigma = 0.0275$, with $Z_o = 104$ ohms. The measured results agree with the computed results for $Z_o = 100$ ohms in the neighborhood of $\ell_1/\lambda = 0.5$. This is an indication that the low frequency edge of the active region remains fixed as σ is changed.

The end effect or the possibility of exciting $3\lambda/2$ elements on an LPD depends on τ and the feeder impedance Z_o. Figure 35 shows the computed

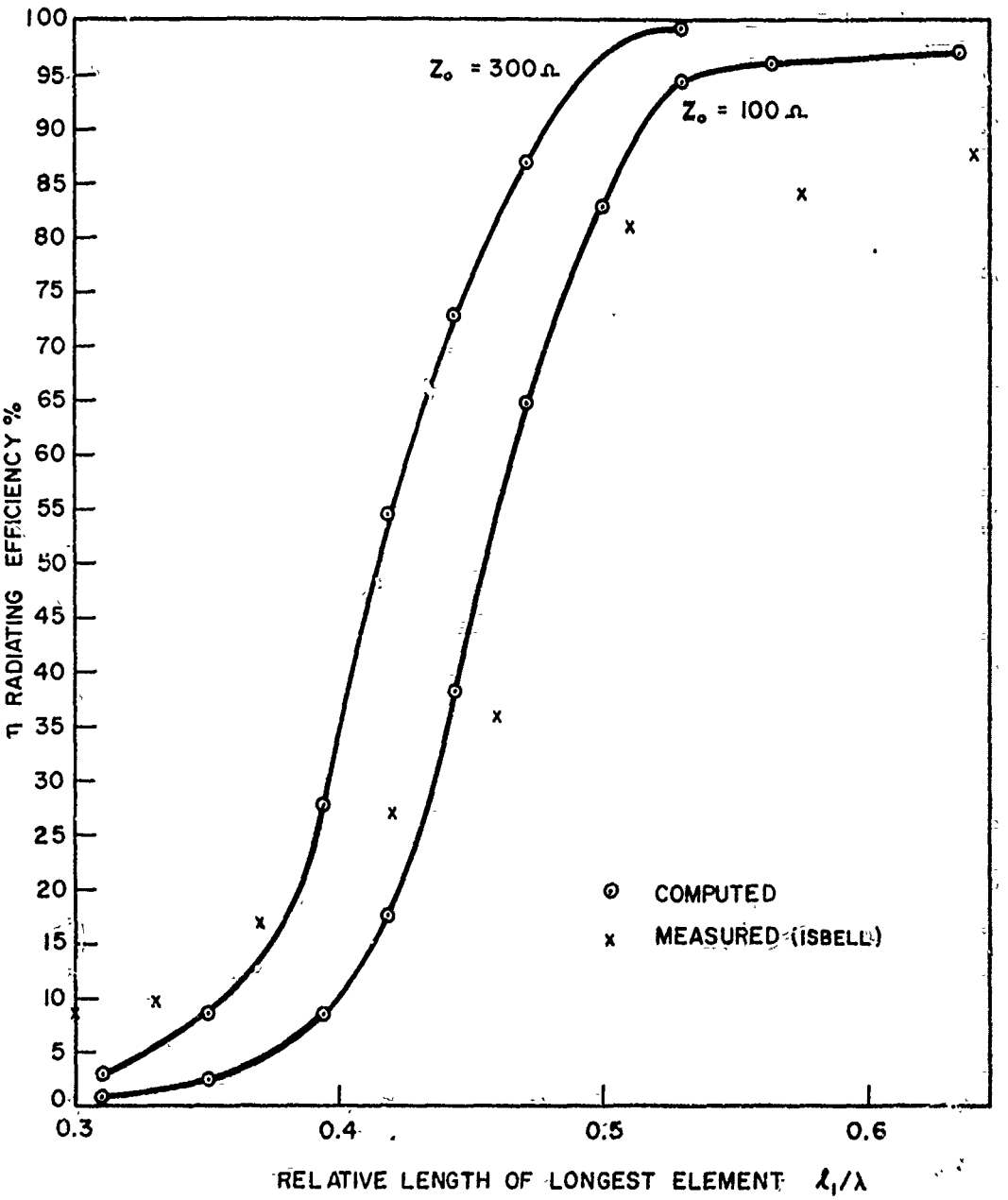

Figure 34. Radiating efficiency of the active region vs. relative length of the longest element.

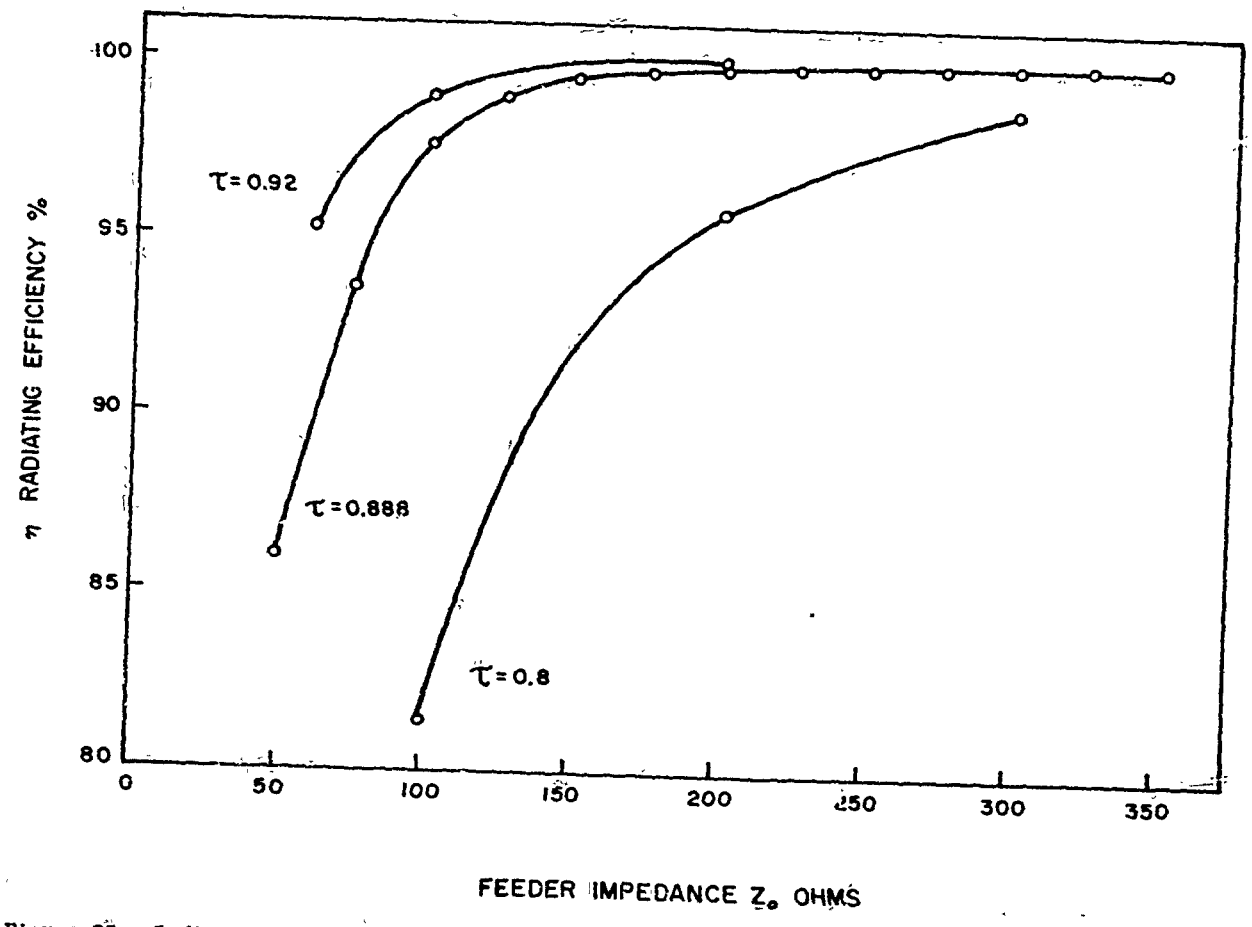

Figure 35. Radiating efficiency of the active region vs. feeder impedance and τ.

efficiency as a function of Z_o for $\tau = 0.92$ and $\ell_1/\lambda = 0.65$, for $\tau = 0.888$ and $\ell_1/\lambda = 0.71$, and for $\tau = 0.800$ and $\ell_1/\lambda = 0.97$. The curves were determined by averaging high, optimum, and low values of σ; the deviation ranges from $\pm$ 3% for $\tau = 0.8$ to $\pm$ 1% for $\tau = 0.92$. For the given values of ℓ_1/λ the active region is well ahead of the longest element. Nevertheless for low values of τ and Z_o an appreciable amount of power remains on the feeder behind the antenna. If the efficiency is less than 85 or 90 percent and the antenna is terminated in a mis-match (e.g. a short circuit), sufficient power will be reflected back into the active region to cause the antenna characteristics to depend on frequency. If an LPD has an operating bandwidth greater than 3:1, at some frequencies $3\lambda/2$ elements will exist on the antenna. If the efficiency of this model is low, the $3\lambda/2$ elements will be energized, and there will be two active regions on the antenna. In severe cases pattern lobing will occur.

Provided the efficiency is greater than 90%, a short circuit at a distance $h_1/2$ behind the longest element is a satisfactory termination for all models in the range $0.8 < \tau < 0.98$ and $0.03 < \sigma < 0.23$. The 90% efficiency requirement places a lower limit on the allowable values of τ and Z_o. This is why it is difficult to achieve, for example, a 50 ohm input impedance if the required feeder impedance is less than 75 ohms and τ is less than 0.888. The relation between feeder impedance and input impedance is discussed in Section 3.4.3.

The absence of end effect is an important feature of frequency independent antennas. It has been found that the frequency dependent performance of many unsuccessful log-periodic structures can be attributed to end effects.

3.4 The Input Impedance

The input impedance of a log-periodic dipole antenna is measured at the

juncture of the feeder and the smallest dipole element. This section considers the input impedance level as being determined primarily by the characteristics of the equivalent line in the transmission region. Data are presented which show how the input impedance depends on the various LPD parameters, and an approximate formula is given which enables one to design an LPD with a required input impedance. A wide practical range of impedance levels can be obtained, and factors which ultimately limit this range are discussed.

3.4.1 General Characteristics of LPD Input Impedance

A plot of input impedance versus frequency for an eight element LPD with $\tau = 0.888$ and $\sigma = 0.089$ is shown on the Smith Chart of Figure 36. The numbers on the chart are the j's in

$$f_j = f_1 \tau^{1-j} \tag{68}$$

where f_1 is the frequency for which element 1 is a half-wavelength long. Except for $f_0, f_{1/2}$, f_7 and f_8 the points cluster around a mean resistance level R_o. To find R_o, a circle is drawn with its center on the resistance axis, enclosing the cluster. The intersections of the circle with the resistance axis determines the minimum and maximum swing of resistance. R_o is then given by

$$R_o = \sqrt{R_{max} R_{min}} \tag{69}$$

The standing wave ratio with respect to R_o is given by

$$SWR = \sqrt{\frac{R_{max}}{R_{min}}} \tag{70}$$

In Figure 36, the mean resistance level is 72 ohms and the standing wave ratio, with respect to 72 ohms, is 1.25:1. The points for f_o and $f_{1/2}$ fall outside

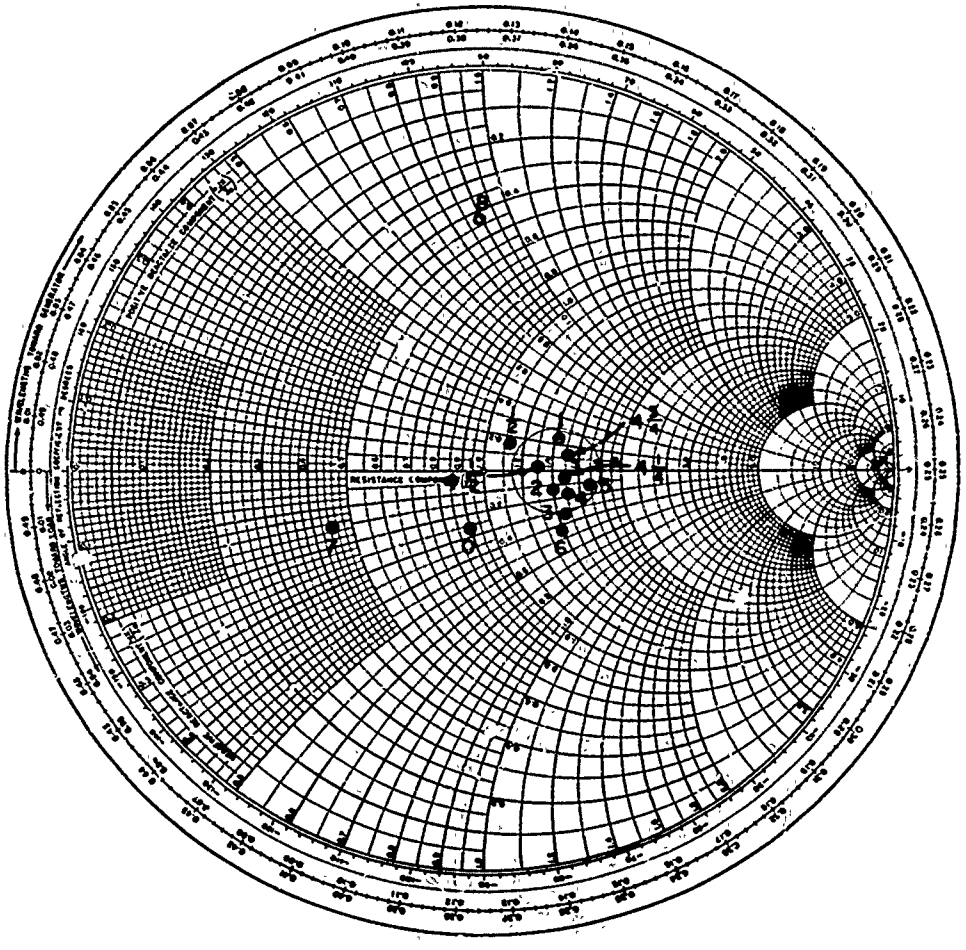

Figure 36. Input impedance vs. frequency of an eight element LPD.

the cluster; this indicates that the low frequency limit has been exceeded. The points f_7 and f_8 also fall outside the cluster, indicating that the high frequency limit has been exceeded. These effects are typical and characterize all LP antennas. To the extent that the SWR can be neglected, the points which make up the cluster define the frequency independent impedance bandwidth of this antenna.

Ideally, the input impedance at the apex of an infinite log-periodic structure should be the same for all frequencies related by the scale factor τ. There is at least one reason why this does not generally hold for LP antennas, even for frequencies within the design band. In any practical LP, the scaling from cell to cell must start at a small but finite element, because the device which delivers energy to the antenna cannot be made arbitrarily small. This means that there is always a portion of the structure missing due to the front truncation. In Section 3.1 it was shown that the transmission region acts as a uniform line. Since a fixed length of this line is missing (the part from the apex to the smallest element), impedances are not transformed to the apex, and a frequency dependent variation is imposed. The departure from the ideal log-periodic variation is negligible only if the removed piece of line is electrically small at the highest operating frequencies. The electrical length of front-truncated line depends on the propagation constant in the transmission region and the distance x_N from the apex to the shortest element. In some cases the front truncation can introduce an appreciable effect. The graph of Figure 36 is one such example. Here the equivalent length of the front truncation amounts to $0.75\lambda_t$ at the high frequency limit (λ_t is the wavelength of the transmission wave). The input impedances at frequencies related by integral powers of τ are not equal. An example of

a case in which the front truncation can be neglected, at least for low frequencies, is shown in Figure 37. This antenna has $\tau = 0.8$ and $\alpha = 30^{\circ}$, with 13 elements. Frequencies f_3 through f_4 are plotted, and the input impedances are practically equal. In this case the front truncation amounted to about $0.072\ \lambda_t$. This example also illustrates the way the impedance varies as frequency changes from f to τf. This typical variation produces a standing wave ratio at the input terminals which is a complicated function of the LPD parameters.

3.4.2 Input Impedance as a Function of τ and σ

The input SWR with respect to R_o of a precisely constructed LPD is usually small no matter how severe the front truncation. This fact suggests that the observed mean resistance level R_o is actually the characteristic impedance of an equivalent line in the transmission region, and that the active region presents a good match to this line. The approximate formula for the constants of the equivalent line, derived in Section 3.1.2, can then be used to find the functional variation of the input impedance of an LPD. Rewriting Equation (57), yields

$$R_o = \frac{Z_o}{\sqrt{1 + \frac{Z_o}{Z_a}\frac{\sqrt{\tau}}{4\sigma}}} \tag{71}$$

One finds that the mean resistance level is a function of all the LPD parameters. Figure 38 is a graph of Equation (71) for $Z_o = 100$ and $Z_a = 350$ as a function of σ for two values of τ, 0.8 and 0.97. This shows that the dependence on τ is not very great. For a given Z_o and Z_a the value of R_o depends primarily on the spacing σ. As σ increases the added loading decreases, so R_o approaches the Z_o of the unloaded feeder. Several computed values are plotted on the graph.

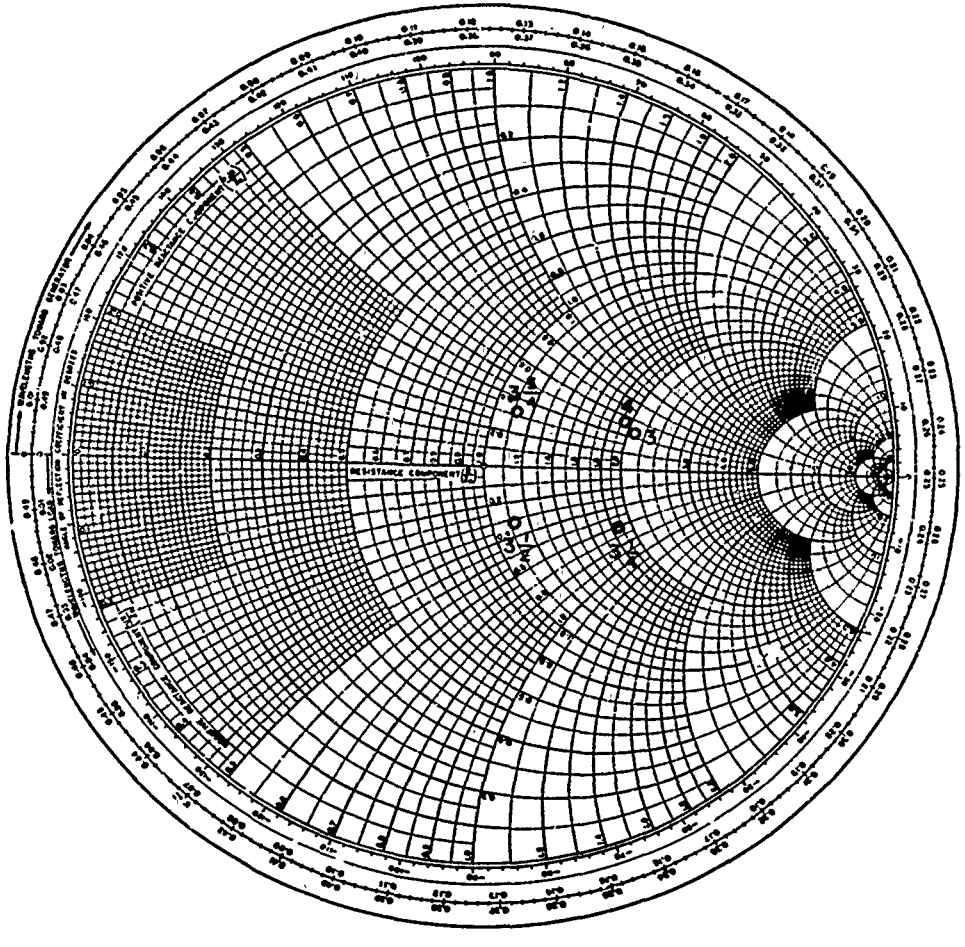

Figure 37. Input impedance showing periodic variation with frequency.

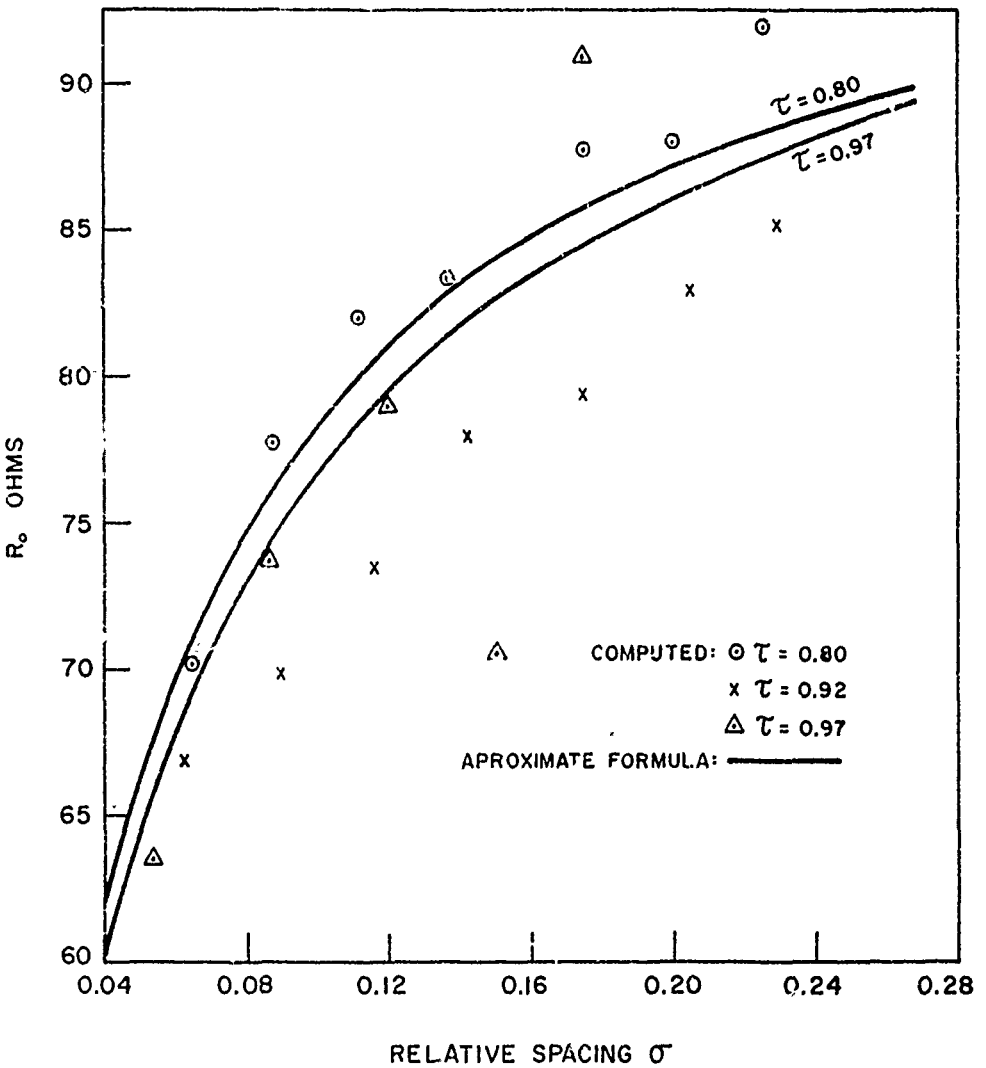

Figure 38. Input impedance R_o vs. σ and τ for Z_o = 100 and h/a = 177.

The error between the approximate formula and measured or computed results is usually less than 10%.

An indication of the nature of the error involved in assuming that the capacitive loading of a small element is distributed uniformly over a section of the feeder can be found. Consider the loading to consist of small, identical elements, uniformly spaced. Assuming the capacitance of a small dipole to be proportional to its length as in Section 3.1.2, the characteristic impedance of this equivalent line can be found. It is

$$R_o = \frac{Z_o}{\sqrt{1 + \dfrac{\dfrac{Z_o}{Z_a}\dfrac{\sqrt{\tau}}{4\sigma}\varphi}{\sin\varphi + \dfrac{i}{2}\dfrac{Z_o}{Z_a}\dfrac{\sqrt{\tau}}{4\sigma}\varphi(\cos\varphi - 1)}}} \qquad (72)$$

Here φ is the electrical length in radians of one section of line. $\varphi = \frac{2\pi d}{\lambda}$, where d is the distance between neighboring elements. As φ goes to zero (72) reduces to (71). A graph of the error involved in using (71) rather than (72) is shown in Figure 39, where the percent error is plotted as a function of d/λ. The error is small for all values of d/λ found in the transmission region of an LPD.

The computed standing wave ratio with respect to R_o as a function of σ for several values of τ is shown in Figure 40. For these models $Z_o = 100$ ohms and $h/a = 177$. The SWR decreases as τ increases, and for low values of τ, a minimum value of SWR exists. For the two large laboratory models which were used for the near field measurements, the values of SWR agreed with the computed values. However, the SWR of pattern models was always greater than

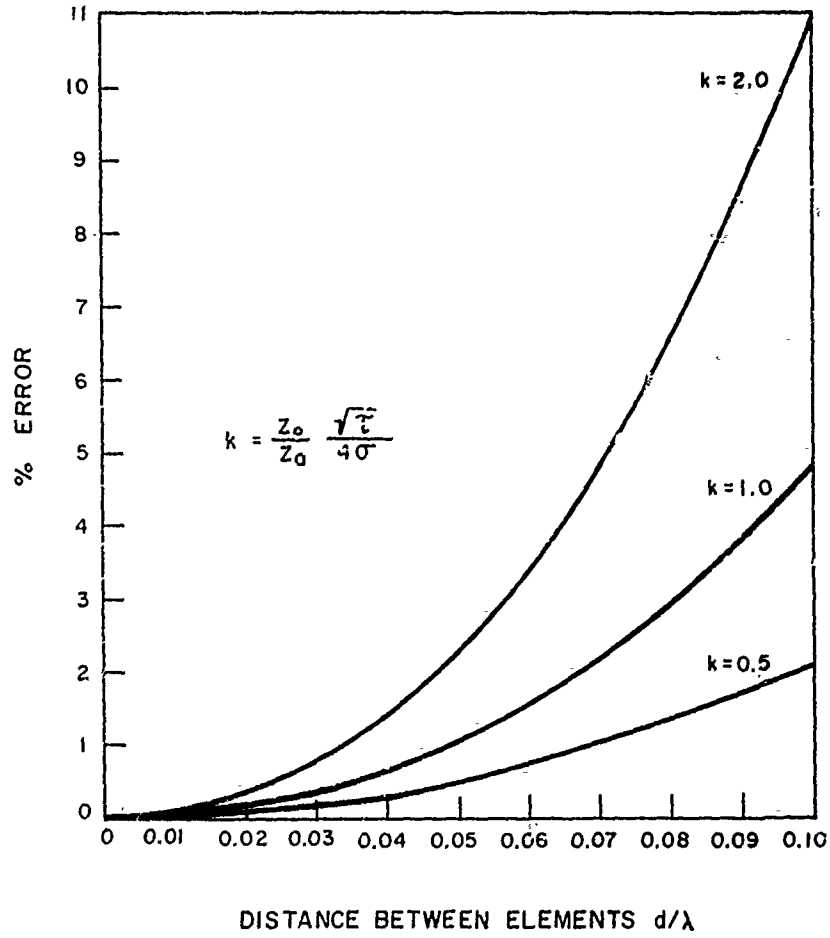

Figure 39. Difference between the approximate discrete formula and approximate distributed formula for R_o, vs. the distance between elements as a percent of the latter.

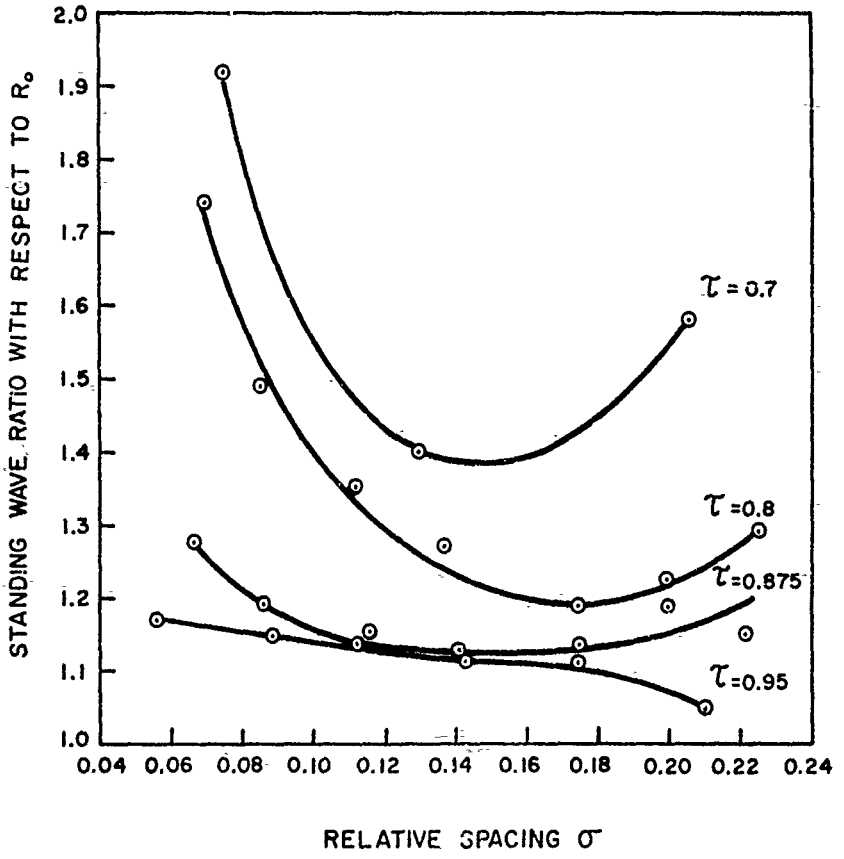

Figure 40. Computed SWR vs. σ and τ, for Z_c = 100 and h/a = 177.

the computed value; this is because the details of the feed-point geometry assume additional importance at higher frequencies.

3.4.3 Input Impedance as a Function of Z_o and h/a

For fixed τ and σ, the mean resistance level is determined by the characteristic impedance of the feeder, Z_o. The graph of Figure 41 shows that R_o increases as Z_o increases. The computed points are shown along with the measured values. In addition, points calculated from the approximate formula (71) are also shown. In all cases the agreement is good, demonstrating the utility of the approximate formula.

Figure 42 shows how R_o depends on Z_o as a function of the mean spacing factor $\sigma' = \sigma/\sqrt{\tau}$, using the approximate formula (71). As σ' increases, the slope of the curves approach unity, indicating that R_o approaches Z_o.

The element thickness as given by the ratio h/a can also be used to control the input impedance. Figure 43 shows the effect of changing h/a with fixed Z_o, for several values of σ'. As h/a increases, the loading decreases and R_o increases.

It can be seen from the preceding graphs that the input impedance of LPD antennas can be adjusted over a wide range. The upper limit is determined by the problems involved in constructing feeder configurations. Even when four wire balanced lines are used, characteristic impedances greater than 600 ohms are difficult to achieve. An added reactance due to the large gap between the two halves of each dipole would possibly cause detrimental effects. In the computed models there was no way of taking this into account; the computer results show that antennas with Z_o = 500 ohms work just as well as antennas with Z_o = 100 ohms. The lower limit of Z_o is determined by the radiating

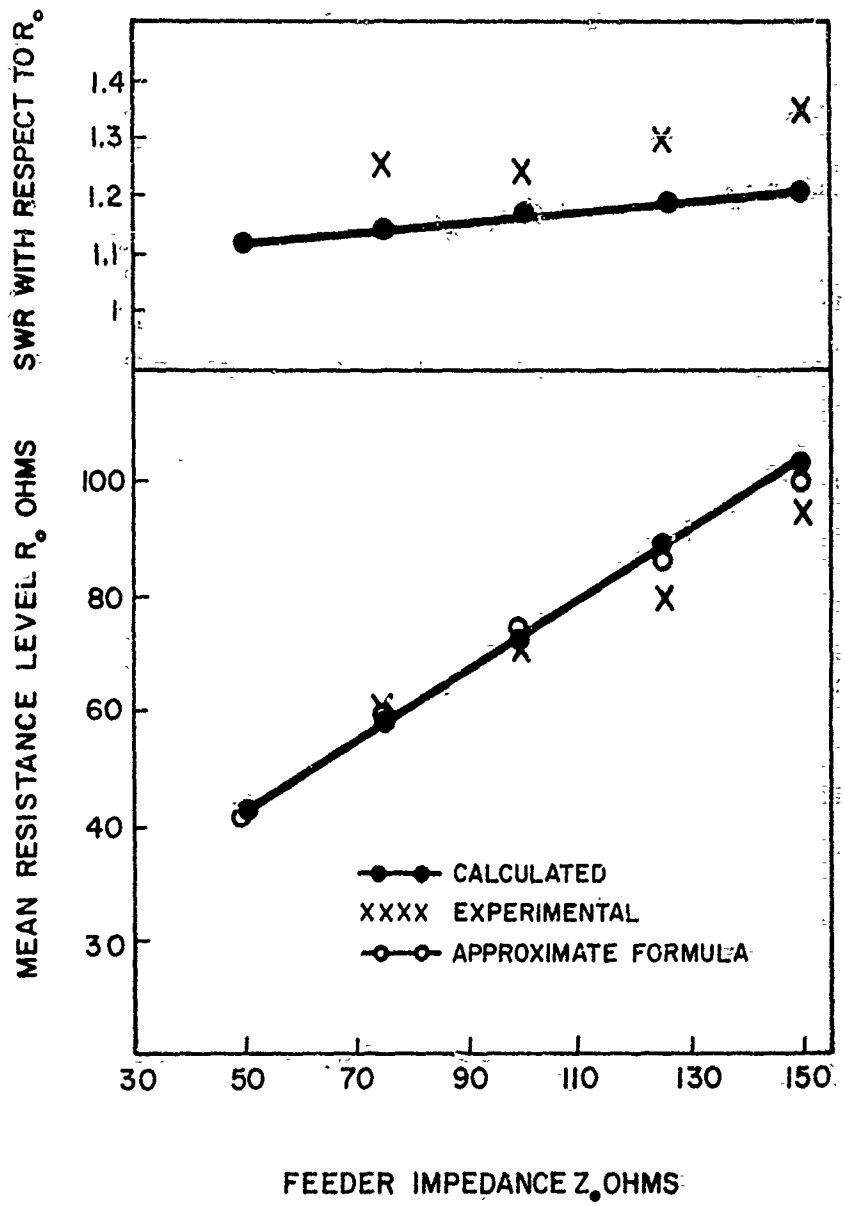

Figure 41. Input impedance R_o vs. feeder impedance Z_o, $\tau = 0.888$, $\sigma = 0.089$, N = 8, h/a = 125.

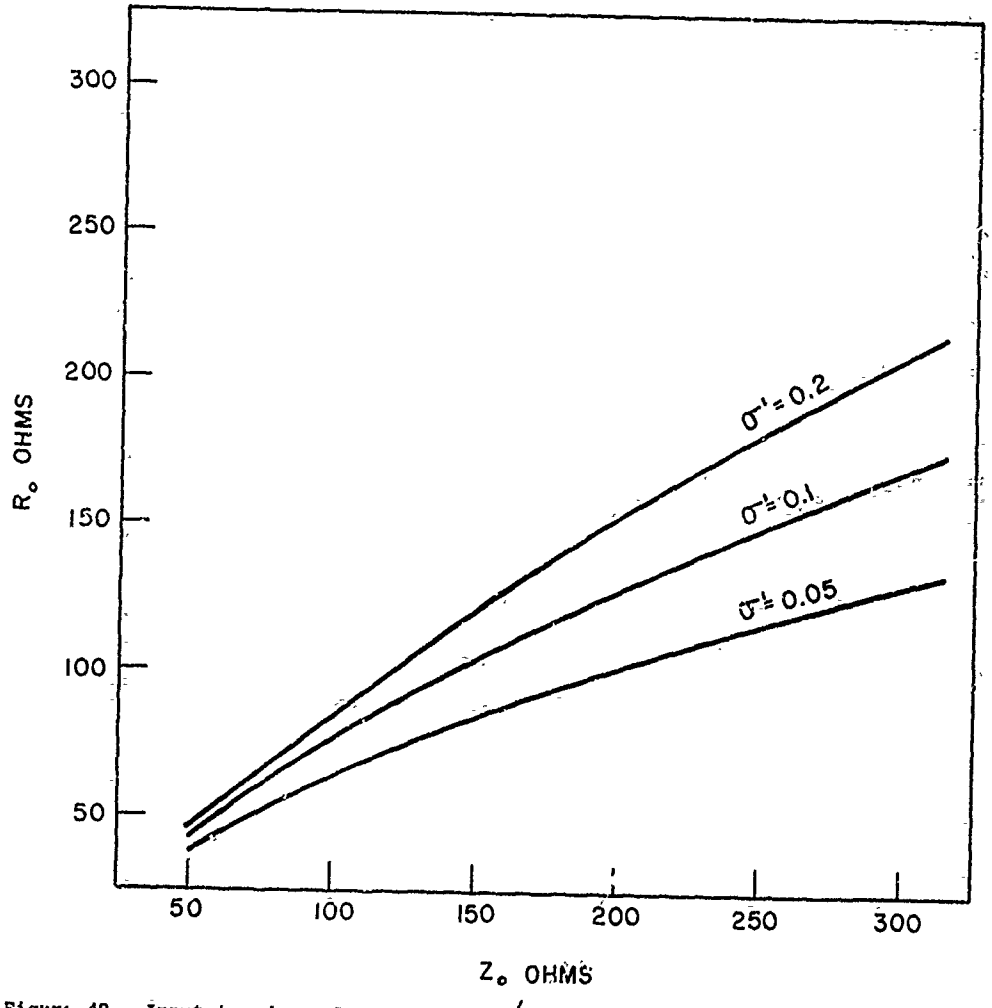

Figure 42. Input impedance R_o vs. Z_o and σ' with h/a = 177, from the approximate formula.

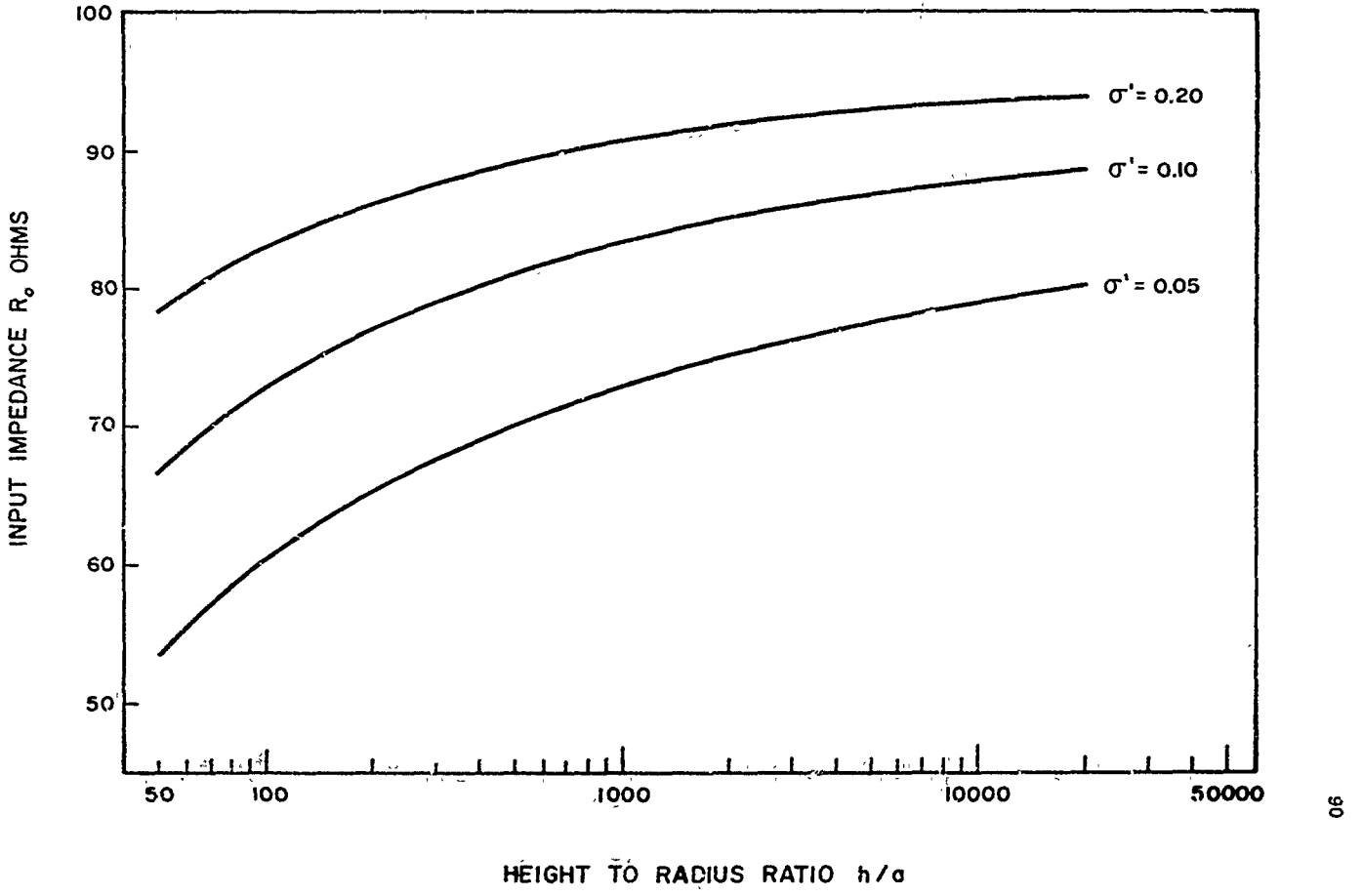

Figure 43. Input impedance R_o vs. h/a and σ , Z_o = 100, from the approximate formula.

efficiency of the antenna. As previously shown in Section 3.3, in all models in which Z_o is less than 75 ohms an appreciable amount of power remains on the feeder at the large end of the antenna. This power is reflected back through the antenna if the feeder is shorted at the large end, as is commonly done, or it is wasted if a resistive termination is used. This effect has been detected in the computed models. Figure 44a shows the input impedance of an LPD with Z_o = 50 ohms, terminated in a 50 ohm resistor. The impedance locus has the same characteristics as for higher values of Z_o. However, when a purely reactive termination is used, the input impedance locus blossoms out as shown in Figure 44b, indicating that the end effect is appreciable. In addition, irregularitites in the pattern occur, otherwise the increased SWR could probably be tolerated.

Formula (71) can be inverted to find the feeder impedance required to achieve a given input impedance. In its most useful form Z_o is normalized with respect to R_o, resulting in

$$\frac{Z_o}{R_o} = \frac{1}{8\sigma' \frac{Z_a}{R_o}} + \sqrt{\frac{1}{\left(8\sigma' \frac{Z_a}{R_o}\right)^2} + 1} \quad . \tag{73}$$

As in Equation (71) Z_a is the average characteristic impedance of a short dipole, given by

$$Z_a = 120 \ (\ln h/a - 2.25). \tag{74}$$

A graph of Z_a versus h/a is given in Figure 45. Figure 46 is a graph of the relative feeder impedance Z_o/R_o versus the relative characteristic dipole impedance Z_a/R_o, for several values of the mean spacing factor σ'. This graph can be used to design for a specific input impedance, given σ' and Z_a.

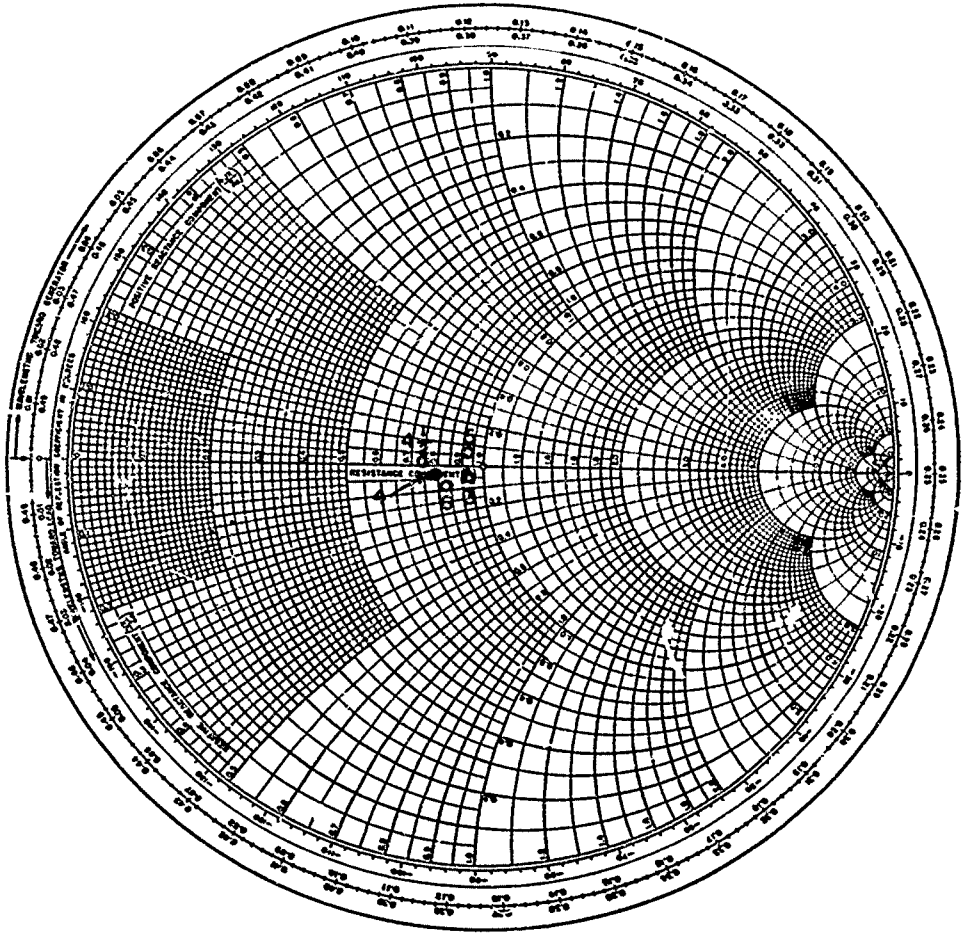

Figure 44à. Input impedance $\tau = 0.888$, $\sigma = 0.089$, $N = 8$, $Z_o = 50$, $Z_T = 50$ at frequencies f_3, f_4, $f_{4\ 1/2}$, f_5 and f_6.

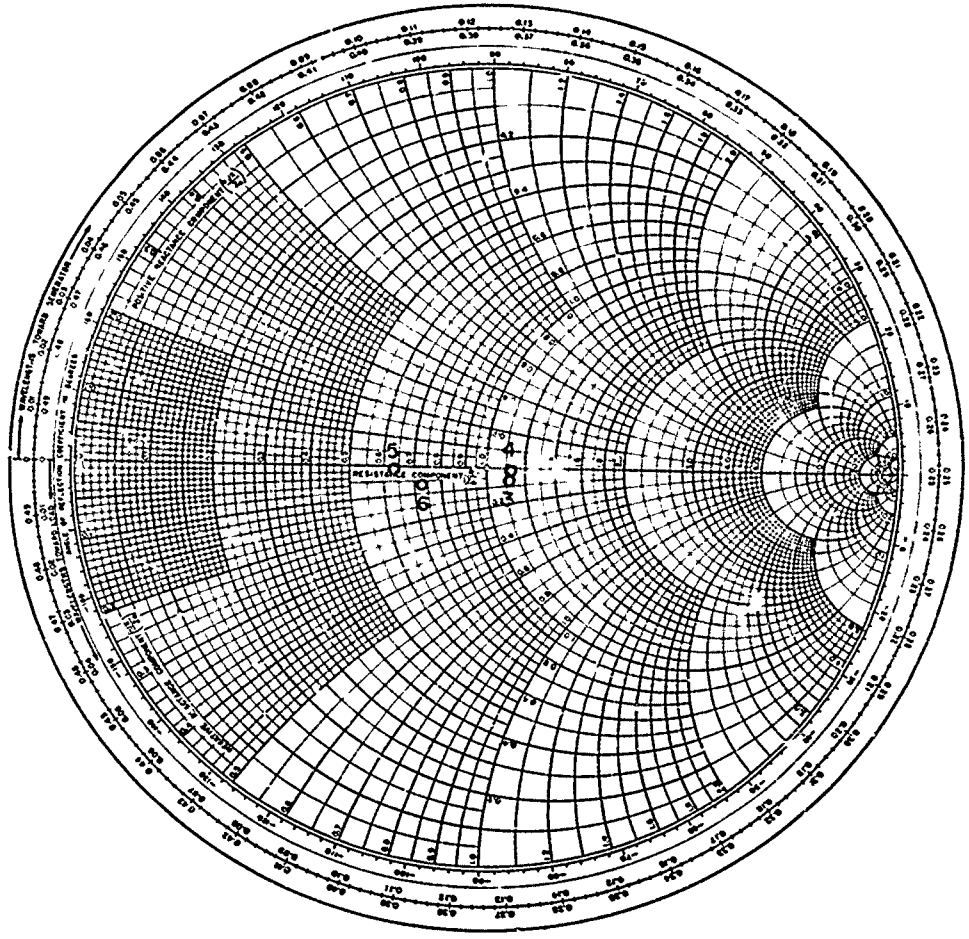

Figure 44b. Input impedance $\tau = 0.888$, $\sigma = 0.089$, $N = 8$, $Z_o = 50$, Z_T = short at $h_1/2$, at frequencies f_3, f_4, f_5 and f_6.

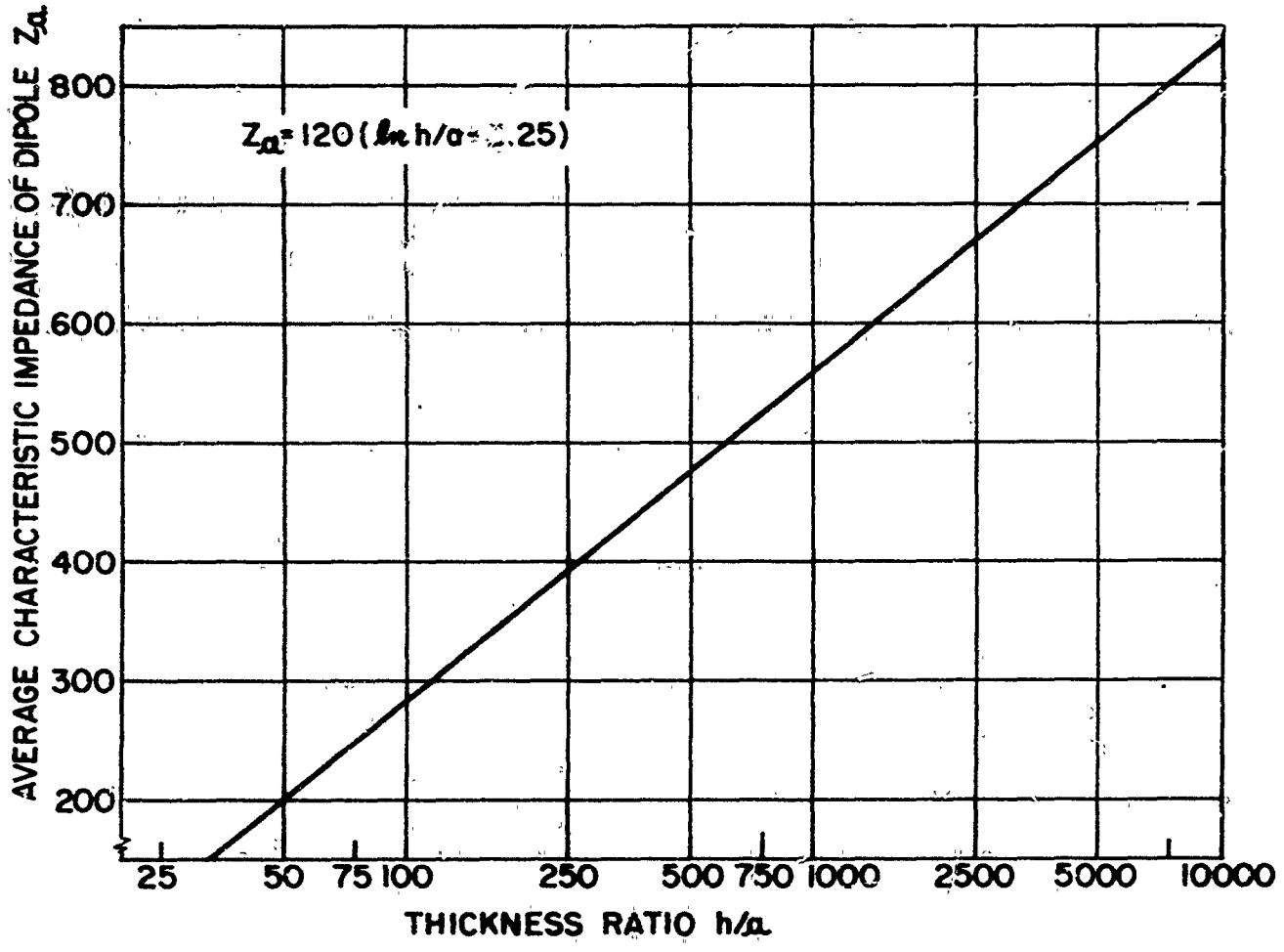

Figure 45. Average characteristic impedance of a dipole Z_a vs. height to radius ratio h/a.

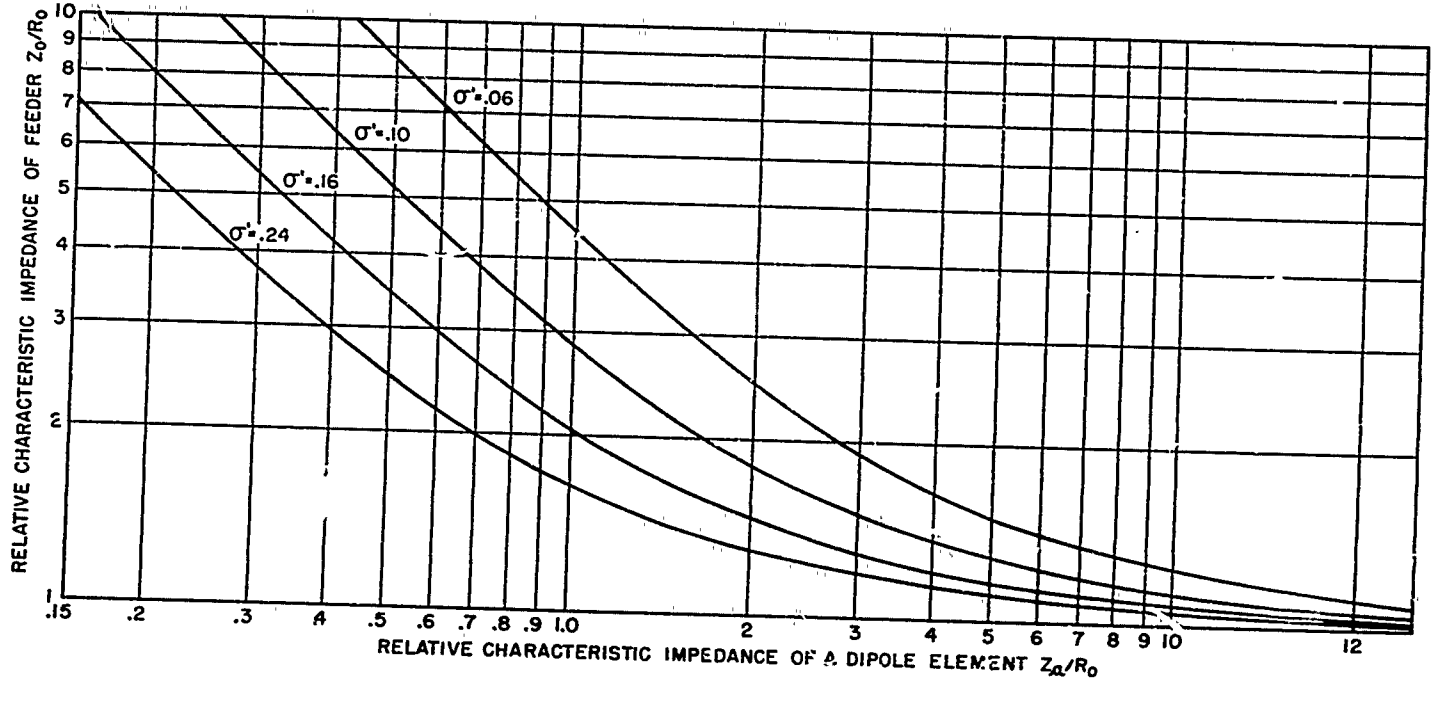

Figure 46. Relative feeder impedance Z_o/R_o vs. relative dipole impedance Z_a/R_o, from the approximate formula.

Input impedance levels from 35 to 200 ohms have been measured using the coaxial line feed method pictured in Figure 9. If higher impedance levels are required for use with balanced twin line, the 4:1 balun transformer scheme suggested by Dr. Jordan can be used. In Figure 47, the feeder of an LPD is shown but the elements are not. R_o represents the antenna input impedance at the front end. This load can be driven in parallel by two coaxial lines of characteristic impedance $2R_o$. Each line is inserted through one of the feeders as shown, and at the back of the antenna they are connected in series. A parallel wire line with characteristic impedance $4R_o$ is then connected to the series combination, resulting in a perfect match to the antenna. This balun transformer scheme has a bandwidth equal to the operating bandwidth of the antenna. Since there is no current on the feeder at the back of the antenna, the quarter-wave choke which is ordinarily used in a 4:1 balun is not required, so the balun does not depend on frequency. This technique has been used with success in the design of LPD television receiving antennas.

3.5 The Far Field Radiation

The far field properties of the LPD antenna are determined from the equations of Section 2.2.2. This section presents computed results which show how the characteristic pattern of an LPD depends on the various parameters. The characteristic pattern of an LPD is defined as the pattern which typifies the antenna for all frequencies within the design band. The computed patterns are compared with patterns of several experimental models, recorded by the University of Illinois Antenna Laboratory pattern range facilities. Consideration is also given to factors which control the relative phase of the far field. The phase center of an LPD is defined, and measured and computed

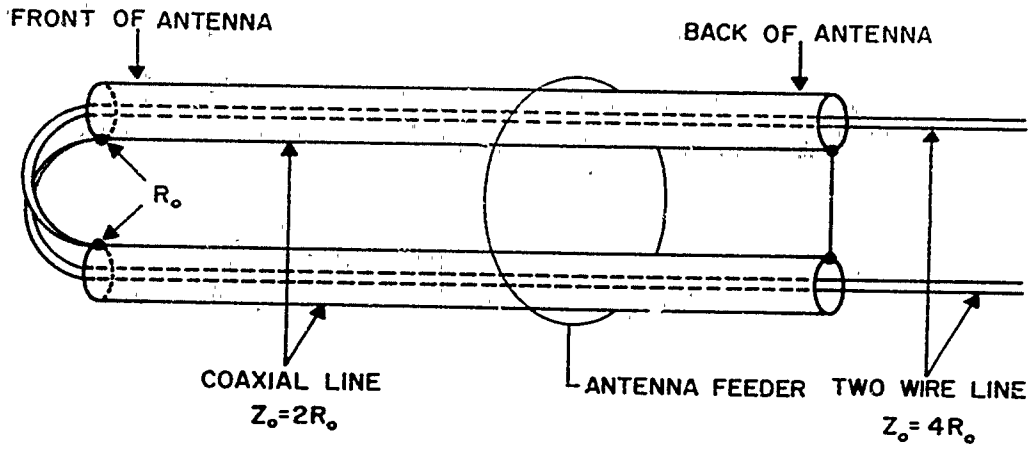

Figure 47. A Frequency independent 4:1 balun transformer for use with LPD antennas

data are presented which show that the phase center is located at the active region.

3.5.1 Radiation Patterns

Examples of the computed relative field intensity patterns are shown in Figure 48. For this LPD, $\tau = 0.888$, $\sigma = 0.089$ and $N = 8$. f_j denotes the frequency

$$f_j = f_1 \tau^{1-j} \tag{75}$$

where f_1 is the frequency for which element number one is a half-wavelength long. The characteristic pattern is observed over the range f_1 to f_7, which yields a pattern bandwidth of approximately $(0.888)^{1-7} = 2.04$. At f_8 definite pattern deterioration has occurred, indicating that the high frequency limit has been exceeded. Figures 53, 54, and 55a are enlarged patterns which show the negligible variation as frequency changes from f to τf. The computed patterns of Figure 49 are for the same antenna with fewer elements, $N = 5$. Again there is no measurable difference. In addition to exhibiting negligible variation over a period, the characteristic pattern of this antenna does not depend on the number of elements, as long as there are enough elements to support the active region. Thus, according to the definition, this antenna can be called frequency independent with respect to its radiation pattern. This behavior is typical of computed and measured LPD patterns. The only exceptions occur when there is an end effect. These exceptions are characterized by patterns which change with frequency. The patterns broaden and sometimes side lobes appear.

The gross pattern behavior can be observed from a plot of the computed half-power beamwidth versus frequency, as in Figure 50. The E-plane pattern holds constant over a wider frequency range than the H-plane pattern.

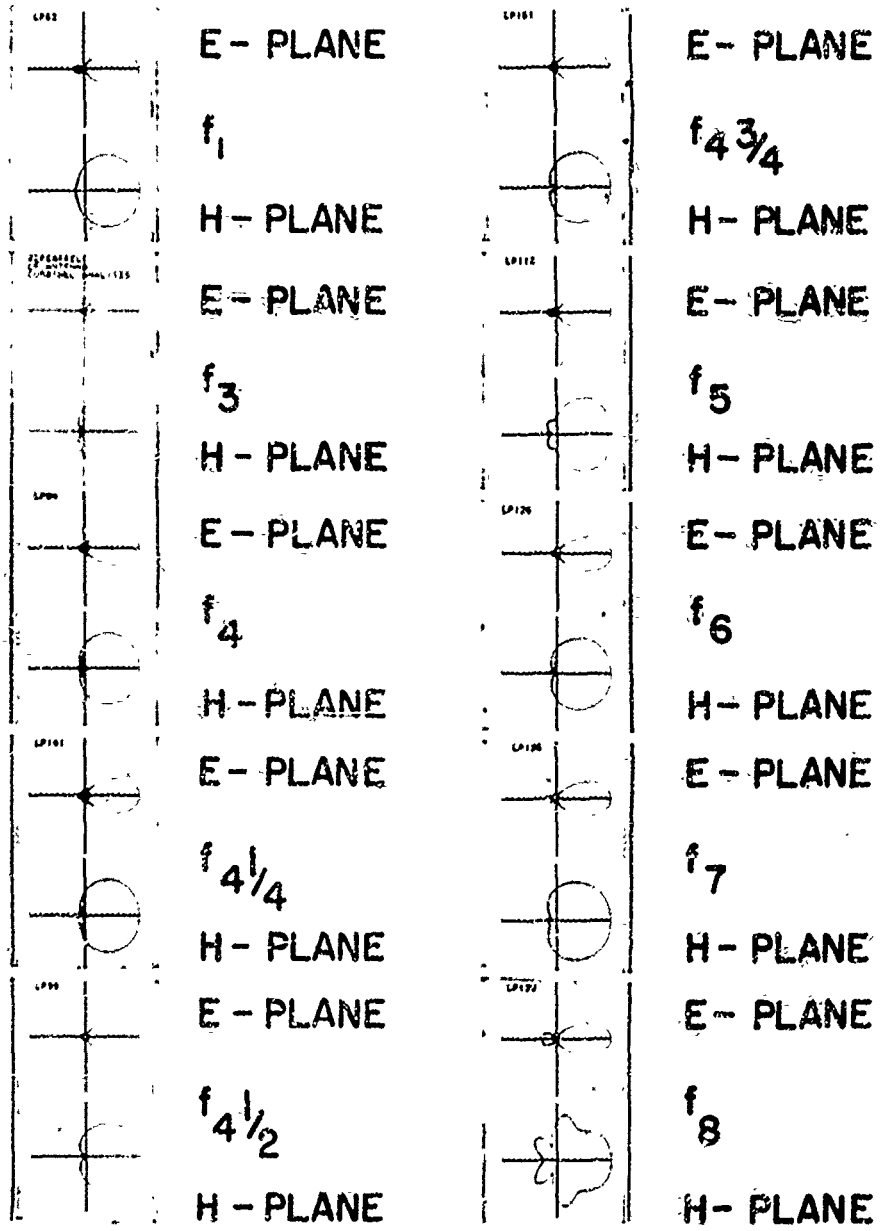

Figure 48. An example of radiation patterns computed by ILLIAC, $\tau = 0.883$, $\sigma = 0.089$, $N = 8$, $Z_o = 100$, Z_T = short at $h_1/2$

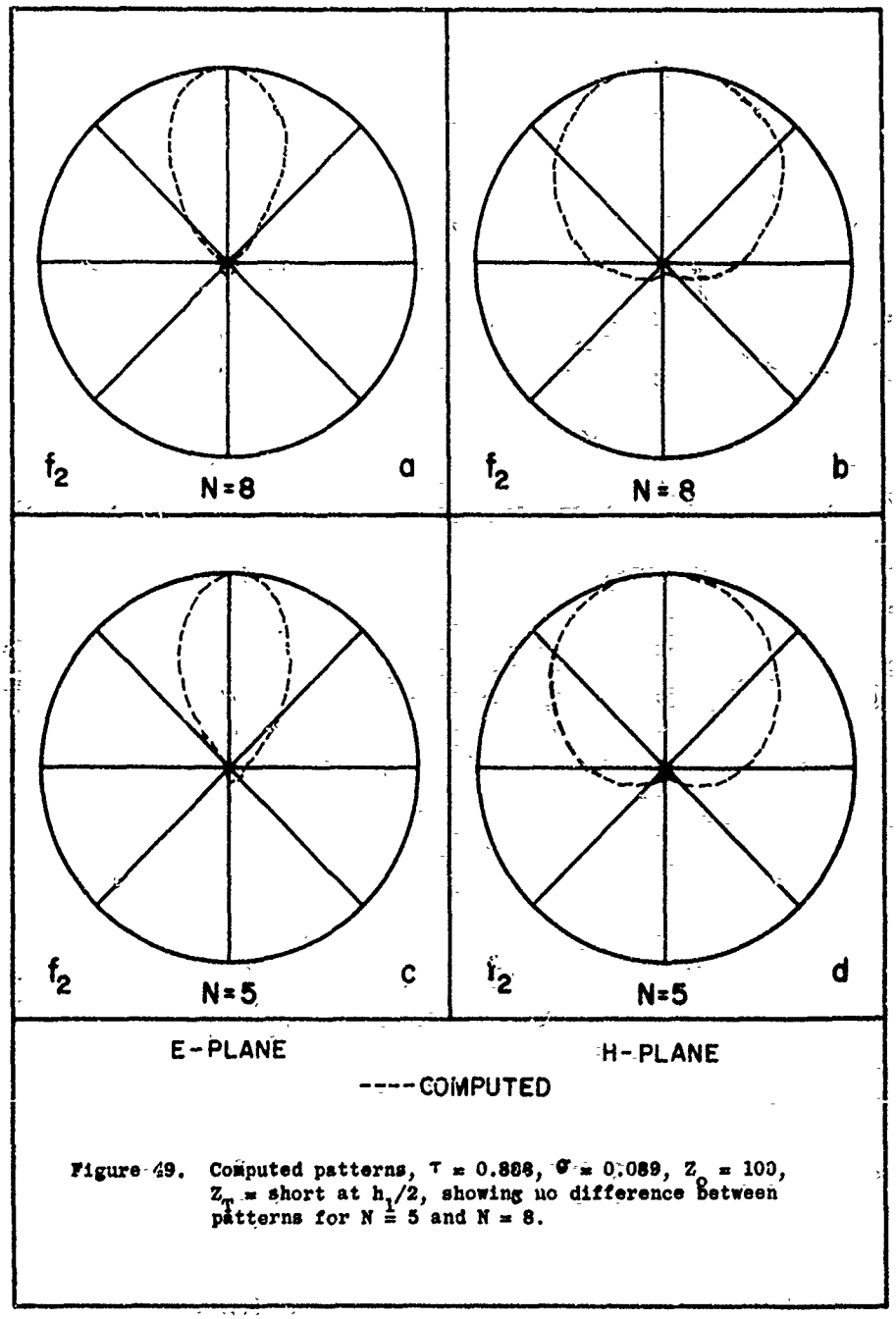

Figure 49. Computed patterns, $\tau = 0.888$, $\sigma = 0.089$, $Z_0 = 100$, Z_T = short at $h_1/2$, showing no difference between patterns for N = 5 and N = 8.

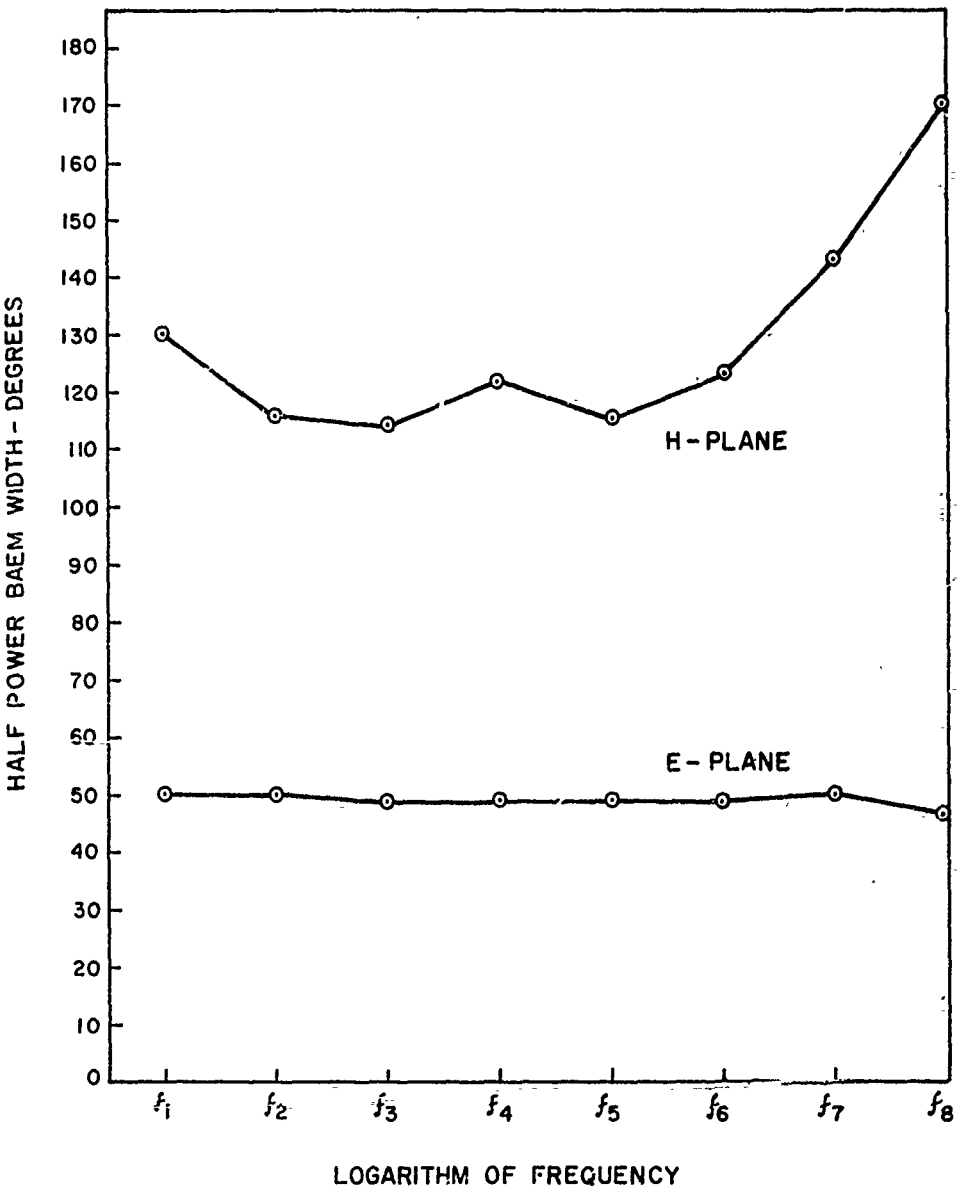

Figure 50. Computed half power beamwidth vs. frequency; $\tau = 0.888$, $\sigma = 0.089$, $N = 8$, $Z_o = 100\Omega$, Z_T = short at $h_1/2$.

This trend is evidenced by all LPD antennas, and results from the strong dependence of the H-plane pattern on the array factor* of the antenna, whereas the more directive E-plane element pattern masks small changes in the array factor. The graph of H-plane beamwidth shows that the active region spans several elements, because the pattern bandwidth is significantly less than the structure bandwidth. The graph also shows that the center of the active region is located somewhat ahead of the half-wavelength element, because the center of the pattern band is located at a lower frequency than the center of the structure band.

Examples of measured and computed patterns are given in Figures 51 through 56 for $\tau = 0.388$ and $\sigma = 0.089$; in Figures 57 through 59 for $\tau = 0.98$ and $\sigma = 0.057$, and in Figures 60 through 62 for $\tau = 0.8$ and $\sigma = 0.137$. The measured cross polarization was found to be more than 20 db below the pattern maximum as long as the spacing between the feeder conductors is small compared to the shortest wavelength of operation. In every case the computed E-plane beamwidth is narrower than the one measured, and the computed H-plane beamwidth is wider than the one measured. These errors tend to compensate each other in the computation of antenna directivity, so the comparison of computed and measured directivity is more accurate than the comparison of computed and measured beamwidth. The error is incurred because the actual current on the dipole elements apparently departs from the assumed sinusoidal form.

---

* Actually, it can be seen from Equations (46) and (47) that the pattern cannot be expressed as the product of an element factor and an array factor, because of the differing element lengths. However, it is convenient to think in these terms here, owing to the dissmilarity between the E-plane pattern of a single element (a figure eight pattern) and the H-plane pattern (omnidirectional).

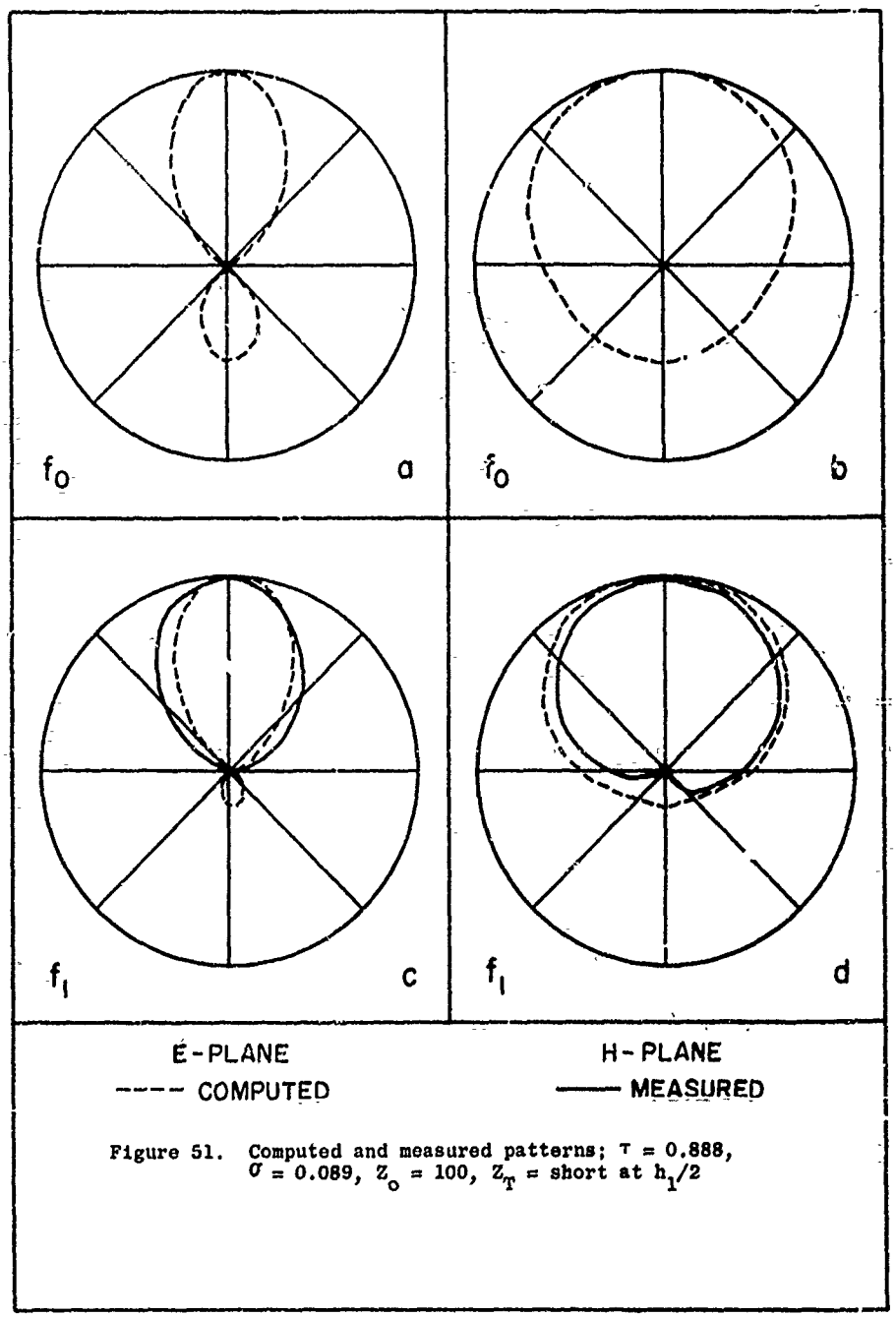

Figure 51. Computed and measured patterns; $\tau = 0.888$, $\sigma = 0.089$, $Z_o = 100$, Z_T = short at $h_1/2$

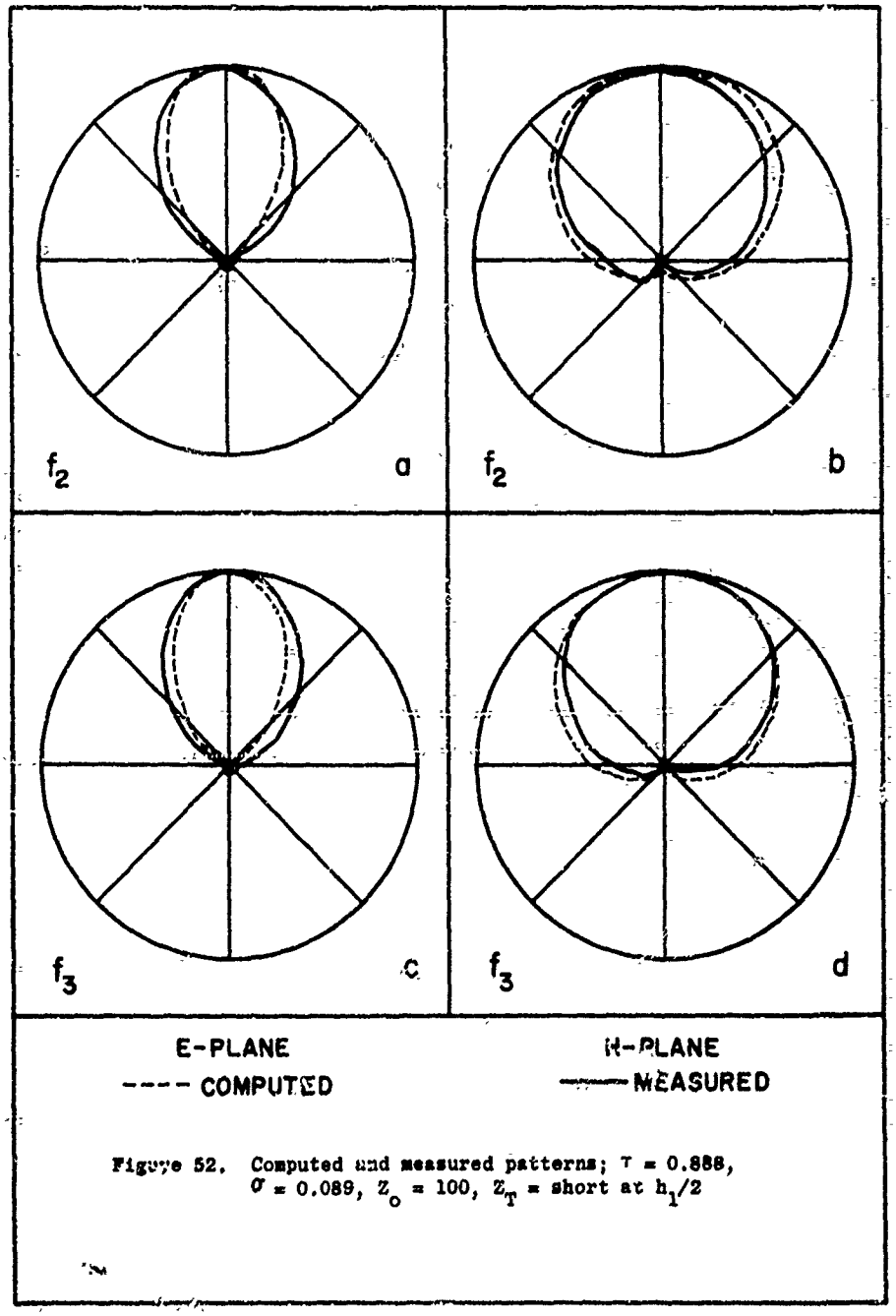

Figure 52. Computed and measured patterns; $\tau = 0.888$, $\sigma = 0.089$, $Z_o = 100$, Z_T = short at $h_1/2$

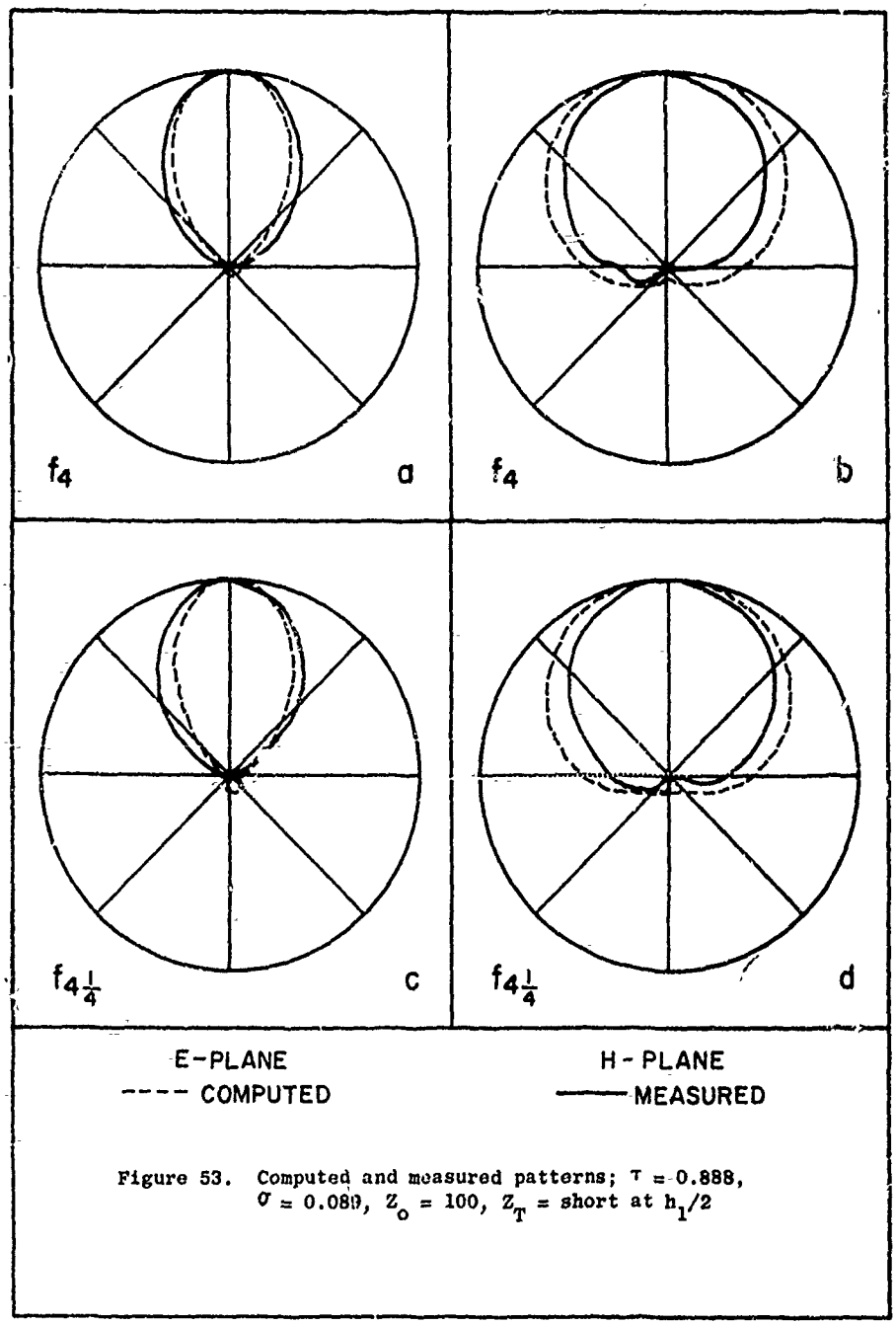

Figure 53. Computed and measured patterns; $\tau = 0.888$, $\sigma = 0.089$, $Z_o = 100$, Z_T = short at $h_1/2$

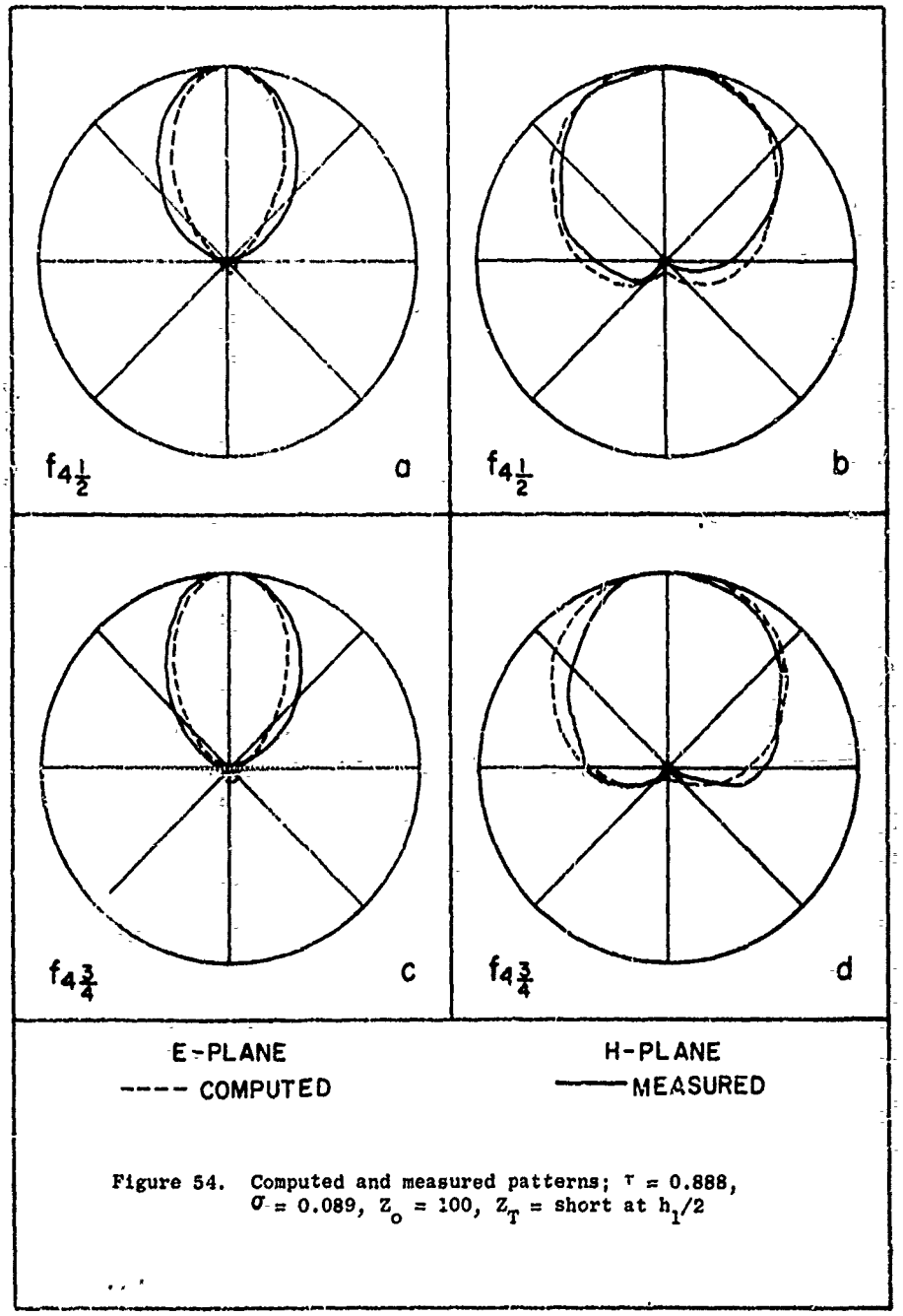

Figure 54. Computed and measured patterns; $\tau = 0.888$, $\sigma = 0.089$, $Z_o = 100$, Z_T = short at $h_1/2$

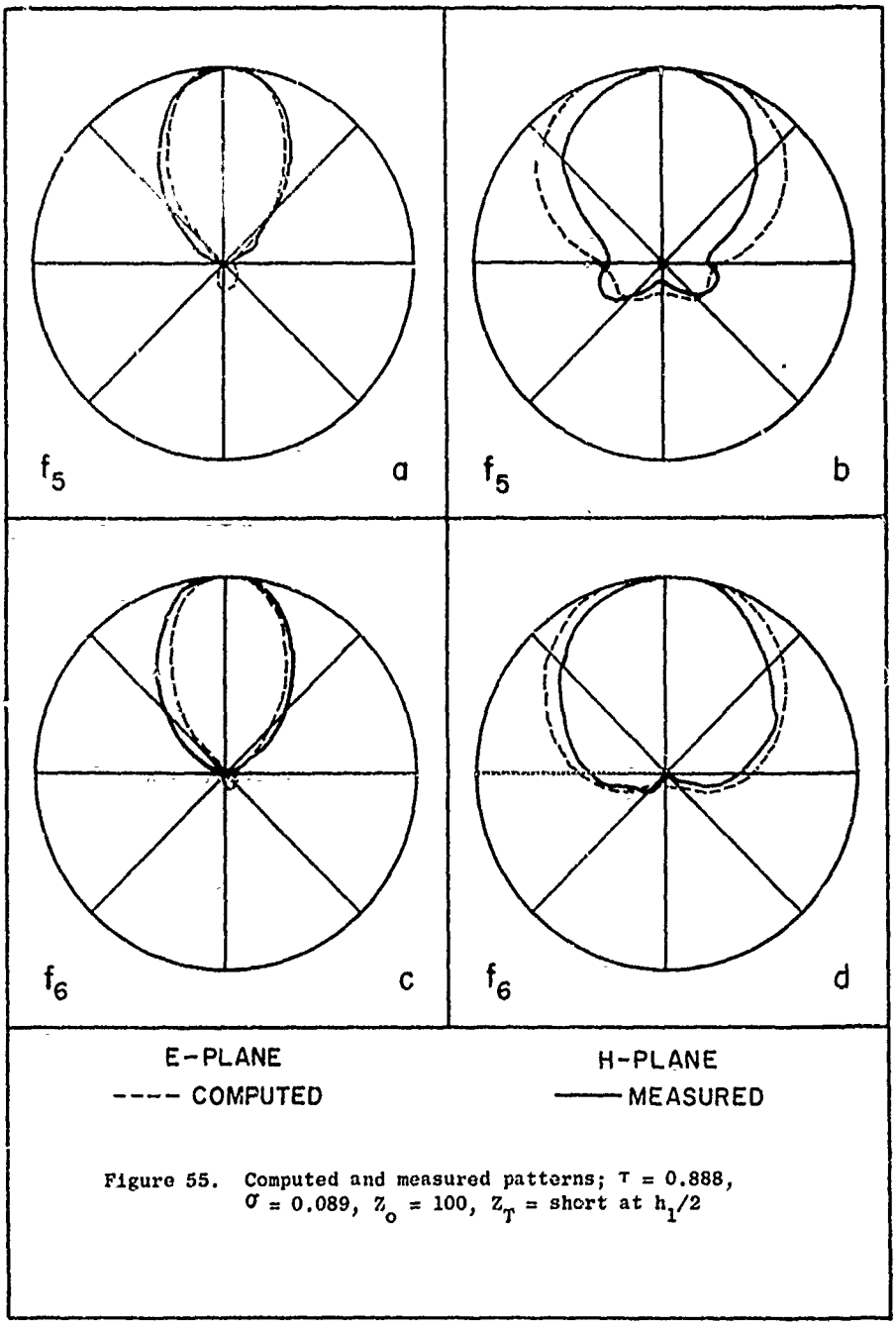

Figure 55. Computed and measured patterns; $\tau = 0.888$, $\sigma = 0.089$, $Z_o = 100$, Z_T = short at $h_1/2$

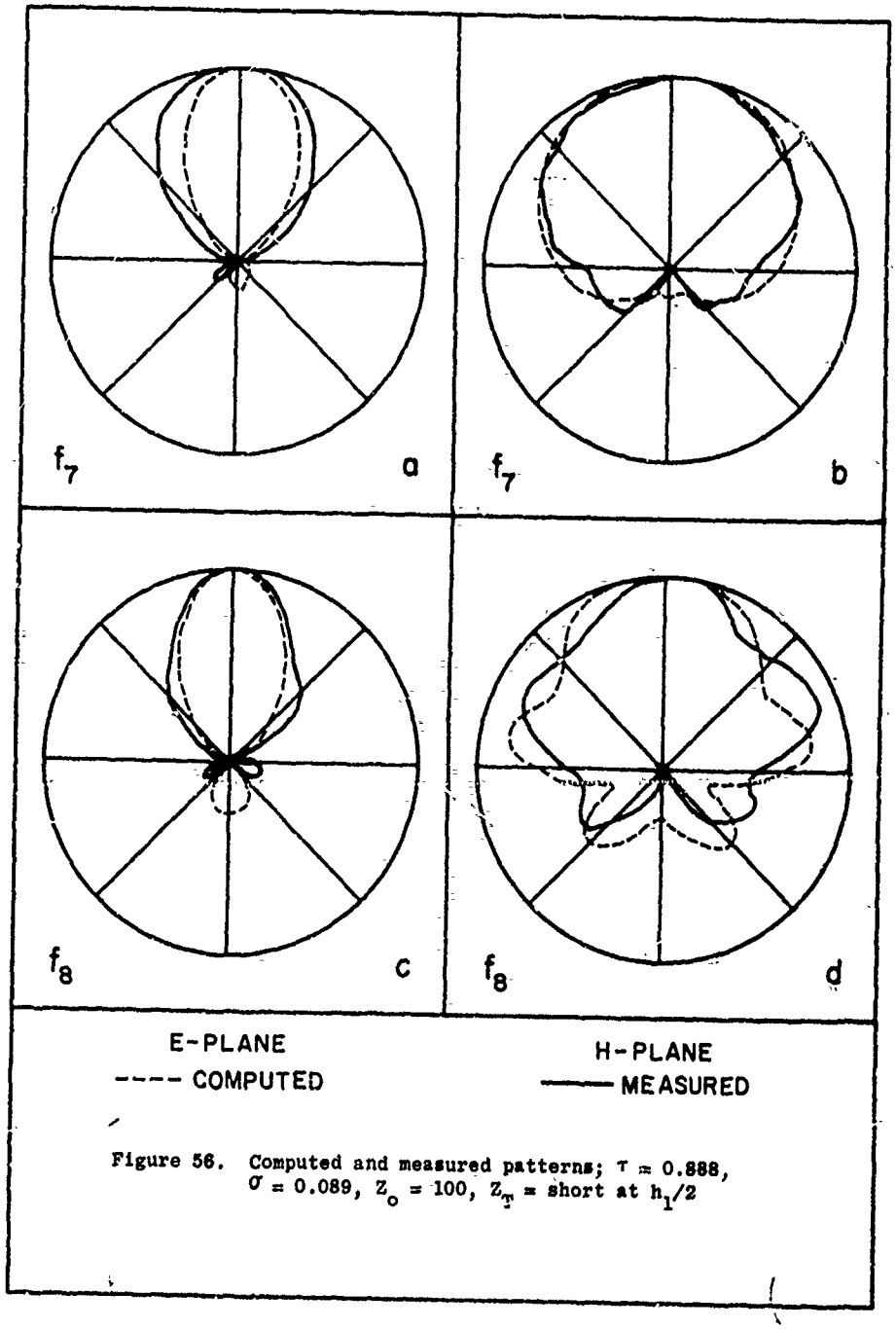

Figure 56. Computed and measured patterns; $\tau = 0.888$, $\sigma = 0.089$, $Z_o = 100$, Z_T = short at $h_1/2$

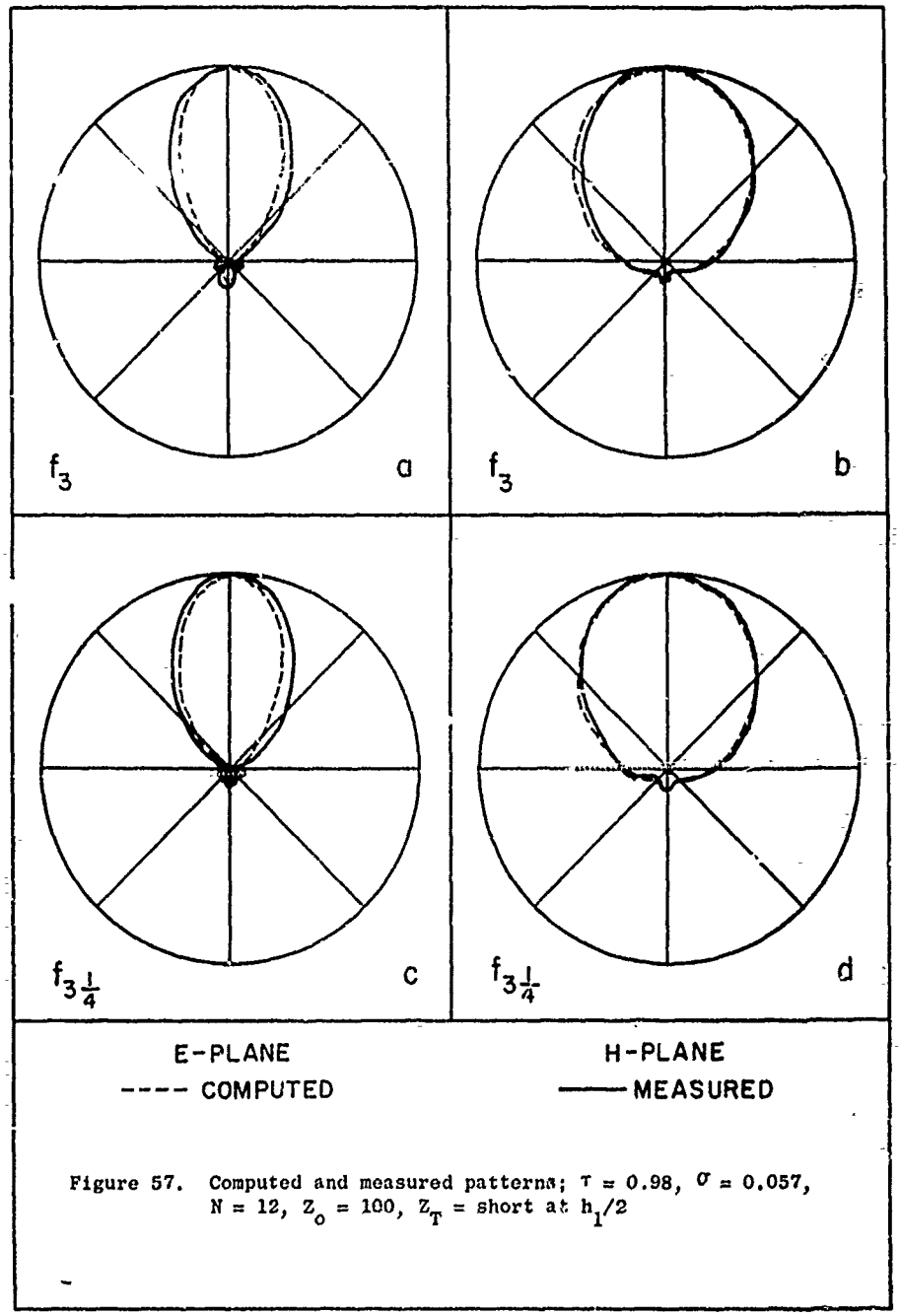

Figure 57. Computed and measured patterns; $\tau = 0.98$, $\sigma = 0.057$, $N = 12$, $Z_o = 100$, Z_T = short at $h_1/2$

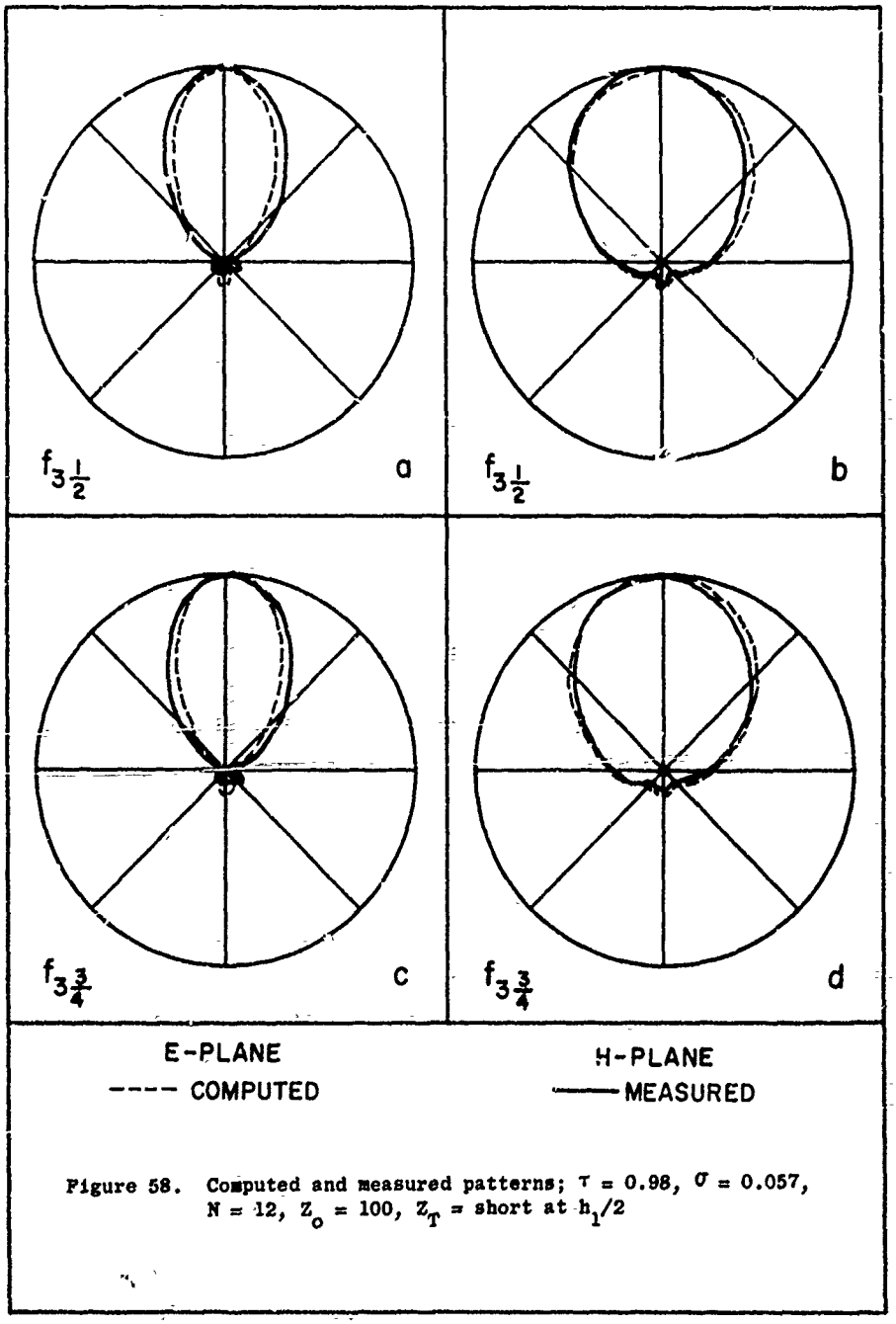

Figure 58. Computed and measured patterns; $\tau = 0.98$, $\sigma = 0.057$, $N = 12$, $Z_o = 100$, Z_T = short at $h_1/2$

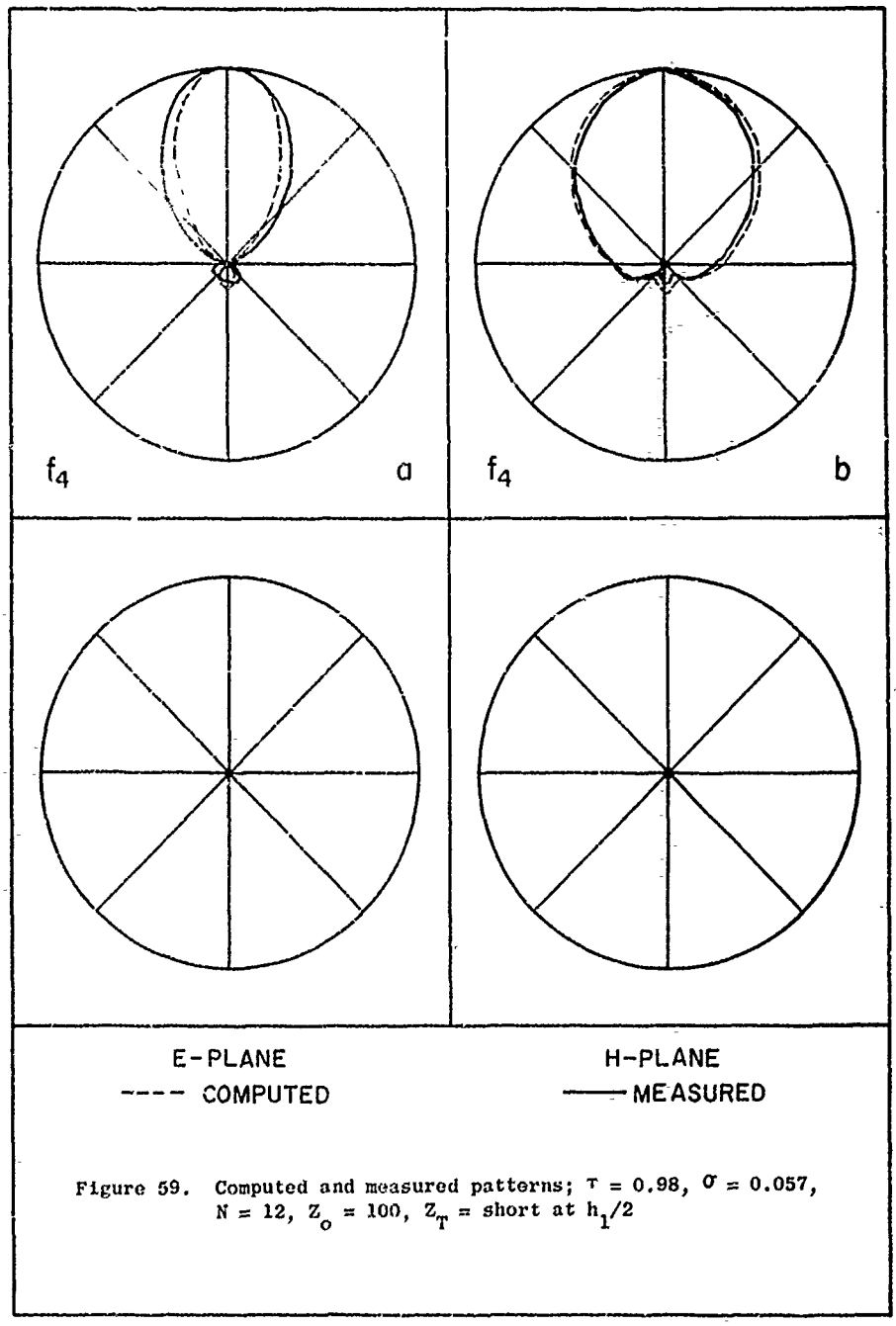

Figure 59. Computed and measured patterns; $\tau = 0.98$, $\sigma = 0.057$, $N = 12$, $Z_o = 100$, Z_T = short at $h_1/2$

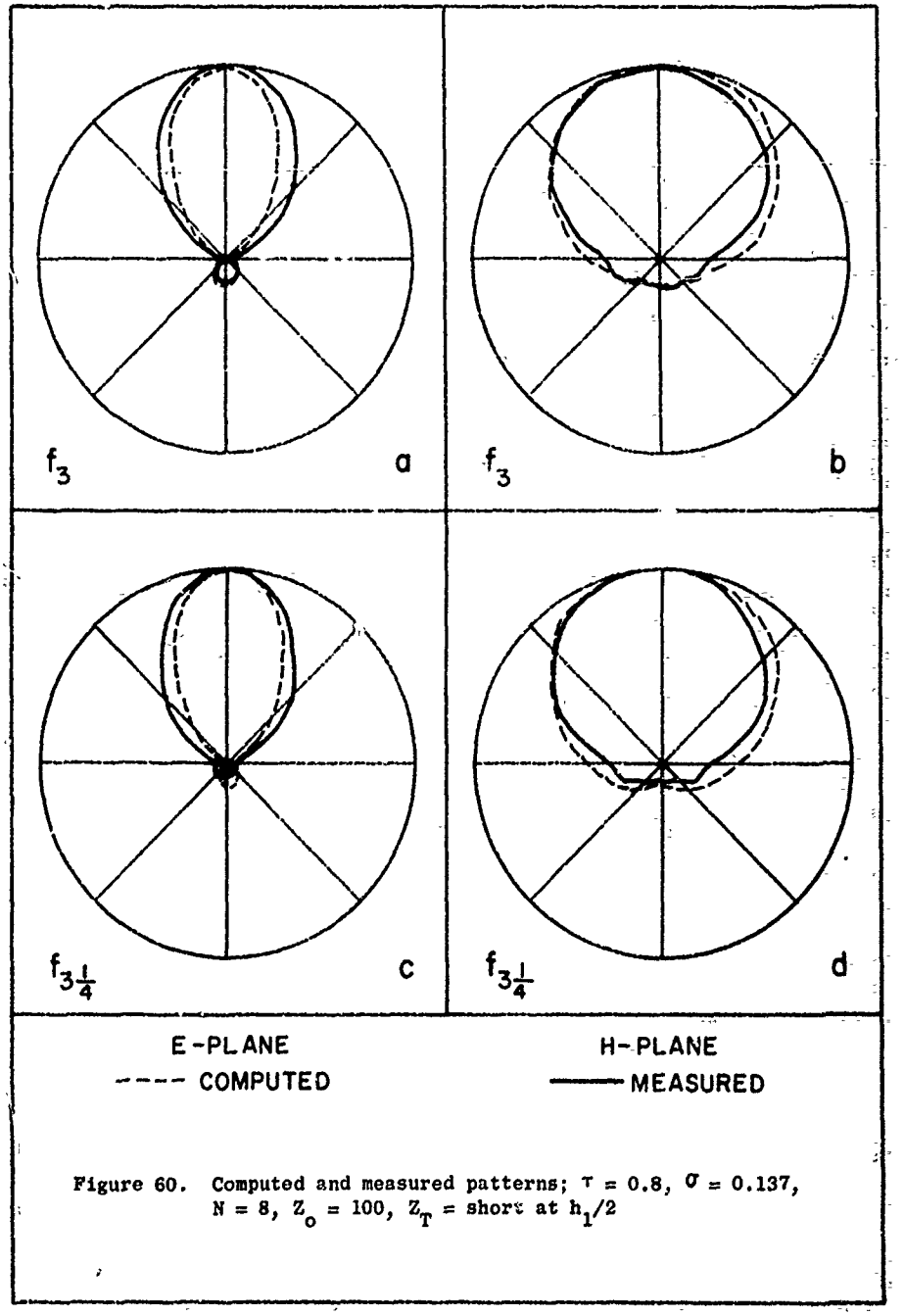

Figure 60. Computed and measured patterns; $\tau = 0.8$, $\sigma = 0.137$, $N = 8$, $Z_o = 100$, Z_T = short at $h_1/2$

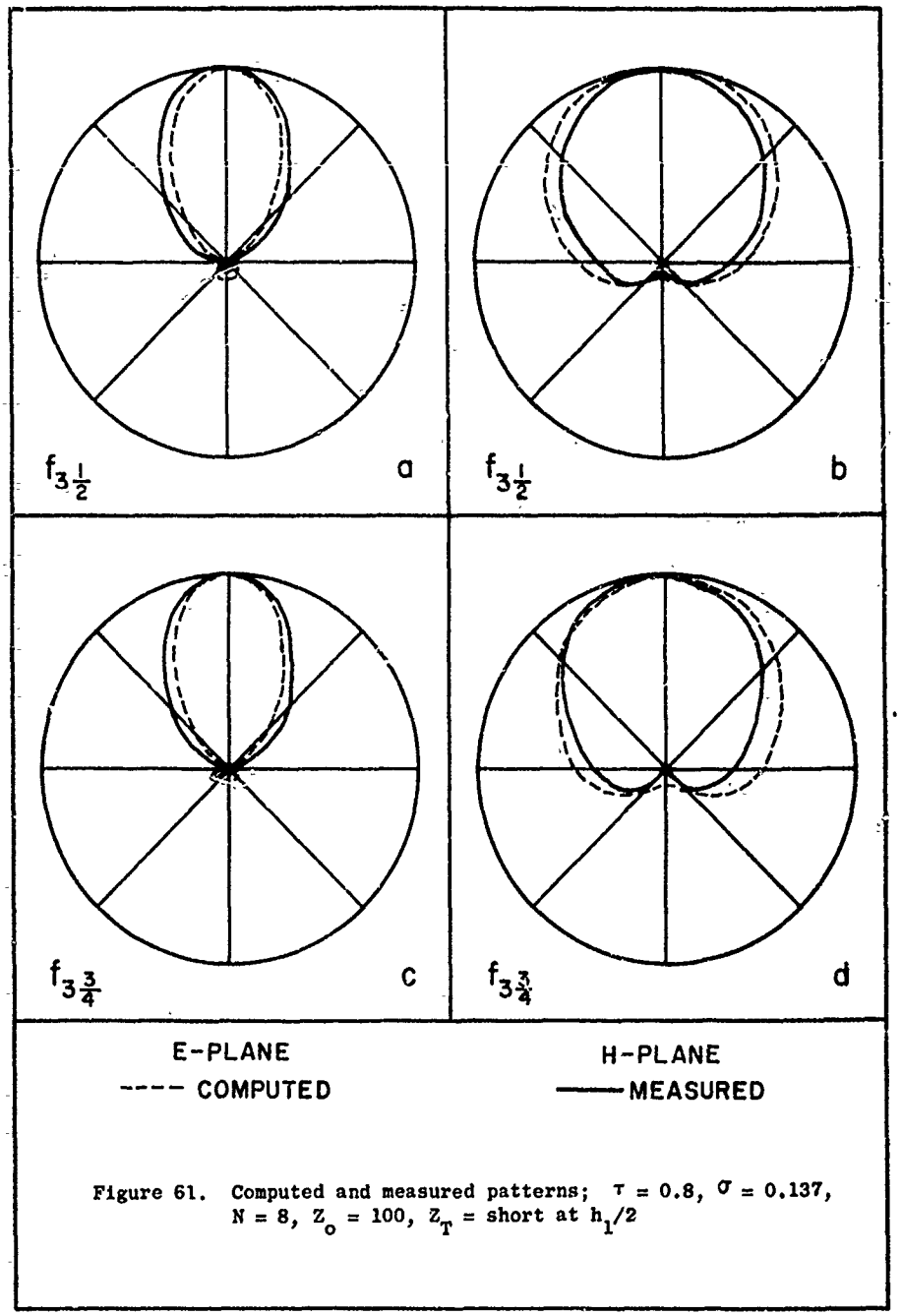

Figure 61. Computed and measured patterns; $\tau = 0.8$, $\sigma = 0.137$, $N = 8$, $Z_o = 100$, Z_T = short at $h_1/2$

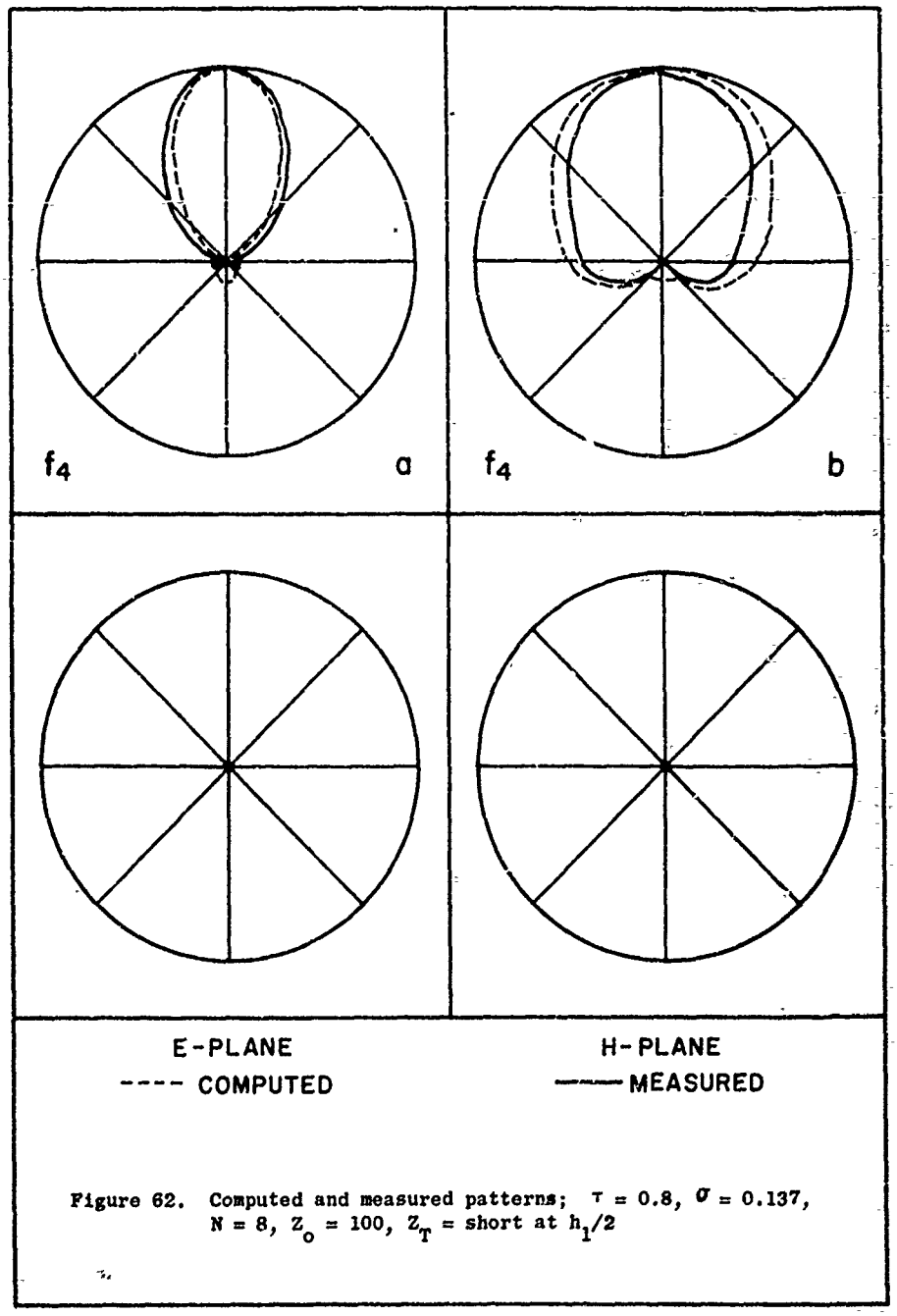

Figure 62. Computed and measured patterns; $\tau = 0.8$, $\sigma = 0.137$, $N = 8$, $Z_o = 100$, Z_T = short at $h_1/2$

It can be shown that the E-plane pattern of a half-wave dipole antenna becomes narrower as the current distribution changes from sinusoidal to uniform. Thus the actual current distribution in the elements must be more nearly uniform than sinusoidal.

3.5.1.1 The Characteristic Pattern as a Function of τ and σ

The scale factor τ and the relative spacing σ exercise primary control over the shape of the radiation patterns of LPD antennas. Figures 63 and 64 are plots of the computed E- and H-plane half power beamwidth as a function of σ for several values of τ. In these curves Z_o = 100 ohms and h/a = 177. Each curve possesses a minimum in the range $0.12 < \sigma < 0.18$. The H-plane beamwidth varies more than the E-plane beamwidth; it should be noted that the scale of the ordinate is different in the two figures.

Using the graphs of Figures 63 and 64, the directivity in decibels can be approximated using the formula from Kraus,[21]

$$D = 10 \log \frac{41253}{(BW_E)\ (BW_H)} \tag{76}$$

BW_E and BW_H are the half-power beamwidths, in degrees. In Figure 65 are plotted contours of constant directivity in decibels, as a function of τ and σ. A scale for the angle α is also given. A straight line connecting equal α indices on the top (or right) and the bottom edges of the graph describes combinations of τ and σ corresponding to the given angle α. All values of τ and σ which result in single-lobed frequency independent patterns fall within this graph. For σ less than 0.05 the directivity falls off rapidly and the front to back ratio decreases. Values of τ greater than 0.98 on the left side of Figure 65 have not been extensively investigated,

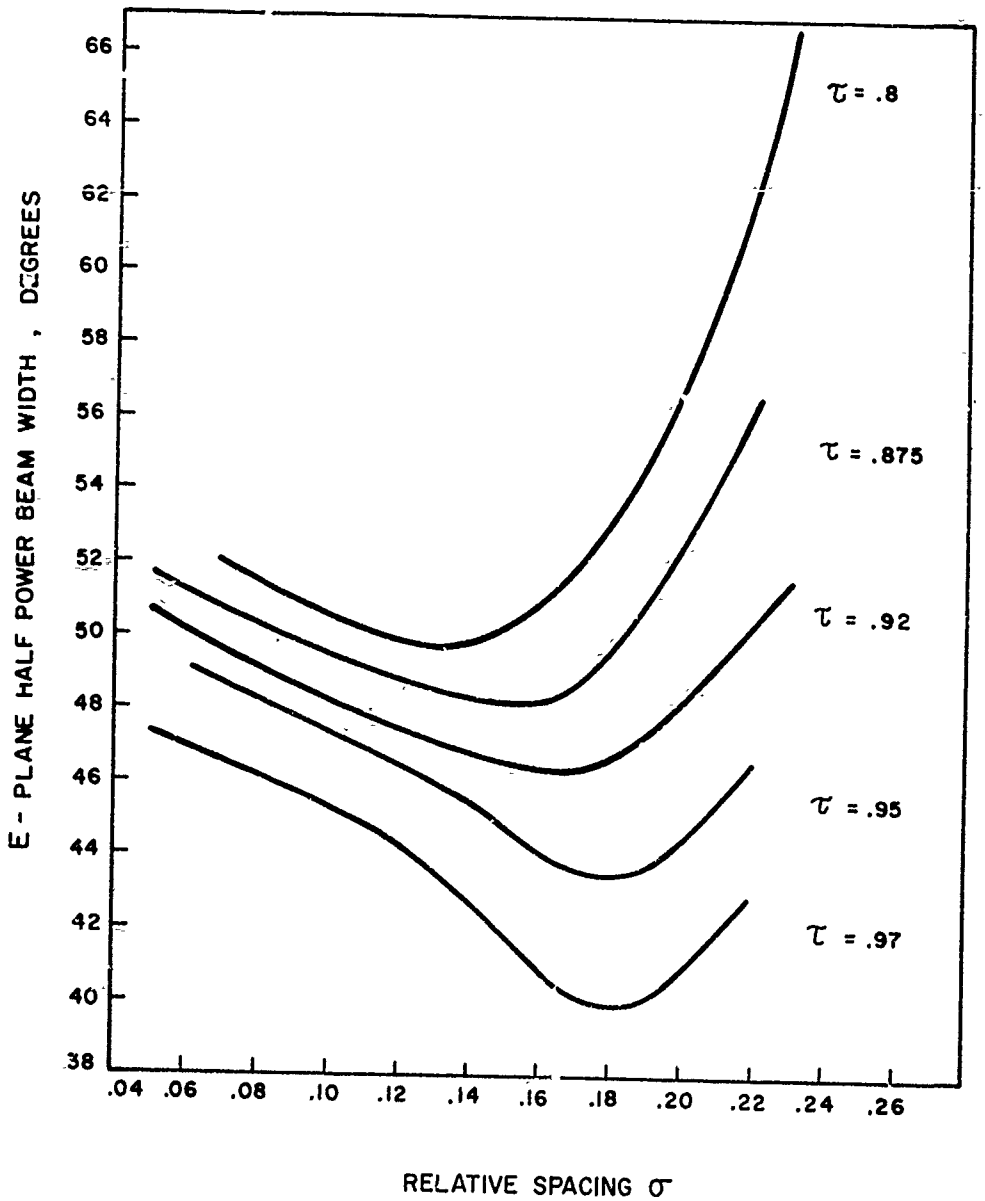

Figure 63. Computed E-plane half-power beamwidth vs. τ and σ; $Z_o = 100$, Z_T = short at $h_1/2$, $h/a = 177$.

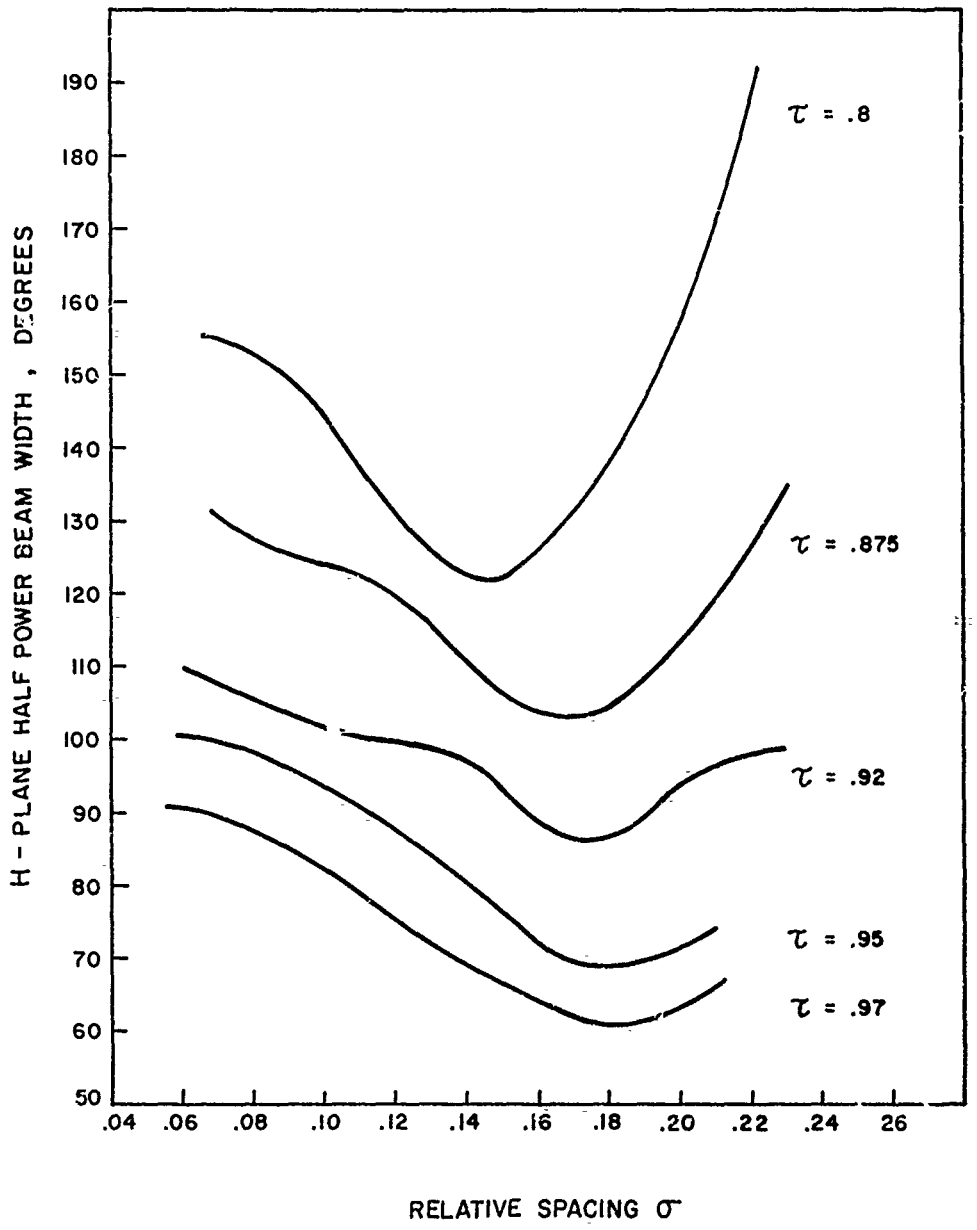

Figure 64. Computed H-plane half-power beamwidth vs. τ and σ; $Z_o = 100$, Z_T = short at $h_1/2$, h/a = 177.

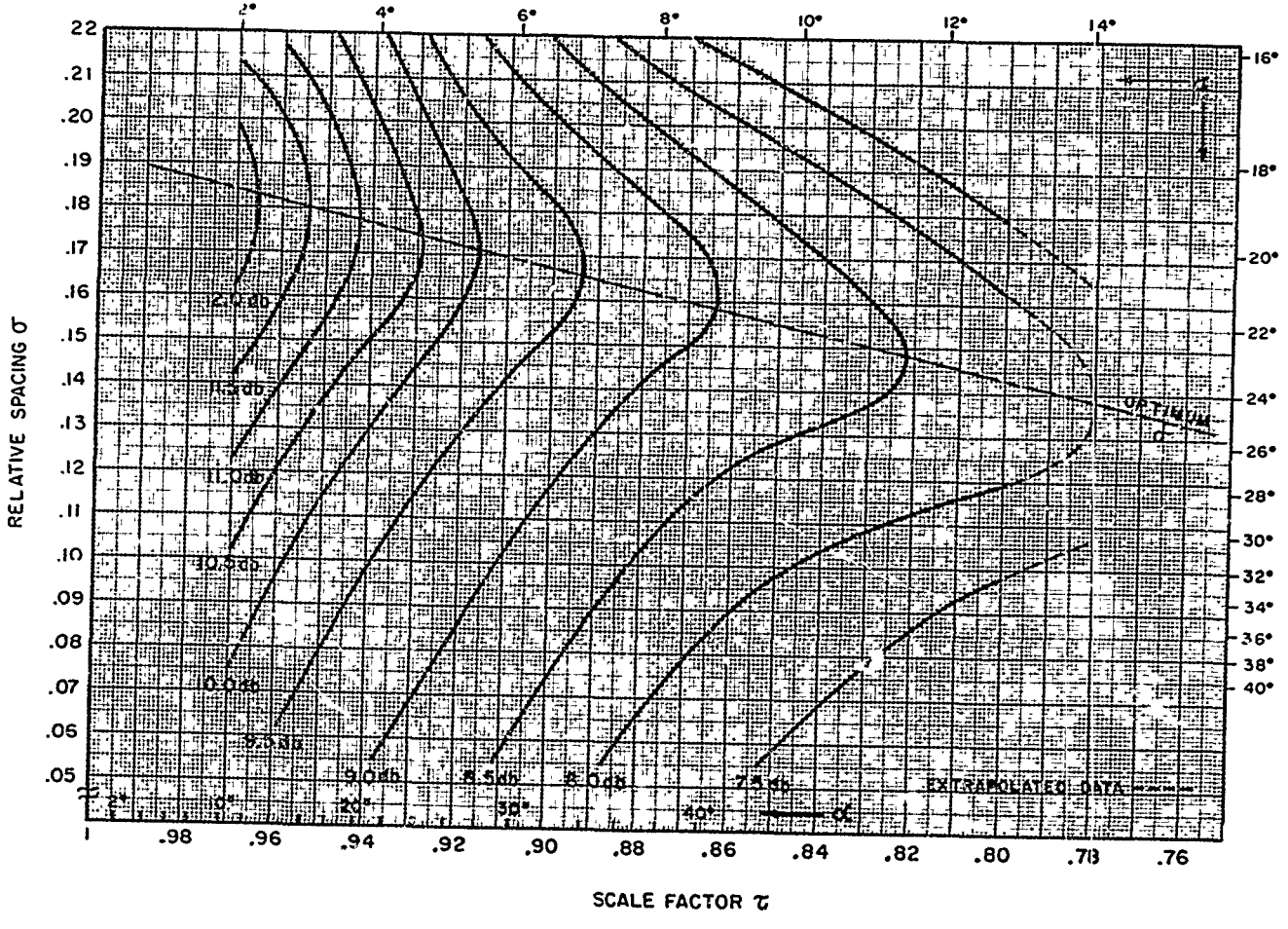

Figure 65. Computed contours of constant directivity vs. τ, σ, and α; $Z_o = 100$, Z_T = short at $h_1/2$, h/a = 177

because the number of elements required to achieve a given bandwidth becomes excessive. For values of σ greater than the optimum σ, the directivity falls off and the patterns either tend toward broadside or side lobes appear. In addition, the length of the antenna for a required bandwidth becomes excessive. For τ less than 0.8, only one dipole is near resonance at a given frequency, and it couples an insufficient amount of energy from the feeder, resulting in end effects which destroy the log-periodic performance. Measured patterns of such an antenna are shown in Figure 66. For this antenna $\tau = 0.7$ and $\sigma = 0.206$. The feeder was terminated by an open circuit at the largest element. The patterns definitely depend on frequency, one pattern has its maximum in the opposite direction. Terminating the feeder in a matched resistor resulted in the measured and computed H-plane patterns of Figure 67. In this case the patterns are more nearly independent of frequency; however, the addition of the matched termination has lowered the computed efficiency to 70%. The patterns of Figure 67 also illustrate the broadside tendency which is characteristic of values of σ much greater than the optimum.

The front-to-back ratio as a function of τ and σ is shown in Figure 68. For $\tau > 0.875$ the calculated F/B is greater than 20 db. The F/B for $\tau < 0.875$ depends on the value of σ; it attains a maximum for σ near the optimum value shown in Figure 65. F/B decreases as the cut-off frequencies are approached. (Compare the patterns of Figures 51 through 56.) This decrease can be limited to some extent by adjusting the reactive determination Z_T. Isbell found that a short circuit at a distance $h_1/2$ behind the largest element resulted in a minimum deviation of F/B from its mid-band value.

3.5.1.2 The Characteristic Pattern as a Function of Z_o and h/a

The computed and measured patterns of an LPD with $\tau = 0.888$, $\sigma = 0.089$, and $Z_o = 150$ ohms are shown in Figures 69 and 70. A comparison of the corresponding patterns of Figures 52, 53, and 55, for $Z_o = 100$ ohms shows

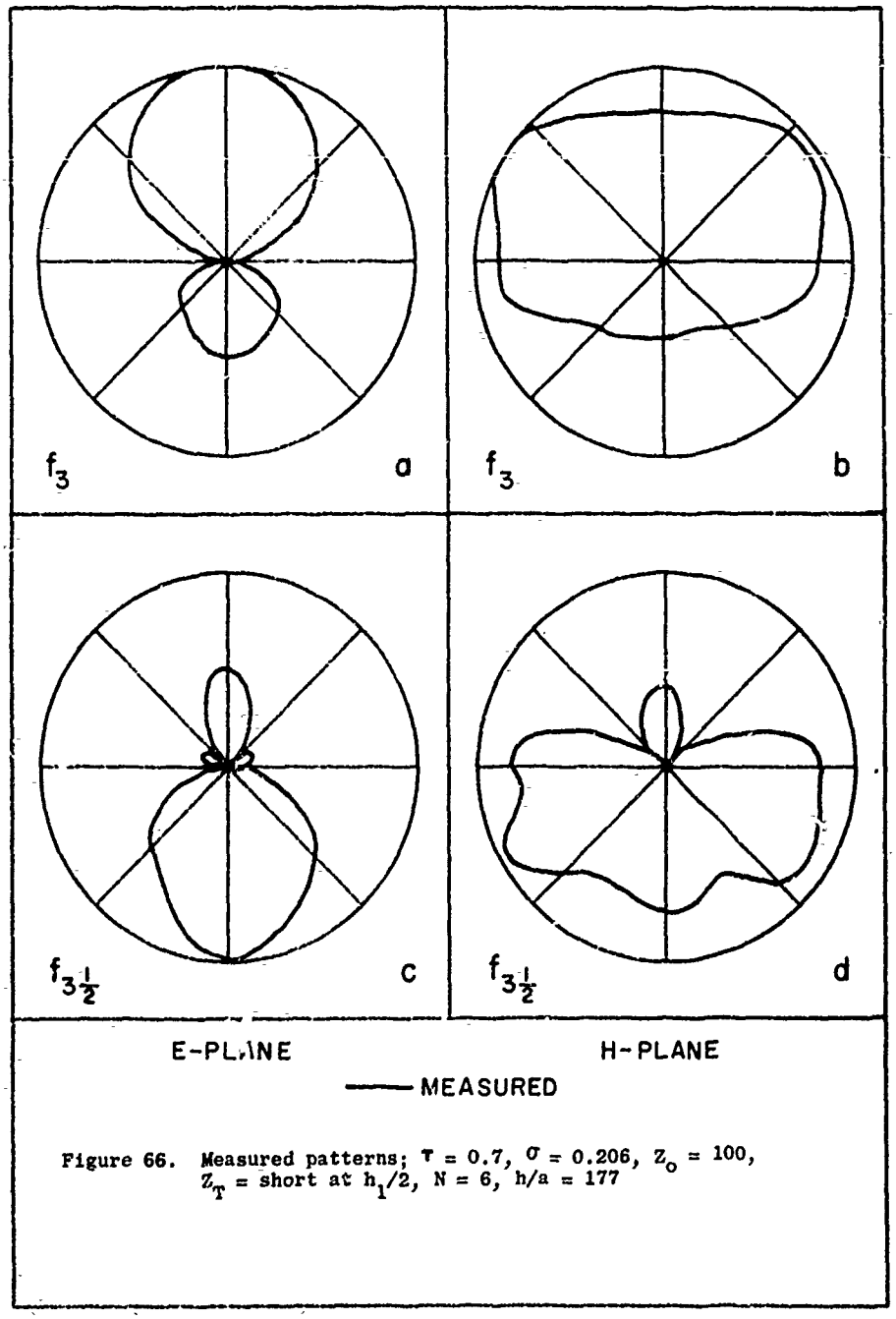

Figure 66. Measured patterns; $\tau = 0.7$, $\sigma = 0.206$, $Z_o = 100$, Z_T = short at $h_1/2$, N = 6, h/a = 177

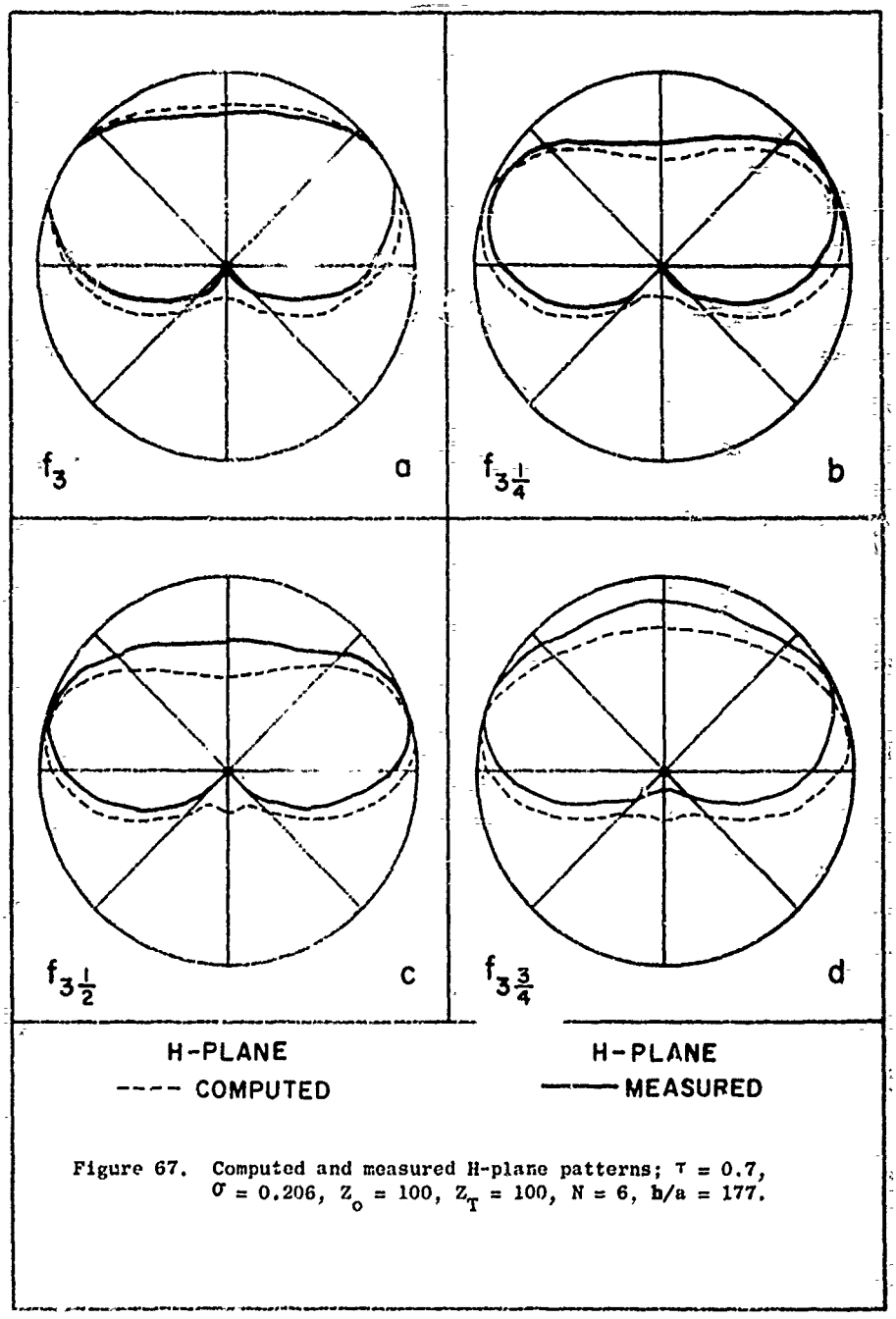

Figure 67. Computed and measured H-plane patterns; $\tau = 0.7$, $\sigma = 0.206$, $Z_o = 100$, $Z_T = 100$, $N = 6$, $b/a = 177$.

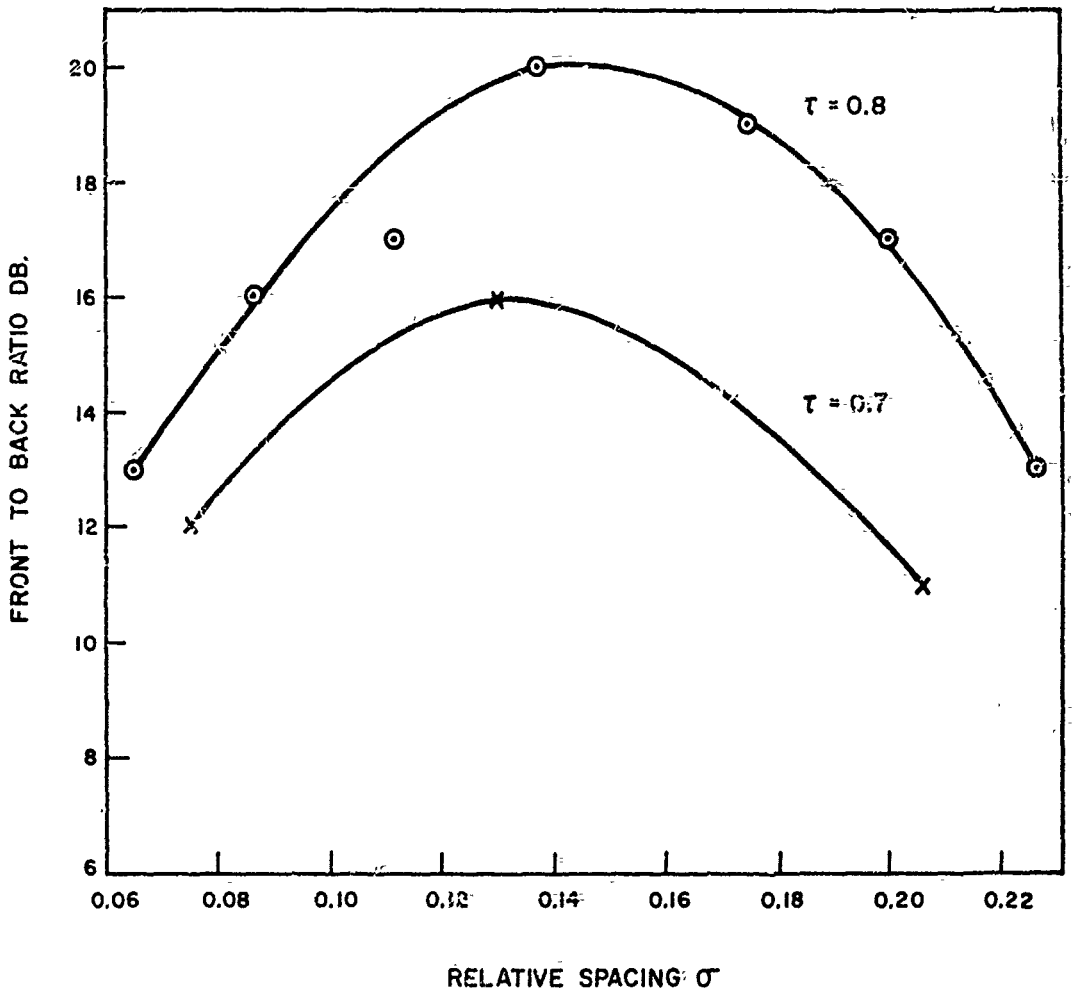

Figure 68. Computed pattern front to back ratio vs. σ and τ; $Z_o = 100$, Z_T = short at $h_1/2$

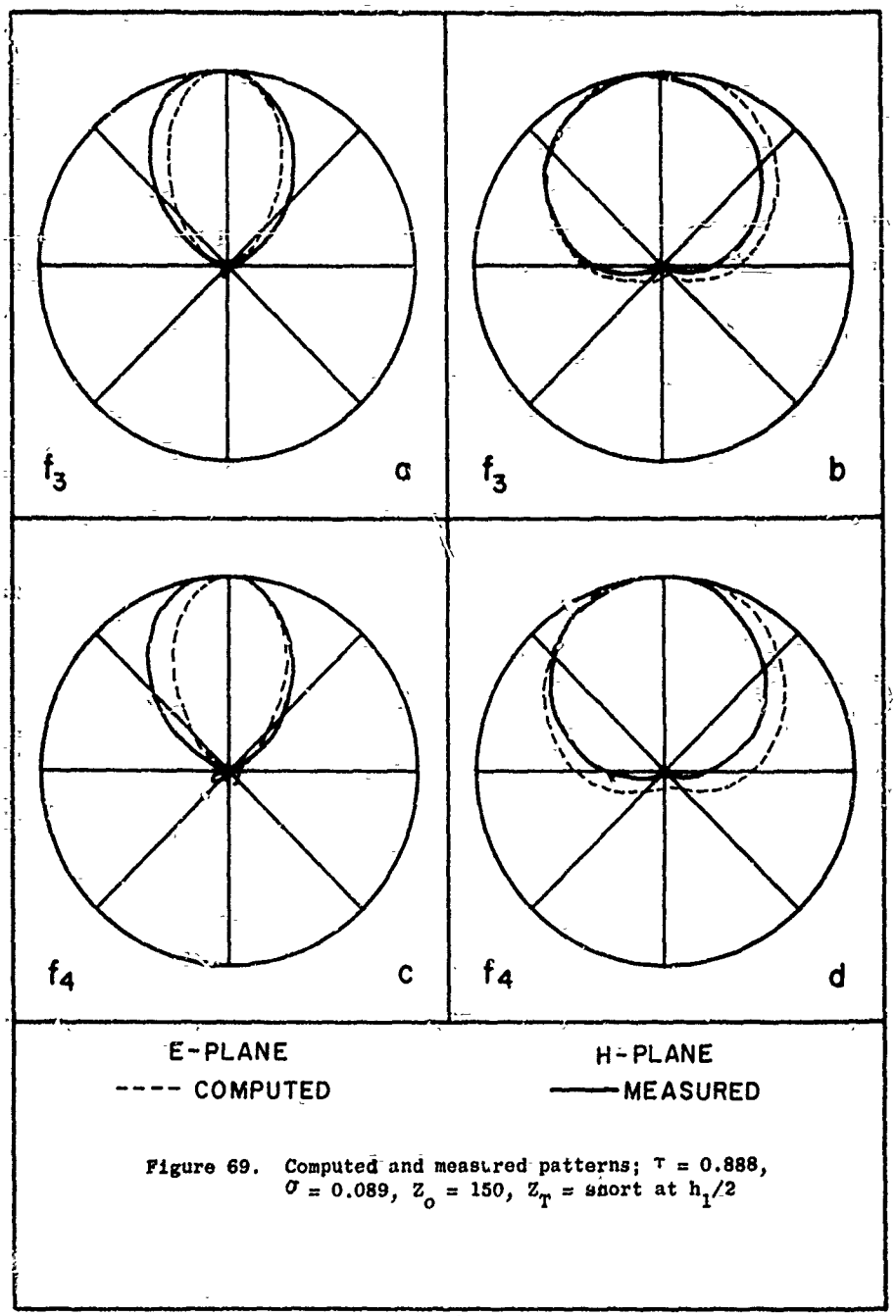

Figure 69. Computed and measured patterns; $\tau = 0.888$, $\sigma = 0.089$, $Z_o = 150$, Z_T = short at $h_1/2$

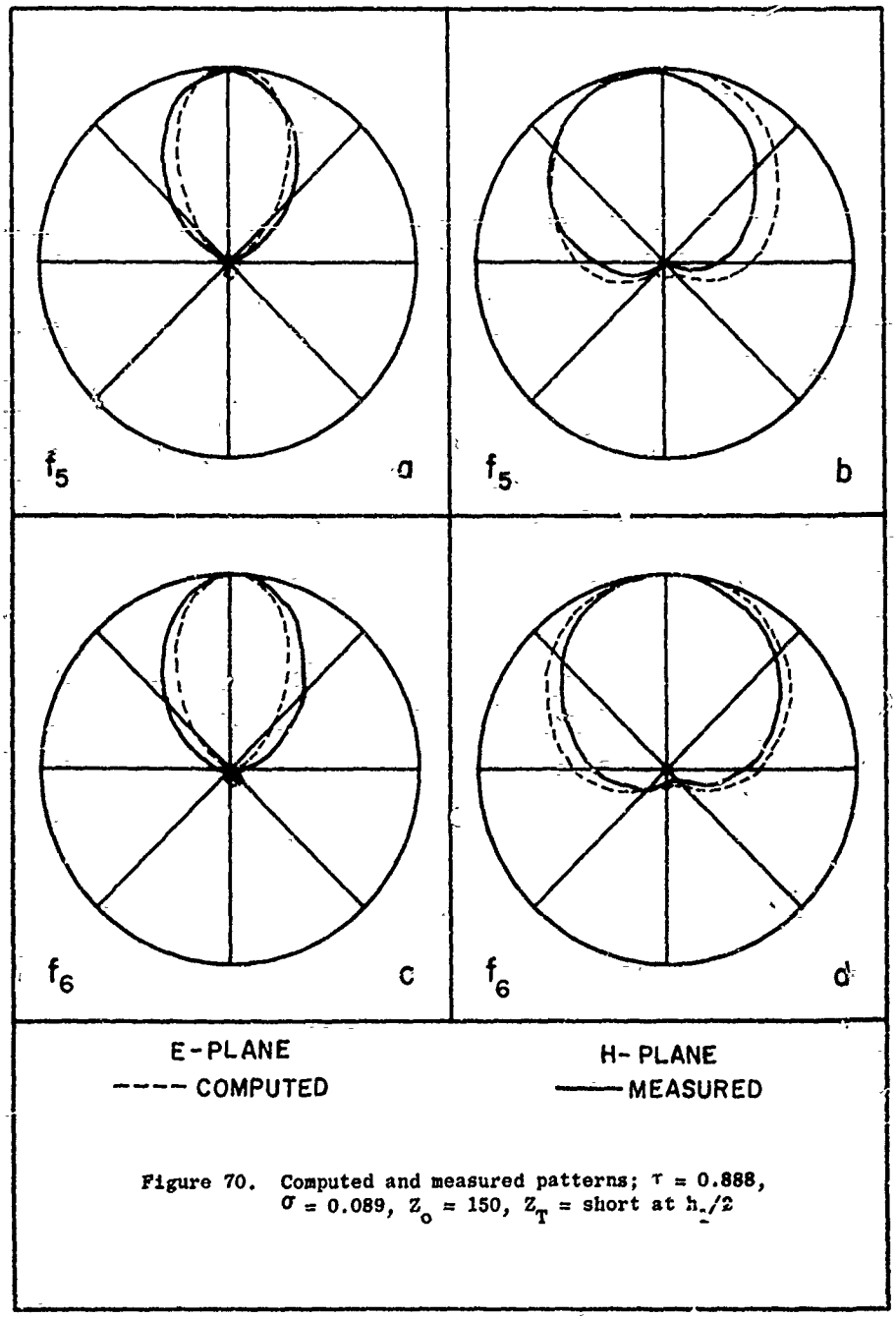

Figure 70. Computed and measured patterns; $\tau = 0.888$, $\sigma = 0.089$, $Z_o = 150$, Z_T = short at $h/2$

that a change in Z_o has little effect on the characteristic patterns. In this model the average directivity decreased by less than one decibel as the feeder impedance increased from 75 to 300 ohms. On nine models with different τ and σ, similar results were observed; antennas with σ greater than optimum lost as much as one db over the range $100 \leq Z_o \leq 300$. For small σ the variation was less than 0.5 db. As an approximation suitable for design purposes, one may assume that the directivity contours of Figure 65 hold for all practical values of Z_o.

The element thickness controls the directivity to some extent. Figure 71 shows that the average directivity decreases as the element height to radius ratio increases. For this model, with $\tau = 0.888$ and $\sigma = 0.089$, the decrease amounts to about 1.2 db over the range $100 < h/a < 100{,}000$. Although the approximations of the theory are best satisfied with large h/a, in the frequency range for which the Antenna Laboratory is equipped, it was impossible to build models with h/a much greater than 800. The two laboratory models with $\tau = 0.888$ and $\sigma = 0.089$ agree with the trend of the curve for $h/a < 800$, although the measured directivity was low. As with Z_o, the variation seems insignificant in the light of the approximations made, and for design purposes the directivity contours of Figure 65 can be used if a small correction is applied.

It has been found that a departure from the exact scaling of the diameter of each element can be tolerated If the diameters of the elements are held constant, the directivity should increase with frequency. This increase was not observed in the laboratory models which covered a 3:1 bandwidth, because other minor pattern variations masked the sought after trend. It is to be expected that the input VSWR will increase if constant diameter elements are used.

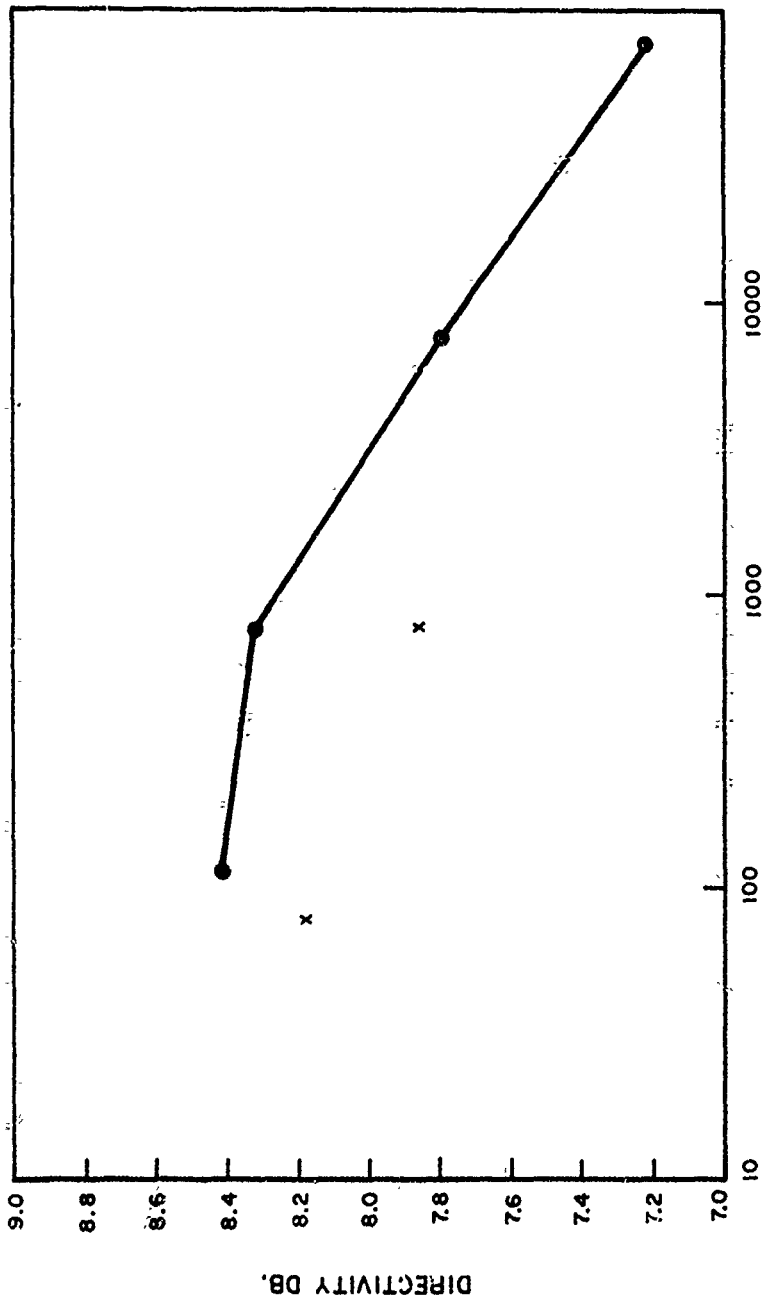

Figure 71. An example of computed and measured directivity vs. h/a.

Table 2 presents a comparison of the measured average directivity of several laboratory models and the corresponding directivity as read from the graph of Figure 65, with a correction for the change in h/a obtained from Figure 71. In general, the computed directivity is higher than the one measured. The mean error is 0.35 db and the maximum error does not exceed 1 db.

3.5.2 The Far Field Phase Characteristics

The far field phase and the phase center are of special interest when one attempts to array several LPD antennas to achieve higher directivity or specially shaped beams, or when an LPD is used as the primary feed in lens or reflector systems[22]. The relative phase in the principal planes of the far field is given by the phase of the complex field quantities $P_H \exp(-j\beta r)$ and $P_E \exp(-j\beta r)$ Written in polar form,

$$P = |P| e^{j[F(\psi,f)-\beta r]} \tag{77}$$

Here P stands for either of the principal plane patterns and the phase F is a function of the relevant angular variable ψ and the frequency f. In the following sections F is used to demonstrate the phase rotation phenomenon. The phase center of an LPD antenna is defined and its dependence on the LPD parameters is determined.

3.5.2.1 The Phase Rotation Phenomenon

In 1958 DuHamel and Berry[23] discovered the phase rotation phenomenon which is characteristic of LP antennas. They verified experimentally that the phase of the electric field at a distant point is measured relative to the phase of the input current at the apex of an LP antenna, the phase of the received signal is delayed by 360° as the structure is expanded through a "cell". The experiment was conducted by building several LP

TABLE 2

Comparison of Measured and Computed Directivity

					Measured			Computed
τ	σ	α	Z_o	h/a	BW_E	BW_H	D	D
0.98	0.057	5.0	100	125	56.5	85.7	9.31	10.0
0.98	0.038	7.5	75	240/148*	54.1	85.7	9.50	9.5
0.975	0.0717	5.0	100	200/151*	52.8	76.6	10.08	10.0
0.95	0.0268	25.0	100	100/26*	68.7	114.2	7.20	---
0.93	0.125	8.0	65	66	60.0	85.0	9.08	9.8
0.92	0.200	5.7	100	142	52.7	69.1	10.53	9.9
0.92	0.160	7.1	100	177	57.0	80.2	9.56	10.0
0.92	0.150	7.6	300	60/20*	54.0	85.4	9.53	9.8
0.92	0.120	9.5	100	118	57.0	81.1	9.52	9.4
0.92	0.080	14.0	100	177	61.5	98.0	8.36	8.9
0.91	0.128	10.0	94	66	59.2	90.8	8.85	9.4
0.89	0.103	15.0	75	80/45*	67.0	106.3	7.68	8.6
0.888	0.089	17.5	100	80	61.8	101.9	8.18	8.7
0.888	0.089	17.5	100	177	63.4	106.6	7.86	8.5
0.888	0.089	17.5	150	177	65.2	112.0	7.52	8.3
0.86	0.080	23.6	200	50	64.3	112.4	7.57	7.9
0.85	0.216	10.0	75	80/49*	71.3	109.6	7.14	7.3
0.84	0.068	30.5	215	50	67.8	128.6	6.83	7.5
0.81	0.364	7.5	75	80/43*	95.0	180.0	3.83	---
0.80	0.137	20.0	100	125	58.5	101.9	8.41	8.3

* In these models, the element diameter was held constant; the h/a of the longest and shortest element is recorded.

antennas with indentical τ and α, the models differing from each other in size. If Kx_n is the distance from the apex of the structure to element n, the expansion factor for each antenna is determined by assigning values of K from 1 to $1/\tau^2$. (The "cell" scaling factor for LPD antennas is τ^2). All other dimensions of the structure are also multiplied by K.

Since an expansion of a log-periodic structure is equivalent to a change of frequency, the phase rotation phenomenon can also be observed by measuring the phase of a given antenna as frequency is increased from f to f/τ^2, provided that the distance r from the apex to the far field point is decreased from r to $\tau^2 r$. The phase of a far field component is given by the exponent of Equation (77), $F(\psi,f)-\beta r$. Under the stated conditions βr is held constant. The phase should be measured relative to the input current at the apex of the antenna, so the front truncation which occurs on most practical antennas must be taken into acccunt for the reasons given in Section 3.1.1. The dotted curve of Figure 72 is for a computed model with $\tau = 0.875$ and $\sigma = 0.067$, from frequency f_2 to f_4. In this model the front truncation was 0.158λ at f_2 and 0.206λ at f_4, and the computed values of F were corrected accordingly. The phase function F was found to be essentially proportional to the logarithm of frequency. The slight deviation from linearity was also observed by DuHamel and Barry.

Since the phase is proportional to the logarithm of frequency, or equivalently to the logarithm of the expansion factor K, it is possible to adjust the phase of an LP antenna in a manner which is independent of the pattern and input impedance. This property has been exploited in the design of phased arrays of LP antennas; for a detailed discussion and

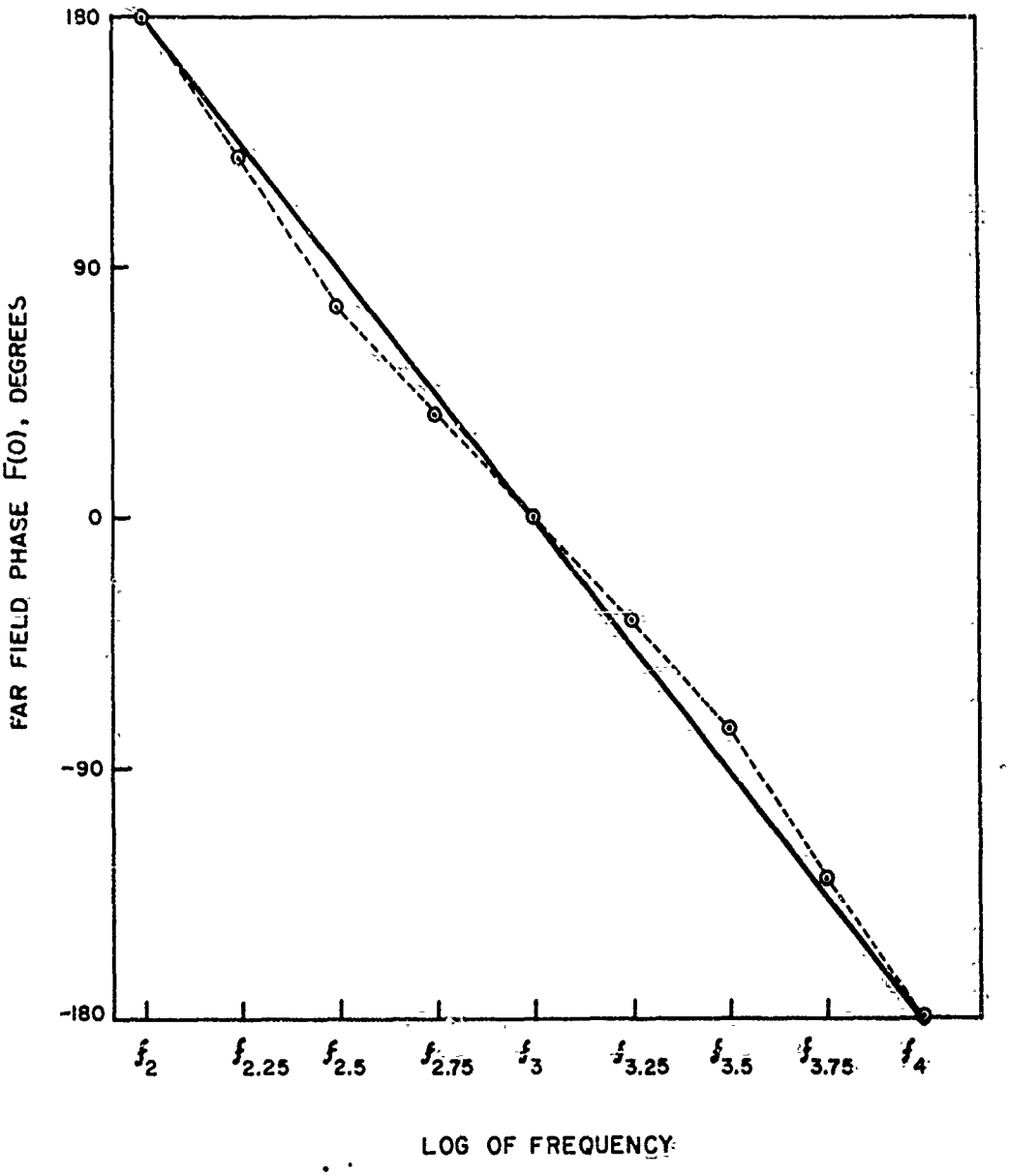

Figure 72. Computed far field phase as a function of frequency, illustrating the phase rotation phenomenon.

several examples, reference 23 should be consulted.

3.5.2.2 The Phase Center

It is well known that the amplitude pattern of the far field is independent of the location of the origin of the coordinate system in which the antenna is situated. However, the phase function F is quite sensitive to the location of the reference point, and it follows that there may be a certain reference point which leads to a simplification of F. If there exists an origin which reduces F to a constant, then this origin is said to be the phase center of the antenna. Since this definition of phase center depends on the polarization of the field and the plane which contains the angular variable ψ, these two quantities must be specified whenever the concept of phase center is used

For most antennas the phase is a function of ψ whatever the origin chosen, but over a limited range of ψ there may exist a point p such that F is practically constant. If p is chosen as the phase center for a given aspect angle ψ_p, then the range of ψ for which the fixed point p can be used as the phase center will depend on the allowable tolerance on F. To find the point p use is made of the evolute of a plane equiphase contour. The evolute is the locus of the center of curvature of the contour, and the center of curvature corresponds to the location of an origin which leads to no change in the phase function over an increment $\Delta\psi$. It will be shown that the knowledge of F as a function of ψ for any origin near the antenna is sufficient to determine the evolute of a far field equi-phase contour.

In the coordinate system of Figure 73 $\overline{OP} = r$ is the distance from the origin to a point on an equi-phase contour S. The ray DP is normal to the tangent line of S at P, therefore DP must go through the center of curvature.

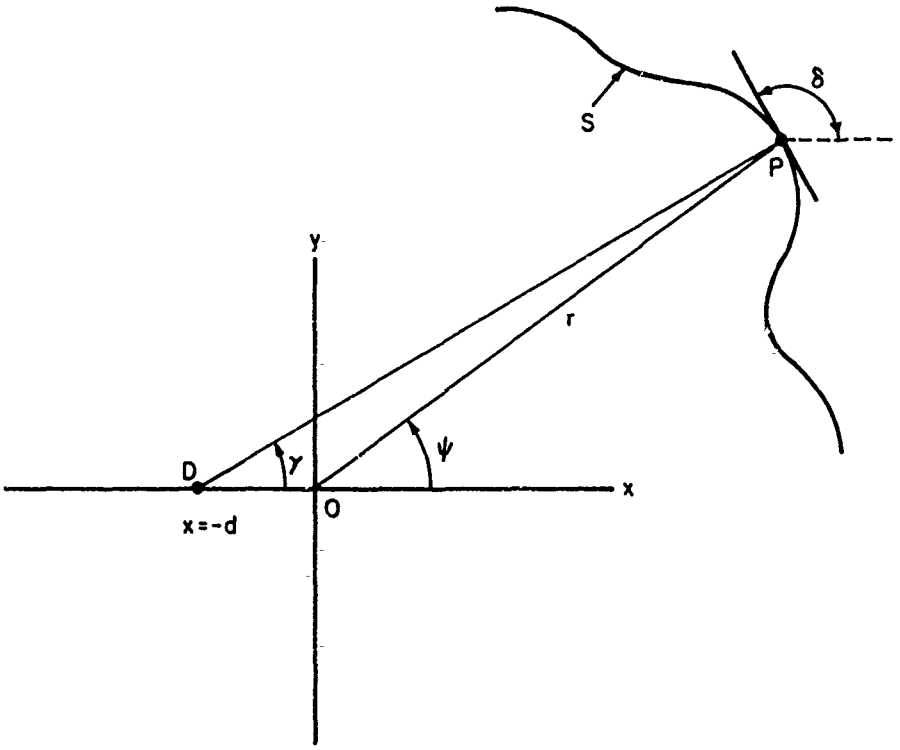

Figure 73. Coordinate system for phase center computations.

In the following development, point D at $x = -d$ is found, then r is made very large so that γ is approximated by ψ. Knowing d and γ for each point on the curve, a pencil of lines such as DP can be determined. The locus of the phase center or equivalently the evolute of S, is traced by the envelope curve of the rays.

Let an equiphase contour in the x, y plane be given by

$$F(\psi) - \beta r = C, \tag{78}$$

where C is an arbitrary constant. The angle δ is given by

$$\tan \delta = \frac{\frac{dr}{d\psi} \sin \psi + r \cos \psi}{\frac{dr}{d\psi} \cos \psi - r \sin \psi} \tag{79}$$

From the geometry of Figure 73,

$$d = -y_o \tan \delta - x_o, \tag{80}$$

where x_o and y_o are the coordinates of point P. Substituting for x_o, y_o and $\tan \delta$, one finds

$$d = \frac{1}{\beta} \frac{F'(F-C)}{(F-C) \sin \psi - F' \cos \psi}, \tag{81}$$

where the prime indicates differentiation with respect to ψ. Changing to the variable

$$u = 2\pi \cos \psi, \tag{82}$$

and writing d in terms of wavelength, results in

$$\frac{d}{\lambda} = \frac{-dF/du}{1 + \frac{udF/du}{\beta r}} \tag{83}$$

For the far field condition r is very large, hence d/λ is approximated by

$$\frac{d}{\lambda} = -\frac{dF}{du} \tag{84}$$

Thus, d/λ is given by the slope of $F(\psi)$ as a function of $2\pi \cos \psi$. d/λ can be computed from the difference equation

$$\frac{d_i}{\lambda} = - \frac{F(\psi_i + \Delta\psi) - F(\psi_i)}{2\pi[\cos (\psi_i + \Delta\psi) - \cos \psi_i]} \tag{85}$$

where ψ_i is a given value of ψ and $\Delta\psi$ is an increment. Once d is found as a function of ψ, rays such as DP can be drawn by setting $\gamma = \psi$. The evolute of the equiphase contour is then the envelope curve of the rays.

Figure 74 shows a pencil of rays and the corresponding evolute for an LPD with $\tau = 0.92$ and $\sigma = 0.12$. Only half of the evolute is shown, because it is symmetric about the axis. For angles other than 0° or 180° the phase center clearly lies off the axis of the antenna. However, for all antennas the departure from the axis is small in terms of wavelengths, and it can be neglected for ψ angles less than 70°. Each LPD antenna exhibits an evolute of the equiphase contour that is peculiar to itself, and no correlation was found between the shape of the evolute and the LPD parameters.

In what follows, the point p_o corresponding to $\psi = 0^\circ$ is chosen as the phase center. Ideally, the distance in wavelengths from the apex to P_o should remain constant as frequency is changed by an integral power of τ. Although a variation with frequency was observed, the computed results similar to those in Figure 75 show that the variation is small. The ordinate is x_p/λ, the distance from the apex to P_o in wavelengths, and the abscissa is the log of frequency. In all cases the variation was less than 5%, so the average value can be used without significant loss

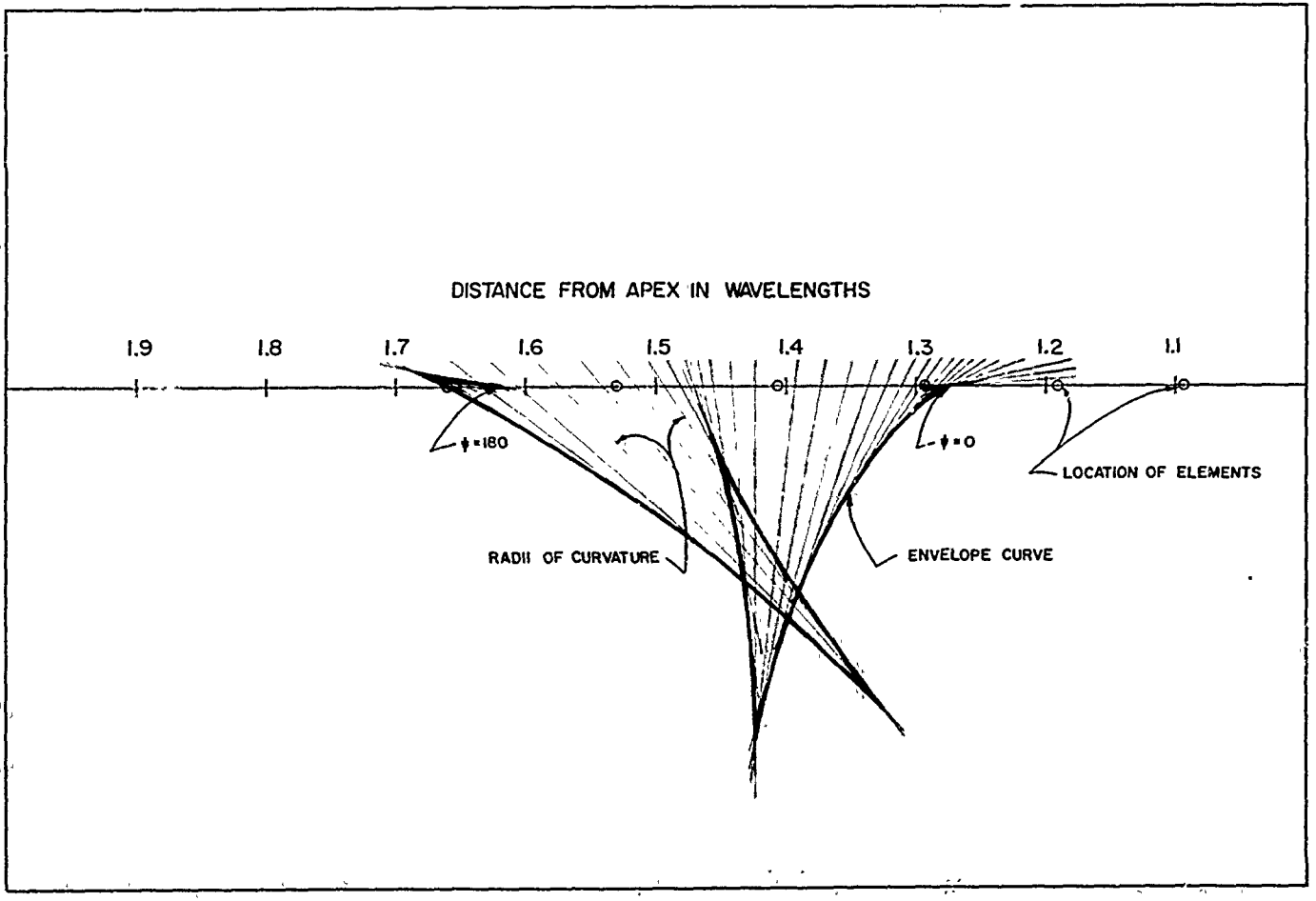

Figure 74. A typical evolute of an equiphase contour, plotted on a wavelength scale

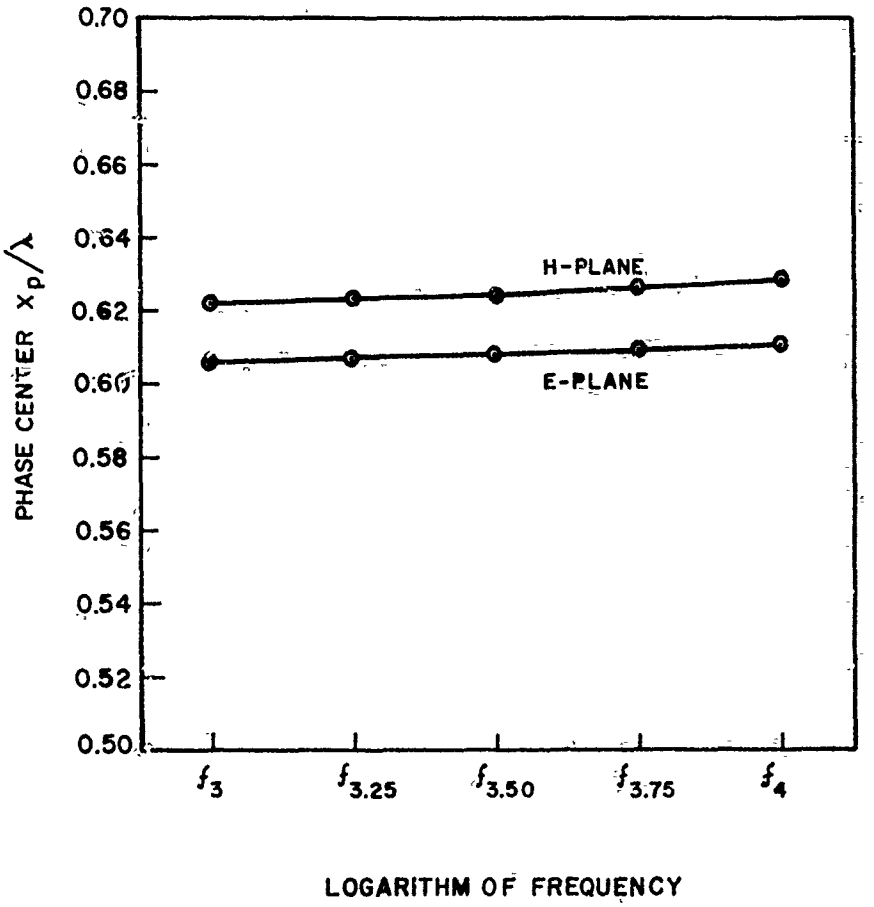

Figure 75. Typical frequency variation of the relative distance from the apex to the phase center.

of accuracy. An example of the measured and computed location of the phase center is shown in Figure 76. The relative magnitude of the element base current is also plotted so that the location of the phase center with reference to the active region can be visualized.

A graph of the computed location of the phase center for models with $Z_o = 100$ and $h/a = .177$ is shown in Figure 77. x_p/λ is the distance to the H-plane phase center in wavelengths, for $\psi = 0^o$. The location of the phase center is independent of τ and σ over the range of α shown. The E-plane phase center was found to lie ahead of the H-plane phase center by an amount which varied linearly from $0.95\ x_p$ for $\alpha = 25^o$ to x_p for $\alpha = 2.5^o$. In all cases $x_p < x_{\lambda/2}$, which is the point where the transverse dimension is a half-wavelength. The shortening factor of Figure 33 can be used to find the change in x_p as Z_o or h/a is changed.

Since no LP antenna exhibits a completely spherical equiphase surface, the question arises as to the utility of using point p_o as the phase center. This, of course, depends on the allowable tolerance between the actual phase at some angle ψ, and the phase computed on the basis of an hypothetical spherical wave which originates at the phase center. Figure 78 shows an equiphase contour S described by $F(\psi)-\beta r = C$, where ψ is the angle subtended at the origin O. S' is an arc of radius $r_o + d$ with center at p_o, the chosen phase center. S' represents an hypothetical circular equiphase contour of value $F(o)-\beta r_o$. The error ΔF is the distance between S and S' at the angle γ, and is given by

$$\frac{\Delta F}{\lambda} = \frac{F(o) - F(\psi)}{2\pi} + \frac{d}{\lambda}\left[1 - \frac{\sin\psi - \sin\gamma}{\sin(\psi - \gamma)}\right]. \qquad (86)$$

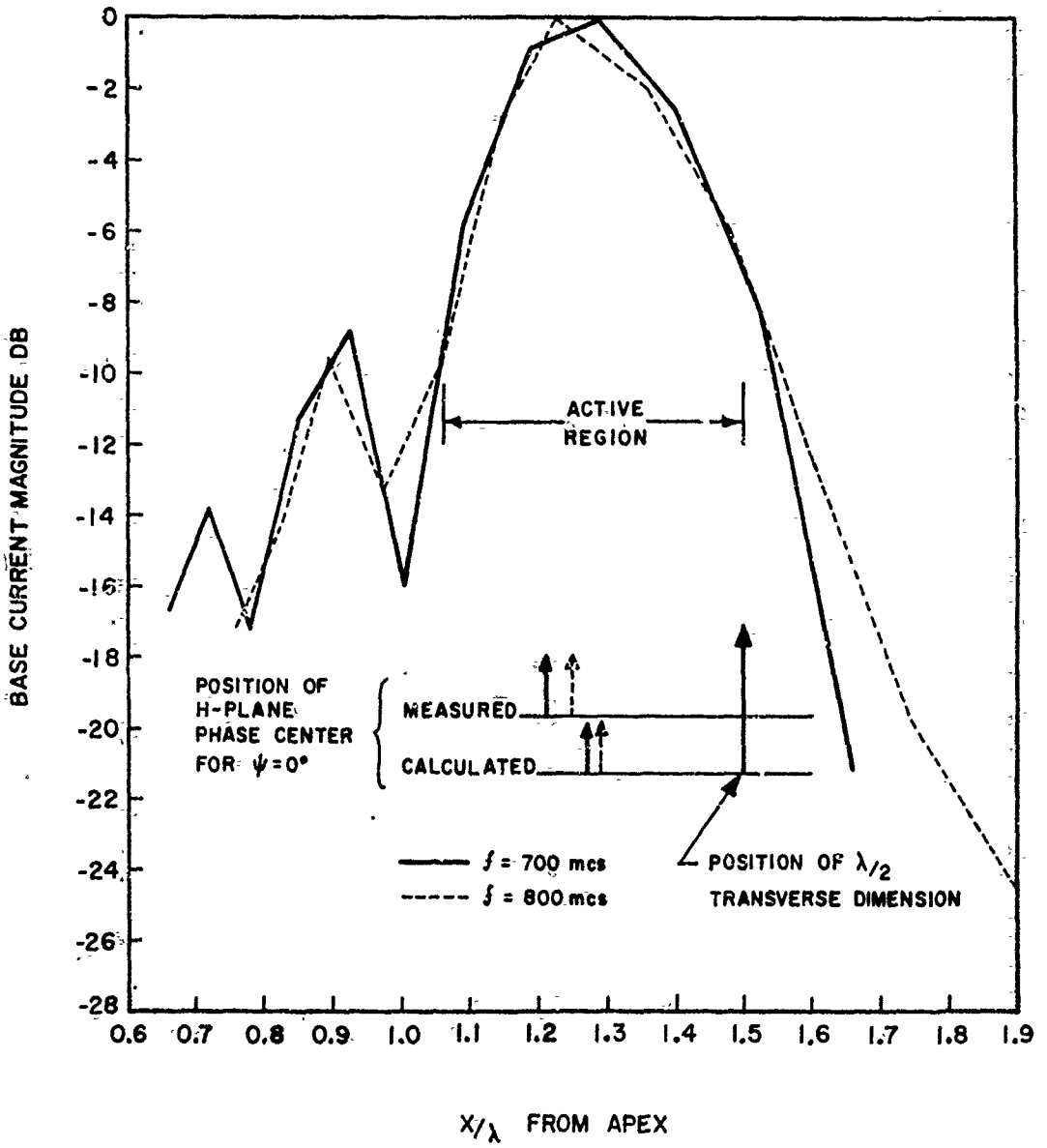

Figure 76. Measured and computed location of the phase center with reference to the active region.

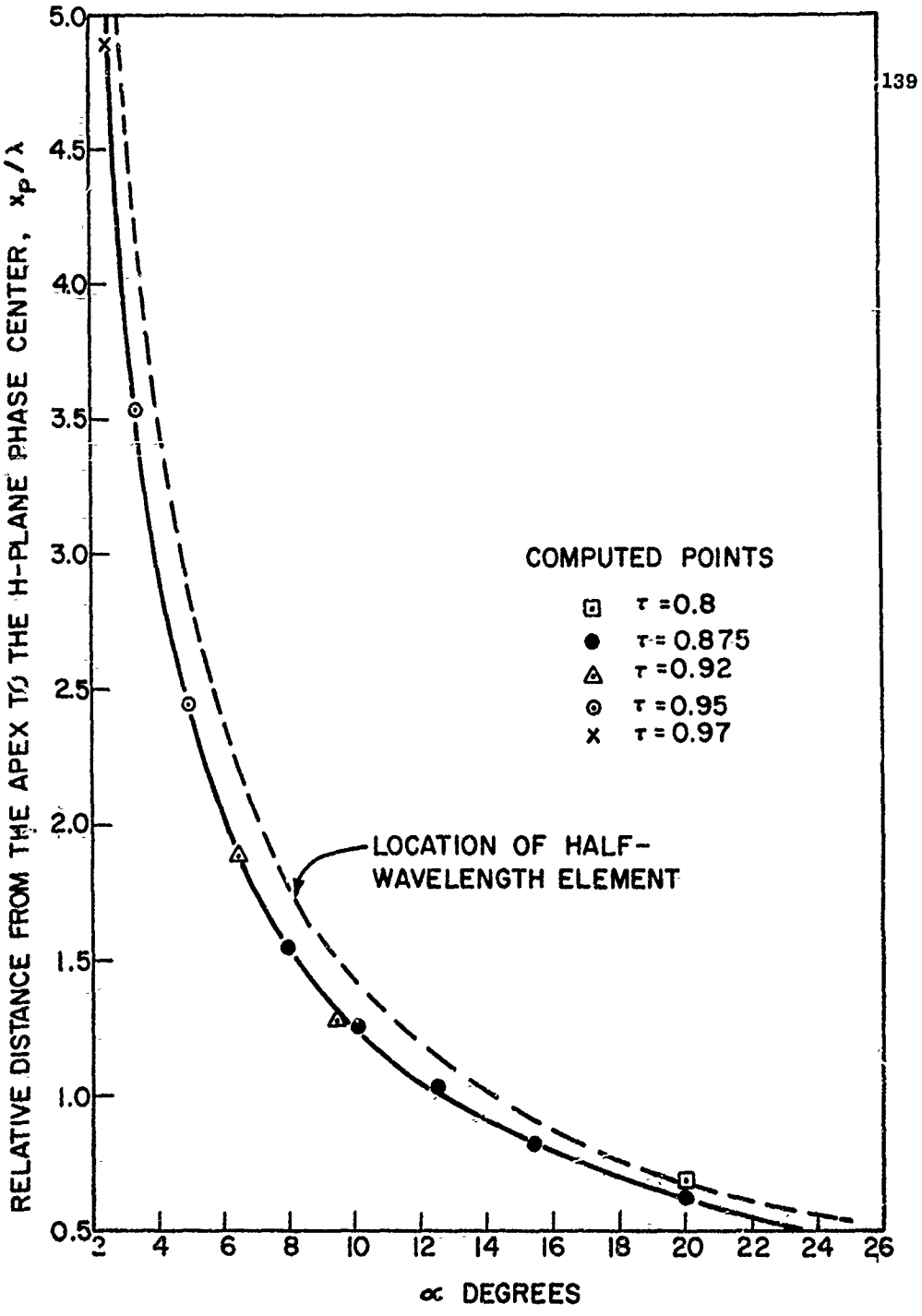

Figure 77. Location of the phase center in wavelengths from the apex

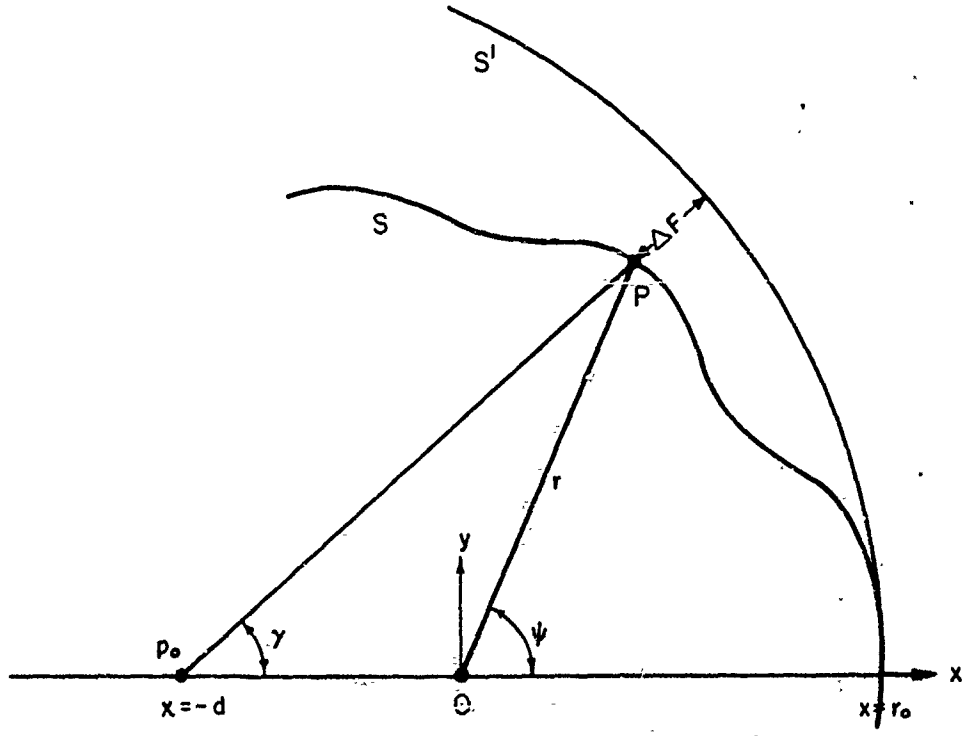

Figure 78. Coordinate system for the computation of the phase tolerance

For the far field condition r approaches infinity and γ becomes equal to ψ, reducing (86) to

$$\frac{\Delta F}{\lambda} = \frac{F(0) - F(\psi)}{2\pi} + \frac{d}{\lambda}(1 - \cos\psi). \tag{87}$$

If a tolerance q is given, a value ψ_q can be found such that

$$\left|\frac{\Delta F}{\lambda}\right| \leq \frac{q}{\lambda} \qquad \text{for} \quad |\psi| \leq \psi_q. \tag{88}$$

This defines the range of ψ over which p_o is a useful phase center, for the tolerance q.

Setting $q = \lambda/16$ and using Equation (87), ψ_q was found by a trial and error process. Little correlation was found between ψ_q and the antenna parameters, because the phase function F was different for each antenna. However, for all but two models in which σ is less than optimum, the value of ψ_q was 90° for the E-plane pattern and greater than 90° for the H-plane pattern. The two exceptions were $\tau = 0.95$, $\sigma = 0.143$, and $\tau = 0.97$, $\sigma = 0.175$; both are high directivity models. For σ greater than optimum, ψ_q decreased to 59° at $\tau = 0.875$ and $\sigma = 0.222$, which was the lowest value of ψ_q recorded. Thus, in all models in the range $0.8 \leq \tau \leq 0.97$, and $0.05 \leq \sigma \leq 0.222$, the error in using p_o as the phase center is less than $\lambda/16$ for all angles within the 3 db beamwidth.

The values of x_p described herein can be used as a guide in the design of arrays of LPD antennas. However, due to the approximations of the theory and the sensitivity to error of phase, it is prudent to measure the location of the phase center in critical designs. An indication of the nature of the error involved in using an incorrect value of d can be determined from

Equation (87). If the error in d is Δd, then the phase error in wavelengths will be $\Delta d(1 - \cos \psi)/\lambda$.

4. THE DESIGN OF LOG-PERIODIC DIPOLE ANTENNAS

This section first reviews the LPD parameters and their effect on the observed antenna performance. A procedure is outlined whereby the physical dimensions of an antenna which meets given electrical specifications can be determined by the use of graphs and nomograms. Finally, several novel designs are given which exploit certain properties of log-periodic dipole antennas.

4.1 Review of Parameters and Effects

To varying degrees all the parameters which specify an LPD have an effect on the observed performance. Table 3 lists the parameters and qualitatively describes how each effects the performance. The principal LPD parameters and their range are listed in the first two columns. At the top of each succeeding column are the features of the antenna. The entries denote how the performance changes with an increase in the pertinent parameter, while all other factors are held constant.

The directivity of an LPD depends primarily on the combination of τ and σ selected. Directivities from 7.5 to 12 db over isotropic have been measured. Since an increase in directivity implies an increased aperture, it is not surprising that high directivity models are characterized by small α and large L/λ_{max}. For a given τ, σ, and element thickness, the input impedance depends on the characteristic impedance of the feeder. Fortunately, the directivity is essentially independent of the feeder impedance. This makes it possible to design an antenna for a given directivity and then, in most cases, the input impedance can be adjusted to the required level. The exceptions occur on models with both low τ and low Z_o. Under this condition the radiating efficiency of the active region

TABLE 3

LPD Parameters and Their Effect on the Observed Performance

Table entries denote the change in performance for an increase in the parameters of the first column.

LPD Parameter*	Bandwidth of Active Region B_{ar}	Input Impedance (always less than Z_o)	Directivity	Phase Center Distance to the Apex x_p	Boom length L/λ_{max} for a fixed Operating Bandwidth B
τ (σ constant)	decrease	small decrease	increase	increase (depends on α)	Decrease to a point depending on B, then increase
τ (α constant)	decrease	small decrease	small increase	independent	decrease
σ (τ constant)	increase	increase	increase	increase (depends on α)	increase
σ (α constant)	increase	increase	small decrease	independent	increase
Z_o	independent but location of AR moves toward apex	increase	small decrease	small decrease	small decrease
h/a	independent, but location of AR moves away from apex	increase	small decrease	small increase	small increase

* The table entries hold true over the following range of parameters for which frequency independent operation has been verified: $0.875 < \tau < 0.98$, $0.05 < \sigma < \sigma_{optimum}$, $100 < Z_o < 500$, and $20 < h/a < 10000$. Any one of τ, σ, or Z_o may take on other values provided the remaining parameters are suitably restricted as explained in the text.

is low, and troublesome end effects appear. Nevertheless, input impedance levels from 50 ohms for high values of τ to 200 ohms for all values of τ have been obtained. If a higher impedance level is required, the suggested 4:1 balun transformer scheme can be used.

Table 4 is a collection of the design equations. The numbers in parentheses refer to the page on which the equations are introduced. The most important relationship, that which relates the directivity to the antenna parameters, has not been put into equation form. For this information reference must be made to the graph of Figure 65.

4.2 Design Procedure

First is presented a method of finding the major design parameters τ and σ for a given value of directivity. Then it is shown how Z_o is adjusted to obtain the required input impedance. An example which illustrates the technique is given.

4.2.1 Choosing τ and σ To Obtain a Given Directivity

For most applications, one is interested in designing an antenna which has a given directivity and input impedance over a given frequency band. Once these electrical characteristics are specified, one must decide the relative importance of minimizing the number of elements or the size of the antenna. These two properties are not independent. The number of elements is determined by τ, as τ increases the number of elements increases. The antenna size is determined by the boom length (the distance between the smallest and largest element), which depends primarily on α. As α decreases the size increases. From the graph of Figure 65, it can be seen that a number of combinations of τ and σ lead to a given value of directivity.

TABLE 4

Numbers in paranthesis refer to the page on which the equations are first introduced

$$\sigma = \frac{1}{4}(1-\tau)\cot\alpha \qquad \tau = 1 - 4\sigma\tan\alpha \qquad \alpha = \tan^{-1}\left(\frac{1-\tau}{4\sigma}\right) \tag{15}$$

$$B_{ar} = 1.1 + 30.7\,\sigma(1-\tau) \qquad B_{ar} = 1.1 + 122.8\,\sigma^2\tan\alpha \qquad B_{ar} = 1.1 + 7.7\,(1-\tau)^2\tan\alpha \tag{69}$$

$$R_o = \frac{Z_o}{\sqrt{1 + \frac{Z_o}{4\sigma' Z_a}}} \tag{54}$$

$$\frac{Z_o}{R_o} = \frac{1}{8\sigma'\frac{Z_a}{R_o}} + \sqrt{\left(\frac{1}{8\sigma'\frac{Z_a}{R_o}}\right)^2 + 1} \tag{91}$$

$$Z_a = 120(\ell n\, h/a - 2.25) \tag{53}$$

$$Z_o = 120\cosh^{-1}\frac{b}{2a} \tag{156}$$

$$B_s = B\,B_{ar} \tag{66}$$

$$l/\lambda_{max} = \frac{1}{4}\left(1 - \frac{1}{B_a}\right)\cot\alpha \qquad l/\lambda_{max} = \left(1 - \frac{1}{B_s}\right)\frac{1}{1-\tau} \tag{147}$$

$$N = 1 + \frac{\log B_s}{\log\frac{1}{\tau}} \tag{147}$$

$$x_p \approx \frac{\lambda}{4}\cot\alpha \tag{137}$$

One of this set (τ, σ) leads to minimum boom length and another leads to a minimum number of elements.

With these facts in mind a preliminary choice of τ and σ can be made from the graph of Figure 65. It is usually best to start with the optimum value of σ and then proceed to lower values. Knowing τ and σ, the value of the dependent variable α can be determined from

$$\tan \alpha = \frac{(1 - \tau)}{4\sigma} \tag{89}$$

or from the nomograph of Figure 79.

The structure bandwidth B_s must be found to determine the boom length and the number of elements. B_s depends on the required operating bandwidth B and the bandwidth of the active region B_{ar}. For the given values of τ, σ and α, B_{ar} can be determined from Figure 32, or from the nomograph of Figure 80. B_s is then given by

$$B_s = B\, B_{ar}. \tag{90}$$

Since the length of element number one is $\frac{\lambda_{max}}{2}$ in the preliminary design, the geometry of the LPD antenna provides an expression for the boom length relative to the longest operating wavelength.

$$\frac{L}{\lambda_{max}} = \frac{1}{4}\left(1 - \frac{1}{B_s}\right)\cot \alpha \tag{91}$$

where L is the boom length between the longest and shortest elements. A nomograph of 91 is given in Figure 81. The number of elements is found from the equation

$$N = 1 + \frac{\log B_s}{\log 1/\tau} \tag{92}$$

a nomograph of which is given in Figure 82.

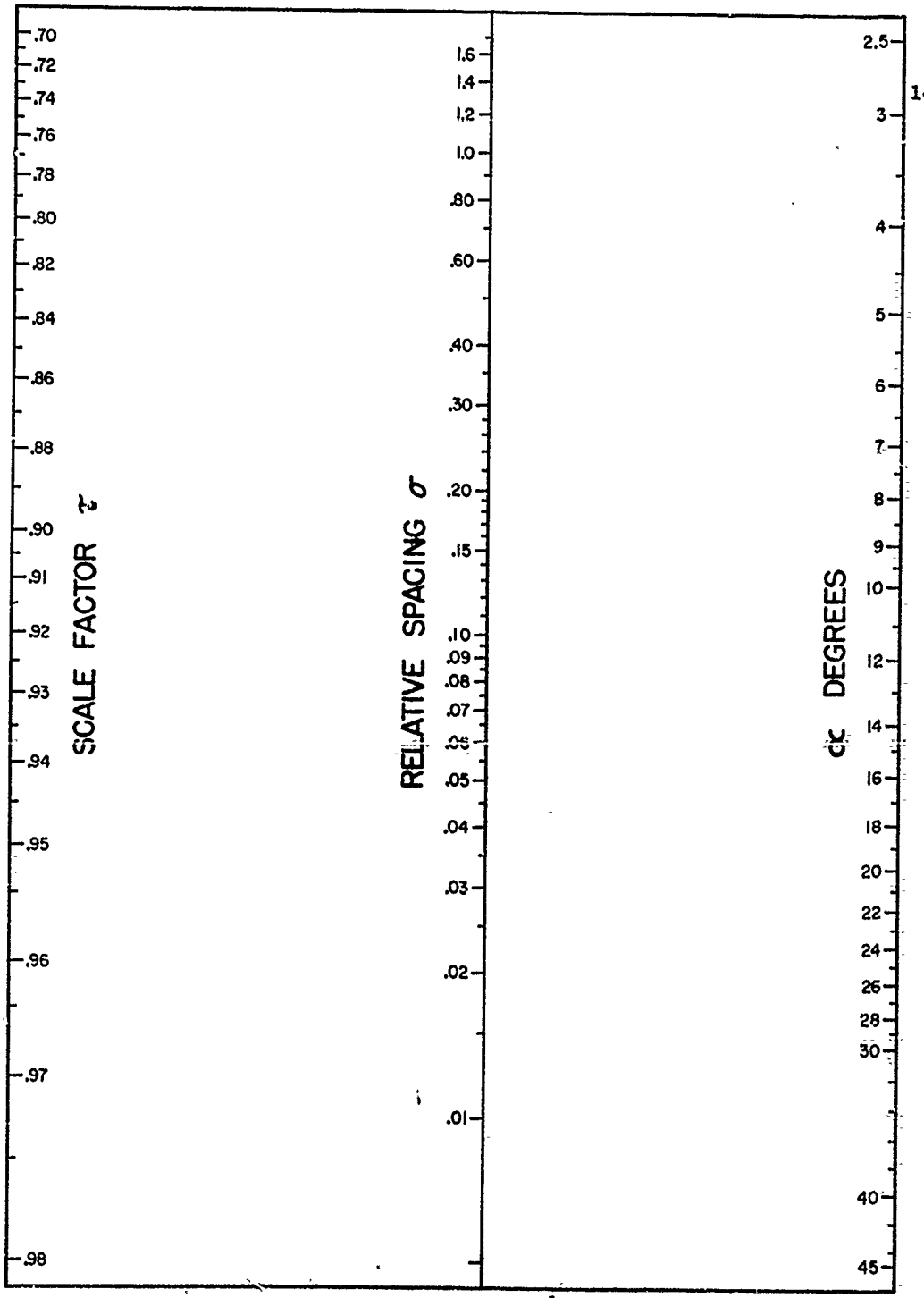

Figure 79. Nomograph, $\sigma = \frac{1}{4}(1 - \tau)\cot \alpha$

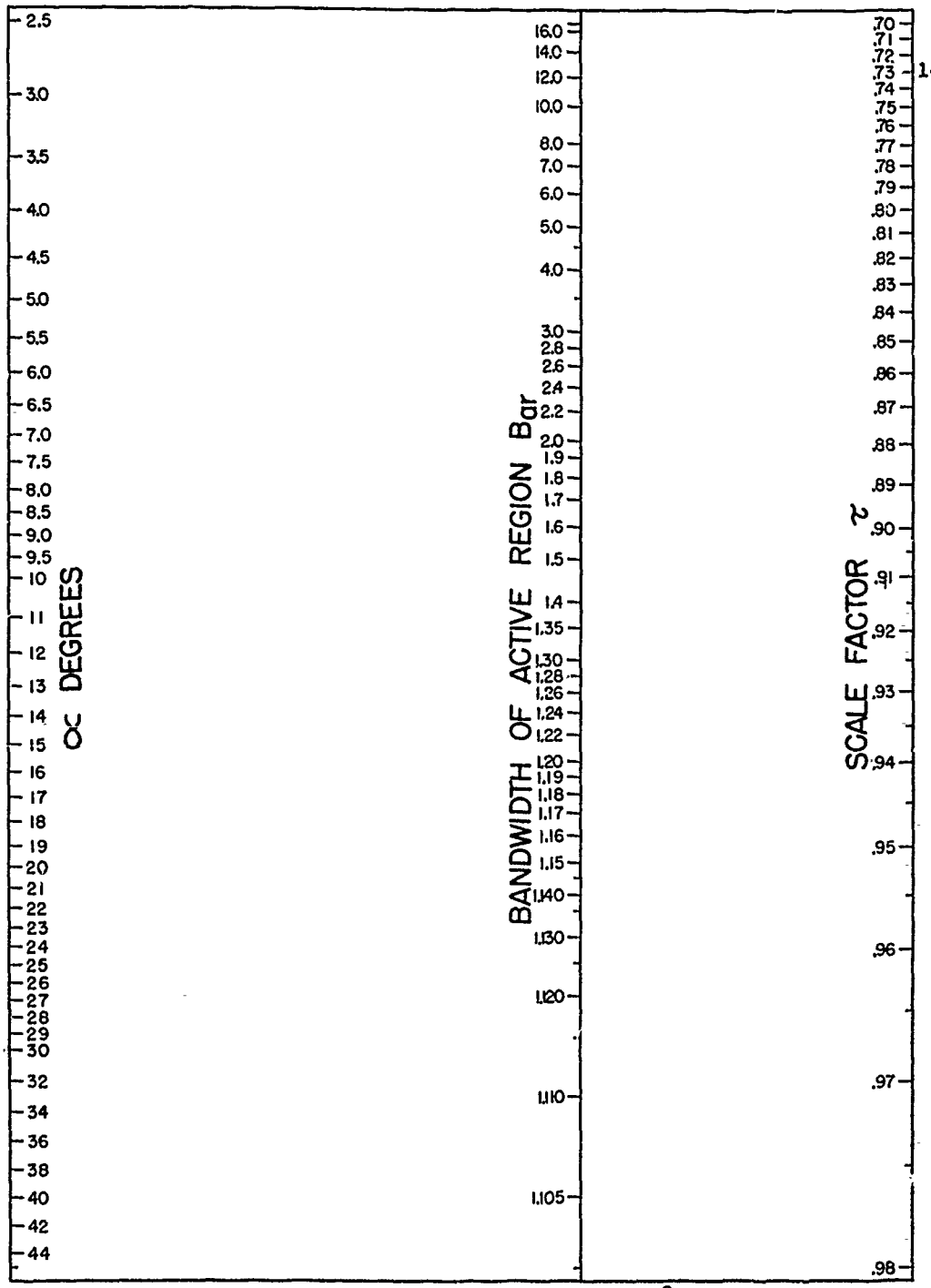

Figure 80. Nomograph, $B_{ar} = 1.1 + 7.7\ (1 - \tau)^2 \cot \alpha$

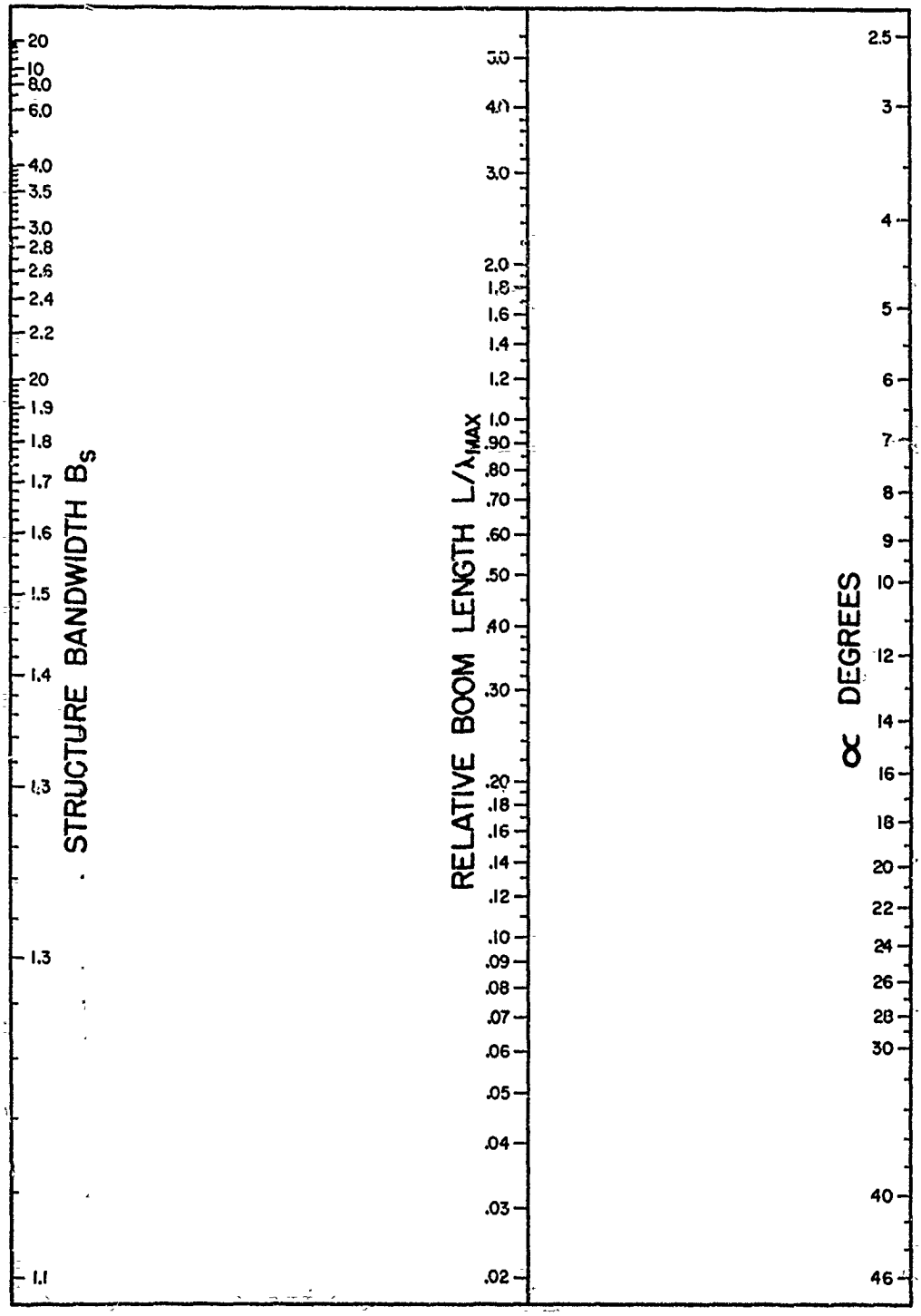

150

Figure 81. Nomograph, $\frac{L}{\lambda_{max}} = \frac{1}{4}(1 - \frac{1}{B_s})\cot \alpha$

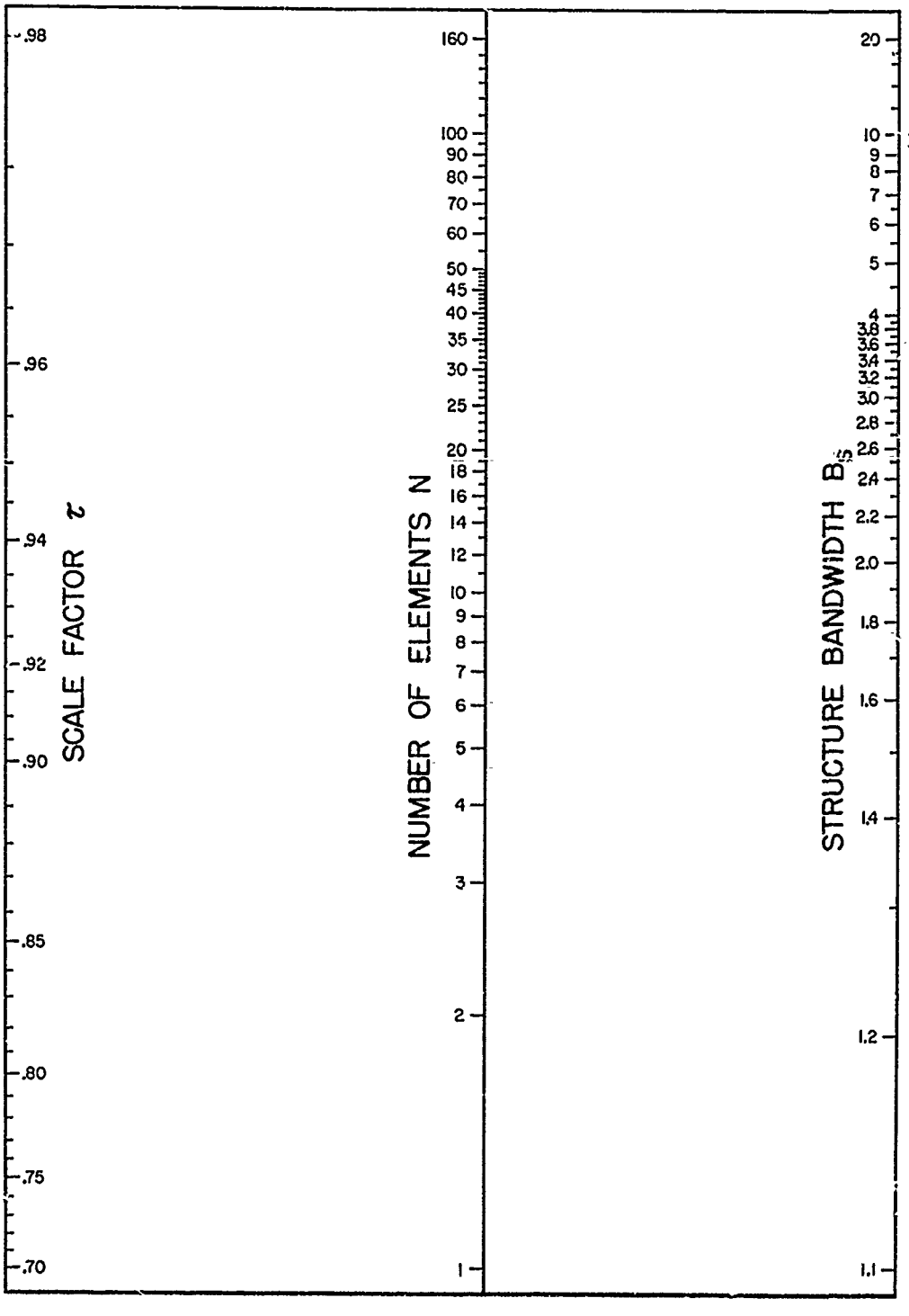

Figure 82. Nomograph, $N = 1 + \frac{\log B_s}{\log \frac{1}{\tau}}$

It is likely that the first estimate of τ and σ will not minimize L or N. Repeating the process for different values of τ and σ will establish the trend, and the minimum designs will become readily apparent. For some values of B_s, minimum L cannot be attained for values of τ and σ within the operating range of the graph of Figure 65. In these cases a compromise will have to be made. If a choice of (τ, σ) exists, and there is no apparent basis for a decision, it should be recalled that the SWR increases and the front to back ratio decreases as σ departs from the optimum value, according to Figures 40 and 68.

Some mention should be made of the secondary factors which effect the directivity, Z_o and Z_a. Since the graph of Figure 65 is based on Z_o = 100 ohms and Z_a = 350, an adjustment should be made if it is anticipated that Z_o and Z_a will depart from these values by more than a factor of 2. The exact value of Z_o is as yet undetermined. However, it is known that the feeder impedance is always greater than the resulting input impedance, so if R_o is greater than 100 ohms the directivity contours of Figure 65 will read a fraction of a decibel high. If the ratio h/a is much different than 177 a correction must be made. According to the curve of Figure 71, the directivity decreases by about 0.1 db for each doubling of h/a; for $h/a > 177$ the constant directivity contours of Figure 65 will read high. One may wish to include an additional safety factor, since a comparison of computed and measured directivity in Table 2 shows that the directivity computed from Figure 65 averages 0.35 db higher than the measured value. The corrected value of directivity, for use in Figure 65, is obtained by adding the above contributions to the required design value.

4.2.2 Designing for a Given Input Impedance

Once the final values of τ and σ are found, the characteristic impedance of the feeder Z_o must be determined so as to give the required input impedance R_o. The ratio h/a is determined from structural considerations, and ideally should be the same for each element. Practically, the element diameters can be scaled in groups, and in the computation of input impedance the average h/a in a group should be used. The average characteristic impedance of a dipole element Z_a can be found from

$$Z_a = 120\ (\ln h/a - 2.25), \tag{93}$$

or from the graph of Figure 45. Inverting Equation(71), gives the characteristic impedance of the feeder relative to R_o,

$$\frac{Z_o}{R_o} = \frac{1}{8\sigma'\frac{Z_a}{R_o}} + \sqrt{\frac{1}{\left(8\sigma'\frac{Z_a}{R_o}\right)^2} + 1}\ , \tag{94}$$

where Z_a/R_o is the average characteristic impedance of a dipole element with respect to the required input impedance R_o, and σ' is the mean relative spacing,

$$\sigma' = \sigma/\sqrt{\tau}\ . \tag{95}$$

A graph of(94)is given in Figure 46.

The major parameters of the required design have now been determined. It remains to find the size of the first element relative to the maximum operating wavelength. As shown in Section 3.2.2, the longest element can be less than $\frac{\lambda_{max}}{2}$ for values of $Z_o > 100$ and $h/a < 177$. The half-length of the longest element is given by

$$h_1 = S \frac{\lambda_{max}}{4} \qquad (96)$$

where S is the shortening factor as read from the graph of Figure 33. Knowing τ, σ, N, Z_o and h_1, one can find the dimensions of all other parts of the antenna.

The impedance Z_T which terminates the feeder has an effect only at the lowest operating frequencies. In practice, the feeder is terminated in a short circuit a distance of $\frac{\lambda_{max}}{8}$ or less behind the largest element, so that Z_T remains inductive at the lowest frequencies.

4.2.3 Application of the Design Procedure: An Example

As an example of the design procedure, let the dimensions of an LPD antenna be determined such that the directivity is 9.5 db, the bandwidth is 1.75, and the input impedance is 80 ohms. Size limitations dictate an h/a of 118. This means that the corrected directivity for use in Figure 65 is between 9.4 and 9.5 db. Starting with a value of σ greater than optimum (to clearly illustrate the trend), the set (τ,σ) which yields a directivity of 9.4 db is recorded from Figure 65 in Table 5.

The values of B_{ar}, L/λ_{max}, and N were determined from the nomographs. The minimum-element design is (0.89, 0.165). The minimum boom length design cannot be attained for values of τ and σ within the operable range. A compromise between length and number of elements is given by $\tau = 0.92$ and $\sigma = 0.12$. This design has $L/\lambda_{max} = 0.89$ and $N = 12$. The average characteristic dipole impedance for h/a = 118 is about 300 ohms (from Figure 45) so $Z_a/R_o = 3.75$. $\sigma' = \sigma/\sqrt{\tau}$ is 0.125, and from the graph of Figure 46, Z_o/R_o is approximately 1.3, therefore the feeder impedance Z_o is 104 ohms. The half-length of element one is set equal to $\lambda_{max}/2$ because the shortening factor is nearly unity (see Figure 33).

TABLE 5

Values of τ, σ and α, which give 9.4 db directivity over a 1.75:1 band

τ	σ	α	B_{ar}	$B_s = BB_{ar}$	L/λ_{max}	N
0 92	0.210	5.4	1.62	2.84	1.72	13+
0.91	0.197	6.6	1.64	2.87	1.41	12
0.90	0.187	7.7	1.68	2.94	1.23	11+
0.89	0.165	9.5	1.66	2.91	0.99	10
0.90	0.148	9.7	1.56	2.73	0.94	10+
0.91	0.135	9.5	1.47	2.57	0.92	11-
0.92	0.120	9.5	1.40	2.45	0.89	12-
0.93	0.105	9.5	1.33	2.33	0.86	13-
0.94	0.090	9.5	1.27	2.22	0.83	14-
0.95	0.070	10.2	1.21	2.12	0.74	15+
0.96	0.050	11.0	1.16	2.03	0.66	18+

TABLE 6

Antenna Dimensions in Inches

n	τ^{n-1}	h_n	x_n	D_n	$2a_n$	Diameter of wire used
1	1.0000	4.66	28.00	16.81	0.079	0.078
2	0.9200	4.29	25.76	14.57	0.073	0.072
3	0.8464	3.95	23.70	12.51	0.067	0.072
4	0.7787	3.63	21.80	10.61	0.062	0.065
5	0.7164	3.34	20.06	8.87	0.057	0.061
6	0.6591	3.07	18.45	7.26	0.052	0.050
7	0.6064	2.83	16.98	5.79	0.048	0.048
8	0.5578	2.60	15.62	4.43	0.044	0.040
9	0.5132	2.39	14.37	3.18	0.041	0.040
10	0.4722	2.20	13.22	2.03	0.037	0.038
11	0.4344	2.02	12.16	0.97	0.034	0.031
12	0.3996	1.87	11.19	0	0.032	0.031

In compiling a table of the dimensions of the antenna, it is best to start with a tabulation of powers of τ which is accurate to at least four decimal places. The half lengths of the elements h_n; the distance from the apex to each element, x_n; the distance from the front of the antenna to each element, D_n; and the element diameters are then computed, as shown in Table 6. The half length of the largest element is 4.66 inches because the desired low frequency cut-off is 635 mcs.

The feeder is spaced to give a characteristic impedance of 104 ohms according to the formula,

$$Z_o = 120 \cosh^{-1} \frac{b}{2a}, \tag{97}$$

where b is the center to center spacing and 2a is the diameter of the feeder conductors. The above described antenna was constructed of coin silver tubing and copper wire, using silver-solder techniques. The resulting model is pictured in Figure 83. The measured input impedance clustered around a mean resistance level R_o of 73 ohms, a bit lower than the design value. This could be brought closer to 80 ohms by increasing the spacing between the feeders. The SWR with respect to 73 ohms is plotted in Figure 84. Taking an SWR of 1.3:1 to define the useful band, one finds that this antenna operates from $f_{1.05}$ to $f_{8.25}$, which gives a bandwidth of 1.82. The measured E-and H-plane half-power beamwidths and the directivity are shown in Figure 85. The average directivity from $f_{1.05}$ to $f_{8.25}$ is about 9.5 db, which just meets the requirement. A comparison of measured and computed patterns for this antenna is shown in Figure 86.

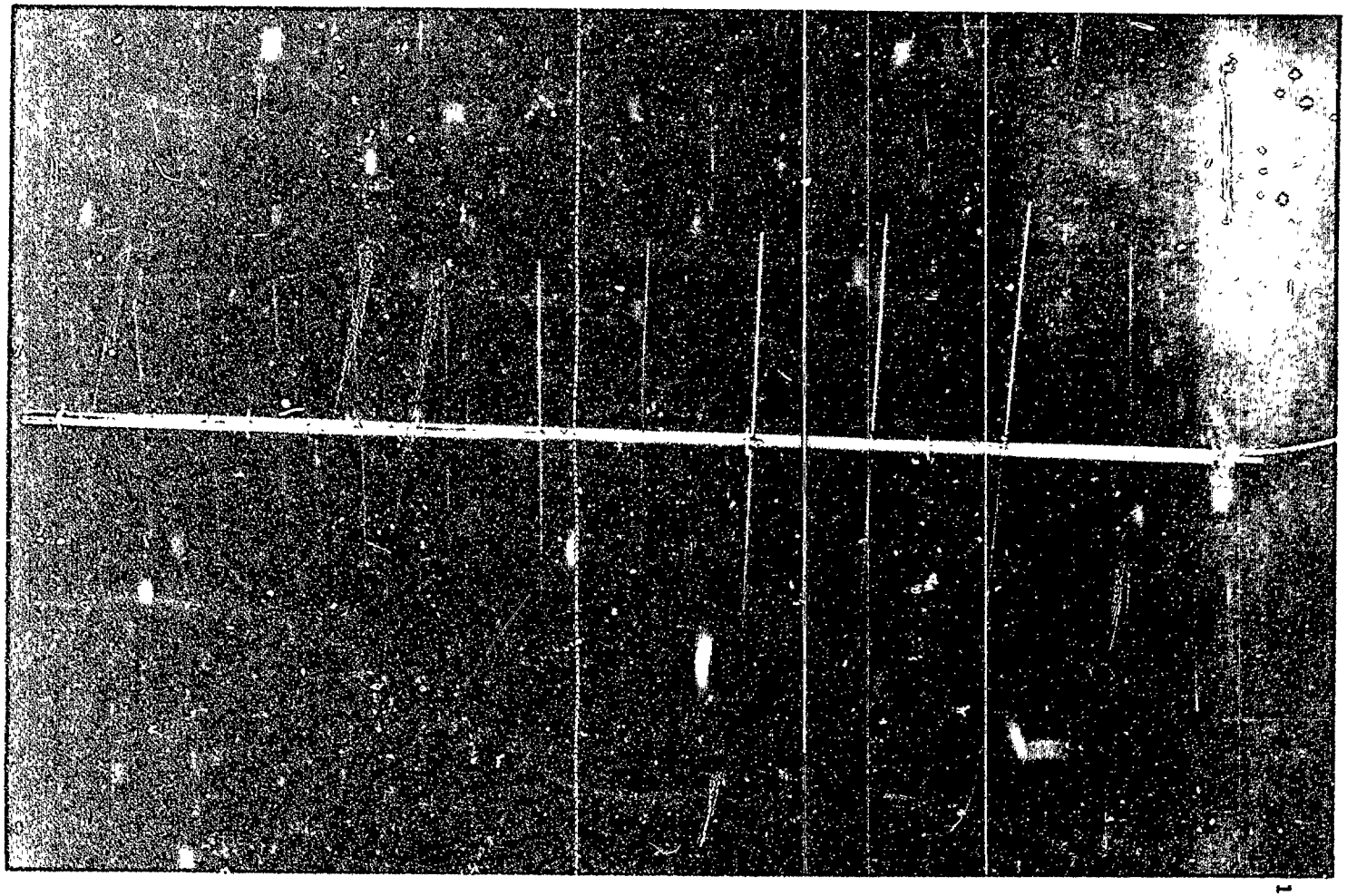

Figure 83. The LPD realized by the design procedure of Section 4.2.3

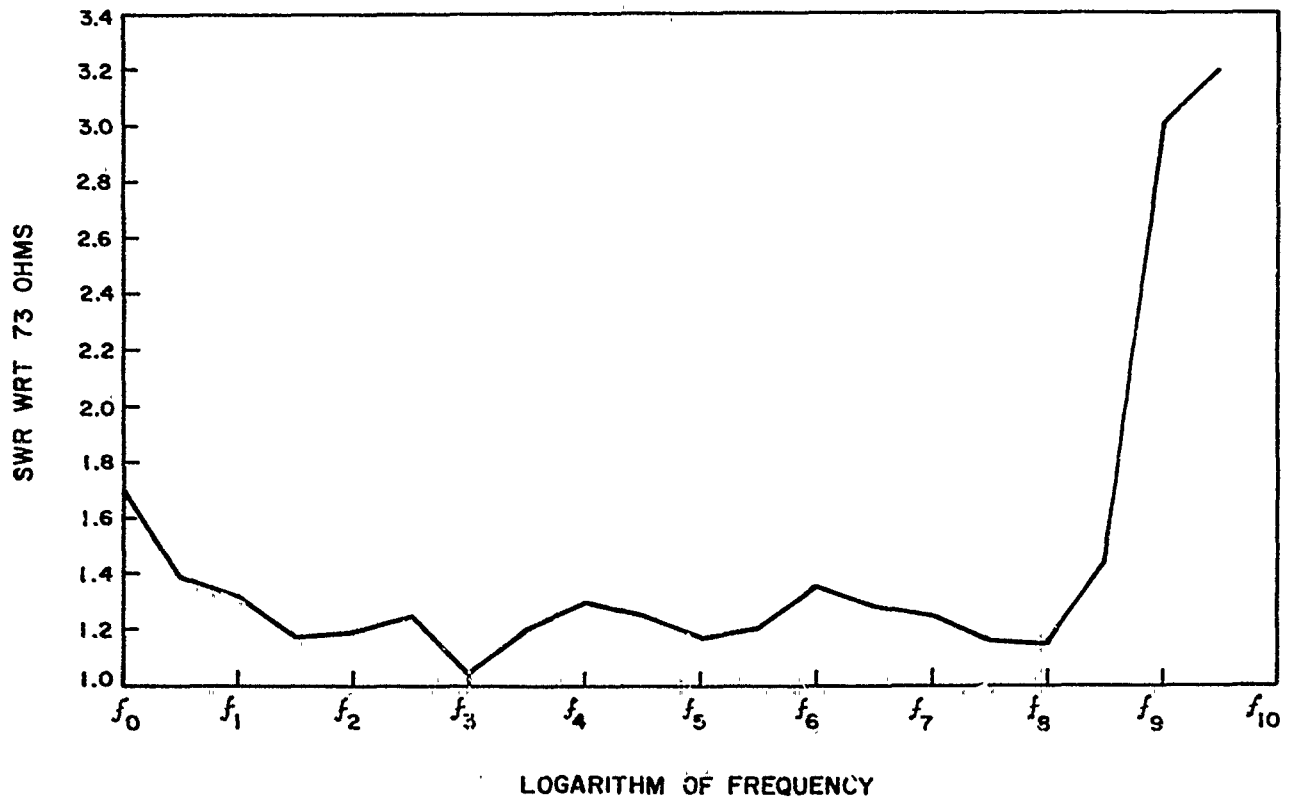

Figure 84. Measured standing wave ratio vs. frequency of the design model.

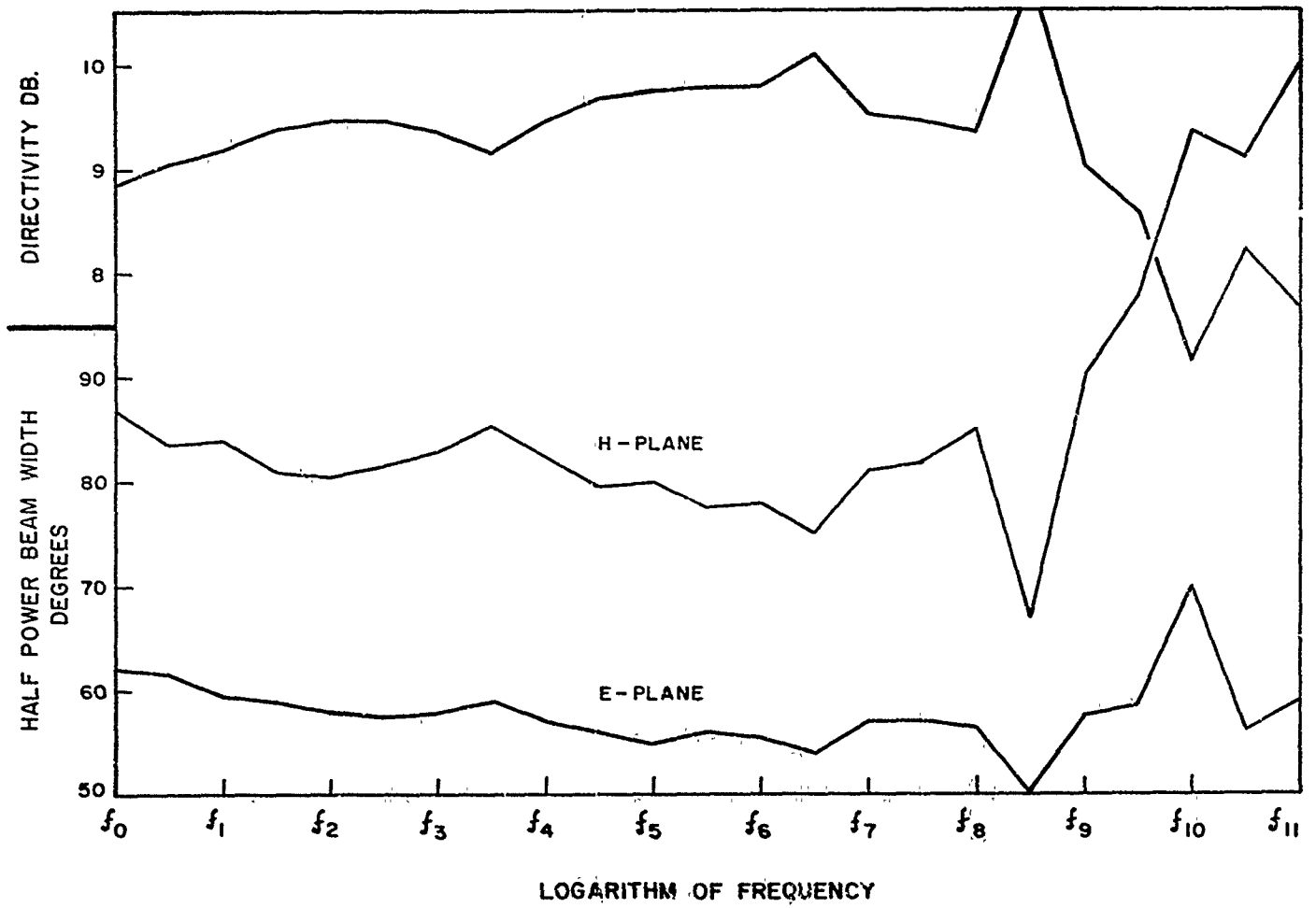

Figure 35. Measured E- and H-plane half-power beamwidth and directivity of the design model

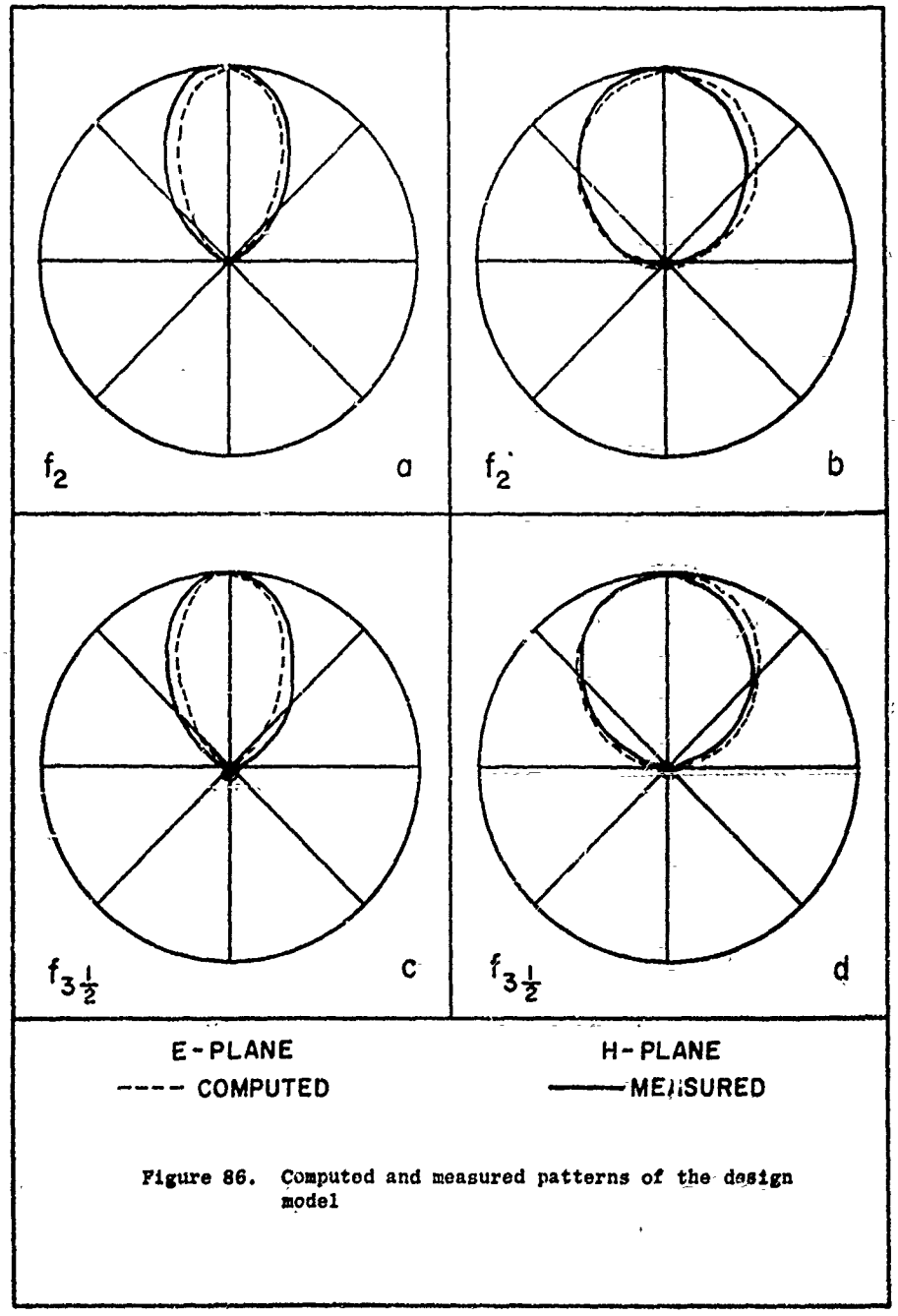

Figure 86. Computed and measured patterns of the design model

This antenna comes close to meeting the required specifications. The agreement between the measured and design value of input impedance is about what can be expected. However, the agreement between the measured and design value of directivity is somewhat better than typical; an error of less than 0.5 db is probably as good as can be expected.

Of course, the outlined procedure is only one of many, and variations will become apparent to those who gain experience in the design of LP antennas. The concept of bandwidth of the active region and its application are new. Heretofore specific bandwidth designs were determined by constructing an antenna which was obviously longer than necessary; the required operating bandwidth was then obtained by a cut-and-try procedure. The graphs and nomograms are particularly useful because they allow one to achieve many preliminary designs without resorting to tedious computations.

4.3 Some Novel Variations in the Log-Periodic Design

The fact that the radiating portion of an LPD at any given frequency is confined to a relatively few elements and is independent of the location of the front or back truncation leads to some novel departures from the true log-periodic forms. If it is desired to operate over two or more separate bands, or if part of a band contains "non-interesting" frequencies, the solution is to eliminate the elements that form the active region at the unwanted frequencies. This amounts to connecting two or more LPD antennas in cascade. Figure 87 shows one such example. If the input impedance is to remain the same over both bands, the two sections should have the same τ and σ. This means that the apices of each section will be different. In the one model constructed according to the scheme of Figure 87, it was found that the presence of Section 2 lowered the low

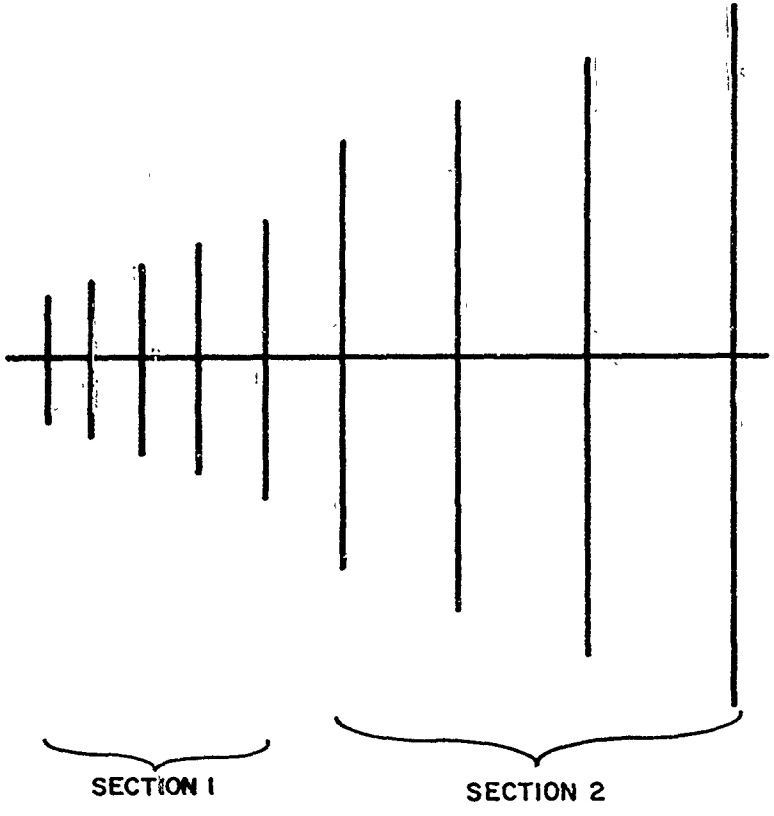

Figure 87. Two LPD antennas in cascade

frequency cut-off of Section 1. The high frequency cut-off of Section 2 was extended somewhat by the proximity of Section 1. The mid-band patterns of each section were characteristic of what would be observed with each antenna operating by itself.

There also exists the possibility of tailoring the directivity characteristic such that the patterns are frequency dependent in a special way. This would require that τ and σ or both be a function of position. In this case σ' should be held constant to achieve a frequency independent input impedance. The above idea was applied to one model in which α was fixed at 25°. The spacing between all elements was a constant, one-half inch. σ varied along the antenna from 0.022 to 0.088. The measured directivity increased with frequency from 5 to 8.5 db, then decreased to 7.5 db.

A high quality dielectric material can be used between the elements as well as in the feeder configuration. The model pictured in Figure 88 was constructed from 0.0625" double copper-clad Rexolite using printed circuit techniques. Its parameters are $\tau = 0.92$, $\bar{\sigma} = 0.08$, and $N = 23$. The equivalent h/a is 138 and Z_o is approximately 105 ohms. Examples of the measured patterns are shown in Figures 89 and 90. The directivity is 8.5 db over the band. The patterns developed scallops at the highest frequency f_{18}, which was 4450 mcs. The measured cross polarization was negligible.

The phase rotation phenomenon has been used in the design of a frequency independent antenna whose beam is circularly polarized on the axis. In this case two LPD antennas are interleaved along a common axis with the elements of one antenna perpendicular to the other. One antenna is also expanded with respect to the other to achieve the 90° phase shift.

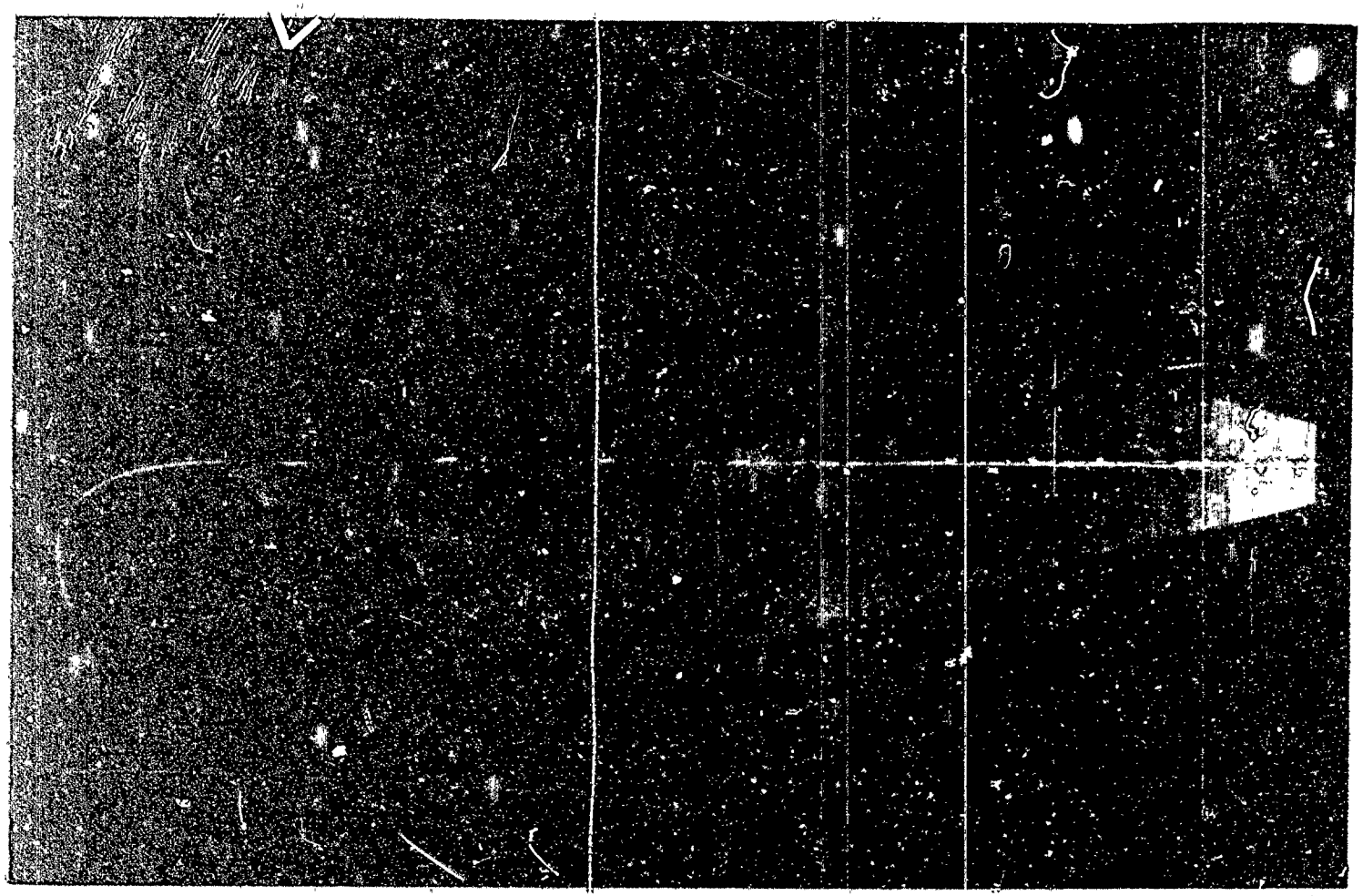

164

Figure 88. An LPD antenna etched from double copper-clad Rexolite

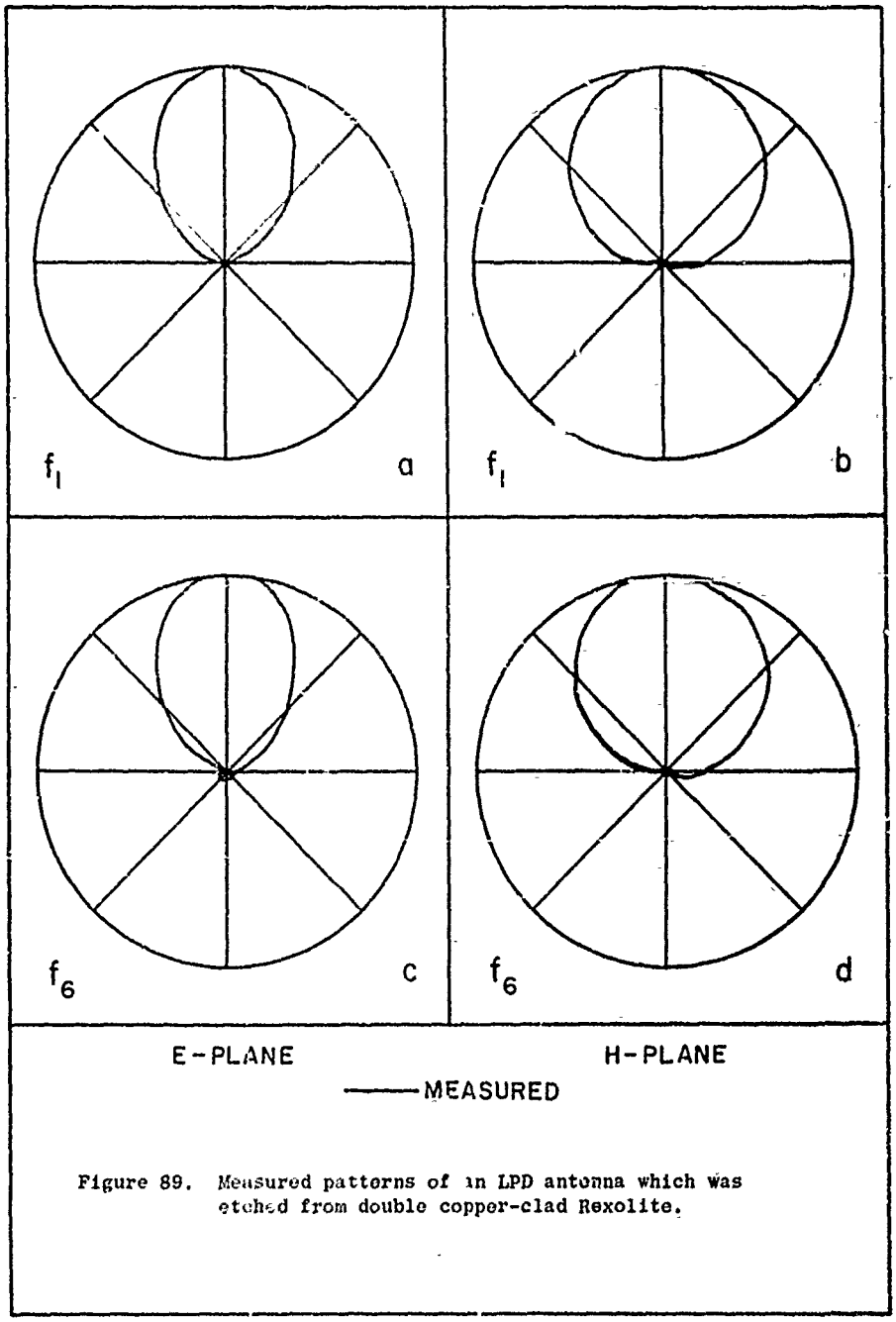

Figure 89. Measured patterns of an LPD antenna which was etched from double copper-clad Rexolite.

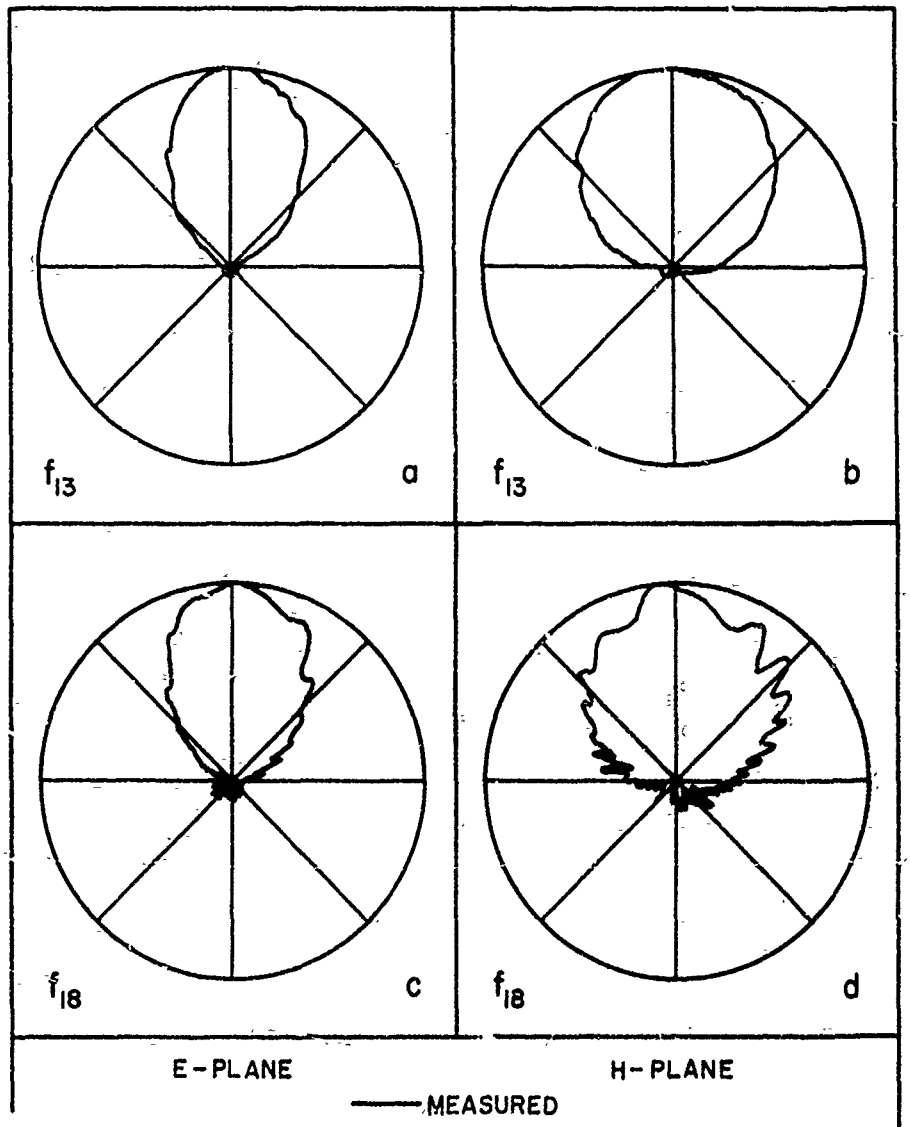

Figure 90. Measured patterns of an LPD antenna which was etched from double copper-clad Rexolite.

Since the phase shift is independent of frequency, the pattern remains circularly polarized over the operating band.

5. CONCLUSION

The object of this research was to provide a mathematical model of the log-periodic dipole antenna. The model was to be general enough to lend insight into the operation of log-periodic antennas, and capable of being used as a design tool. The model described herein was shown to fulfill these objectives.

In this research the known properties of dipole antennas were used to determine the self and mutual impedances in a log-periodic array of dipoles. The properties of the dipoles were described by an impedance matrix which relates the voltage and current at the base of each dipole. A feeder system, which determines the relative excitation of each element, was also described by an impedance matrix. The feeder and element circuits were joined, and the voltage and current at the base of each dipole element were found. From these quantities the input impedance and properties of the radiated field were determined.

It was shown that three regions exist on a frequency independent log-periodic dipole antenna: the transmission region, the active region, and the unexcited region. The transmission region was shown to be equivalent to a section of uniform transmission line, and the characteristic impedance and propagation constant of this line were determined. The active region was shown to consist of several elements of approximately half-wavelength dimensions on which the current amplitude is considerably greater than that on the remaining elements. The magnitude and phase of the currents in the active region determines the characteristic pattern of the LPD, and it was shown that the phase progression from element to element in the

active region was that required to produce the backward wave which is characteristic of all LP antennas. The low input standing wave ratio indicates that the active region presents a good match to the transmission region. In the unexcited region, it was shown that in most cases a negligible amount of power remains on the feeder beyond the active region, and that the current in the elements that are longer than a half-wavelength is very small. For these reasons the truncation at the large end of the antenna has no effect for all frequencies within the operating band.

The bandwidth and location of the active region were defined, and these quantities were used to determine the size of an antenna which covers a given frequency band. The relations between the observed characteristics of the antenna, directive gain, input impedance, and location of the phase center, and the antenna parameters were shown. A design procedure was outlined whereby the physical dimensions of a log-periodic dipole antenna which meets given electrical specifications can be determined. The good agreement between measured and computed results reaffirmed once again the validity of certain engineering approximations that have been used since the beginning of antenna analysis. They are, the assumption of a sinusoidal current distribution along straight conductors of small cross-section, and the applicability of circuit theory concepts to certain parts of an antenna structure that are small compared to wavelength.

This is the first time a digital computer has been used by the Antenna Laboratory to simulate and test a complicated antenna model. The successful results of this study indicate the possibility of utilizing the computer in even more complex problems. It is estimated that at least seven man-days would be needed to build a model and perform the measurements which the

computer has done in a matter of minutes. On the other hand, this work also illustrates one drawback in using a computer for experimental research. That is, each model tested represents a "new" problem to the computer, so a large mass of data must be collected to establish a trend. Perhaps a more sophisticated computer program could provide some data processing and interpolation, but in the end the utility of the results depends on the ability of the researcher to draw conclusions from them. This is not as easy as it may seem. Because of past training and experience, the researcher has certain prejudices that favor analysis of mathematical equations and not computed data. However, once these prejudices are set aside, one will find many new areas of research in which modern day computers can play increasingly important roles.

BIBLIOGRAPHY

1. J. A. Stratton, Electromagnetic Theory, Mc Graw-Hill, New York, N. Y., 1941, p. 488.

2. A. G. Kandoian, "Three New Antenna Types and Their Applications", Proc. IRE, Vol. 34, pp. 70w-75w, February, 1946.

3. J. S. Chatterjee, "Radiation Field of a Conical Helix," J. Appl. Phys., Vol. 24, p. 550, May, 1953.

4. V. H. Rumsey, "Frequency Independent Antennas", IRE National Convention Record, Pt. I, pp. 114-118, 1957. Technical Report No. 20, Contract AF33(616)-3220, Antenna Lab., University of Illinois, Urbana, Illinois, October, 1957.

5. S. A. Schelkunoff, Electromagnetic Waves, D. Van Nostrand Co., Inc., New York, 1943, pp. 441-459.

6. R. L. Carrel, "The Characteristic Impedance of Two Infinite Cones of Arbitrary Cross Section", IRE Transactions, Vol. AP-6, No. 2, April, 1958, pp. 197-201. Technical Report No. 25, Contract AF33(616)-3220, Antenna Lab., University of Illinois, Urbana, Illinois, August, 1957.

7. J. D. Dyson, "The Equiangular Spiral Antenna", IRE Transactions, Vol. AP-7, April, 1959, pp. 181-187. Technical Report No. 21, Contract No. AF33(616)-3220, Antenna Lab., University of Illinois, Urbana, Illinois, September, 1957.

8. J. D. Dyson, "The Unidirectional Equiangular Spiral Antenna," IRE Transactions, Vol. AP-7, October 1959, pp. 329-334. Technical Report No. 33, Contract No. AF33(616)-3220, Antenna Lab., University of Illinois, Urbana, Illinois, July, 1958.

9. R. H. DuHamel and D. E. Isbell, "Broadband Logarithmically Periodic Antenna Structures," IRE National Convention Record, Pt. I, pp. 119-128, 1957. Technical Report No. 19, Contract No. AF33(616)-3220, Antenna Lab., University of Illinois, Urbana, Illinois, May, 1957.

10. D. E. Isbell, "Non-Planar Logarithmically Periodic Antenna Structures," Technical Report No. 30, Contract No. AF33(616)-3220, Antenna Lab., University of Illinois, Urbana, Illinois, February, 1958.

11. D. E. Isbell, "Log Periodic Dipole Arrays," IRE Transactions, Vol. AP-8, No. 3, May, 1960, pp. 260-267, Technical Report No. 39, Contract No. AF33(616)-6079, Antenna Lab., University of Illinois, Urbana, Illinois, June, 1959.

12. H. E. King, "Mutual Impedance of Unequal Length Antennas in Echelon," IRE Transactions, Vol. AP-5, No. 3, July, 1957, pp. 306-313.

13. O. Zinke, "Fundamentals of Voltage and Current Distributions along Antennas," Arch. Elektrotech., Vol. 35, pp. 67-84, 1941.

14. R. L. Bell, C. T. Elfving, R. E. Franks, "Near Field Measurements on a Logarithmically Periodic Antenna," Technical Memorandum EDL-M231, Contract No. DA-36-039-SC-78281, Electronic Defense Laboratories, Mountain View, California, December, 1959.

15. E. C. Jordan, Electromagnetic Waves and Radiating Systems, Prentice-Hall, Inc., New York, 1950, p. 464.

16. E. Siegel and J. Labus, "Apparent Resistance of Antennas," Hochf. and Elck., Vol. 43, 1934, p. 166.

17. P. E. Mayes, G. A. Deschamps, W. T. Patton, "Backward Wave Radiation from Periodic Structures and Application to the Design of Frequency Independent Antennas," Proceedings of IRE, Vol. 49, No. 5, May, 1961.

18. R. L. Carrel, "The Design of Log-Periodic Dipole Antennas," 1961 IRE International Convention Record, pt. I, March, 1961.

19. Smith Electronics Co., Brecksville, Ohio, Private Communications.

20. P. E. Mayes and R. L. Carrel, "Logarithmically Periodic Resonant-V Arrays," Technical Report No. 47, Contract No. AF33(616)-6079, Antenna Lab., University of Illinois, Urbana, Illinois, July, 1960.

21. J. D. Kraus, Antennas, Mc Graw-Hill, New York, N. Y., 1950, p. 25.

22. R. H. DuHamel and F. R. Ore, "Log Periodic Feeds for Lens and Reflectors," IRE National Convention Record, pt. I, 1959, p. 128.

23. R. H. DuHamel and D. G. Berry, "Logarithmically Periodic Antenna Arrays," IRE WESCON Convention Record, pt. I, August, 1958.

24. E. Jahnke and F. Emde, Tables of Functions, Dover Publications, New York, 1945.

25. Tables of Sine, Cosine, and Exponential Integrals, Federal Works Agency, Work Projects Administration for the City of New York, sponsored by the National Bureau of Standards, 1940.

26. H. S. Wall, The Analytic Theory of Continued Fractions, D. Van Nostrand Co., Inc., New York, 1948.

27. G. Kron, Tensor Analysis of Networks, J. Wiley & Sons, Inc., New York, N. Y., 1939.

28. J. D. Dyson, "Measuring the Capacitance Per Unit Length of Biconical Structures of Arbitrary Cross Section," Technical Report No. 29, Contract No. AF33(616)-3220, Antenna Lab., University of Illinois, Urbana, Illinois, January, 1958.

29. G. A. Deschamps, "Impedance Properties of Complementary Multiterminal Planar Structures," Technical Report No. 43, Contract No. AF33(616)-6079, Antenna Lab., University of Illinois, Urbana, Illinois, November, 1959.

30. R. H. DuHamel, "Logarithmically Periodic Circuits," Research Division Technical Memorandum, Collins Radio Company, Cedar Rapids, Iowa, November, 1960.

31. R. H. DuHamel and F. R. Ore, "Logarithmically Periodic Antenna Designs", 1958 IRE National Convention Record, pt. I, p. 139.

32. R. E. Franks and C. T. Elfving, "Reflector-Type Periodic Broadband Antennas," 1958 IRE WESCON Convention Record, p. 266.

33. R. H. DuHamel and D. G. Berry, "A New Concept in High Frequency Antenna Design," 1959 IRE National Convention Record, pt. I, p. 42.

34. J. R. Tomlinson and M. N. Fullilove, "Very Broadband Feed for Paraboloidal Reflectors," 1959 IRE National Convention Record, pt. I, p. 147.

35. J. K. Shimizee, E. M. J. Jones, and R. C. Honey, "A Sinuous Flush-Mounted Frequency Independent Antenna," Technical Report No. 3, Contract No. AF19(604)-3502, Stanford Research Institute, October, 1959.

36. D. E. Isbell, "A Log-Periodic Reflector Feed," Proc. IRE, Vol. 47, p. 1152, June, 1959.

37. P. E. Mayes and R. L Carrel, "Logarithmically Periodic Resonant-V Arrays," Technical Report No. 47, Contract AF33(616)-6079, Antenna Lab., University of Illinois, Urbana, Illinois, July, 1960.

38. R. L. Carrel, "Analysis of the Log-Periodic Dipole Antenna," Abstracts of the 10th Annual Symposium on Air Force Antenna Research and Development, University of Illinois, October, 1960.

39. D. G. Berry and F. R. Ore, "Log-Periodic Monopole Array," Collins Research Report No. CRR-220, Collins Radio Company, Cedar Rapids, Iowa, October, 1960; 1961 IRE International Convention Record, pt. I, March, 1961.

40. J. W. Carr, "Some Variations in Log-Periodic Antenna Structures," Trans. IRE., Vol. AP-A, pp. 229-230, March, 1961.

41. H. Jasik, Antenna Engineering Handbook, Mc Graw-Hill, New York, N. Y., 1961, Chapter 18.

APPENDIX A

COMPUTATIONAL CONSIDERATIONS

This section describes several parts of the computer program for the solution of the equations of Section 2. The expansions used to evaluate the sine- and cosine-integral functions are given in detail, and the method used to solve the system of linear equations is outlined.

Since the accuracy of the over-all program depends on the accuracy of the several parts, care was taken to avoid programming blunders which lead to accumulated round-off errors. Each section of the program was checked by special test routines and compared with calculations performed on a desk calculator before being incorporated into the whole. In general, priority was placed on accuracy rather than computational speed, and standard ILLIAC library routines were used wherever possible.

A.1 The Cosine- and Sine-Integral Functions

The cosine-integral and sine-integral functions are defined as[24]

$$\mathrm{Ci}(x) = -\int_x^\infty \frac{\cos u}{u}\,du \tag{98}$$

and

$$\mathrm{Si}(x) = \int_0^x \frac{\sin u}{u}\,du \,. \tag{99}$$

Two distinct methods were used to compute $F(x) = \mathrm{Ci}(x) + j\,\mathrm{Si}(x)$. For $0 < x \leq 6$ a series expansion was used. For $x > 6$ a continued fraction expansion was used. The crossover point $x = 6$ was determined by the computer time required to achieve 8 or 9 accurate significant digits, using either method. A plot of computer time vs. x is shown in Figure 91. The crossover point $x = 6$ was chosen from this plot. The series representations

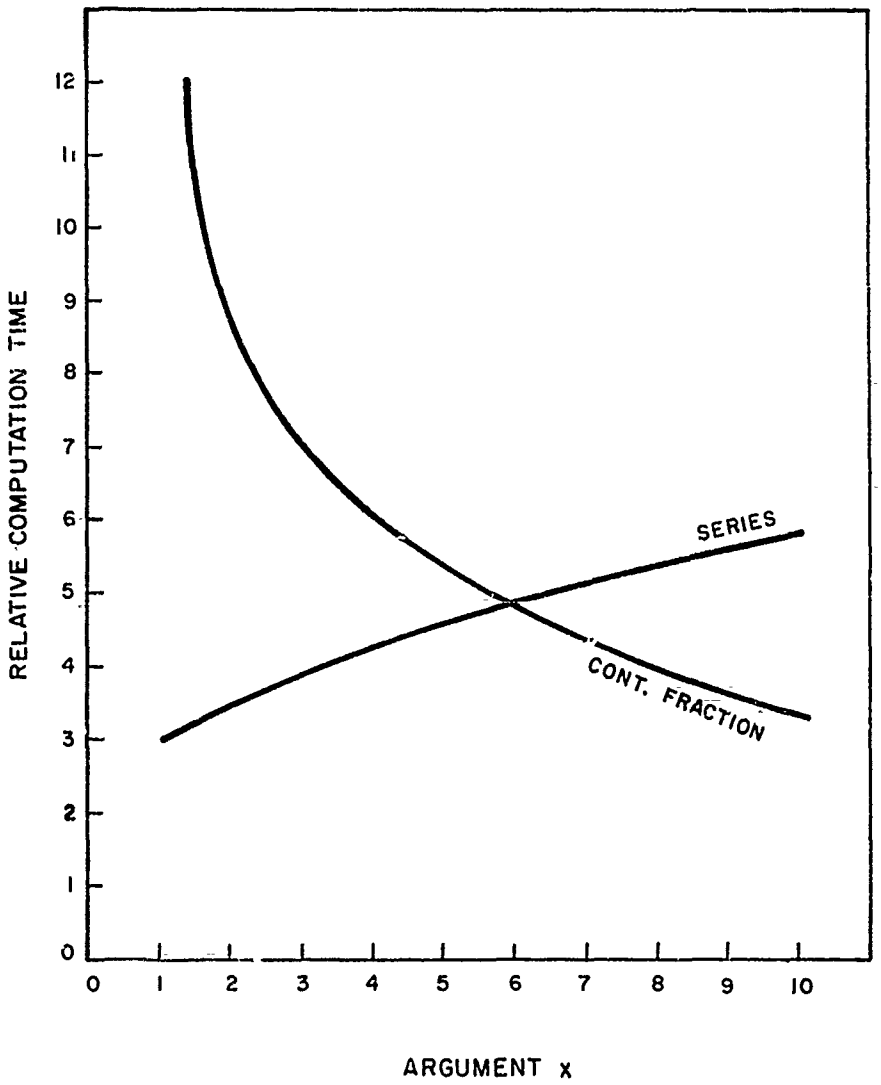

Figure 91. Computation time vs. argument x for the series and continued fraction expansion of $K(x) = Ci(x) + j\,Si(x)$

used were[25]

$$Ci(x) = C + \ell n(x) + \sum_{n=1}^{\infty} \frac{(-1)^n x^{2n}}{(2n)!\,2n} \tag{100}$$

where C = 0.57721 is Euler's constant, and

$$Si(x) = \sum_{n=1}^{\infty} \frac{(-1)^n x^{2n+1}}{(2n+1)!\,(2n+1)} \quad . \tag{101}$$

Both the above series are uniformly convergent for all finite values of x. The convergence of these series is slow, and the number of terms required for a given accuracy increases with x. Fifteen terms were required for eight place accuracy with x equal to 6. However the terms of the series are monotonically decreasing and alternating in sign, so the error involved in using n terms is numerically less than the n + 1st term. This fact allows one to compute until a given accuracy is attained, and this advantage outweighs the fact that the convergence is slow. The two series of Equations 100 and 101 were computed together as

$$K(x) = C + \ell n(x) \sum_{n=1}^{\infty} \frac{(jx)^n}{n!\,n} \quad . \tag{102}$$

To find the continued fraction expansion for K(x) observe that

$$K(x) = Ci(x) + jSi(x) = Ei(jx) + j\frac{\pi}{2} \tag{103}$$

where

$$-Ei(-z) = \int_z^{\infty} \frac{e^{-u}}{u}\, du \quad , \tag{104}$$

As a function of the complex variable z, Ei(-z) has a logarithmic branch point at z = 0, therefore the argument $z = |z|\, e^{j\theta}$ is restricted such that $-\pi < \theta < \pi$. A continued fraction expansion exists for (104),[26]

$$e^z \int_z^\infty \frac{e^{-u}}{u}\, du = \frac{1}{z} + \frac{1}{1} + \frac{1}{z} + \frac{2}{1} + \frac{2}{z} + \frac{3}{1} + \ldots \tag{105}$$

By means of an equivalence transformation (105) can be rewritten

$$e^z \int_z^\infty \frac{e^{-u}}{u}\, du = \frac{1}{z} + \frac{1}{1} + \frac{1}{z} + \frac{1}{\frac{1}{2}} + \frac{1}{z} + \frac{1}{\frac{1}{3}} + \frac{1}{z} + \ldots \tag{106}$$

This is a continued fraction of Stieltjes. The general form of the Stieltjes continued fraction is

$$\frac{1}{k_1 z} + \frac{1}{k_2} + \frac{1}{k_3 z} + \frac{1}{k_4} + \frac{1}{k_5 z} + \frac{1}{k_6} + \ldots \tag{107}$$

The continued fraction (107) is uniformly convergent in the cut z-plane due to the fundamental convergence theorem of Stieltjes, which states that if the k_p are positive constants and the series $\Sigma\, k_p$ diverges the continued fraction is uniformly convergent over every finite closed domain of z whose distance from the negative half of the real axis is positive, and its value is an analytic function of z for all z not on the negative half of the real axis. Therefore K(x) may be computed from (106). By means of another equivalence transformation,

$$K(x) = j\frac{\pi}{2} + \frac{e^{jx}}{jx} \cdot \frac{1}{F(jx)} \tag{108}$$

where

$$F(jx) = 1 - \frac{1/jx}{1} - \frac{1/jx}{1} - \frac{2/jx}{1} - \frac{2/jx}{1} - \frac{3/jx}{1} \cdots \tag{109}$$

The p^{th} approximate of F, A_p/B_p, is given by the fundamental recurrence formulas:

$$A_{p+1} = b_{p+1} A_p + a_{p+1} A_{p-1},$$

$$B_{p+1} = b_{p+1} B_p + a_{p+1} B_{p-1}, \tag{110}$$

with

$$A_{-1} = 1,\ B_{-1} = 0,\ A_o = b_o,\ B_o = 1, \tag{111}$$

and

$$a_p = \frac{-(p+1)/2}{jx}, \qquad p = 1,3,5, \cdots,$$

$$a_p = \frac{-p/2}{jx}, \qquad p = 2,4,6, \cdots, \tag{112}$$

$$b_p = 1.$$

The fundamental recurrence formulas allow one to compute the successive approximates of F rather than start with a given p and rationalize F_p. In the ILLIAC program for the continued fraction expansion of K(x), it was found that nine place accuracy for Ci(x) or Si(x), whichever was larger, was achieved when

$$\left| \frac{A_p}{B_p} \right| - \left| \frac{A_{p-1}}{B_{p-1}} \right| \leq 10^{-9}, \tag{113}$$

for $x \geq 1.5$. The number of iterations required ranged from 73 for x = 1.5 to 15 for x = 9.

The subroutine for K(x) was programmed to test x to determine the type of expansion to use and then to compute K(x) to nine sigificant digits. It is worthy of note that continued fraction expansions exist for many transcendental functions, some of which are given by Wall[26], and that in certain cases the continued fraction is more rapidly convergent than the corresponding series expansion.

A.2 Matrix Operations

The program which computes $\bar{T} = (\bar{U} + \bar{Y}_F \bar{Z}_A)$ was straightforward. The prime difficulty in this case is the systematic addressing of the storage locations of the matrix elements.

The solution of

$$\bar{I} = \bar{T}\,\bar{I}_A \tag{114}$$

employs the upper triangularization and back-substitution method. The steps in this method are as follows. First the augmented matrix $\bar{T}_a$ is set up, using $\bar{T}$ and $\bar{I}$.

$$\bar{T}_a = \begin{bmatrix} t_{11} & t_{12} & t_{13} \cdots t_{1N} & - & i_1 \\ t_{21} & t_{22} & t_{23} \cdots t_{2N} & - & i_2 \\ \cdots & \cdots & \cdots & \cdots & \cdots \\ \cdots & \cdots & \cdots & \cdots & \cdots \\ t_{N1} & t_{N2} & t_{N3} \cdots t_{NN} & - & i_N \end{bmatrix} \tag{115}$$

Here the t_{ij}'s are the elements of $\bar{T}$ and the i_i's are the elements of $\bar{I}$. $\bar{T}_a$ is a matrix which represents the equation

$$\bar{T}\,\bar{I}_A - \bar{I} = 0 \quad . \tag{116}$$

By the elementary determinate operations, $\bar{T}_a$ can be upper triangularized, yielding

$$\bar{T}_a' = \begin{bmatrix} 1 & t'_{12} & t'_{13} \cdots t'_{1,N+1} \\ 0 & 1 & t'_{23} \cdots t'_{2,N+1} \\ \cdots & \cdots & \cdots \\ 0 & 0 & 0 \cdots 1 \; t'_{N,N+1} \end{bmatrix} \quad . \tag{117}$$

i_{A_N}, $i_{A_{N-1}}$, $i_{A_{N-2}}$ ··· can be successively determined by a series of back-substitutions,

$$i_{A_N} = - t'_{N,N+1}$$

$$i_{A_{N-1}} = - t'_{N-1,\ N+1} - t'_{N-1,\ N}\, i_{A_N} \tag{118}$$

$$\vdots$$

Several test matrices were employed to check the accuracy of this part of the program. It was found that nine significant digit accuracy was preserved in solving equations in four unknowns. Nine significant digits is the maximum accuracy that can be obtained using the ILLIAC in the floating-point mode. It was expected that the accuracy decreased as the number of equations increased. However, a sample calculation of an eight element antenna using the entire LPD analysis program, agreed in the first five significant digits with the computations performed on a desk calculator (which, incidently, took three weeks to perform).

APPENDIX B

MEASUREMENT CONSIDERATIONS

This section discusses several types of measurements which were performed in the experimental phase of this research. The procedure used in the measurement of the near field amplitude and phase will be considered in detail, whereas the input impedance, radiation pattern, and phase center measurements will be given only summary remarks. Except for the near field phase measurements standard techniques were used, and a majority of problems that arose were concerned with the application of these techniques to the particular antenna structures under investigation.

In any measurement involving log-periodic or log-spiral structures, one is faced with the problem of obtaining a great amount of data over a wide range of frequencies, if the frequency independence of the antenna is to be confirmed. The large bandwidth (4:1 or greater) over which the measurements must be performed places certain requirements on the experimental set-up and on the construction of the model. The experimental set-up must be changed several times throughout the course of a measurement because of the relatively narrow bandwidth of some testing equipment. This means that certain pieces of equipment are operated under slightly differing conditions, hence the set-up should provide for easy calibration and tuning.

Of equal importance is the actual fabrication of the model antenna. Construction tolerance should be figured on the basis of the shortest wavelength of operation. Thus, to some extent, the size of the antenna is determined by the accuracy which can be maintained in the model shop. The transverse dimensions of the feeder configuration of an LPD must remain small compared to the length of the shortest element. Nevertheless, the minimum

diameter of the feeder members is limited by the size of the internal feed coax. This again places a limit on the size of the antenna and the range of useful testing frequencies.

The above requirements led to the choice of the 100 mcs to 400 mcs range for the models used for impedance and near field measurements. A picture of one of the impedance models is shown in Figure 92. The feeder diameter was 0.420 inches, just large enough to accommodate the teflon dielectric RG-115 A/U coaxial cable which was chosen for its low loss and excellent uniformity. The pattern models were built for the 500 mcs to 2000 mcs range, the low frequency limit being dictated by the antenna pattern range facilities.

B.1 Near Field Measurements

The near field measurements consisted of determining the amplitude and phase of the voltage between the feeder conductors and the current into each dipole element. The voltage between the feeder conductors was found by measuring the signal received by a small probe antenna as pictured in Figure 93. The coax which energizes the antenna model runs through one of the hollow feeders. The other feeder member is equipped with a milled slot which guides the probe assembly throughout the length of the antenna. The probe is connected to a length of RG 58/U coaxial cable which is contained in a thin walled tube. The end of the tube opposite the probe assembly is fitted with a pointer which moves along the length of a rule, permitting accurate and repeatable positioning of the probe. The input impedance of the antenna was found to change 1.4% as the position of the probe was changed from the front of the antenna to the back. This is due to a small change in the feeder impedance owing to the presence of the milled slot. The variation

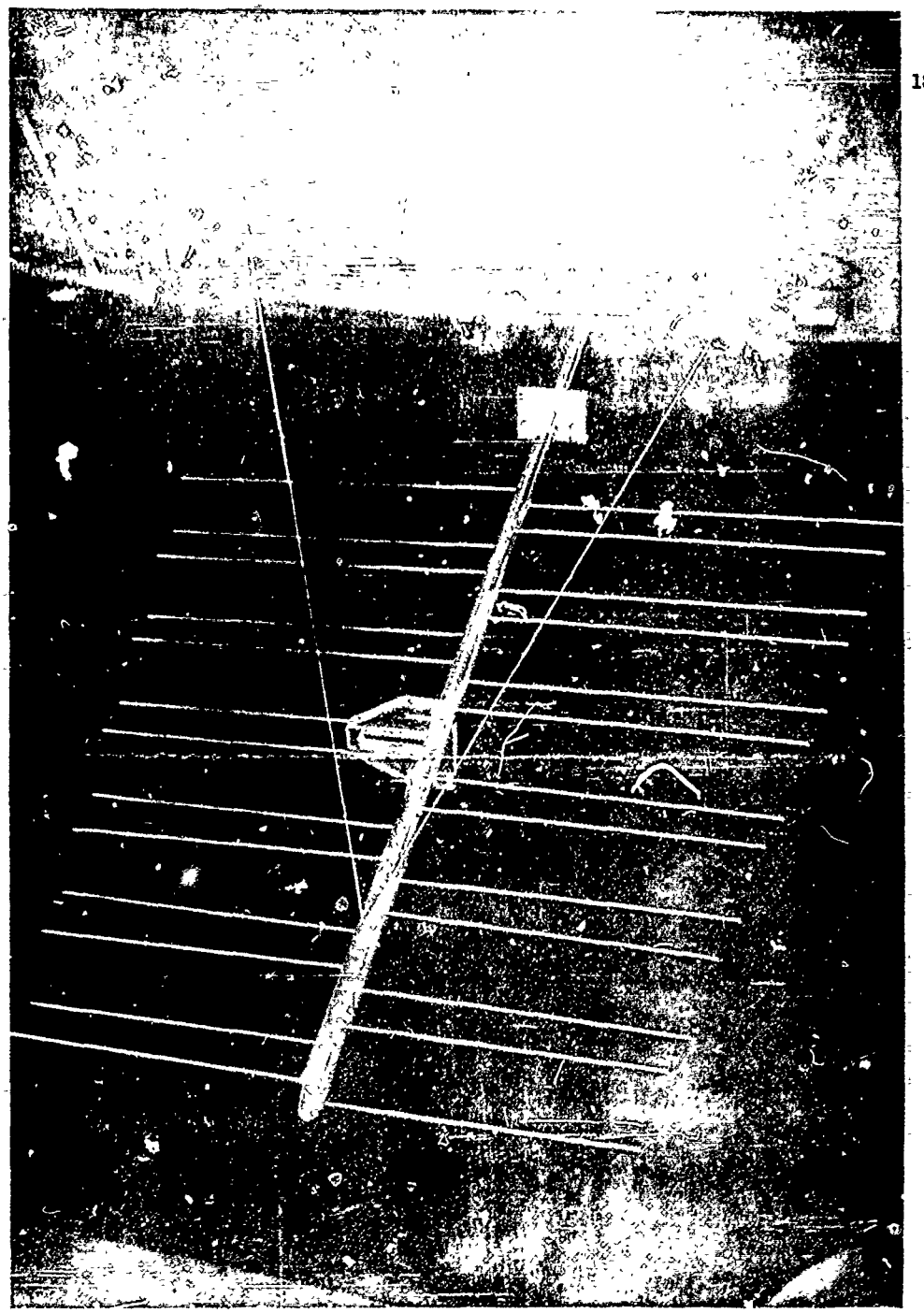

Figure 92. A picture of one of the antennas used for near field measurements

CONTINUOUSLY VARIABLE
E FIELD PROBE

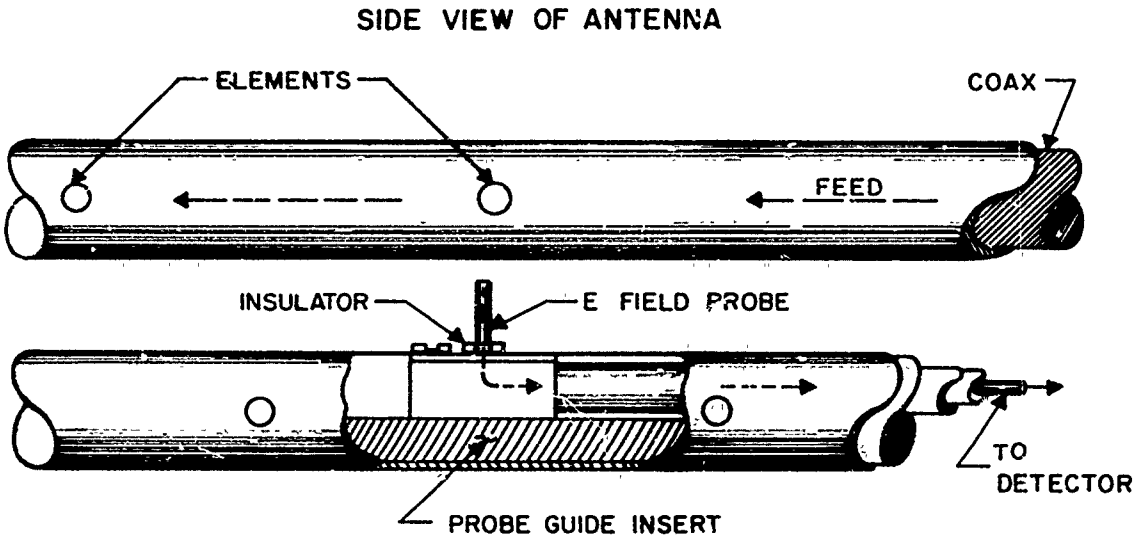

Figure 93. Details of the probe used for measuring the voltage between the feeder conductors

of the measured data was found to be independent of the length of the probe, which was varied from one eight to one quarter inch.

The measurement of the dipole element current was accomplished by the loop probe shown in Figure 94. The loop was designed to measure the magnetic field encircling the dipole, and was located as close to the base of the dipole as possible. Many difficulties were encountered in the selection of the proper loop size, spacing, and location. Shielding was necessary, as indicated by initial results with an unshielded loop. However, a completely shielded loop could not be constructed small and accurately, because there was no space to extend the pick-up coax through the guide assembly. The partially shielded loop in Figure 94 was selected as a compromise. The figure also shows the delectric disk which encloses the loop. This device was used to accurately position the loop at a constant distance from the dipole and in a plane containing the dipole element and the loop. The diameter of the loop and the dielectric was chosen such that a minimum amount of transverse motion was required in going from an element connected to one feeder to an element connected to the other. The configuration shown in Figure 94 was found to yield repeatable results although effects of undesired field components were never entirely eliminated. The largest extraneous component was thought to be due to the proximity of the current on the neighboring dipoles. It was estimated that this component was down at least 15 db from the desired component. The agreement between measured and computed results of the element current is therefore not as good as that of the feeder voltage.

B.1.1 Amplitude Measurements

A block diagram of the circuit used for the amplitude measurements is

CONTINUOUSLY VARIABLE
H FIELD PROBE

FRONT VIEW OF ANTENNA

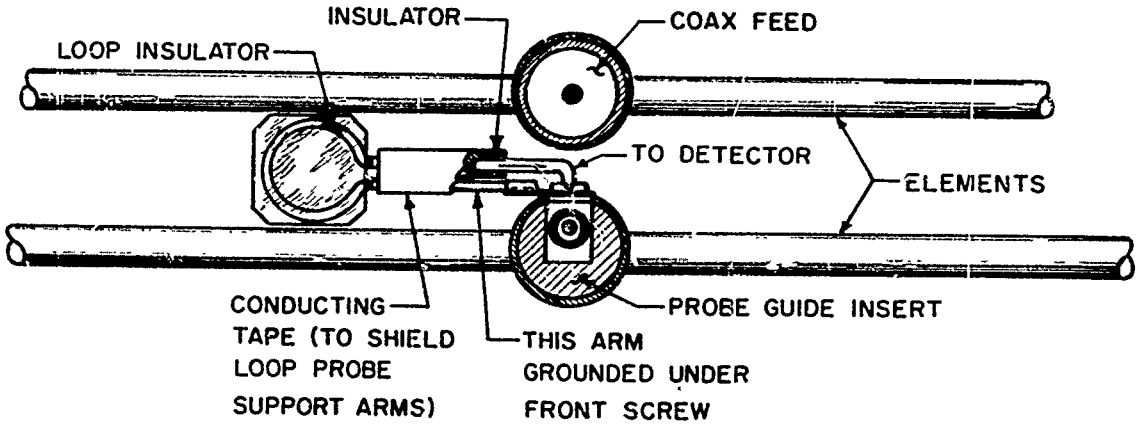

Figure 94. Details of the probe used for measuring the dipole element current

shown in Figure 95. The filtered output of the square wave modulated power oscillator is delivered to the antenna through a double stub tuner, which was adjusted for maximum signal to the probe. The square law detected output of the tuned probe is displayed on a SWR amplifier, peak tuned to the modulation frequency of 1000 cps. In performing the measurement, the probe was moved back and forth until the location of maximum signal was found. This point was taken as the 0 db reference. A reading was taken every centimeter throughout the length of the antenna. A power output from the oscillator on the order of several watts was required for a dynamic range of 40 db above noise.

B.1.2 Phase Measurements

The phase measuring circuit is diagrammed in Figure 96. The principal features are the hybrid junction and the balanced input adapter. The measurement theory is as follows: A CW reference signal, whose phase can be adjusted by means of the slotted section and line stretcher, is injected into the series arm (4) of the hybrid junction. The modulated test signal feeds the shunt arm (3). The RF phasor sum of these signals is impressed across the load connected to output (1) and the phasor difference appears at output (2). The balanced input adapter takes the audio difference of these detected signals from the hybrid junction and also provides the bias voltage for the bolometers. As shown in Figure 97, a sharp null is observed at the output of the balanced adapter when the reference signal is 90° out of phase with the test signal. Figure 97 compares the phasor relations and the nulls obtained of the balanced detection method and the single detection method. In the latter method only the difference channel would be used; the null is obtained when the reference and test signals are in phase, provided

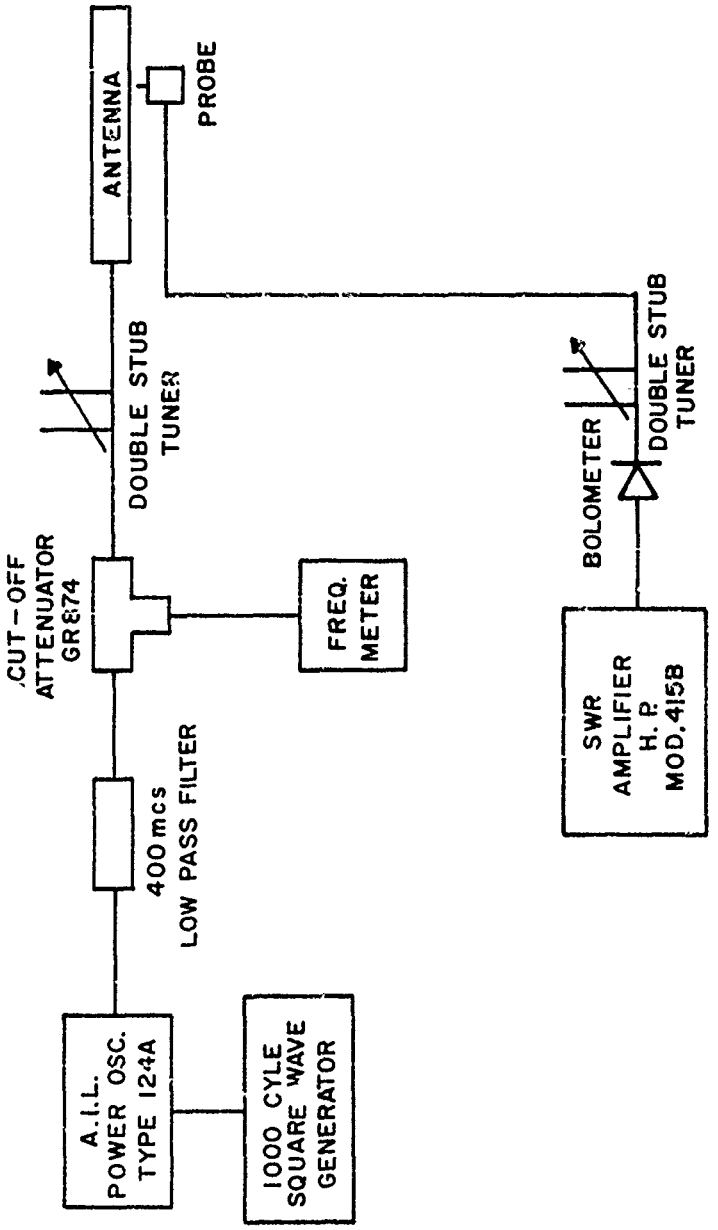

Figure 95. A block diagram of the amplitude measuring circuit

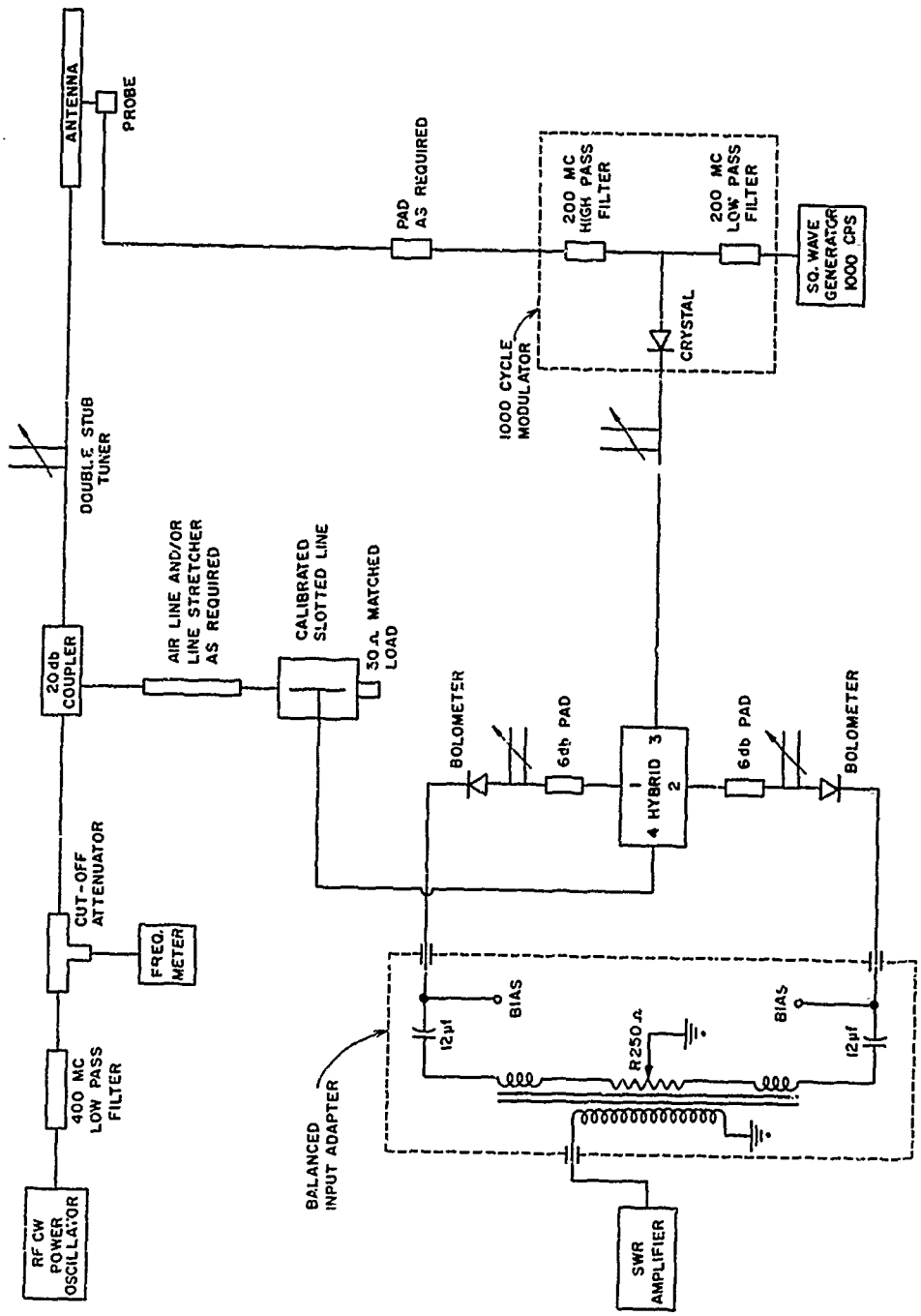

Figure 96. A block diagram of the phase measuring circuit

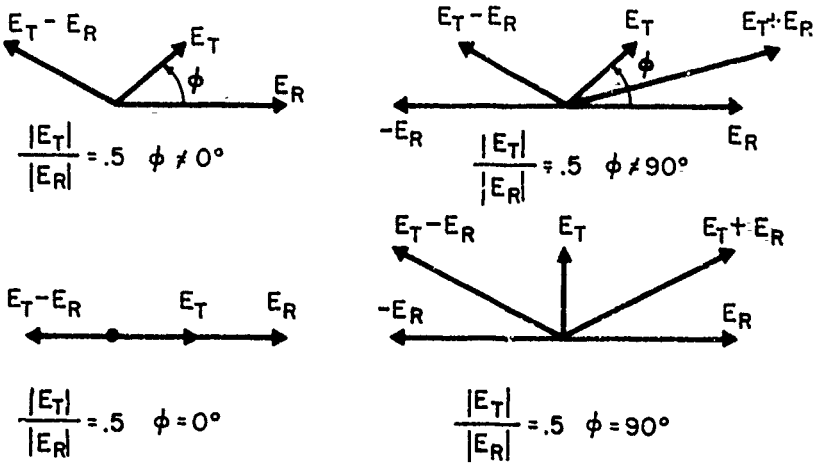

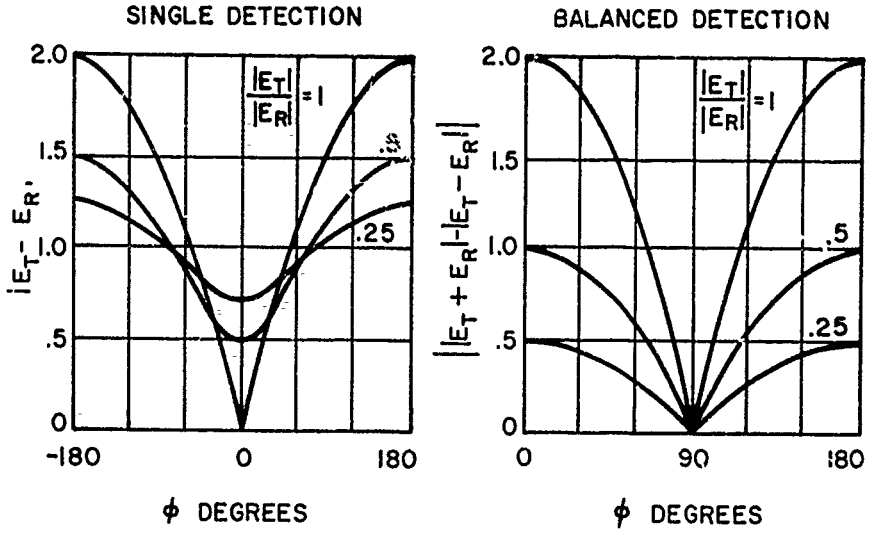

Figure 97. Phasor relations and the nulls obtained for values of $|E_T|/|E_R|$ for two methods of measuring relative phase. E_T is the test signal, E_R is the reference signal.

both signals have equal amplitude. Since the amplitude of the test signal varies, this method would require a precision variable attenuator calibrated for amplitude and phase. The advantage of the balanced detection system is that a well defined null is obtained even when the test and reference signals are of unequal amplitude. However a 180^{o} ambiguity exists in the balanced detection method. This can be resolved by carefully following the incremental phase shift as the probe is moved away from the reference position.

For phase measurements the probe signal, rather than the oscillator is modulated. This results in a sharper null than would otherwise be obtained. Even though the unmodulated reference signal, which may be larger than the test signal, is present at the detectors, the result is only a DC component of current to the transformer. The only error from the reference signal is due to leak-through in the hybrid junction. This is negligible; in commercially available instrument hybrids the decoupling is on the order of 50 db.

The experimental set-up for the near field phase measurements is shown in Figure 98. All the equipment was mounted on a bench which could be rolled up to a second story window in the Antenna Laboratory, in order for the model under test to look into an uncluttered environment. The most predominant feature in the picture is the take-up reel for the cable which is connected to the probe. In the phase measurements it is important that the flexing of the cable be controlled and held to a minimum; the take-up reel serves this purpose.

The following procedure was carried out to balance the hybrid circuit after each change of frequency. Refer to Figure 96. The connection at terminal (4) is broken and replaced with a matched load. The bias to

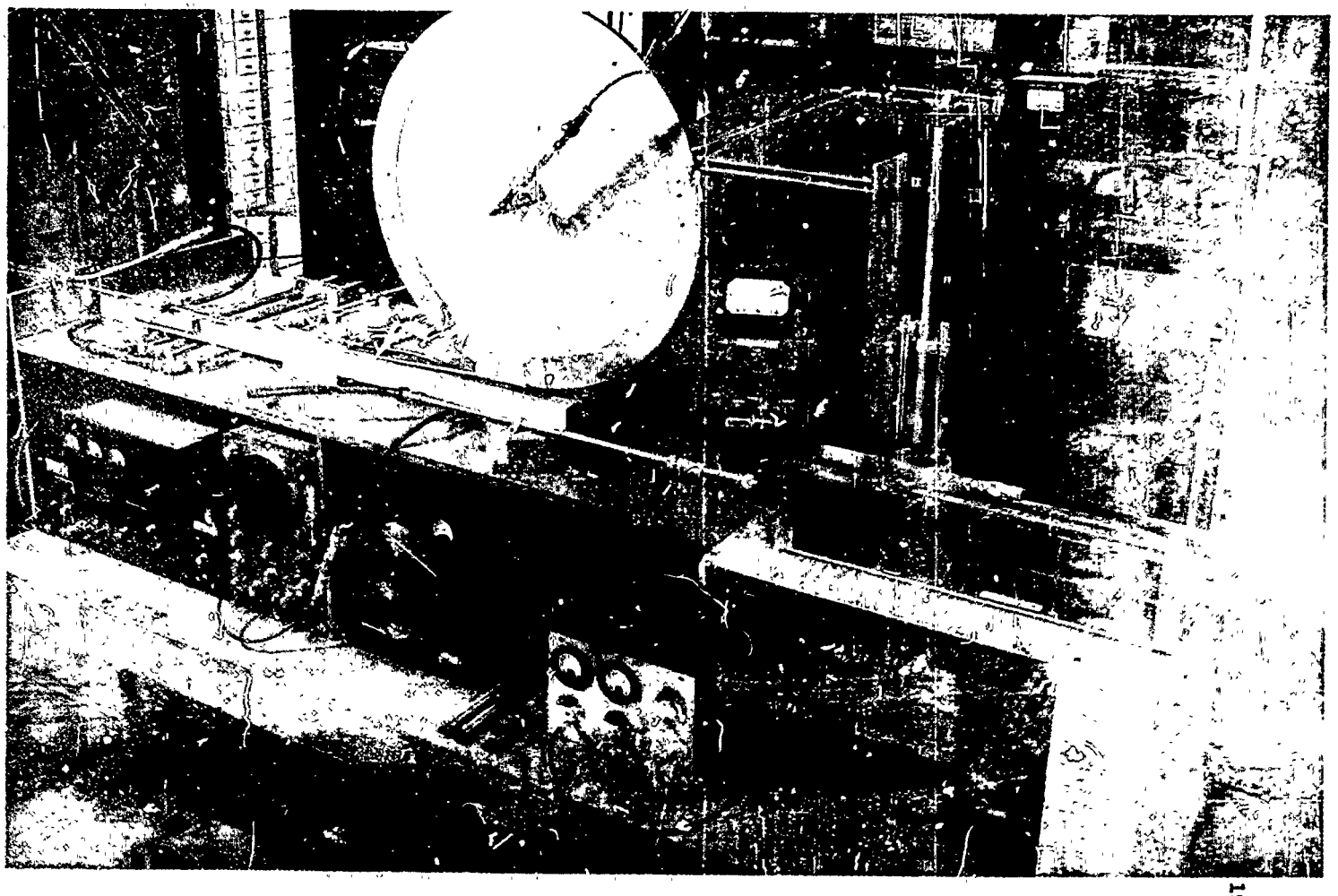

Figure 96. A picture of the equipment arrangement used in the near field measurements

each bolometer was adjusted to 8.75 ma. One bolometer was then disconnected and the balancing potentiometer was adjusted for maximum output. The tuning stubs throughout the circuit were then tuned for maximum output. The other bolometer was reconnected and the first was disconnected. The balancing potentiometer was again adjusted for maximum output, and only the stubs associated with the operative bolometer were tuned, the others were left as previously adjusted. With both bolometers connected, the balancing potentiometer was adjusted to null the signal. This step had the effect of balancing out any leak-through component of the test signal; it also equalized any residual unbalance which might have existed between the two bolometers. The slotted line was reconnected, completing the tune-up procedure.

The probe was positioned at a chosen point and the phase of the reference signal was changed to obtain a null. This was repeated every centimeter along the feeder of the antenna. By recording the phase change introduced by the slotted line, the relative phase of the test signal was determined.

B.2 Impedance Measurements

The input impedance of the LPD models was determined by the SWR and null shift method. The set-up incorporated a PRD standing wave indicator or alternatively a HP slotted line, and a tuned amplifier using a bolometer detector.

The short circuit reference plane for the impedance measurements was taken at the front of the antenna, as shown in Figure 99. This choice of a reference plane lumps the gap or terminal impedance in with the antenna impedance. For this reason, extra care was taken in the construction of the feed region. After several trials it was found that the feed region

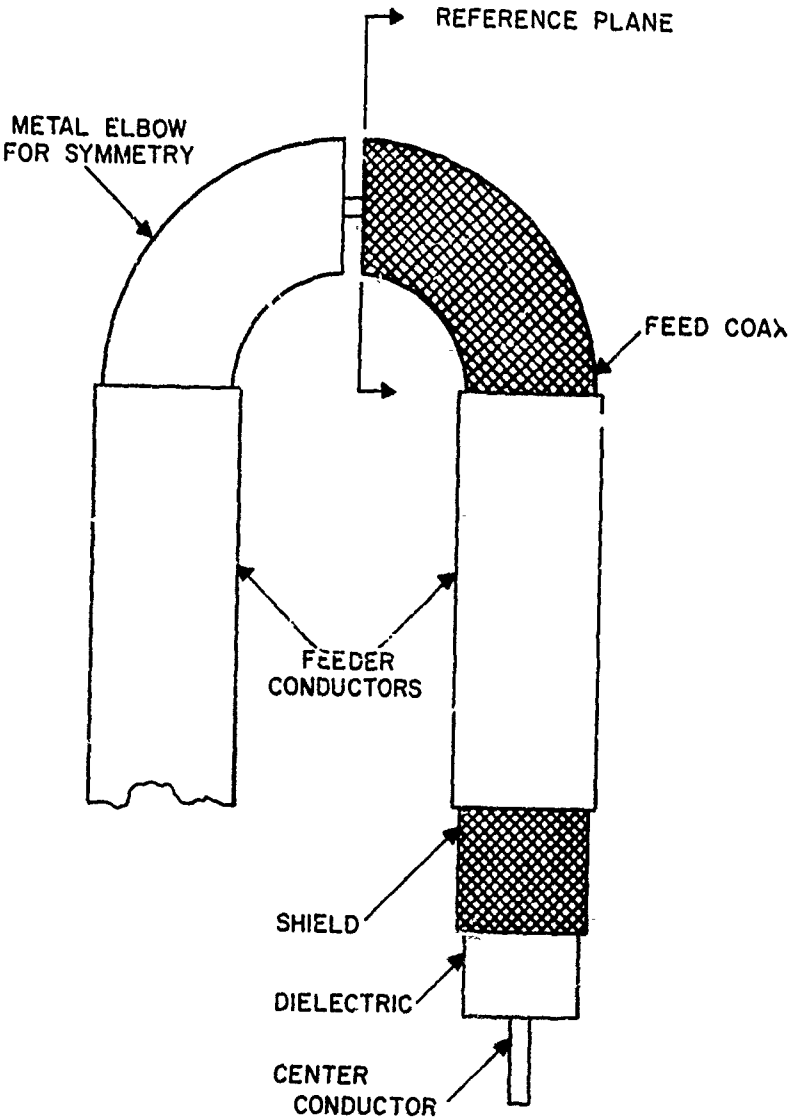

Figure 99. Details of the symmetrical feed point, showing the reference plane for impedance measurements

configuration shown in Figure 99 was best from the standpoint of introducing a minimum unbalanced current component and a minimum gap reactance. Ideally, the reference measurement should be made at every frequency, just before or after the corresponding load measurement. This was not done because of the large number of test frequencies involved and because of the uncertainty in reconstructing an identical feed configuration each time. Instead, the electrical length of the coax from the reference plane to a reference on the measuring device was determined for all the frequencies within the band, prior to taking the load measurements. Several lengths of cable were tested; the one which yielded the most uniform results was used.

B.3 Far Field Measurements

The radiation patterns of the LPD models were recorded by the commercially equipped University of Illinois Antenna Laboratory pattern range facilities. The tower and an LPD model are pictured in Figure 100. Using a bolometer as the square law detector, the system was found to have a linear dynamic range of greater than 20 db. Since the LPD models tested had an operating bandwidth of 3:1 or greater, interference from other sources operating within this band sometimes presented a problem. Except for the signal from an S-band radar that was 250 yards away, the interference problem was eliminated by filtering and tuning techniques.

The phase center measurements were accomplished using the balanced detector shown in Figure 96, except that the model under test assumed the role of the probe antenna. The test model was mounted on a tower in such a way that the axis of rotation could be moved toward or away from the transmitting antenna. The relative phase of the received signal was plotted as a function of the azimuth angle over the range $\pm$ 40 degrees from the dead

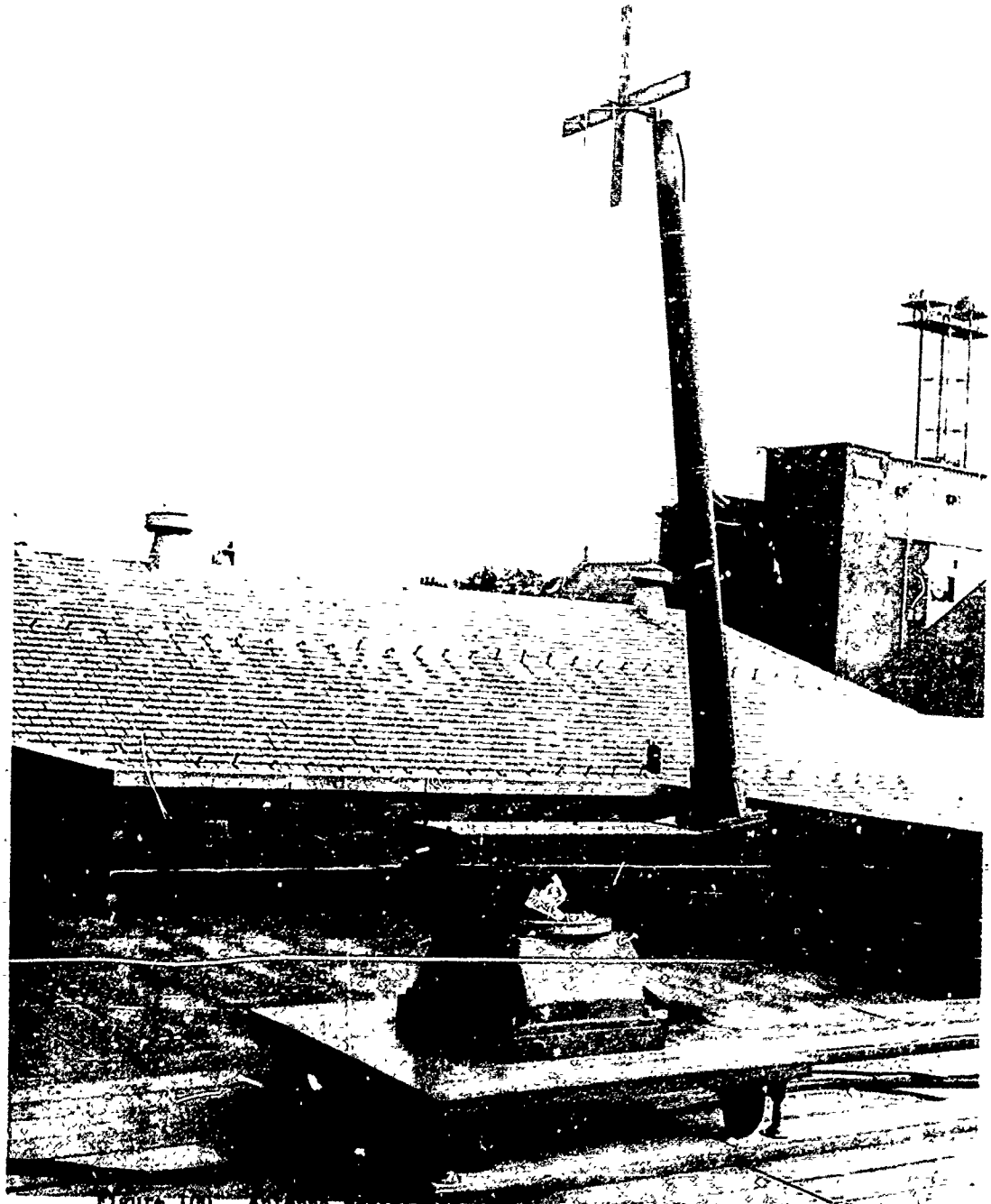

Figure 100. Antenna positioner and tower at the University of Illinois Antenna Laboratory

ahead position. The center of rotation of the model was varied from one plot to the next until a position was found such that the phase was most nearly constant over the range of the azimuth angle. The boresight and positioning accuracy was such that the location of the phase center could be determined within an error of $\pm$ 0.125 inch, which was about 0.01 λ at the testing frequencies.

ANTENNA LABORATORY
TECHNICAL REPORTS AND MEMORANDA ISSUED

Contract AF33(616)-310

"Synthesis of Aperture Antennas," Technical Report No. 1, C.T.A. Johnk, October, 1954.*

"A Synthesis Method for Broad-band Antenna Impedance Matching Networks," Technical Report No. 2, Nicholas Yaru, 1 February 1955.*

"The Asymmetrically Excited Spherical Antenna," Technical Report No. 3, Robert C. Hansen, 30 April 1955.*

"Analysis of an Airborne Homing System," Technical Report No. 4, Paul E. Mayes, 1 June 1955 (CONFIDENTIAL).

"Coupling of Antenna Elements to a Circular Surface Waveguide," Technical Report No. 5, W. E. King and R. H. DuHamel, 30 June 1955.*

"Axially Excited Surface Wave Antennas," Technical Report No. 7, D. E. Royal, 10 October 1955.*

"Homing Antennas for the F-86F Aircraft (450-2500mc)," Technical Report No. 8, P. E. Mayes, R. F. Hyneman, and R. C. Becker, 20 February 1957, (CONFIDENTIAL).

"Ground Screen Pattern Range," Technical Memorandum No. 1, Roger R. Trapp, 10 July 1955.*

Contract AF33(616)-3220

"Effective Permeability of Spheroidal Shells," Technical Report No. 9, E. J. Scott and R. H. DuHamel, 16 April 1956.

"An Analytical Study of Spaced Loop ADF Antenna Systems," Technical Report No. 10, D. G. Berry and J. B. Kreer, 10 May 1956.

"A Technique for Controlling the Radiation from Dielectric Rod Waveguides," Technical Report No. 11, J. W. Duncan and R. H. DuHamel, 15 July 1956.*

"Directional Characteristics of a U-Shaped Slot Antenna," Technical Report No. 12, Richard C. Becker, 30 September 1956.**

"Impedance of Ferrite Loop Antennas," Technical Report No. 13, V. H. Rumsey and W. L. Weeks, 15 October 1956.

"Closely Spaced Transverse Slots in Rectangular Waveguide," Technical Report No. 14, Richard F. Hyneman, 20 December 1956.

"Distributed Coupling to Surface Wave Antennas," Technical Report No. 15, Ralph Richard Hodges, Jr., 5 January 1957.**

"The Characteristic Impedance of the Fin Antenna of Infinite Length," Technical Report No. 16, Robert L. Carrel, 15 January 1957.*

"On the Estimation of Ferrite Loop Antenna Impedance," Technical Report No. 17, Walter L. Weeks, 10 April 1957.*

"A Note Concerning a Mechanical Scanning System for a Flush Mounted Line Source Antenna," Technical Report No. 18, Walter L. Weeks, 20 April 1957.

"Broadband Logarithmically Periodic Antenna Structures," Technical Report No. 19, R. H. DuHamel and D. E. Isbell, 1 May 1957.

"Frequency Independent Antennas," Technical Report No. 20, V. H. Rumsey, 25 October 1957.

"The Equiangular Spiral Antenna," Technical Report No. 21, J. D. Dyson, 15 September 1957.

"Experimental Investigation of the Conical Spiral Antenna," Technical Report No. 22, R. L. Carrel, 25 May 1957.**

"Coupling between a Parallel Plate Waveguide and a Surface Waveguide," Technical Report No. 23, E. J. Scott, 10 August 1957.

"Launching Efficiency of Wires and Slots for a Dielectric Rod Waveguide," Technical Report No. 24, J. W. Duncan and R. H. DuHamel, August 1957.

"The Characteristic Impedance of an Infinite Biconical Antenna of Arbitrary Cross Section," Technical Report No. 25, Robert L. Carrel, August 1957.

"Cavity-Backed Slot Antennas," Technical Report No. 26, R. J. Tector, 30 October 1957.

"Coupled Waveguide Excitation of Traveling Wave Slot Antennas," Technical Report No. 27, W. L. Weeks, 1 December 1957.

"Phase Velocities in Rectangular Waveguide Partially Filled with Dielectric," Technical Report No. 28, W. L. Weeks, 20 December 1957.

"Measuring the Capacitance per Unit Length of Biconical Structures of Arbitrary Cross Section," Technical Report No. 29, J D. Dyson, 10 January 1958.

"Non-Planar Logarithmically Periodic Antenna Structure," Technical Report No. 30, D. W. Isbell, 20 February 1958.

"Electromagnetic Fields in Rectangular Slots," Technical Report No. 31, N. J. Kuhn and P. E. Mast, 10 March 1958.

"The Efficiency of Excitation of a Surface Wave on a Dielectric Cylinder," Technical Report No. 32, J. W. Duncan, 25 May 1958.

"A Unidirectional Equiangular Spiral Antenna," Technical Report No. 33, J. D. Dyson, 10 July 1958.

"Dielectric Coated Spheroidal Radiators," Technical Report No. 34, W. L. Weeks, 12 September 1958.

"A Theoretical Study of the Equiangular Spiral Antenna," Technical Report No. 35, P. E. Mast, 12 September 1958.

Contract AF33(616)-6079

"Use of Coupled Waveguides in a Traveling Wave Scanning Antenna," Technical Report No. 36, R. H. MacPhie, 30 April 1959.

"On the Solution of a Class of Wiener-Hopf Integral Equations in Finite and Infinite Ranges," Technical Report No. 37, Raj Mittra, 15 May 1959.

"Prolate Spheroidal Wave Functions for Electromagnetic Theory," Technical Report No. 38, W. L. Weeks, 5 June 1959.

"Log Periodic Dipole Arrays," Technical Report No. 39, D. E. Isbell, 1 June 1959.

"A Study of the Coma-Corrected Zoned Mirror by Diffraction Theory," Technical Report No. 40, S. Dasgupta and Y. T. Lo, 17 July 1959.

"The Radiation Pattern of a Dipole on a Finite Dielectric Sheet," Technical Report No. 41, K. G. Balmain, 1 August 1959.

"The Finite Range Wiener-Hopf Integral Equation and a Boundary Value Problem in a Waveguide," Technical Report No. 42, Raj Mittra, 1 October 1959.

"Impedance Properties of Complementary Multiterminal Planar Structures," Technical Report No. 43, G. A. Deschamps, 11 November 1959.

"On the Synthesis of Strip Sources," Technical Report No. 44, Raj Mittra, 4 December 1959.

" Numerical Analysis of the Eigenvaluc Problem of Waves in Cylindrical Waveguides," Technical Report No. 45, C. H Tang and Y. T. Lo, 11 March 1960.

"New Circularly Polarized Frequency Independent Antennas with Conical Beam or Omnidirectional Patterns," Technical Report No. 46, J D. Dyson and P. E. Mayes, 20 June 1960.

"Logarithmically Periodic Resonant-V Arrays," Technical Report No. 47, P. E. Mayes and R. L. Carrel, 15 July 1960

"A Study of Chromatic Aberration of a Coma-Corrected Zoned Mirror," Technical Report No. 48, Y. T. Lo.

"Evaluation of Cross-Correlation Methods in the Utilization of Antenna Systems," Technical Report No. 49, R. H. MacPhie, 25 January 1961.

"Synthesis of Antenna Product Patterns Obtained from a Single Array," Technical Report No. 50, R. H. MacPhie.

---

* Copies available for a three-week loan period.

** Copies no longer available.

AF 33(616)-6079

DISTRIBUTION LIST

One copy each unless otherwise indicated

Armed Services Technical Information Agency
Attn: TIP-DR
Arlington Hall Station
Arlington 12, Virginia (10 copies)

Aeronautical Systems Division
Attn: (ASRNRE-4)
Wright-Patterson Air Force Base
Ohio (3 copies)

Aeronautical Systems Division
Attn: ASDSED, Mr. Mulligan
Wright-Patterson Air Force Base
Ohio

Aeronautical Systems Division
Attn: ASAD - Library
Wright-Patterson Air Force Base
Ohio

Aeronautical Systems Division
Attn: AFCIN-4B1A
Wright-Patterson Air Force Base
Ohio

Air Force Cambridge Research Laboratory
Attn: CRRD
Laurence G. Hanscom Field
Bedford, Massachusetts

AOGC
Attn: PGTRI, Technical Library
Eglin Air Force Base
Florida

Commander
Air Force Missile Test Center
Patrick Air Force Base
Florida

Commander
Air Force Missile Development Center
Attn: Technical Library
Holloman Air Force Base
New Mexico

Air Force Ballistic Missile Division
Attn: Technical Library, Air Force Unit Post Office
Los Angeles, California

Director
Ballistics Research Laboratory
Attn: Ballistics Measurement Lab.
Aberdeen Proving Ground, Maryland

National Aeronautics & Space Adm.
Attn: Librarian
Langley Field, Virginia

Rome Air Development Center
Attn: RCLTM
Griffiss Air Force Base
New York

Research & Development Command
Hq USAF (AFDRD-RE)
Washington 25, D. C.

Office of Chief Signal Officer
Engineering & Technical Division
Attn: SIGNET-5
Washington 25, D. C.

Commander
U. S. Army White Sands Signal Agency
Attn: SIGWS-FC-02
White Sands, New Mexico

801 Air Division
Attn: DCTID
Lockbourne Air Force Base
Ohio

Director
Surveillance Department
Evans Area
Attn: Technical Document Center
Belmar, New Jersey

Commander
U. S. Naval Air Test Center
Attn: WST-54, Antenna Section
Patuxent River, Maryland

Material Laboratory, Code 932
New York Naval Shipyard
Brooklyn 1, New York

Commanding Officer
Diamond Ordnance Fuse Laboratories
Attn: 240
Washington 25, D. C.

Director
U. S. Navy Electronics Laboratory
Attn: Library
San Diego 52, California

National Bureau of Standards
Department of Commerce
Attn: Dr. A. G. McNish
Washington 25, D. C.

Adams-Russell Company
200 Sixth Street
Attn: Library (Antenna Section)
Cambridge, Massachusetts

Aero Geo Astro
Attn: Security Officer
1200 Duke Street
Alexandria, Virginia

NASA Goddard Space Flight Center
Attn: Antenna Section, Code 523
Greenbelt, Maryland

Airborne Instruments Labs., Inc.
Attn: Librarian (Antenna Section)
Walt Whitman Road
Melville, L. I., N. Y.

American Electronic Labs
Box 552 (Antenna Section)
Lansdale, Pennsylvania

American Systems Inc.
Attn: Technical Library
(Antenna Section)
3412 Century Blvd.
Inglewood, California

Andrew Alfred Consulting Engineers
Attn: Librarian (Antenna Section)
299 Atlantic Ave.
Boston 10, Massachusetts

Amphenol-Borg Electronic Corporation
Attn: Librarian (Antenna Section)
2801 S. 25th Avenue
Broadview, Illinois

Bell Aircraft Corporation
Attn: Technical Library
(Antenna Section)
Buffalo 5, New York

Bendix Radio Division of
Bendix Aviation Corporation
Attn: Technical Library
(For Dept 462-4)
Baltimore 4, Maryland

Boeing Airplane Company
Aero Space Division
Attn: Technical Library
M/F Antenna & Radomes Unit
Seattle, Washington

Boeing Airplane Company
Attn: Technical Library
M/F Antenna Systems Staff Unit
Wichita, Kansas

Chance Vought Aircraft Inc.
THRU: BU AER Representative
Attn: Technical Library
M/F Antenna Section
P. O. Box 5907
Dallas 22, Texas

Collins Radio Company
Attn: Technical Library (Antenna
Section)
Cedar Rapids, Iowa

Convair
Ft. Worth Division
Attn: Technical Library (Antenna
Section)
Grants Lane
Fort Worth, Texas

Convair
Attn: Technical Library (Antenna
Section)
P. O. Box 1950
San Diego 12, California

Dalmo Victor Company
Attn: Technical Library (Antenna Section)
1515 Industrial Way
Belmont, California

Dorne & Margolin, Inc.
Attn: Technical Library (Antenna Section)
30 Sylvester Street
Westbury, L. I., N. Y.

Dynatronics Inc.
Attn: Technical Library (Antenna Section)
Orlando, Florida

Electronic Communications, Inc.
Research Division
Attn: Technical Library
1830 York Road
Timonium, Maryland

Fairchild Engine & Airplane Corporation
Fairchild Aircraft & Missiles Division
Attn: Technical Library (Antenna Section)
Hagerstown 10, Maryland

Georgia Institute of Technology
Engineering Experiment Station
Attn: Technical Library
M/F Electronics Division
Atlanta 13, Georgia

General Electric Company
Electronics Laboratory
Attn: Technical Library
Electronics Park
Syracuse, New York

General Electronic Labs., Inc.
Attn: Technical Library (Antenna Section)
18 Ames Street
Cambridge 42, Massachusetts

General Precision Lab., Division of General Precision Inc.
Attn: Technical Library (Antenna Section)
63 Bedford Road
Pleasantville, New York

Goodyear Aircraft Corporation
Attn: Technical Library
M/F Dept 474
1210 Massilon Road
Akron 15, Ohio

Granger Associates
Attn: Technical Library
Antenna Section
974 Commercial Street
Palo Alto, California

Grumman Aircraft Engineering Corp.
Attn: Technical Library
(M/F Avionics Engineering)
Bethpage, New York

The Hallicrafters Company
Attn: Technical Library (Antenna Section)
4401 W. Fifth Avenue
Chicago 24, Illinois

Hoffman Laboratories Inc.
Attn. Technical Library (Antenna Section)
Los Angeles 7, California

John Hopkins University
Applied Physics Laboratory
8621 Georgia Avenue
Silver Springs, Maryland

Hughes Aircraft Corporation
Attn: Technical Library (Antenna Section)
Florence & Teal Street
Culver City, California

University of Illinois
Attn: Technical Library (Dept of Electrical Engineering)
Urbana, Illinois

ITT Laboratories
Attn: Technical Library (Antenna Section)
500 Washington Avenue
Nutley 10, New Jersey

Lincoln Laboratories
Massachusetts Institute of Technology
Attn: Document Room
P. O. Box 73
Lexington 73, Massachusetts

Litton Industries
Attn: Technical Library (Antenna Section)
4900 Calvert Road
College Park, Maryland

Lockheed Missile & Space Division
Attn: Technical Library (M/F Dept-58-40, Plant 1, Bldg. 130)
Sunnyvale, California

The Martin Company
Attn: Technical Library (Antenna Section)
P. O. Box 179
Denver 1, Colorado

The Martin Company
Attn: Technical Library (Antenna Section)
Baltimore 3, Maryland

The Martin Company
Attn: Technical Library (M/F Microwave Laboratory)
Box 5837
Orlando, Florida

W. L. Maxson Corporation
Attn: Technical Library (Antenna Section)
460 West 34th Street
New York 1, New York

McDonnell Aircraft Corporation
Attn: Technical Library (Antenna Section)
Box 516
St. Louis 66, Missouri

Melpar, Inc.
Attn: Technical Library (Antenna Section)
3000 Arlington Blvd.
Falls Church, Virginia

University of Michigan
Radiation Laboratory
Willow Run
201 Catherine Street
Ann Arbor, Michigan

Mitre Corporation
Attn: Technical Library (M/F Electronic Warfare Dept. D-21)
Middlesex Turnpike
Bedford, Massachusetts

New Mexico State University
Attn: Technical Library (M/F Antenna Dept)
University Park, New Mexico

North American Aviation Inc.
Attn: Technical Library (M/F Engineering Dept.)
4300 E. Fifth Avenue
Columbus 16, Ohio

North American Aviation Inc.
Attn: Technical Library (M/F Dept 56)
International Airport
Los Angeles, California

Northrop Aircraft, Inc.
NORAIR Division
Attn: Technical Library (M/F Dept 2135)
Hawthorne, California

Ohio State University Research Foundation
Attn: Technical Library (M/F Antenna Laboratory)
1314 Kinnear Road
Columbus 12, Ohio

Philco Corporation
Government & Industrial Division
Attn: Technical Library (M/F Antenna Section)
4700 Wissachickon Avenue
Philadelphia 44, Pennsylvania

Radio Corporation of America
RCA Laboratories Division
Attn: Technical Library
(M/F Antenna Section)
Princeton, New Jersey

Radiation Inc.
Attn: Technical Library (M/F)
Antenna Section
Drawer 37
Melbourne, Florida

Radioplane Company
Attn: Librarian (M/F Aerospace Lab)
8000 Woodly Avenue
Van Nuys, California

Ramo-Wooldridge Corporation
Attn: Librarian (Antenna Lab)
Conoga Park, California

Rand Corporation
Attn: Librarian (Antenna Lab)
1700 Main Street
Santa Monica, California

Rantec Corporation
Attn: Librarian (Antenna Lab)
23999 Ventura Blvd.
Calabasas, California

Raytheon Electronics Corporation
Attn: Librarian (Antenna Lab)
1089 Washington Street
Newton, Massachusetts

Republic Aviation Corporation
Applied Research & Development
Division
Attn: Librarian (Antenna Lab)
Farmingdale, New York

Sanders Associates
Attn: Librarian (Antenna Lab)
95 Canal Street
Nashua, New Hampshire

Southwest Research Institute
Attn: Librarian (Antenna Lab)
8500 Culebra Road
San Antonio, Texas

H. R. B. Singer Corporation
Attn: Librarian (Antenna Lab)
State College, Pennsylvania

Sperry Microwave Electronics Company
Attn: Librarian (Antenna Lab)
P. O. Box 1828
Clearwater, Florida

Sperry Gyroscope Company
Attn: Librarian (Antenna Lab)
Great Neck, L. I., New York

Stanford Electronic Laboratory
Attn: Librarian (Antenna Lab)
Stanford, California

Stanford Research Institute
Attn: Librarian (Antenna Lab)
Menlo Park, California

Sylvania Electronic System
Attn: Librarian (M/F Antenna &
Microwave Lab)
100 First Street
Waltham 54, Massachusetts

Sylvania Electronic System
Attn: Librarian (Antenna Lab)
P. O. Box 188
Mountain View, California

Technical Research Group
Attn: Librarian (Antenna Section)
2 Aerial Way
Syosset, New York

Ling Temco Aircraft Corporation
Temco Aircraft Division
Attn: Librarian (Antenna Lab)
Garland, Texas

Texas Instruments, Inc.
Attn: Librarian (Antenna Lab)
6000 Lemmon Ave.
Dallas 9, Texas

A. S. Thomas Inc.
Attn: Librarian (Antenna Lab)
355 Providence Highway
Westwood, Massachusetts

Westinghouse Electric Corporation
Air Arms Division
Attn: Librarian (Artenna Lab)
P. O. Box 746

Wheeler Laboratories
Attn: Librarian (Antenna Lab)
Box 561
Smithtown, New York

Electrical Engineering Research Laboratory
University of Texas
Box 8026, Univ. Station
Austin, Texas

University of Michigan Research Institute
Electronic Defense Group
Attn: Dr. J. A. M. Lyons
Ann Arbor, Michigan

New Mexico State University
Head Antenna Department
Physical Sci. e Laboratory
University Park, New Mexico

Bell Telephone Laboratories, Inc.
Whippany Laboratory
Whippany, New Jersey
Attn: Technical Reports Librarian
Room 2A-165

Robert C. Hansen
Aerospace Corporation
Box 95085
Los Angeles 45, California

Dr. D. E. Royal
Ramo-Wooldridge, a division of Thompson Ramo Wooldridge Inc.
8433 Fallbrook Avenue
Canoga Park, California

Dr. S. Dasgupta
Government Engineering College
Jabalpur, M.P.
India

Dr. Richard C. Becker
10829 Berkshire
Westchester, Illinois

Dr. Harry Letaw, Jr.
Raytheon Company
Surface Radar and Navigation Operations
State Road West
Wayland, Massachusetts

Dr. Frank Fu Fang
IBM Research Laboratory
Poughkeepsie, New York

Mr. Dwight Isbell
1422 11th West
Seattle 99, Washington

Dr. A. K. Chatterjee
Vice Principal
Birla Engineering College
Pilani, Rajasthan
India